Jointless Bridges:

Volume III—Summary Report

PUBLICATION NO. FHWA-RD-03-056

MAY 2007

U.S. Department of Transportation
Federal Highway Administration

Research, Development, and Technology
Turner-Fairbank Highway Research Center
6300 Georgetown Pike
McLean, VA 22101-2296

Foreword

These five reports contain the results of a Federal Highway Administration (FHWA) study of the thermal response of jointless bridges. The objective of this analytical and experimental research was to provide a scientific engineering basis for designing jointless bridges. Although jointless bridges have been built by a number of States, the design procedures were essentially empirical and based on the experience of the organization designing the bridge. In some quarters, thlack of a specification or rigorous design procedure created a barrier to the adoption of the jointless bridge. It is hoped that the information contained in this report will encourage the wider use of jointless bridges.

This report will be of interest to bridge designers and engineers; Federal, State and municipal agencies; other bridge owners; contractors; bridge designers; and researchers and educators.

This is the summary report of a five-report series. The other manuscripts in this series contain research and field notes, and will be distributed only through the National Technical Information Service (NTIS). Go to www.NTIS. gov for more information about the other volumes in this jointless bridge series. The reports in this series include:

- *Jointless Bridges: Volume I: Experimental Research and Field Notes: Part 1*. (NTIS Tracking Number: PB2007-108154
- *Jointless Bridges: Volume I: Experimental Research and Field Notes: Part 2*. (NTIS Tracking Number: PB2007-108155
- *Jointless Bridges: Volume I: Experimental Research and Field Notes: Part 3*. (NTIS Tracking Number: PB2007-108156
- *Jointless Bridges: Volume II: Analytical Research and Proposed Design Procedures*. (NTIS Tracking Number: PB2007-108157
- *Jointless Bridges: Volume III: Summary Report. Available on the Web at www.tfhrc.gov.* (FHWA Publication Number: FHWA-RD-03-056)

Gary L. Henderson
Director, Office of Infrastructure
Research and Development

Notice

Quality Assurance Statement

The Federal Highway Administration (FHWA) provides high-quality information to serve Government, industry, and the public in a manner that promotes public understanding. Standards and policies are used to ensure and maximize the quality, objectivity, utility, and integrity of its information. FHWA periodically reviews quality issues and adjusts its programs and processes to ensure continuous quality improvement.

1. Report No. FHWA-RD-03-056	2. Government Accession No.	3. Recipient's Catalog No.
4. Title and Subtitle Jointless Bridges: Volume III—Summary Report		5. Report Date May 2007
		6. Performing Organization Code 230430
7. Author(s) Ralph Oesterle, Habib Tabatabai, T.J. Larson, T. Refai, J.S. Volz, A. Scanlon		8. Performing Organization Report No.
9. Performing Organization Name and Address CTL Group 5420 Old Orchard Road Skokie, IL 60077-1030		10. Work Unit No.
		11. Contract or Grant No. DTFH61-92-C-00154
12. Sponsoring Agency Name and Address Office of Infrastructure R&D (HRDI-07) Federal Highway Administration 6300 Georgetown Pike McLean, VA 22101-2296		13. Type of Report and Period Covered Final Report: September 1992 – September 2005
		14. Sponsoring Agency Code

15. Supplementary Notes
Contracting Officer's Technical Representatives: John O'Fallon, P.E. (HRDI-07) and Glenn Washer, Ph.D. (HRDI-10)

16. Abstract

This is the third of three volumes reporting on an experimental and analytical study of the response of jointless bridges to thermal (and other) changes. Volume I provides a detailed report on the experimental phase of the study. Volume II describes the analytical research performed and considers a proposed design procedure. This volume contains an abridged, but still detailed, description of the experimental and analytical research reported in the first two volumes and presents proposed design procedures and valuable recommendations on retrofitting jointed structures.

The experimental phase (volume I) consisted of material, thermal restraint, beam and component, and pile tests, plus field surveys and tests of jointless bridges. This phase addressed thermal movements and stresses, creep and shrinkage, environmental effects, pile behavior, and passive soil pressure. The beam tests used two full-scale, two-span continuous, composite steel and prestressed concrete (PS/C) sections with slab sections attached that were exposed outside for 2 years. The survey was of 15 jointless bridges in Tennessee. The objectives of the experimental phase were to study the significance of short-term, environmentally-dependent creep and shrinkage and their influence on the relief of thermal continuity and internal restraint stresses; the magnitude of bridge movements and continuity stresses caused by diurnal and seasonal temperature changes; fatigue of the piles under integral abutments; and experimental data for validation and refinement of analytical models.

The analytical phase (volume II) studied the following six areas to expand knowledge and provide a scientific basis for design: Abutment Soil-Structure interaction, Pile Behavior, Longitudinal Bridge Movement, Secondary Continuity Forces, Skewed Bridge Behavior, and Construction Sequences. The objectives of this analytical phase were to establish criteria that limited the length of jointless bridges; the range of applicability for integral abutments, including those on spread footings; the effect of length changes on superstructure stresses; the significance of continuity moments from thermal gradients, creep, and shrinkage; design criteria for piers; the effects of different construction sequences including retrofitting; limitations and special considerations for curved and skewed structures; and development of more uniform (and standard) design criteria and methods for new and retrofitted bridges.

This is the only one of the 3 volumes available on the Web. Volumes I and II are available through the National Technical Information Service, Springfield, VA 22161, or at: http//www.ntis.gov. NTIS tracking numbers: Volume I, Part 1—PB2007-108154; Volume I, Part 2—PB2007-108155; Volume I, Part 3—PB2007-108156; Volume II—PB2007-108157.

17. Key Words	18. Distribution Statement
bridge, jointless, thermal movement, thermal gradient, integral abutment, recommendations	No restrictions. This document is available to the public through the National Technical Information Service, Springfield, VA 22161.

19. Security Classif. (of this report)	20. Security Classif. (of this page)	21. No of Pages	22. Price
Unclassified	Unclassified	375	

SI* (MODERN METRIC) CONVERSION FACTORS

APPROXIMATE CONVERSIONS TO SI UNITS

Symbol	When You Know	Multiply By	To Find	Symbol
		LENGTH		
in	inches	25.4	millimeters	mm
ft	feet	0.305	meters	m
yd	yards	0.914	meters	m
mi	miles	1.61	kilometers	km
		AREA		
in^2	square inches	645.2	square millimeters	mm^2
ft^2	square feet	0.093	square meters	m^2
yd^2	square yard	0.836	square meters	m^2
ac	acres	0.405	hectares	ha
mi^2	square miles	2.59	square kilometers	km^2
		VOLUME		
fl oz	fluid ounces	29.57	milliliters	mL
gal	gallons	3.785	liters	L
ft^3	cubic feet	0.028	cubic meters	m^3
yd^3	cubic yards	0.765	cubic meters	m^3
		NOTE: volumes greater than 1000 L shall be shown in m^3		
		MASS		
oz	ounces	28.35	grams	g
lb	pounds	0.454	kilograms	kg
T	short tons (2000 lb)	0.907	megagrams (or "metric ton")	Mg (or "t")
		TEMPERATURE (exact degrees)		
°F	Fahrenheit	5 (F-32)/9 or (F-32)/1.8	Celsius	°C
		ILLUMINATION		
fc	foot-candles	10.76	lux	lx
fl	foot-Lamberts	3.426	$candela/m^2$	cd/m^2
		FORCE and PRESSURE or STRESS		
lbf	poundforce	4.45	newtons	N
lbf/in^2	poundforce per square inch	6.89	kilopascals	kPa

APPROXIMATE CONVERSIONS FROM SI UNITS

Symbol	When You Know	Multiply By	To Find	Symbol
		LENGTH		
mm	millimeters	0.039	inches	in
m	meters	3.28	feet	ft
m	meters	1.09	yards	yd
km	kilometers	0.621	miles	mi
		AREA		
mm^2	square millimeters	0.0016	square inches	in^2
m^2	square meters	10.764	square feet	ft^2
m^2	square meters	1.195	square yards	yd^2
ha	hectares	2.47	acres	ac
km^2	square kilometers	0.386	square miles	mi^2
		VOLUME		
mL	milliliters	0.034	fluid ounces	fl oz
L	liters	0.264	gallons	gal
m^3	cubic meters	35.314	cubic feet	ft^3
m^3	cubic meters	1.307	cubic yards	yd^3
		MASS		
g	grams	0.035	ounces	oz
kg	kilograms	2.202	pounds	lb
Mg (or "t")	megagrams (or "metric ton")	1.103	short tons (2000 lb)	T
		TEMPERATURE (exact degrees)		
°C	Celsius	1.8C+32	Fahrenheit	°F
		ILLUMINATION		
lx	lux	0.0929	foot-candles	fc
cd/m^2	$candela/m^2$	0.2919	foot-Lamberts	fl
		FORCE and PRESSURE or STRESS		
N	newtons	0.225	poundforce	lbf
kPa	kilopascals	0.145	poundforce per square inch	lbf/in^2

*SI is the symbol for the International System of Units. Appropriate rounding should be made to comply with Section 4 of ASTM E380.
(Revised March 2003)

TABLE OF CONTENTS

LIST OF FIGURES

LIST OF TABLES

1. EXECUTIVE SUMMARY

A typical jointless bridge consists of a continuous concrete deck supported on continuous beams. The beam ends are commonly connected integrally to the abutments. Approach slabs are usually used between the abutments and the pavement. These approach slabs are supported on and tied to the abutments at one end and slide with respect to the pavement at the other end. Therefore, the bridge is continuous and jointless between the far ends of the approach slabs.

Because these bridges are jointless, they require less maintenance, improve riding quality, lower impact loads, reduce snowplow damage, and have structural continuity for live load and seismic resistance. However, the thermal movements of the bridge must still be accommodated. Because the entire bridge is tied together, there are restraint forces from the abutments and piers. The general design philosophy is to build flexibility into the support structures to the extent feasible while providing sufficient strength for restraint forces that cannot be completely eliminated. However, the magnitude of the expected thermal movements and the effective stiffnesses of restraining elements considered in determining design forces are uncertain. The design of these bridges has, for the most part, been based on judgment and empirical rules rather than on scientific and engineering understanding of material and structural responses. This study was conducted, therefore, to develop a more scientific basis for the design of such bridges.

The results of this project are presented in three volumes: a detailed experimental report, a detailed analytical report, and a summary report. This summary report includes abridged descriptions of the experimental and analytical research performed and presents proposed design procedures.

The overall experimental program consisted of the following six tasks:

1. Material property tests.
2. Internal thermal restraint tests.
3. Beam and component tests.
4. Pile tests.
5. Field surveys.
6. Field tests.

The experimental phase of the research addressed thermal movements and stresses; creep and shrinkage movements, including the effects of exposure to the outside environment; pile behavior; and passive soil pressure. An experimental program involved both field and laboratory studies. This program included the construction and monitoring of a two-span continuous "bridge" built outside the structural laboratory and the instrumentation and monitoring of a bridge in Tennessee, as well as a field survey of 15 jointless bridges in Tennessee.

The following is a general summary of the results of the experimental program:

1. The minimum and maximum effective bridge temperatures can be estimated accurately based on available minimum and maximum shade air temperatures in different parts of the United States. The bridge movements resulting from seasonal temperature variations can also be estimated using procedures developed and presented in the analytical report for this study. It should be noted that the procedures developed apply to jointed as well as jointless bridges.

2. Although the experimentally measured maximum and minimum temperature gradients were smaller than the design values recommended in the American Association of State Highway and Transportation Officials Load and Resistance Factor Design (AASHTO LRFD) specifications,[1] the resulting continuity forces were comparable. This is because of the difference in the coefficients of thermal expansion between the deck slab and the beam. Therefore, it is recommended that these design values for thermal gradients, be used pending further studies at different locations in the United States.

3. In skewed bridges, depending on their geometry, transverse movement of the abutment could be expected in response to thermal expansion, and must be considered in the design .

4. The creep and shrinkage of the prestressed concrete (PS/C) beams (relative to the deck slab) and the positive temperature gradients combine to cause positive secondary moment and vertical cracking in positive-moment connection regions over the piers. The cracking leads to a reduction in live load continuity. More importantly, the positive secondary moment that develops over the pier because of the presence of a positive-moment connection can significantly negate and even totally overcome the live-load negative moment so that zero (or even negative) effective continuity can occur when considering *total* moments. Negative effective continuity means that total-moment's stresses in the midspan

region are higher than if the beams are simply supported. This phenomenon is typically more likely when prestressed beams are relatively young when the deck slab is cast.

5. The amount of reinforcement in the bottom region of the pier diaphragm in PS/C beams should be strictly controlled to limit the amount of positive moment that could be induced into the span from creep, shrinkage, and thermal strains. The reinforcement in the moment connection in the two-span continuous bridge built outside the structural laboratory reached yield strain because of the restraint of creep, shrinkage, and thermal strains. Yet this connection provided sufficient restraint so that the effective continuity for live load was negative. If more reinforcement had been provided, even higher positive secondary moments would have been induced. The observed behavior demonstrates that positive-moment reinforcement can be designed as a "fuse" to yield and therefore limit the amount of positive secondary moment that can be induced in a continuous PS/C beam.

6. The failure criteria proposed by R.E. Abendroth, et al., provide a reasonable basis for determining the displacement limit for steel piles in integral abutments when combined with appropriate load and/or safety factors.[2] In PS/C piles, the allowable displacements for such piles must be limited to a lower value to control damage.

7. In general, the environment-dependent creep and shrinkage of concrete contributes to the partial relief of thermal stresses. However, this relief is relatively small and can be ignored in the design. It is also anticipated that the expected deck shrinkage strains (as calculated based on indoor tests) would not materialize in the outside environment, except in arid or semiarid areas. This can influence calculations of continuity forces and internal restraint stresses.

8. For the 126.77-meter (m) (415.92-foot [ft]) field instrumented bridge (the longest steel bridge with integral abutments in Tennessee) with a skew angle of 59 degrees, the strain in the beams resulting from seasonal and diurnal changes was small compared to strains associated with allowable stresses. This confirmed the analytical findings regarding restraint forces, including passive soil pressures.

9. The field survey of 15 jointless bridges in Tennessee indicated that the overall field performance of jointless bridges was satisfactory, especially when appropriate details were used. Special attention to details is vital to the successful application of the jointless bridge concept.

The overall analytical program consisted of studies of the following six areas of interest, to expand knowledge of behavior and to provide a scientific basis for the design:

1. Abutment soil-structure interaction.
2. Pier behavior.
3. Longitudinal bridge movement.
4. Secondary continuity forces.
5. Skewed bridge behavior.
6. Construction sequences.

In general, the analytical research is used to evaluate the response of a jointless bridge to various design parameters, to quantify the levels of force and stress induced in the components of the bridge related to these parameters. In some cases, the research demonstrates that existing design procedures and engineering data can be used to adequately quantify the structural response and design forces for the structure. In other cases, the results of more complex analyses were used to develop simplified design relationships and procedures.

Chapter 2 of this volume provides the background for the research and the scope of the work. A description of the experimental work is presented in chapter 3. The analytical research is summarized in chapter 4 and proposed design recommendations based on this research are presented in chapter 5. In addition, the concept of jointless construction is appropriate for the retrofitting of existing jointed bridges to eliminate the joints and reduce future maintenance in these bridges; therefore, chapter 6 presents recommendations for the design of retrofitted jointless bridges. Chapter 7 presents recommendations for further research.

Based on the successful experience of certain State transportation departments that have been using the jointless bridge concept for many years, a jointless bridge is a viable option for reducing bridge maintenance costs. However, because of some uncertainty as to how jointless bridges work, there have been relatively restrictive limits placed on the use of the concept by other States. Based on the knowledge gained from this jointless bridge project, combined with other research cited in this report, designers can gain a better understanding of how jointless bridges work. Therefore, confidence in the jointless concept should increase and the use of jointless bridges should be expanded.

2. INTRODUCTION

2.1 BACKGROUND

Over the years, many types of expansion joints, expansion bearings, and other structural release mechanisms have been used on long, multispan highway bridges, to accommodate thermal movements. The desirable characteristics of an expansion joint are smooth rideability, low noise level, resistance to wear, and resistance to damage caused by snowplow blades. The performances of many joint systems, however, are disappointing. When subjected to traffic and bridge movement, they fail in one or more important aspects, notably water tightness.[3]

Current design trends are toward the elimination of bridge joints, to avoid potential maintenance problems. In general, bridges without deck joints (jointless bridges or integral bridges) have performed more effectively, remain in service for longer periods of time and require less maintenance and fewer repairs. Jointless bridges also offer the advantages of improved riding quality, lower impact loads, reduced snowplow damage, and structural continuity for live load and seismic resistance. On a jointless bridge, however, special considerations are required for movement and/or restraint stresses resulting from creep, shrinkage, and thermal strains, when designing and detailing the piers, abutments, and approach slabs. The general design philosophy is to build flexibility into the support structures to the extent feasible, while providing sufficient strength for the restraint forces that cannot be completely eliminated.

This jointless bridge concept has gradually been applied to longer bridges with consistent success, culminating in the construction of the Holston River Bridge near Kingsport, TN. This dual, 29-span bridge has only two roadway expansion joints, one at each abutment more than 0.8 kilometer (km) (0.5 mile [mi]) apart. However, the Holston River Bridge is considered to be an exceptionally long bridge, and the jointless concept has many more applications in the 30-m to 250-m (100-ft to 800-ft) length range. In this range of bridge lengths, deck joints are completely eliminated, with the superstructure integrally or semi-integrally connected to the abutment.

Jointless bridges and integral abutments have gained acceptance in many States. However, their design is more complex than that of a simply supported, jointed bridge, and uncertainty exists about their behavior and design requirements. The uncertainty about behavior has led to a variety of design and construction requirements. For example:

1. The maximum length limit for bridges with integral abutments varies from 60 m to 250 m (200 ft to 800 ft), depending on the State and type of bridge material (steel, concrete, or prestressed concrete).
2. Some States require calculation of pile stresses caused by lateral movement, while others do not.
3. Some States rely on the flexibility of abutments supported on a single row of piles to accommodate bridge movement. Other States design integral abutments to slide on fixed substructures.
4. Steel H-piles may be required to be oriented so that bending is about their weak axis or about their strong axis, depending upon the State.
5. Some States require predrilled, oversized holes for piles and compressible material behind backwalls, while others do not.
6. For some bridges, the abutment and pier connections to the superstructure are designed to transfer moment and shear (integral connections), while for other bridges, only shear forces (semi-integral connections) are transferred.
7. Some States design semi-integral piers to carry superstructure vertical loads only, while other States design the same piers for both vertical and horizontal forces.
8. Some States (Tennessee, in particular) typically use U-shaped abutments with the wingwalls parallel to the alignment of the bridge. In some States, the U-shaped abutments are normally not used (because of economics).
9. Some States give special treatment to approach slabs, while others do not. Approach slabs may be attached rigidly to the abutment and bridge deck with a moment connection or by a pinned connection only. Some States provide an expansion joint between the approach slab and the bridge deck.
10. Some States limit the maximum skew to 10° to 30°, others have no limits.
11. Some designers use a soil pressure equal to either the full passive pressure or 50 percent of it, whereas other designers completely ignore soil pressure.

The uncertainty and complexity in behavior and design have made some States and designers reluctant to use the jointless concept and have probably led to some extra conservatism in design by those States and designers that do use the concept.

As more bridges are slated for repair or replacement, consideration is being given to either converting existing structures to jointless bridges or replacing them with jointless structures. This introduces the need to consider ways to retrofit bridges to make them jointless. Areas of particular concern are connection details at the piers and abutments and the stiffness of the existing substructure.

2.2 PROBLEM STATEMENT

The design and construction of jointless bridges started with relatively short structures that had only a few spans. The success in eliminating joints with these structures has led to the use of jointless bridges for increasingly longer structures. Although these structures have generally performed well, their design and construction have been principally based on experience obtained over the years. When problems have occurred, the causes have been identified and the procedures improved for the next structure. Therefore, the design of jointless bridges has, for the most part, been based on empirical rules rather than on science and engineering principles. Therefore, although there has been success in using jointless bridges, there are still problems to be resolved.

Major questions identified in this study include determining the:

1. Effect of annual temperature variations, including the influence of internal restraint and thermal mass on movement due to temperature changes.
2. Effect of diurnal temperature variations.
3. Effective coefficients of thermal expansion.
4. Effects of creep and shrinkage on thermal expansion.
5. Foundation stiffness, particularly the relationship between passive earth pressure and abutment movement, and the capacity of abutment piles to accommodate that movement.
6. Pier stiffness and load transfer to the piers.
7. Response of skewed and curved jointless bridges to annual and diurnal temperature variations.

2.2.1 Effective Temperature Variations

The effective temperature variations to consider in bridge analysis include the effects of annual temperature variation on the total length change and the effects of diurnal temperature variation on the thermal gradient.

The effective annual temperature variation is related to the time lag between the ambient temperature and the structure's temperature, the range of ambient air temperatures, and the increment of expansion related to solar heating of the bridge deck. The magnitude of the time lag is different for concrete and steel structures, and this difference can be attributed to the generally larger mass of concrete structures and the dissimilarity in their thermal conductivity and diffusivity. Temperatures in structural steel follow the extremes of ambient temperature more closely. Also, the lower conductivity and higher thermal mass of concrete result in greater nonlinear thermal gradients in response to diurnal temperature changes. Internal restraint stresses created by the nonlinear gradients decrease some overall movement. Therefore, to understand the influence of ambient temperature on bridge movement, it is desirable to quantify the effects of thermal mass and restraint stresses on overall bridge movement.

As determined through a review of the literature,[4] M. Emerson[5] correlated the effective annual temperatures to 48-hour mean shade, 24-hour mean shade, and extreme shade air temperatures for concrete, composite steel-beam bridges, and noncomposite steel bridges, respectively.[6] R.A. Imbsen, et al., extrapolated these correlations for temperature ranges in the United States.[7] These correlations can be used to account for the thermal mass and time lag for different types of bridges. The major remaining uncertainties are verification of the extrapolation of the temperature ranges to the United States and reexamination of the extreme air temperatures to be used with these correlations depending on the bridge location in the United States. This extrapolation of the correlation was primarily for low temperatures. However, the data used by Emerson for Great Britain did not include a significant number of measurements .[5] Also, Imbsen, et al., proposed temperatures based on "normal daily minimum and maximum temperatures."[7] These are average temperature data, however, and are quite different from the extremes. In addition, the solar increment proposed was based on data from Great Britain. Therefore, there is a need to establish appropriate effective annual temperature range criteria for the design of different types of bridges within the United States.

2.2.2 Effects of Diurnal Temperature Variations

The literature review regarding diurnal temperature variations indicated there has been significant analytical and experimental research on temperature gradients through the thickness of bridge decks and girders.[4] Imbsen, et al., presented a review of this information and recommended temperature gradients for design depending on solar radiation zones within the United States, based on analyses by I.C. Potgieter and W.L. Gamble.[7-9] Imbsen's recommendations are for types of PS/C bridges with no established performance history; similar design temperature gradients were included in the AASHTO LRFD specifications,[1] however, with the provision that the load factor for the effects of temperature gradient be determined on a project-specific basis. This resulted from the uncertainty about the effects of cracking, yielding, creep, and other nonlinear responses that diminish the effect of the temperature gradient.

The major uncertainty in determining the effects of diurnal temperature variation, therefore, is in determining the stress variations that result from diurnal temperature gradients. Calculated elastic thermal gradient stress caused by the combination of internal restraint and secondary continuity moments can be very high. However, there have not been many cases of distress related to these thermal stresses. There has also been no direct and reliable measurement of thermal gradient restraint stresses. Only strains have been measured, and strain is not proportional to stress in this situation. However, previous research has indicated that there may be some stress relief in that the strains may include some inelastic strains from short-term thermal creep and shrinkage. In the Transport and Road Research Laboratory (TRRL) Supplemental Report 442, Price discussed the potential effects of a "transitional thermal creep" occurring over short periods of time.[6] T. Wah and R.E. Kirksey measured a reversal of deflections during short time periods of about 30 minutes in laboratory beams heated on the top surface.[10] They attributed that reversal to creep. Also, shrinkage was accelerated by heating. The possible effects of short-term thermal creep and shrinkage on the relief of thermal gradient stresses need to be investigated. Concrete cracking and/or steel yielding can also relieve restraint stress. The potential for cracking and/or yielding is affected by the combination of all sources of restraint stress, including external restraint from the abutments and piers and continuity forces related to differential creep and shrinkage in concrete. There is a need to examine the effects of temperature gradient in combination with other sources of restraint stress, and when considering cracking and yielding, to establish the significance of these effects on jointless bridges.

2.2.3 Effective Coefficient of Thermal Expansion

The literature review indicated that the coefficient of thermal expansion of concrete varies depending on aggregate type, cement content, water-cement ratio, temperature ranges, concrete age, and relative humidity.[4] Both experiment and field-testing data have indicated that researchers are able to reasonably calculate expected overall bridge movement, given the proper temperature range and appropriate coefficients of thermal expansion. However, there is significant uncertainty with both of these values, and also with the other factors that influence bridge movement and the temperature of the bridge during construction. These other factors include creep, shrinkage, and the elastic modulus of the concrete; the stiffness of the piers and abutments in response to bridge movement; and the setting temperature of the concrete during construction. The expected maximum bridge movement is an important design parameter for jointless bridges, particularly when related to the demands made on the substructure in supporting the bridge while accommodating the movement and on the details in accommodating the movement. Therefore, there is a need to develop procedures to determine expected bridge movement, which account for the uncertainty of the coefficient of thermal expansion and other effects.

2.2.4 Effects of Creep and Shrinkage on Thermal Expansion

In addition to the possible relief of thermal gradient stresses (as discussed in section 2.2.2), creep and shrinkage effects may reduce annual bridge movement. Creep associated with the elastic restraint stresses may reduce thermal expansion. Also, there is an alternating increase and decrease in creep and shrinkage corresponding to seasonal wetting and drying that is out of phase, which, to some degree, may compensate for seasonal heating and cooling. There is a need to examine the potential effects of creep and the potential effects of seasonal variations on creep and shrinkage.

2.2.5 Foundation Stiffness and Passive Earth Pressure on Abutments

Based on a review of the literature, it appears that reasonable estimates of an upperbound for passive pressure versus abutment movements can be developed using finite element analyses.[11]

A.M. Wolde-Tinsae and J.E. Klinger carried out parametric analytical studies of integral abutment bridges to investigate superstructure stresses resulting from passive pressure resistance to thermal expansion; they concluded that under certain extreme conditions, thermal stresses can be significant in prestressed and reinforced concrete bridges.[12]

However, creep and shrinkage effects in the concrete were not considered. Creep and shrinkage of concrete may relieve some stress related to overall length change, but may also add to thermal stresses caused by secondary continuity moments.

There seems to be a need to investigate the magnitude of soil passive pressure and the combined effects of passive pressure and seasonal concrete creep and shrinkage on integral abutment bridges. Another uncertainty with abutments is the structural integrity of stub abutment piles under high-amplitude load reversals. Testing of piles under integral abutments indicated that yielding in the top of the piles will occur, with a horizontal movement of about 12.7 millimeters (mm) (0.5 inch).[13] Design criteria developed from analyses and testing at Iowa State University by Abendroth, et al., include a ductility capacity criteria for H-piles rather than a limiting stress criteria, since the pile must yield to accommodate thermally related abutment movement.[2] Therefore, the ability of the pile to sustain vertical load and lateral-load capacity while undergoing deformations with a significant amount of plastic strain was uncertain because of the potential for low-cycle fatigue.

2.2.6 Stiffness and Load Transfer Through Piers

Typically, the bridge superstructure is connected to the piers by pinned or fixed bearings, so that the top of the pier moves with the bridge. The primary questions are the effective stiffness of the pier when considering creep, cracking, and the soil/structural response of the foundation, and the level of stress induced in the superstructure from the restraint provided by the pier. A sensitivity study is needed to evaluate the forces induced in the piers by the bridge movement and the relative magnitude of superstructure restraint stresses that are dependent on pier stiffness and connection parameters.

2.2.7 Response of Skewed and Curved Bridges

Skewed and curved bridges respond to temperature change with both longitudinal and transverse movement. Uncertainties include the expected transverse movement as a result of the bridge geometry and the magnitude of the restraint forces on integral abutments and piers from annual thermal cycling. In addition, the angle between the beams, abutments, and piers influences the moment and shear distribution within the bridge beams and the shear and torsion in the abutments. The effects of bridge geometry on secondary continuity moments caused by creep, shrinkage, and thermal gradients, and the redistribution of these moments and shears with time, are uncertain. There is a need, therefore, for analytical research to improve understanding of the response of skewed and curved bridges.

2.3 OBJECTIVES AND SCOPE

The overall objectives of this research effort were to develop a greatly expanded knowledge of the behavior of jointless bridges and to provide a scientific basis for their design. Specific design recommendations were to be made.

This research work consisted of two primary programs: an experimental program and an analytical program. Detailed descriptions of each of these programs are given by H. Tabatabai, et al.,[14] and R.G. Oesterle, et al.,[15] The scope of work included jointless bridges with composite steel, PS/C, and reinforced concrete beams subjected to gravity loads combined with thermal loads, and the time-dependent effects of concrete creep and shrinkage.

The experimental work included material-component and girder-component tests, including building two full-scale, two-span continuous girders in an outdoor environment and monitoring them for a period of 20 months. The experimental work also included field surveys of 15 jointless bridges and field monitoring of a long, heavily skewed jointless bridge.

The analytical work included an assessment of the interaction of jointless bridge superstructures with integral abutments and piers and of the effects of secondary continuity forces in combination with end-restraint forces. Skew effects were included and retrofitting of existing jointed bridges to eliminate expansion joints was addressed. The field survey of jointless bridges also included curved bridges. Analytical assessment of the restraint forces and of the movement of curved jointless bridges, however, was deemed to be beyond the scope of this project.

The following sections of this volume describe the various aspects of the two programs and their results. This volume also includes a set of recommendations for the design of jointless bridges.

3. SUMMARY OF EXPERIMENTAL WORK

Although many parameters affecting the design of jointless bridges were addressed through the analytical program (summarized in chapter 4 of this volume), a number of significant questions could not be answered through purely analytical means. The experimental program was therefore designed to answer those questions and complement the analytical program, in pursuit of the overall objective of developing a simplified design methodology.

The main objective of the experimental program, then, was to address issues crucial to the success of the study, which could not be answered from a purely analytical standpoint. Test programs were developed to address the following issues:

1. The significance of short-term, environment-dependent creep and shrinkage, and their influence on the relief of thermal continuity and internal restraint stresses.
2. The magnitude of bridge movements and continuity stresses and movements caused by diurnal temperature gradients and seasonal temperature changes.
3. The limitations, if any, imposed by repetitive inelastic deformations of piles in integral abutments.
4. Experimental data for validation and refinement of analytical models.

The overall experimental program consisted of six tasks (F.1 through F.6). These tasks were as follows:

F.1—Material property tests.

F.2—Internal thermal restraint tests.

F.3—Beam and component tests.

F.4—Pile tests.

F.5—Field surveys.

F.6—Field tests.

The following sections of this chapter describe the work accomplished and summarize the findings for each of the tasks in the experimental studies. The details of these tasks and their test results are presented in the experimental report.[14]

3.1 TASK F.1—MATERIAL PROPERTY TESTS

This task consisted of a series of tests to evaluate the short-term creep and shrinkage behavior of concrete. The test specimens were 152 by 305-mm (6 by 12-inch) cylinders and were subjected to various environmental and stress conditions. This allowed specific creep and shrinkage parameters to be either evaluated directly or derived algebraically from measurements of material response parameters.

The objectives of this task were to measure the short-term creep and shrinkage parameters of concrete under different environmental and stress conditions, and to evaluate the significance of these short-term parameters for possible relief of diurnal thermal stresses.

The specific short-term parameters under consideration were:

- ε_t temperature strains
- ε_s shrinkage strains
- ε_{se} environment-dependent shrinkage strains
- ε_c creep strains
- ε_{ce} environment-dependent creep strains
- ε_{so} outdoor shrinkage strains
- ε_{co} outdoor creep strains.

Concrete cylinders were used to fabricate three sets of test specimens. The three sets of test specimens were designated as A, B, and C, as shown in table 3-1. Test Sets A, B, and C were assembled when the concrete was 39, 187, and 382 days old, respectively. Each test set consisted of five specimen types. Specimen types were numbered C1 through C5. Specimen types are shown in the test matrix of table 3-2.

Two whole cylinders and two half cylinders were used to assemble a single stacked specimen type. The two whole cylinders were in the middle of the stack, while the half cylinders were placed at the ends. This arrangement is usually used for creep test specimens. Cylinders were capped with a sulfur compound prior to assembly. Specimens were instrumented with displacement transducers to measure longitudinal strains.

Each specimen type was subjected to a different combination of environmental and stress conditions, as shown in tables 3-1 and 3-2. In each test set, Specimens C1, C2, and C3

were unstressed. Specimens C4 and C5 were stressed to 6.89 megapascals (MPa) (1,000 pounds force per square inch [lbf/inch^2]) in creep frames to represent typical compressive stress values in PS/C beams. Specimen C2 was coated with an epoxy-based vapor-barrier coating for concrete (Sikagard® 62) to prevent moisture movement into and out of the concrete. This prevented shrinkage and swelling caused by the movement of moisture to and from the environment outside of the specimen. Specimens C2, C3, and C4 were subjected to daily temperature variations by placing these specimens outdoors in the shade. Specimens C1 and C5 were kept indoors in a controlled room with a constant temperature of 23 degrees Celsius (C) (73 degrees Fahrenheit [F]) and a relative humidity of 50 percent.

Table 3-3 shows how the various strain parameters are derived from different strain readings. The strain in each test specimen is considered to be the sum of the various strain components, based on exposure and stress conditions. The primary parameters are temperature, laboratory shrinkage, and laboratory creep strains. Laboratory shrinkage and creep strains are obtained from specimens under laboratory conditions that reflect constant temperature and humidity. In an outdoor environment subject to changes in temperature, humidity, wind speed, etc., the interaction between these parameters is highly complex, interdependent, and nonlinear. Therefore, direct superposition of these primary parameters to arrive at a predicted outdoor response is not valid. In this study, the differences between the superimposed primary parameters and the actual outdoor responses are defined as environment-dependent creep and shrinkage strains. These secondary parameters are therefore used to obtain estimates of the degree of deviation from primary (indoor) creep and shrinkage strains in an outdoor environment. This test matrix is a vehicle to address the highly complex issue of short-term and long-term inelastic concrete strains in an outdoor environment.

A number of strain monitoring tests were performed on the three sets of specimens. Not all creep specimens were loaded at the same time. The creep specimens for Test Sets A, B, and C were subjected to creep loading at approximately 1 month, 6 months, and 12 months, respectively. This was done to examine the effects of concrete aging and the longer duration of creep-load applications on the measured strain parameters. In summary, these short-term investigations at various times indicated the relative influences of the short-term creep and shrinkage parameters as a function of variations in the ambient conditions and the age of the concrete. Test information and a summary of the data are shown in tables 3-1 and 3-4, respectively. The information shown in table 3-4 includes changes in the subsequent peaks of temperature strains ($\Delta\varepsilon_t$), the ratio of

changes in environment-dependent shrinkage ($\Delta\varepsilon_{se}$) to the corresponding $\Delta\varepsilon_t$, and the ratio of changes in environmentally dependent creep ($\Delta\varepsilon_{ce}$) to the corresponding $\Delta\varepsilon_t$. The shaded areas in table 3-4 indicate data with absolute $\Delta\varepsilon_t$ values of less than 60 millionths.

This magnitude of change in the temperature strain corresponds to a temperature change of approximately 5 °C (9 °F). These data are not included in further analysis of the results; this is done to minimize possible distortion of the analyzed results based on fewer specimens.

Tests 1 and 2 were performed on the same test set (Set A) during a span of a few days. Therefore, the results of these two tests can be combined for comparison with the other tests. Similarly, the results of Tests 4, 5, 8, and 9 are combined and shown in table 3-5. Additionally, the results of all tests conducted during winter (Tests 3, 4, and 5) are combined for comparison with the results of all nonwinter tests. Finally, the results of all tests are combined to obtain an overall view of the influence of the two environment-dependent parameters.

Based on an evaluation of the test results and the data shown in table 3-5, the following conclusions can be made:

1. Environmental conditions influence the short-term creep and shrinkage behavior of concrete cylinders.

2. Short-term environment-dependent creep and shrinkage can be very high compared to indoor (laboratory) creep and shrinkage occurring within the same short-duration time period. However, each is limited to a maximum of approximately 15 percent (and an average of approximately 6 percent) of the corresponding changes in the temperature strains.

3. Environment-dependent creep tends to compensate for temperature strains. As the temperature increases (positive temperature strain), environment-dependent creep increases (negative strain). On average, ε_{ce} is approximately -6 percent of ε_t. However, with all the data, extreme values range from -16.2 percent to +3.6 percent of ε_t. There does not appear to be clear trends in the data regarding the influence of concrete age, the season in which the tests were conducted, or the time elapsed since application of creep loading.

4. Environment-dependent shrinkage also tends to compensate for temperature strains, except in cases when the concrete temperature is below the freezing point

(0 °C [32 °F]). The average value of ε_{se} is -6.3 percent of ε_t for all tests except those conducted during winter. The average ε_{se} value for winter tests is +4.7 percent of ε_t. It appears that the transformation of water into ice inside concrete can substantially affect the environment-dependent shrinkage values. Therefore, under freezing conditions, ε_{se} and ε_t are of the same sign (additive). Extreme values with all the data range from -13.5 percent to +13.2 percent of ε_t. There does not appear to be a correlation between the results and the age of the concrete.

5. When the temperature stays above freezing (nonwinter tests), it is expected that the combination of environment-dependent creep and shrinkage strains helps reduce the effect of temperature strains by an average of approximately 12 percent. This contribution is reduced to an average of approximately 3 percent during winter.

3.2 TASK F.2—INTERNAL THERMAL RESTRAINT TESTS

It is widely known that variations in weather parameters (such as temperature, solar radiation, wind, etc.) generate varying nonlinear temperature distributions through the depth of a bridge beam. For instance, solar radiation during daylight hours can heat the top of the bridge deck to a higher temperature than that of the middle and the bottom of the beam. This condition is defined as a positive temperature gradient. The gradient could also be negative, in which case the top of the deck is cooler than the rest of the bridge cross section. Figure 3-1 shows a nonlinear temperature distribution through the depth of a bridge member for a positive temperature gradient.

When subjected to a nonlinear temperature gradient through its cross section, a structural member will develop internal restraint stresses, as indicated in figure 3-2. These stresses are called self-equilibrating or eigenstresses. If free to move, each fiber in the cross section would strain in proportion to its temperature, the constant of proportionality being the coefficient of thermal expansion of the material. However, if this were to occur, the nonlinear temperature distribution would result in a nonlinear strain distribution. Such a nonlinear strain diagram would be in violation of the Navier-Bernoulli hypothesis (plane sections remain plane). Therefore, the fibers are constrained to a linear strain distribution. Internal restraint stresses develop as a consequence of the section constraints.

The primary objectives of Task F.2 were to develop a method to measure internal thermal restraint stresses and, with this method, to evaluate the possible influence of short-term creep and shrinkage of concrete in reducing these internal restraint stresses. The approach

used in this task was to (1) develop and verify the technique using metal specimens with known coefficients of thermal expansion and no creep or shrinkage effects, and (2) apply the technique to two different sizes of concrete specimens.

The use of metal specimens allows the restraint stresses to be theoretically calculated and compared with measured values, and therefore the effectiveness of the test method can be evaluated. Assuming that the test procedures are valid, the difference between the measured and calculated stresses in all-metal specimens should be negligible, because creep and shrinkage would not be contributing factors. If creep and shrinkage effects are present (e.g., in concrete), calculated and measured stresses might not agree. Such a difference would represent the effects of creep and shrinkage in relieving stresses. If calculated and measured stresses for the concrete specimen are in close agreement, then the effects of creep and shrinkage would be considered insignificant.

The test specimens consisted of a sandwich of three elements clamped together at the ends. The outer two elements were made of aluminum 2024 with a coefficient of thermal expansion of approximately twice that of steel (23.2 millionths/°C [12.9 millionths/°F]). The inner element was either steel (as shown in figure 3-3) or concrete (as shown in figure 3-4). In each test set, one element of 1018 low-carbon steel and one element of unreinforced concrete were prepared to form the inner layer of the sandwich. Two different sets of specimens were used. Set A incorporated smaller elements than Set B. Specimen ASA in each set included aluminum and steel elements, while specimen ACA included aluminum and concrete elements. Strain gauges and specimens were clamped and subjected to varying environmental conditions (mostly outdoors).

Using compatibility and equilibrium of forces, equations were developed that relate the stresses and strains in the three elements, including the effects of creep and shrinkage (or swelling caused by the moisture gain) in the concrete element.

In addition to the tests described above, a different type of test was performed to explore issues related to the restraint of swelling caused by the moisture gains (without the influence of the temperature changes). The objective of this test was to investigate the level of stress that can develop in concrete under compressive stress (prestressed) when it is allowed to shrink and is then rewetted and undergoes restrained swelling. Two test specimens initially used in Task F.1 were used. These two specimens had been stored in a temperature-and-humidity-controlled room for over a year. This room was maintained at a temperature of 23 °C (73 °F) and a relative humidity of 50 percent. These specimens were made up of concrete cylinders that were cast at the same time. One specimen

consisted of stacked cylinders inside a spring-loaded creep frame. The creep stress applied was 6.89 MPa (1,000 lbf/inch^2). The other specimen was of similar construction but was not placed inside a creep frame. A total of 12 mechanical strain gauge points were attached to the cylinders to create six measurement points on each specimen, with a gauge length of 254 mm (10 inches).

An initial set of readings were taken while the specimens were inside the temperature-and-humidity-controlled room. Subsequently, the specimens were moved into another temperature-controlled room (23 °C [73 °F]), with a relative humidity of 100 percent. Mechanical strain readings were taken periodically. After a few days, the specimens were removed and placed back into the room with the 50 percent relative humidity. Again, the strains were monitored over a period of several months.

Further details on the specimens, test procedures, and results are presented by Tabatabai, et al.[(14)] Based on the tests conducted in Task F.2, the following conclusions can be made:

1. The test methodology developed is a simple yet effective method of examining the thermal restraint stresses in concrete. The use of coated and uncoated dummy bars and titanium silicate bars are effective tools for direct determination of restraint and total strains, including the corrections for temperature effects on the gauge. It is clear, however, that the clamping system needs modification to allow development of greater restraint stresses without slippage. Some tests in this series did not exhibit equal total strains for aluminum and concrete, especially when large moisture gains were evident in the concrete bar. Attainment of equal strains is necessary for verification of the assumption of the compatibility of the strains. Only tests (or portions of tests) exhibiting equal total strains in the aluminum and concrete are analyzed and presented here.

2. The measured effective moduli of concrete in the restraint tests are approximately equal to the elastic moduli. The predicted and actual restraint strains in the concrete and aluminum bars were also relatively close. Therefore, the effect of creep on the relief of thermal restraint stresses is believed to be limited. The results of the material property tests from Task F.1 (section 3.1 of this report) also indicated similar responses.

3. A test was performed to evaluate the potential for the development of stresses caused by the restraint of moisture gain (swelling). Based on this limited test, it is tentatively concluded that substantial relief of restraint stresses can be expected

because of creep. This may be a function of the initial moisture content of the concrete, and may also be an indication of the energy associated with moisture gain for different levels of initial moisture content. Unless the moisture gain has sufficient energy associated with it, the restraint stresses can only be partially developed. More studies are recommended to clarify the issue further and to augment this limited test.

3.3 TASK F.3—BEAM AND COMPONENT TESTS

This task constituted a major portion of the experimental program. It consisted of beam tests and component tests, which are discussed separately in this report.

3.3.1 Beam Tests

The beam test program consisted of the design, construction, monitoring, and evaluation of two full-size, two-span continuous beams with deck slabs in an outdoor environment, to monitor diurnal and seasonal bridge movements and stresses caused by environmental factors. These two adjacent yet separate structures included a PS/C beam and a steel beam.

This task was designed to address a number of uncertainties about the behavior of bridges subjected to varying environmental conditions. These uncertainties included the following:

1. What are the actual changes in bridge length caused by temperature changes in an unrestrained condition?
2. What are the extreme effective bridge temperatures as a function of air temperatures? This question will be important in determining design temperature variations for use in different geographic locations with varying temperature ranges.
3. What are the extreme magnitudes and shapes of positive and negative temperature differentials across the depth of the bridge cross section?
4. What are the magnitudes of temperature-induced continuity forces or stresses and how do those measured forces compare with predicted values? Continuity forces (stresses) are developed in a continuous structure because of curvatures resulting from temperature gradients and creep and shrinkage strains. Varying coefficients

of thermal expansion between the deck and the beam will also generate thermal curvatures and continuity forces even when temperature changes are uniform.

5. How does the degree of structural continuity for live loads change with age and environmental conditions, and how do secondary continuity moments influence the effective structural continuity for total loads (as compared with simply supported spans)?

The objectives of this task were to:

1. Determine continuity stresses caused by diurnal temperature gradients.
2. Determine temperature distribution through the depth of the bridge cross sections.
3. Measure daily and seasonal thermal strains and bridge movements.
4. Measure the magnitude and time variations of dead load continuity moments.
5. Determine the influence of environment-dependent creep and shrinkage on the continuity stresses.
6. Determine the significance of the season and of cloud cover on the degree of continuity of the beams and their total moments, through load testing.
7. Provide experimental data for evaluation and refinement of analytical models.

This task included the design and construction of the beams, design and installation of instrumentation, and conduct of monitoring, maintenance, load testing, and evaluation of the results.

To meet the above objectives, two, 2-span continuous structures were constructed outdoors, adjacent to the structural laboratory in Skokie, IL (a suburb of Chicago). Each structure consisted of one line of beams composite with a 203-mm (8-inch) deck slab. One structure contained PS/C beams (AASHTO Type II) and the other contained steel beams (30 by 108). The concrete and steel beams were placed adjacent to each other. Figures 3-5 through 3-8 show the plan, elevation, cross section and overall view of the test beams. Although the beams shared the same abutments and pier, their superstructures were completely isolated from each other. Both beams had expansion joints at the abutments. The deck slab for the prestressed beam was cast when the beam was 26 days old. Both beams were heavily instrumented with strain gauges, load cells, thermocouples, displacement transducers, etc. A weather station provided information on ambient weather conditions. Details of the beams, instrumentation, and results are provided in the

experimental report.[14] All sensors were monitored at 30-minute intervals for a period of approximately 20 months, which produced an extremely large database of information on the long-term environmental responses of these beams. In addition, eight load tests were performed. The load tests were performed on a sunny and on a cloudy day in each of the four seasons. In each load test, two point loads were increased incrementally to levels that would produce the same maximum positive and negative moments as by an AASHTO HS-20 truck.

Anumber of equations were developed and/or used to analyze sensor readings and to develop calculated sensor readings based on an assumption of linear elastic behavior. For example, the predicted curvature, average strain, load-cell reactions, strains, effective bridge temperature, etc., resulting from the measured temperature distribution were calculated at each measurement time (every 30 minutes).

A brief overview of some of the findings of this task follows:

1. Figure 3-9 shows measured shade air temperatures during the monitoring period. The minimum and maximum recorded air temperatures were 29.9 °C (-21.8 °F) and 36.6 °C (97.8 °F), respectively. Therefore, the maximum seasonal change in air temperature at the test site was 66.5 °C (119.6 °F).

2. Figures 3-10 and 3-11 show the effective temperatures of the concrete and steel beams, respectively, during the monitoring time period. The effective bridge temperature is the uniform temperature that would result in the same length change as the nonlinear temperature distribution. The ranges of effective bridge temperatures (from minimum to maximum) were 62.7 °C (113 °F) and 68.9 °C (124 °F) for the concrete and steel composite beams, respectively. Therefore, the range of effective temperatures for the steel composite beam was higher than that for the concrete beam by 6.2 °C (11 °F) (10 percent). Considering that the calculated effective composite coefficient of thermal expansion of the steel beam was higher than the corresponding concrete coefficient by 8.8 percent, the longitudinal thermal movement of the steel beam is expected to be higher than that of the concrete beam by approximately 20 percent. This comparison of movements does not include movements resulting from creep and shrinkage of concrete. For comparison, section 3.16 of the AASHTO *Standard Specifications for Highway Bridges* recommends a temperature range of -34.4 °C (-30 °F) to 48.9 °C (120 °F) for metal structures in cold climates.[16] It also recommends a

temperature rise of 19.4 °C (35 °F) and a fall of 25.0 °C (45 °F) with a range of 44.4 °C (80 °F) for concrete structures in cold climates.

3. The minimum and maximum effective bridge temperatures can be accurately and linearly related to the minimum and maximum shade air temperatures through a set of linear equations, which are presented in the experimental report.[14] Chapter 5 of this volume provides detailed recommended procedures for the calculation of effective bridge temperatures in different parts of the United States.

4. The top of the deck slab reached temperatures substantially higher than the ambient air temperatures, mainly as a result of solar radiation. Temperatures at the bottom of the beams were closer to the ambient air temperatures. The intensity of solar radiation is highest around the summer solstice (June 21). Figure 3-12 shows the measured solar radiation levels. Positive temperature differentials (the temperature at the top of the deck minus the temperature at midheight of the beam) are also highest around the summer solstice (at the peak of solar radiation intensity). The most extreme negative temperature differentials occur around the winter solstice (December 21). However, data on negative differentials have far more scatter than the corresponding data for positive temperature differentials. The variation in overall positive temperature differentials over a year can be closely approximated by a sine curve with peaks at December 21 and June 21. Figures 3-13 and 3-14 show measured temperature differentials for the west spans of the concrete and steel beams, respectively.

5. The largest negative temperature differential for the concrete beam was approximately -7.8 °C (-14.0 °F), while the maximum positive temperature differential was approximately 15.1 °C (27.2 °F). The minimum (negative) and maximum (positive) temperature differentials for the steel beam were -10.6 °C (-19 °F) and 12.2 °C (22.0 °F), respectively. Therefore, the steel beam exhibited a smaller maximum differential and a larger minimum differential when compared to concrete.

6. The general shape of the measured temperature distributions for the concrete and steel beams at maximum (positive) differential temperatures was relatively similar to the design curves provided by AASHTO LRFD[1] and National Cooperative Highway Research Program (NCHRP) Report 276.[7] However, the shapes of the temperature distributions corresponding to the monthly minimum (negative) differential were substantially different from the design curves for both concrete

and steel beams. The measured peak positive temperature differentials in the concrete and steel beams were approximately 41 percent and 42 percent, respectively, less than those recommended by AASHTO LRFD for the Chicago area (Zone 2). The measured peak negative temperature differential for the concrete beam was approximately 39 percent less than that recommended by AASHTO LRFD; the measured peak negative temperature differential for the steel beam, however, was equal to that recommended by AASHTO LRFD. Figures 3-15 through 3-18 show temperature distributions corresponding to the extreme maximum and minimum temperature differentials for the concrete and steel beams.

7. The bridge thermal equilibrium occurs daily between 6 a.m. and 8 a.m. for the concrete beam and between 5 a.m. and 8 a.m. for the steel beam. The maximum daily temperature differential occurs between 11 a.m. and 2 p.m. for the concrete beam, and between 12 p.m. and 3 p.m. for the steel beam. The minimum daily gradient data for both the concrete and steel beams show a relatively wide scatter. However, it appears that the minimum generally occurs between 11 p.m. and 6 a.m. for the concrete beam, and between 11:30 p.m. and 8 a.m. for the steel beam.

8. Figures 3-19 and 3-20 show measured and calculated length changes (based on measured temperature and fully elastic behavior) for the concrete and steel beams, respectively. The length change of the PS/C beam was influenced significantly by creep and shrinkage, resulting in a reduction in the peak extension of the beam. This effect is highest during the first year of construction and will dissipate with age; this effect, however, results in a permanent shortening of the concrete beam. In the steel beam, the observed nonlinearities resulted from shrinkage and cracking in the deck slab. The measured effect of creep and shrinkage on the reduction of expansion of the steel beam was less than that observed on the concrete beam. The magnitudes of the shortening between peaks during winter and summer of 1994 were 222 millionths and 112 millionths for the concrete and steel beams, respectively. The effect of the moisture gain by the concrete during winter on the beam length changes was evident on both beams.

9. Transverse cracks were noted on the deck slab for the steel beam. These cracks probably contributed to a 26.5 percent reduction in the contribution of the deck slab to the daily change in beam length. There was no reduction from the contribution of deck-slab cracking in the concrete beam because no transverse

cracks were noted on that deck. Figure 3-21 shows the cracks observed on the deck slab over the steel beam. Figure 3-22 shows cracking in the diaphragm area of the concrete beam.

10. The actual movements of the bridge can be estimated with reasonable accuracy using conventional calculations. Chapter 5 of this volume provides procedures to determine expected end movements of a bridge, using an effective coefficient of thermal expansion for the composite beam, a temperature range for the specific location of the bridge, and factors that account for the uncertainty of material properties and setting temperature of the bridge.

11. Temperature differentials across the depth of the bridge beams and differential creep and shrinkage between the deck slab and the beam generate continuity forces within the continuous bridge beams. Reaction forces at the supports change in response to curvature changes imposed by temperature gradients or differentials in creep and shrinkage. Figures 3-23 and 3-24 show variations in both measured and calculated (based on measured temperatures and elastic uncracked section analyses) center pier reactions for the concrete and steel beams, respectively. Changes in the pier reaction result in the development of secondary continuity moments. The seasonal unrestrained curvature trends for the concrete and steel beams caused by uniform temperature change were the opposite of each other: the concrete beam achieved higher (positive) curvatures during summer and smaller curvatures during winter, whereas the steel beam exhibited the reverse of the seasonal trend shown by the concrete beam. This is related to relative differences between the coefficients of thermal expansion of the concrete and steel beams and the concrete deck. This results in continuity reactions and moments caused by the uniform seasonal temperature change that are opposite in sign for the concrete and steel beams.

12. The heat of hydration generated in the deck slabs after casting and the resulting increase in the temperature of the deck at the time of the initial setting of the concrete produced a locked-in temperature differential between the deck and the beams. This locked-in temperature differential caused a shift in the dead load reactions of the beam away from the pier and toward the end supports. The estimated locked-in temperature differentials between the deck slab and the concrete and steel beams were 7.8 °C (14.1 °F) and 2.5 °C (4.5 °F), respectively. The locked-in temperature differential caused by the heat of hydration during

construction could have a significant influence in changing the dead load moments from that originally assumed in the design.

13. The differences in the coefficients of thermal expansion of the deck and the beam will augment the continuity effects caused by the temperature differentials. If the deck slab has a higher coefficient of thermal expansion than the beam, then uniform temperature changes in the composite beam from 5 a.m. to 1 p.m. will also contribute to continuity forces generated by the temperature differential at 1 p.m. For example, although the maximum measured temperature differential in the concrete beam was approximately 15 °C (27 °F), or approximately half that recommended by AASHTO LRFD specifications,[1] daily maximum reaction changes were in line with those calculated using the AASHTO LRFD temperature differential.

14. The concrete beam gradually lost its effective live load continuity over the pier. This live load continuity was determined from the change in reaction forces from the application of live load only. The percentage of live load continuity is determined from the ratio of the *measured* change in the center pier reaction (above the simply supported reaction) to the *expected* change in the center pier reaction (above the simply supported reaction) for a fully continuous beam. An effective live load continuity of less than 100 percent means that the center pier reaction did not reach the reaction anticipated for a fully continuous beam. Therefore, the negative continuity moment over the pier did not reach the fully continuous negative moment, i.e., a loss of continuity. The result of this loss of continuity was an increase in the positive moments caused by the live load. The lowest measured percentage of full live load continuity was 48 percent and occurred on a cloudy day during summer. For the most part, the steel beam retained nearly its full live load continuity except on the summer/cloudy day when its response was reduced to 78 percent of full live load continuity.

15. The live load continuity described above in item 14 considers only the change in reaction forces from the application of live load. Using continuous beams, rather than simply supported beams, reduces midspan positive moments since the negative-moment over the piers tends to offset the positive moment in the span. The continuity presumably provides for a more structurally efficient beam. However, the continuity also induces secondary moments caused by differential creep, shrinkage, and thermal strains in the composite beams. Therefore, to

evaluate the *effective* continuity, total moments should be considered. In the long term, the total continuity for the maximum positive moment (dead load plus live load plus secondary moments) in the midspan of the **concrete beam** did not benefit from the negative-moment continuity provided over the center pier. In fact, this total moment, in two load tests, was slightly higher than the anticipated corresponding positive moment in a simply supported beam. Therefore, the *effective* continuity in the concrete beam was negative (i.e., less than 0 percent). The steel beam, on the other hand, realized between 30 percent and 40 percent reduction in the total positive midspan moment as a result of continuity. Tables 3-6 and 3-7 show the results for the concrete and steel beams, respectively.

16. It is significant to note the effect of the positive-moment connection over the prestressed beam center pier on the effective continuity (live load or total) in the test beam. The creep and shrinkage of the beam (relative to the deck slab) and the positive temperature gradients combine to cause positive secondary moment and vertical cracking over the support piers (figure 3-22). The cracking leads to a reduction in live load continuity, i.e., a reduction in negative continuity moment developed at the piers with the application of live load. More importantly, the positive secondary moment developed over the pier because of the presence of positive-moment connection can significantly negate and even totally overcome the live load negative moment such that zero (or even negative) effective continuity can occur when considering total moments. A negative effective continuity means that stresses in the midspan region, because of total moment, are higher than if the girders were simply supported. This phenomenon is typically more likely when the prestressed beam is relatively young when the deck slab is cast, as was the case with the test beam. Chapters 4 and 5 of this volume provide specific recommendations for the design for the positive-moment connection.

17. The jointless bridges surveyed in Tennessee exhibited vertical cracking at the pier diaphragms because of combined creep and shrinkage effects and the positive temperature gradients. These cracks actually serve to relieve stresses and do not appear to compromise the long-term durability of the bridge, as long as they are confined within the diaphragm concrete between the two beams supported on the pier. In the test beam, vertical cracks appeared in early spring in the intermediate diaphragm between the two prestressed beam ends (figure 3-22). The size and length of these cracks grew with time. The effect of this cracking was reflected in the strain readings, especially in those gauges located in the diaphragm area.

Strain gauges on the hooked bars providing the positive-moment connection indicated that stresses in the bars approximately reached or exceeded yield stress.

18. In cases where the positive-moment connection detail is over-reinforced to control crack sizes, cracking could potentially occur in a far more critical area (i.e., within the span), particularly at the termination points of the added reinforcing steel. Therefore, the amount of reinforcement in the bottom region of the pier diaphragm must be strictly controlled to limit the amount of positive moment that could be induced in the span. One of the concepts proposed in chapters 4 and 5 of this volume is based on the idea of designing the positive-moment reinforcement as a "fuse" to yield and therefore limit the amount of moment transferred to less than the moment that could cause beam cracking.

3.3.2 Component Tests

The component test program of Task F.3 was designed to evaluate long-term environment-dependent creep and shrinkage parameters on large-size specimens. (Work performed in Task F.1 was limited to the short-term behavior of concrete cylinder specimens.) Component test specimens in Task F.3 consisted of 2.44-m (8-ft) lengths of beams and slabs similar to those used in the beam tests.

Eight slab components, five PS/C beam components, and five composite components (steel and PS/C beams with deck slabs) were used. Figure 3-25 shows diagrams of these four categories of component test specimens. The strand pattern for the prestressed beam component was modified from that used in the beam tests so that the components had approximately the same stress distribution as the midspan of the larger beams (i.e., the effect of dead load was included through changes in the strand pattern). Figure 3-26 shows two photographs of the component specimens placed outdoors.

In a manner similar to that used in the tests in Task F.1, the component specimens were placed in different environmental conditions. Some specimens were coated with a vapor barrier to prevent the movement of moisture into and out of those specimens. Unlike in the tests performed in Task F.1, two separate outdoor conditions were used in Task F.3: outdoors in the sun and outdoors in the shade. Tables 3-8 and 3-9 show the exposure conditions for the slab components and the procedures through which various strain parameters were extracted.

The following are some of the major conclusions from the component tests:

1. Figure 3-27 shows indoor (laboratory) shrinkage (ε_s), outdoor in the shade shrinkage (ε_{so}), and outdoor in the sun shrinkage (ε_{ss}) for the deck components. The cyclical wetting and moisture gain (expansion) by the concrete deck slab during winter reduced the overall deck shrinkage substantially.

2. Figure 3-28 shows indoor creep (ε_c) and outdoor in the shade creep (ε_{co}) for the beam components at a location 76 mm (3 inches) above the soffit of the beam. Environmental conditions have a significant influence on long-term shrinkage behavior and a minor influence on long-term creep behavior of full-size bridge components. The measured responses discussed here are based on measurements in the Chicago, IL area (Midwestern United States). Other areas of the country will probably exhibit different responses.

3. In all cases, the measured outdoor (in the shade) shrinkage was far less than the corresponding indoor laboratory shrinkage. This is believed to be caused by the concrete gaining moisture from the environment (or the lack of moisture loss), particularly during winter. The maximum yearly outdoor shrinkage ranged between 60 millionths and 100 millionths during summer and recovered to near zero during winter.

4. Environment-dependent shrinkage strains can be considered to include two components superimposed on laboratory shrinkage. One component consists of progressively increasing positive (swelling) strains (up to the saturation of concrete). This component is believed to be related to overall moisture gain from the environment (or lack of moisture loss). The second component includes seasonal variations that consist of negative (contraction) strains during summer and positive strains during winter. This strain component is believed to be caused by the movement of moisture into and out of concrete as a result of temperature changes. The environment-dependent shrinkage will probably be a function of the geographical location. In arid regions, long periods of drying combined with high temperatures would be expected to increase the net shrinkage, and recovery with periodic moisture gain may not be as complete.

5. In deck components, the maximum (relative) indoor shrinkage strain was approximately -200 millionths during the monitoring time period. However, the corresponding ε_{so} (total outdoor shrinkage in the shade) and ε_{ss} (total outdoor shrinkage in the sun) strains were approximately +20 millionths and −25 millionths, respectively. The highest ε_{so} and ε_{ss} strains were approximately −82

millionths and −90 millionths, respectively. These highest strains occurred in June 1994. The overall trend of solar radiation-dependent shrinkage (ε_{sr}) strain was not positive. In fact, ε_{sr} was generally flat during winter and negative during summer.

6. Outdoor creep strains in beams could be approximated as a summation of indoor creep strains and seasonal creep effects. This seasonal strain was approximately ±50 millionths at the location near the soffit of the beam component. The seasonal creep effects decreased the total creep strains during winter and increased them during summer.

3.4 TASK F.4—PILE TESTS

Piles beneath integral abutments must accommodate the horizontal movement of the abutment, caused by the thermal strain of the bridge, while supporting the dead and live loads. The movement thus imposed on the pile can generate substantial local stresses in the pile. Consequently, it is necessary to find the upper limit in the expected movements that can be safely accommodated by the pile during the entire service life of the bridge; in other words, the role, if any, of abutment piles in limiting the lengths of jointless bridges must be ascertained. The majority of the piles used by various States under integral abutment bridges are steel H-piles. However, steel-pipe piles and PS/C piles are also used.

Based on previous research, it is clear that as the length of a jointless bridge increases, the abutment movements will probably cause yielding of the steel pile at the pile cap. During the life of the structure, these seasonal movements result in repetitive back-and-forth movements and yielding. Therefore, there has been concern regarding the ability of the steel pile to undergo these inelastic strain reversals without compromising its load-carrying capacity.

PS/C piles are expected to be cracked by relatively small abutment movements. Again, it has been uncertain whether such piles can sustain relatively large repetitive movements. The issue is complicated by the fact that the prestressed piles are usually embedded in the concrete cap less than 1,220 mm (2 ft). This is far less than the development length of the strand, and the strands may slip with relatively small movements. The long-term effect of such slippage on the pile was also of interest. To address these issues, tests were performed on models of steel and PS/C piles in the laboratory.

The objective of the pile tests was to evaluate the significance of subjecting steel and PS/C piles to repetitive, inelastic reversible strains under integral abutments. To

determine the maximum amount of seasonal abutment movement (i.e., maximum bridge length change) that could be safely sustained by the piles during their service life, two test models incorporating a length of pile embedded in a typical concrete pile cap were tested. One steel pile specimen and one PS/C pile specimen were tested. Figures 3-29 and 3-30 show the test setup for the steel and concrete piles, respectively.

The steel pile cross section used in this test was an HP10x42, which is commonly used in integral abutments. The PS/C pile used for this test was a 356-mm (14-inch) square pile manufactured in accordance with the Kentucky Transportation Cabinet's (KYTC) standard details for such piles (BPC-011-04). Both steel and concrete piles were embedded 610 mm (24 inches) into concrete pile caps designed and built for the tests. The steel pile was oriented such that the abutment movements would theoretically generate weak-axis bending in the pile.

The steel and concrete piles were cantilevered 2,311 mm (91 inches) and 3,505 mm (138 inches), respectively, from the pile cap. The lateral loads for the steel and concrete piles were applied 2,032 mm (80 inches) and 3,430 mm (135 inches), respectively, from the face of the cap. In both tests, the axial load of 400 kilonewtons (kN) (90,000 pounds force [kips]) was applied horizontally at the end of the pile. Pin assemblies were used between the pile and the two load-cells to minimize moment transfer at those points.

The end of the pile was therefore modeled as a hinge. This point would correspond to the inflection point on an actual pile. The length of the steel pile in the test setup (or the distance from the pile cap to the inflection point) was determined using a computer program for the analysis of laterally loaded piles (COM624P).[17] Soil was modeled as loose sand ($\Phi = 35°$) and a yield stress of 248 MPa (36 kips/inch^2) was assumed. According to the model, a displacement of approximately 11.4 mm (0.45 inch) and a lateral load of 53.4 kN (12 kips) would result in the first yield.

The point of inflection was determined for two conditions. In the first condition, the extreme fiber pile stresses at the cap interface were at first yield, while in the second condition, the pile formed a plastic hinge at the interface with the cap. The calculated distances from the inflection point to the cap in the first and second models were 1,143 and 2,921 mm (45 and 115 inches), respectively. Because the tests would mostly involve states found between the first condition (yielding) and the second condition (plastic hinge), the length of the pile was chosen to be the average of the two conditions (2,032 mm [80 inches]).

Alternatively, the following approximate equation 3-1 (in U.S. units) was used to estimate the equivalent effective cantilever length of the steel pile, L_e.[(2)] For the maximum moment in a fixed-head pile with no free length above ground:

$$L_e = 2.4 (E I / K_h)^{0.25} \quad (3\text{-}1)$$

where E, I, and K_h are the modulus of elasticity, moment of inertia, and the horizontal stiffness of soil, respectively. For an E of 18.5×10^4 MPa (26.85×10^6 lbf/inch^2), an I of 29.8×10^6 mm^4 (71.7 inches^4), and a K_h of 2.71×10^{-2} N/mm^3 (100 lbf/inch^3), and in soft soil, An L_e of approximately 4,040 mm (159 inches) is calculated. Therefore, the midheight (inflection point) of the equivalent cantilever pile will be at a distance of approximately 2,020 mm (79.5 inches) from the cap. This is essentially identical to the estimated value based on the COM624P computer program for the analysis of laterally loaded piles.

The length of the PS/C pile in the test setup was determined using the following data:

E = modulus of elasticity of concrete = 36.5 MPa (5,290 kips/inch^2)

I = moment of inertia = 13.3×10^8 mm^4 (3,201 inches^4)

K_h = horizontal stiffness of soil = 2.71×10^{-2} N/mm^3 (100 lbf/inch^3) (assuming soft soil).

Substituting the above values into equation 3-1:

L_e = 6,860 mm (270 inches) (as opposed to 4,040 mm [159 inches] for the steel pile).

Therefore, the midheight (inflection point) of the equivalent cantilever pile will be at a distance of approximately 3,430 mm (135 inches) from the cap.

The selected displacement ranges for the tests were 25 percent, 50 percent, and 100 percent of the displacement at failure. For the steel piles, "failure" was defined as local buckling of the flange. A displacement at which local buckling of the flange could be expected was calculated to be 122.7 mm (4.83 inches) from equations proposed by Abendroth, et al.,[2] Since the end of the pile test specimen corresponded to the inflection point, displacement relative to the inflection point at the local flange-buckling limit was one-half (61.5 mm [2.42 inches]). Therefore, for the steel pile, the selected displacement ranges were ±15.2 mm (0.6 inch), ±30.5 mm (1.2 inches), and ±61.0 mm (2.4 inches). The number of displacement cycles for the range of ±15.2 mm (0.6 inch) was 100, while

50 cycles were applied for each of the other two ranges (±30.5 mm [1.2 inches], and ±61.0 mm [2.4 inches]).

For the concrete pile, the theoretical failure displacement was calculated based on the condition of reaching the moment capacity of the pile at the face of the pile cap. The displacement corresponding to the calculated moment capacity of the pile was determined by numerically integrating a moment-curvature relationship over the length of the equivalent cantilever. The moment-curvature relationship was determined from the equilibrium and compatibility using nonlinear stress-strain relationships for the concrete and prestressing steel. The calculated moment capacity was based on an assumed compressive strain limit of 0.003 in the extreme fiber of the concrete. The displacement corresponding to this limit was calculated to be 128 mm (5.0 inches); the displacement corresponding to the inflection point was one-half of that (64 mm [2.5 inches]). Therefore, displacement ranges were ±16 mm (0.63 inch), ±32 mm (1.25 inches), and ±64 mm (2.50 inches). Fifty cycles were applied for each displacement range, for a total of 150 cycles. Since a major displacement cycle in a bridge is expected to be completed in 1 full year, the number of cycles in the test represented the expected service life of a bridge, which lasts from 50 to 100 years.

Figures 3-31 and 3-32 show the condition of the steel and concrete piles at the conclusion of the test cycles. Figures 3-33 and 3-34 show sample load-deflection curves for the steel and concrete piles, respectively, for the load cycles at 100 percent of the calculated failure displacement. Based on the results of laboratory tests performed on steel and PS/C pile specimens, the following conclusions are drawn:

1. Tests indicate that the cyclic movement of the steel pile at the displacement level corresponding to the calculated inelastic rotational capacity of a plastic hinge in the pile resulted in local distortion (buckling), but did not result in major damage or loss of axial strength. Therefore, the failure criteria proposed by Abendroth, et al.,[(2)] provide a reasonable basis for determining the displacement limit for steel piles in integral abutments when combined with appropriate load and/or safety factors.

2. The PS/C pile specimen also sustained the axial loads during the cyclic displacement tests. However, the damage it incurred was extensive and unacceptable. Therefore, the allowable displacement limits for such piles must be set at a lower value unless steps are taken to control cracking in the vicinity of the cap. It may be feasible to provide a flexible pile-abutment connection for precast

concrete piles, such as in the details recommended by M.R. Kamel, et al.[18] Specific procedures for the design of piles in integral abutments are provided in Chapter 5 of this volume.

3.5 TASK F.5—FIELD SURVEYS

Field surveys of jointless bridges were incorporated into the research program to evaluate, through inspections, bridges and details that may have worked well, or those that may have performed poorly. Because the Tennessee Department of Transportation (TDOT) is a pioneer in the design and construction of a large number and variety of jointless bridges, that State was the obvious choice for the surveys. Edward P. Wasserman, P.E., Engineering Director of the TDOT, accompanied two project researchers on a survey of 15 bridges in different parts of the State over a 3-day period in May 1995.

The bridges inspected included a variety of materials: steel, prestressed, and reinforced concrete; types: I-beams, box beams, and an arch; and alignments: straight, curved, and skewed bridges; as well as as-designed or retrofitted jointless bridges. A total of 15 jointless bridges were inspected. A summary of the information on these bridges is provided in table 3-10. Detailed descriptions and photographs of each bridge are provided in chapter 10 of the experimental report.[14]

Overall, the field performances of these bridges were satisfactory. The distress observed, for the most part, were related to inadequate details for accommodating movement. The following summary is divided into observations for the superstructure, abutments, piers, approach slabs, details, and retrofitted bridges.

1. Observations related to the superstructure include the following:

    a. Vertical cracks, as seen in figure 3-35, were usually evident at the bottom of the diaphragms between the precast, prestressed beams over the piers (positive-moment connection region) for the fascia beams. For the interior beams with ends encased in the diaphragm concrete, spalling at the concrete near the bottom flange, as shown in figure 3-36, can result from movements associated with positive moment. These cracks served to relieve tensile stresses developed because of creep, shrinkage, and positive temperature gradients. However, in general, these cracks were probably not detrimental to the long-term performance of the structure. Over-reinforcement of this region

may result in cracking in far more undesirable locations (i.e., within the span at the termination point of added reinforcement).

b. Transverse deck cracking over the piers was noted on four bridges, although the majority of the bridges inspected had an asphalt overlay. Very minor (hairline) cracks were noted in the decks of two of the retrofitted bridges (Bridges 4 and 5) directly over the piers. These structures were retrofitted to be continuous-deck bridges without making the girders continuous.

c. The reinforced concrete box structure for Bridge 10 had noticeable cracking in the bottom flange (positive-moment cracking) near the stub abutment end, where most of the movement was occurring. This cracking is seen in figure 3-37. Restraint from slope paving against the forward face of the stub abutment possibly contributed to this cracking.

2. Observations related to abutments include the following:

a. Horizontal cracks and efflorescence were commonly observed on the front face of integral abutments at the construction joint between the footing and abutment wall. The efflorescence was typically most noticeable directly below the bearing of the beams, as seen in figure 3-38. However, the efflorescence was distributed along the entire abutment in some bridges.

b. Washout and/or settlement of soil beneath the pile cap, as shown in figure 3-39, was found at several abutments. Note that several inches of an abutment pile are clearly visible.

c. Gaps observed between the slope pavement and the front face of the abutments indicate that the abutments were initially partially restrained from contraction by the slope pavement until the bridge pushed the pavement toward the center of the bridge.

d. Abutment piles were usually oriented for strong-axis bending in resisting longitudinal movement. Also, drawings indicated that, typically, approximately one-half of the abutment piles were to be battered forward at a slope of 2:12.

e. Wingwalls typically paralleled the bridge alignment to form U-shaped abutments in plan. These wingwalls were supported by one or more piles, depending on the wall length, although some short (2.4 to 3.0 m [8 to 10 ft])

wingwalls were cantilevered from the abutment. Wingwall piles were typically oriented with their weak axis resisting the longitudinal movement of the bridges.

f. One structure, which has a full-height abutment and U-type wingwalls (Bridge 8), exhibited significant cracking in the wingwalls, as seen in figure 3-40.

g. Indications of significant transverse movement of the abutments were observed in bridges with large skews and/or horizontal curves. U-type wingwalls on these abutments would be expected to be subjected to lateral resisting forces from soil passive pressure and from the piles. The stub abutment wingwalls observed were performing well.

3. Observations related to piers include the following:

a. Most of the piers for the bridges inspected had pinned bearings. There were no distresses observed with any of these connections.

b. One bridge was fully integral, with the bridge beams embedded in transversely post-tensioned pier caps. Relatively minor cracking, because of moment transfer at this connection,.was observed at the interface of the column and the pier cap

c. With the exception of the Holston River Bridge (Bridge 12), there was no noticeable cracking in the semi-integral piers. For the exceptionally long Holston River Bridge, however, slender piers near the end of the bridge exhibited well-distributed flexural cracks, as seen in figure 3-41, and one short pier exhibited shear cracks. However, there was no distress or evidence of corrosion associated with the observed cracks.

d. The first pier on several bridges was partially restrained at a height significantly above the footing by the slope paveing.. Figure 3-42 shows cracking in the slope pavement at the first pier of Bridge 10. The slope pavement was cast around the pier with inadequate anticipation of the bridge movement.

4. Observations related to approach slabs include the following:

a. Two of the bridges inspected did not have approach slabs. These include retrofitted Bridge 5 and retrofitted Bridge 13. The continuous decks for these bridges were 75 m (246 ft) and 69.7 m (228.6 ft) long, respectively. Some

faulting, pavement settlement, and unraveling of deck concrete were observed at the interface of the asphalt pavement and backwall of the abutment, as shown in figure 3-43.

b. Three types of connections were observed between the reinforced concrete approach slab and the abutment backwall:

   - One type included supporting the end of the approach slab on a haunched corbel or notch on the rear face of the abutment backwall, but without horizontal reinforcement tying the approach slab to the abutment. With this connection, cyclic expansion and contraction jacks the approach slab away from the abutment, leaving a gap. Figure 3-44 shows a large opening between the approach slab and the abutment of Bridge 1, which had been constructed without any horizontal reinforcement tying them together.

   - A second type included top and bottom reinforcement extending from the deck concrete into the approach slab. This moment connection apparently resulted in a relatively minor crack located 0.45 to 0.90 m (18 to 36 inches) into the approach slab.

   - A third type included reinforcement to effect a pinned connection, as shown in figure 3-45. .

c. Settlement of the far end of the approach slab (away from the bridge) was commonly observed. The settlement is partially associated with washout from drainage. It is also partially attributed to settlement of the backfill behind the abutment with cyclic contraction and expansion that is associated with creep, shrinkage, and thermal strains, combined with the use of relatively short approach spans such that the far ends of the approach slabs are within a zone of soil influenced by abutment movement. The relatively new details used in Tennessee and depicted in figure 3-45 include a span of 7.3 m (24 ft) and drainage within the first half of the approach slab span.

d. Two bridges included in the inspection survey had concrete pavement adjacent to the approach slab. In both cases, the approach slabs were in good condition, whereas the pavement had significant faulting cracks, as seen in figure 3-46. Typically, the ends of the approach slab settle, and the relatively rigid concrete pavement cannot adequately accommodate the settlement.

e. The majority of the bridges inspected had asphalt pavement adjacent to the approach slabs. Asphalt patching was commonly observed, as seen in figure 3-47, for releveling the pavement at its joint with the approach slab interface.

5. Observations related to other details include the following:

   a. Settlement of the approach slab can cause damage to attached barrier walls. Barrier walls should be jointed at both ends of the approach slabs to accommodate differential settlement.

   b. Transverse movement of integral abutments associated with large skews or horizontal curves should be anticipated in the design of the details for the barrier walls, drainage structures, and ends of the approach slabs.

   c. Pavement used for slope protection and cast directly against the inside of the abutment or enclosed piers can produce partial restraint of the contraction movement of the abutments and interior piers. Slope protection should be constructed to allow for sufficient unrestrained movement. The two bridges that were under construction at the time of the survey were using stone for slope protection rather than concrete pavement.

6. Observations related to retrofitted bridges include the following:

   a. Two PS/C bridges were retrofitted with continuous decks, but without continuous beams. Typically, the end of at least one beam was connected to each pier cap to effect a pinned connection between the superstructure and the pier so that the pier caps would move with the bridge superstructure. The other ends of the beam (from the adjacent spans) were supported on expansion bearings. These two bridges exhibited minor (hairline) cracks in the decks at the piers.

   b. Two bridges were retrofitted to make the decks and girders continuous. One bridge, an arch span with three approach spans on each end, had new PS/C girders with continuity connections at the diaphragms for the approach spans. The other bridge was a steel girder structure with top and bottom flanges spliced to effect moment connections over the piers.

   c. Two bridges (Bridges 4 and 6) were retrofitted by removal and complete replacement of the deck. One deck, with Bridge 5, was retrofitted by scarifying it 25.4 mm (1 inch) and adding a 114.3-mm (4.5-inch) overlay.

Extra reinforcement was placed in the overlay over the piers. Another deck, with Bridge 13, was retrofitted by scarifying it 6.35 mm (0.25 inch) and removing a full-depth 711-mm- (28-inch-) wide strip of deck on each side of the expansion joints while retaining the existing rebars. Two layers of No. 4 bars at 152.4-mm (6-inch) centers were spliced with the existing rebar to form continuous reinforcement in the deck, and the opening was filled with new concrete. Then, a 31.8-mm (1.25-inch) polymeric concrete overlay without reinforcement was added.

d. For three of the retrofitted bridges, the existing abutments' pile caps or "footings" were used with new concrete doweled to the existing concrete, encasing the ends of the girders to develop integral abutments. All new abutments were constructed for the fourth retrofitted bridge.

e. The length of the retrofitted bridges range from approximately 61 m (200 ft) to 107 m (350 ft).

3.6 TASK F.6—FIELD TESTS

A bridge that carries Interstate 40 (I-40) over Ramp 2B (to I-75) in Knoxville, TN, was selected for field instrumentation and monitoring. This is the longest steel-beam jointless bridge in the State. The 126.77-m (415.92-ft) bridge has three spans of 42.62 m (139.83 ft), 63.40 m (208 ft), and 20.75 m (68.08 ft). The skew angle is 59.09° and the width of the bridge is 40.23 m (132 ft). The superstructure consists of 12 steel-plate girders spaced at 3.43 m (11.25 ft) apart, composite with a 235-mm (9.25-inch) slab. Figures 3-48 and 3-49 show plan and elevation views and a cross-section view, respectively, of the instrumented bridge.

As a skewed jointless bridge expands and contracts because of diurnal and seasonal temperature changes (and creep and shrinkage effects), it tends to rotate about a vertical axis because of the abutment's restraint of thermal movements. The lateral abutment movement may be resisted during expansion to some extent by the shear friction of soil behind the abutments; however, with a large skew angle, this friction could be overcome. Therefore, in addition to longitudinal movement, the abutment could be expected to move laterally, with resistance to movement coming, in part, from the abutment piles and wingwalls. The end restraint of longitudinal movement provided by the abutments induces strains in steel stringers, the magnitude of which is indicative of the degree of restraint. Since analytical models indicated that the abutment restraint has a relatively

minor influence on beam stresses,[15] this field study was designed to verify this analytical finding. Finally, the effect of bridge skew on the bridge response to diurnal temperature gradients was also of interest. In this section of the report, various aspects of this field program, including objectives, bridge details, instrumentation plan, and test results, are presented.

The overall objectives of this field instrumentation program were to:

1. Assess the longitudinal and transverse movements of abutments.
2. Obtain indications of the effect of abutment restraint on longitudinal expansion and contraction.
3. Evaluate the effect of bridge skew on the bridge response to diurnal temperature gradients.

Strain, temperature, and displacement gauges were installed on the east span of the bridge. The issue of passive soil pressure was indirectly evaluated in this study through the measurement of strain changes in the beams. The bridge was also sharply skewed at a 59-degree angle. The northeast corner of the instrumented span had an acute corner from the skew. The sensors installed on the bridge were monitored for 1 year using an automated solar-powered data acquisition system. Most measurements were taken at 6 a.m. to evaluate seasonal (not daily) variations. However, in several 48-hour periods (including the summer and winter solstices), hourly measurements were performed to obtain diurnal data.

The minimum, maximum, and average daily (6 a.m.) air temperatures for the 1-year monitoring period were -18.1 °C (-0.6 °F), +26.9 °C (80 °F), and +12.1 °C (53.8 °F), respectively. The minimum and maximum daily air temperatures occurred on February 5, 1996, and June 25, 1996, respectively. The minimum, maximum, and average structure temperatures were -14.0 °C (6.9 °F), +29.4 °C (85.0 °F), and +14.1 °C (57.3 °F), respectively. Therefore, the overall maximum seasonal air and structure temperature (6 a.m.) changes (maximum minus minimum) were 45.0 °C (80.9 °F) and 43.4 °C (78.1 °F), respectively.

The following are some of the conclusions from the field tests:

1. Relative longitudinal and transverse movements between the top and bottom of the east pier were negligible.

2. For the seasonal data, the longitudinal movement ranges (maximum minus minimum) for the steel girders with respect to the top of the east pier were higher at the north fascia (14.43 mm [0.568 inch]) as compared to the center (7.89 mm [0.311 inch]) and south beams (7.65 mm [0.301 inch]). The overall transverse displacement ranges for the center and south gauges were 5.16 mm (0.203 inch) and 2.95 mm (0.116 inch), respectively. Therefore, transverse movement was substantial relative to the longitudinal movement.

3. Length changes in the north and south beams in the east span were also measured. For the north beam, an overall measured displacement range of 9.60 mm (0.378 inch) was recorded for the seasonal data. This displacement was very close to the estimated (theoretical) girder length change of 9.3 mm (0.37 inch). For the south beam, an overall length change of 10.19 mm (0.401 inch) was measured for the same temperature range.

4. For the seasonal data, changes in the average stringer strains from the hottest day (June 25, 1996) to the coldest day (February 5, 1996) were +171, +52, and +28 millionths for the north, center, and south girders, respectively. It is clear that the north beam was subjected to the largest strain changes. However, these strains are all small compared to the allowable stresses. The maximum strain of 171 millionths corresponds to a stress of 35.37 MPa (5,130 lbf/inch^2). This maximum strain is reduced to 37 millionths when considering the effect of the differences in the assumed coefficients of thermal expansion for steel and concrete. Similar results were also obtained for the measured web strains at midheight of the girders.

5. During the 48-hour periods selected to measure hourly diurnal data, the maximum and minimum recorded structure temperatures were 32.8 °C (91 °F) and -0.8 °C (31 °F), respectively. The maximum structure temperature variation of 9.2 °C (16.6 °F), as measured during a 48-hour period, occurred during the July 17-19, 1996, time period. The maximum measured positive and negative temperature differentials between the deck and beam were 10.0 °C (18 °F) and −2.4 °C (−4.3 °F), respectively.

6. External restraint strain changes in the north fascia were opposite (in sign) to the corresponding changes in the south. As temperature and solar radiation increase in the afternoon hours, the north experienced more compressive external restraint strains, while the south girder experienced tensile strains.

7. Overall, the magnitudes of the strains in the beams resulting from seasonal and diurnal changes in this bridge were small compared to the allowable stresses. Also, the effect of skew tends to increase deflections and strains on the acute corners of the bridge.

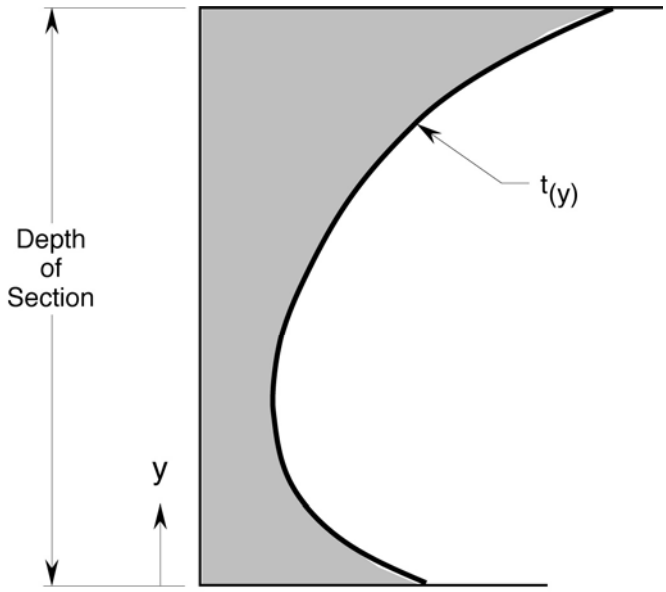

Figure 3-1. Example of positive nonlinear temperature distribution.

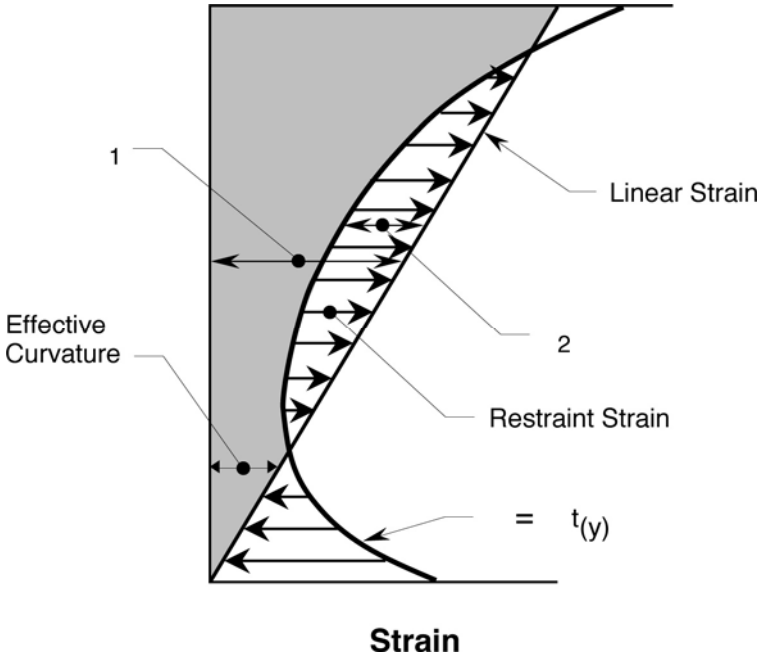

Figure 3-2. Unrestrained and restraint strains caused by nonlinear temperature distribution.

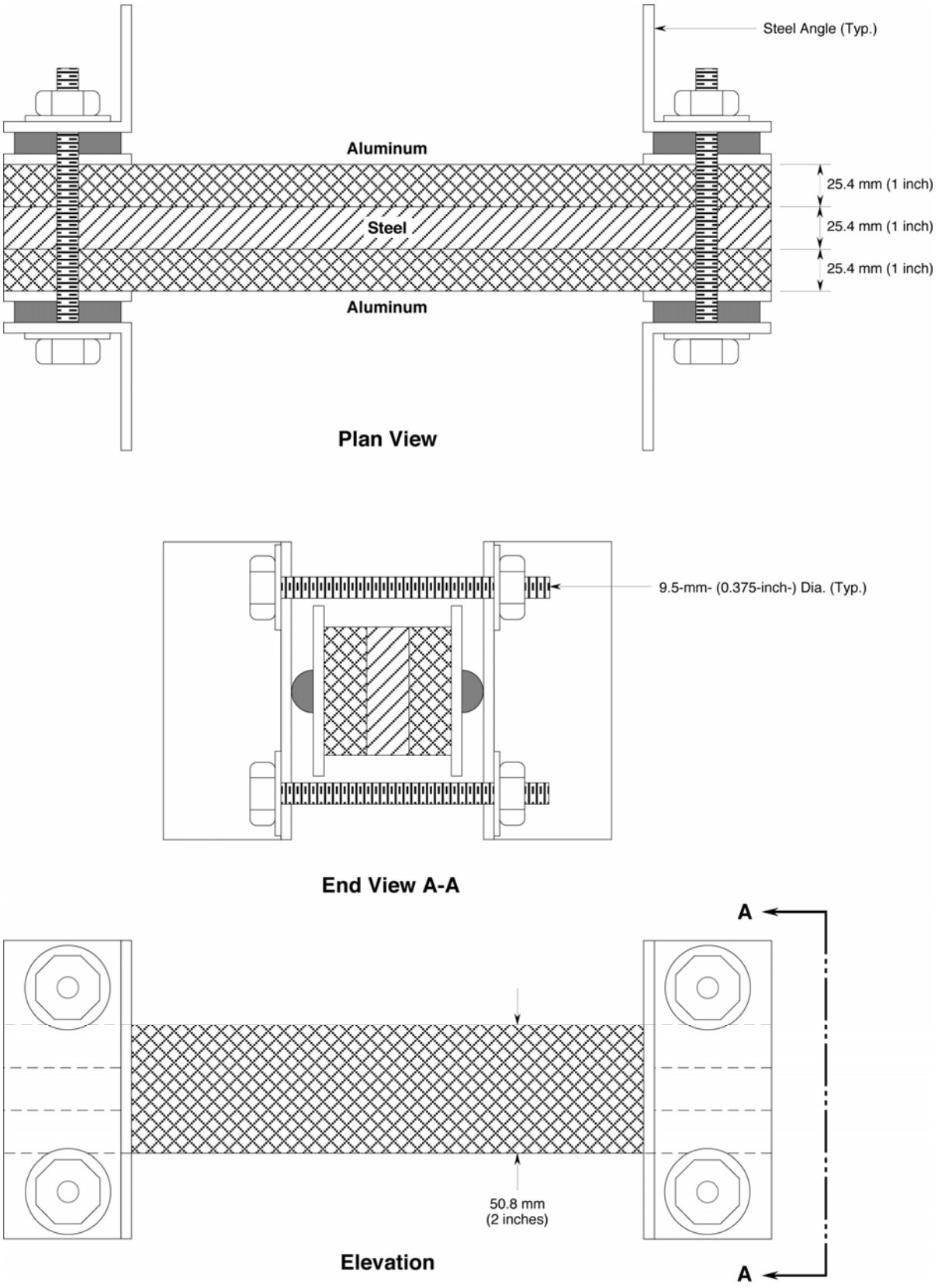

Figure 3-3. Aluminum-steel-aluminum sandwich (ASA) test specimen.

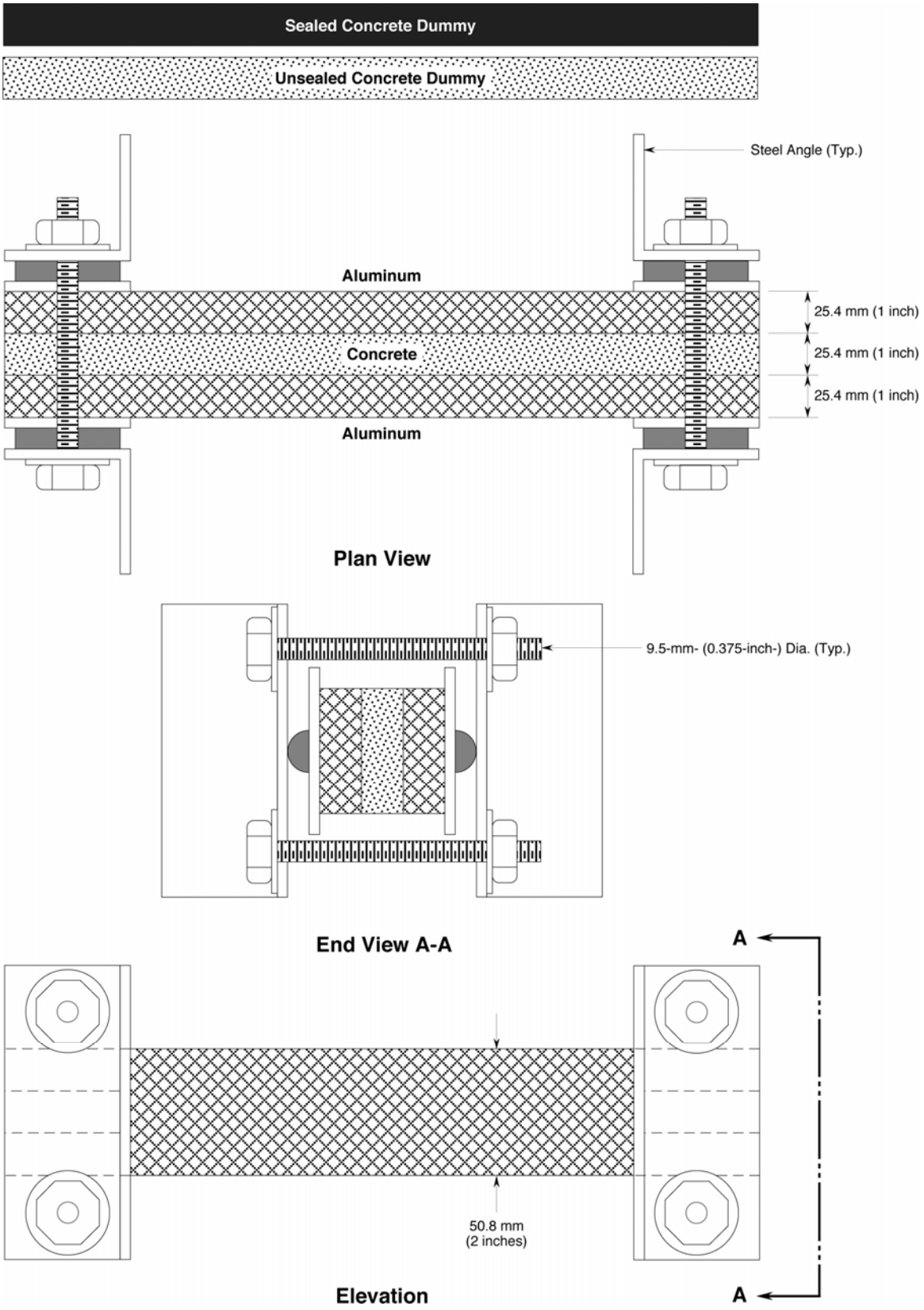

Figure 3-4. Aluminum-concrete-aluminum sandwich (ACA) test specimen.

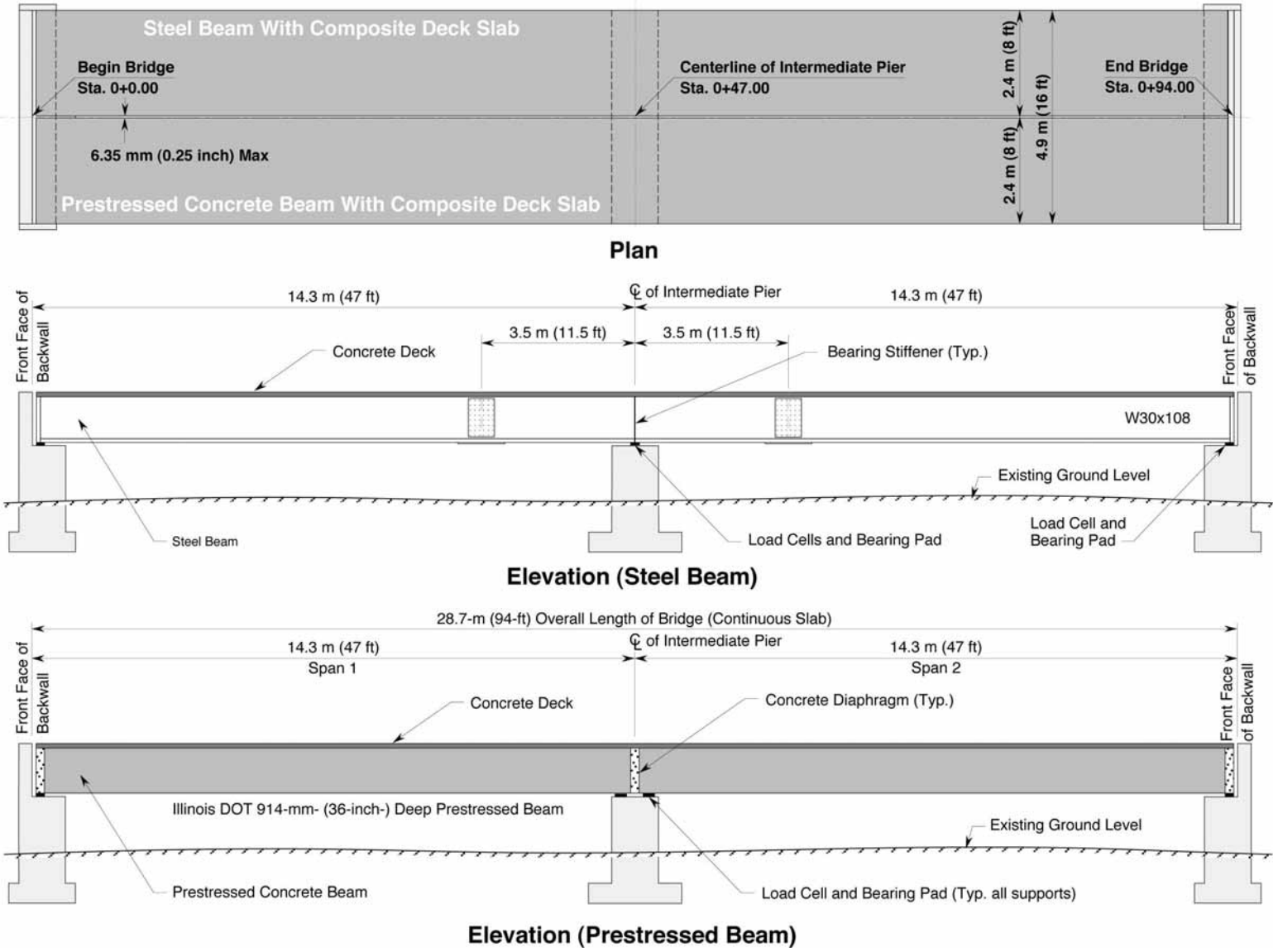

Figure 3-5. Plan and elevation of test beams.

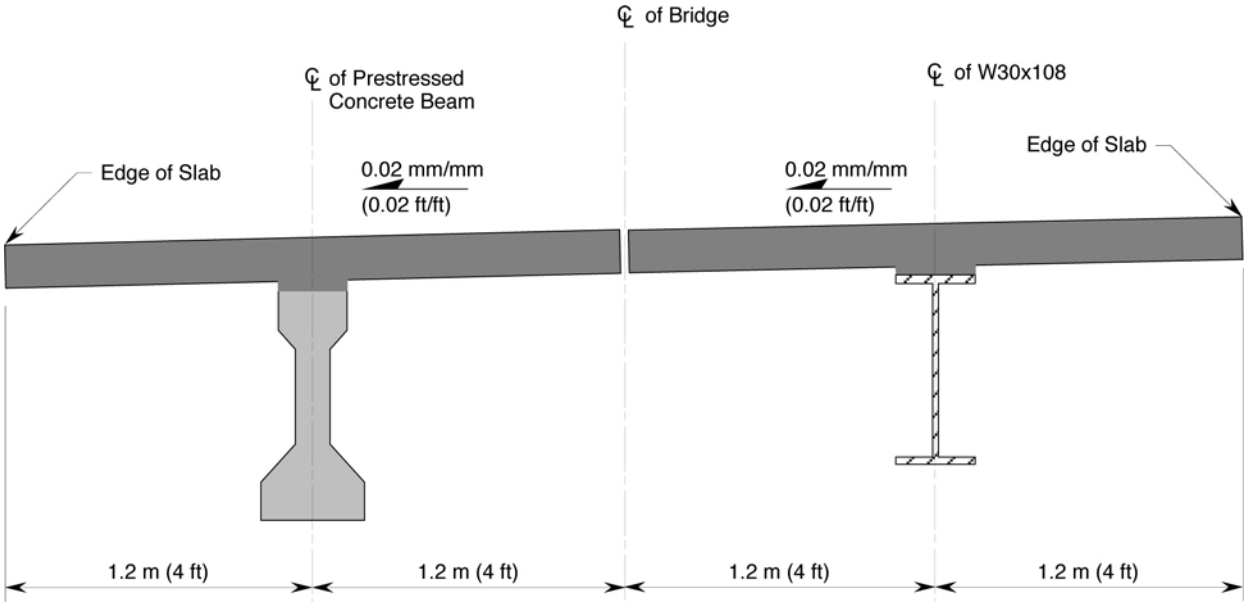

Figure 3-6. Cross section of test beams.

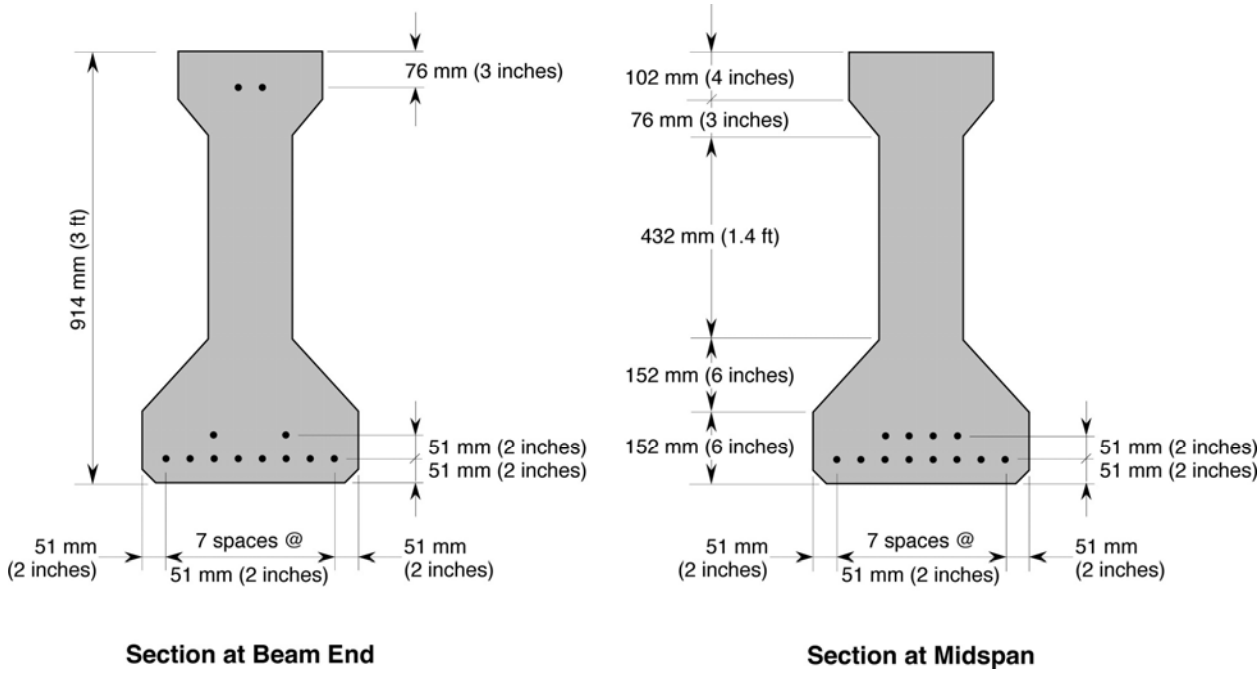

Figure 3-7. Cross section of prestressed beams.

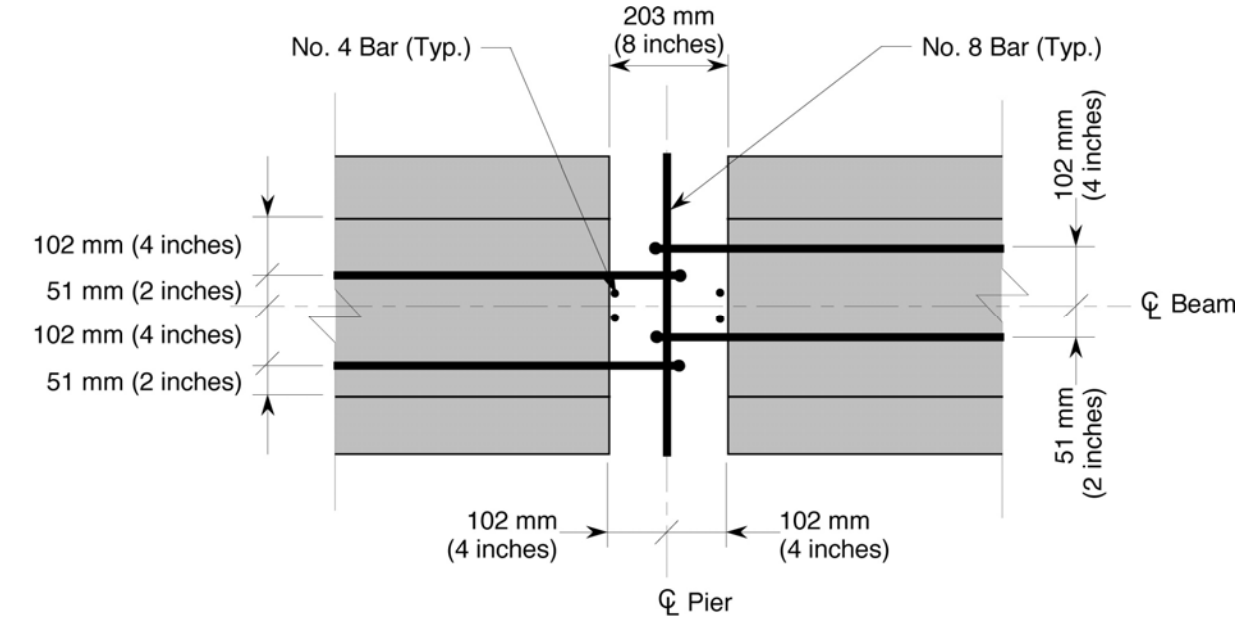

Plan

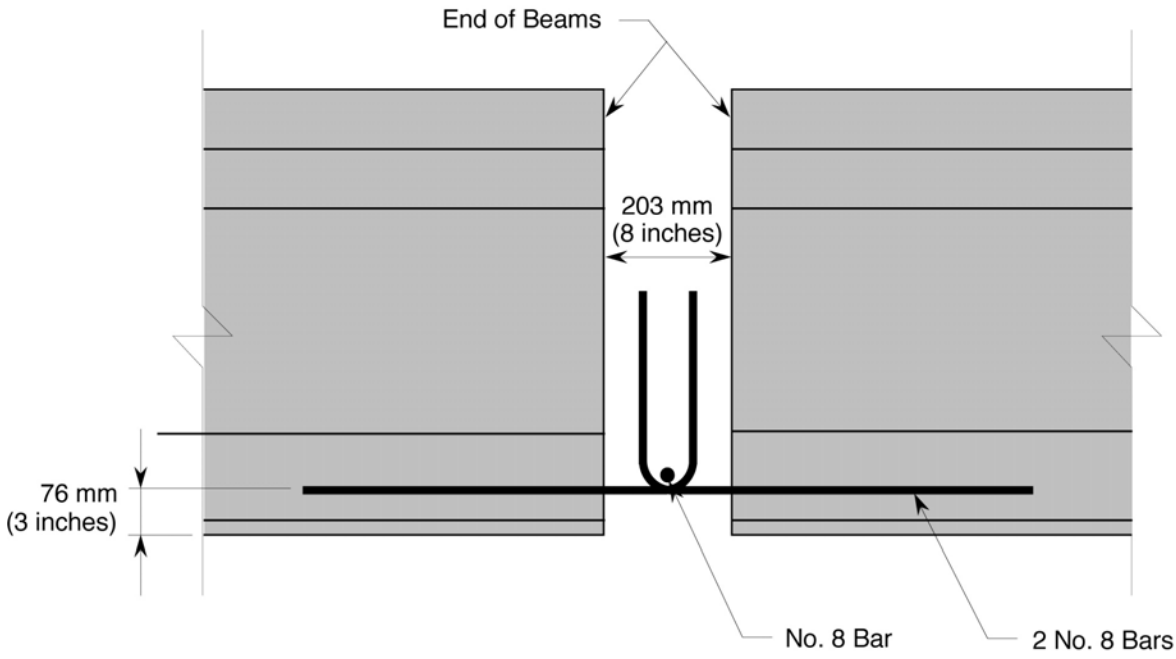

Elevation

Positive-Moment Connection Details

Figure 3-8. Positive-moment connection details.

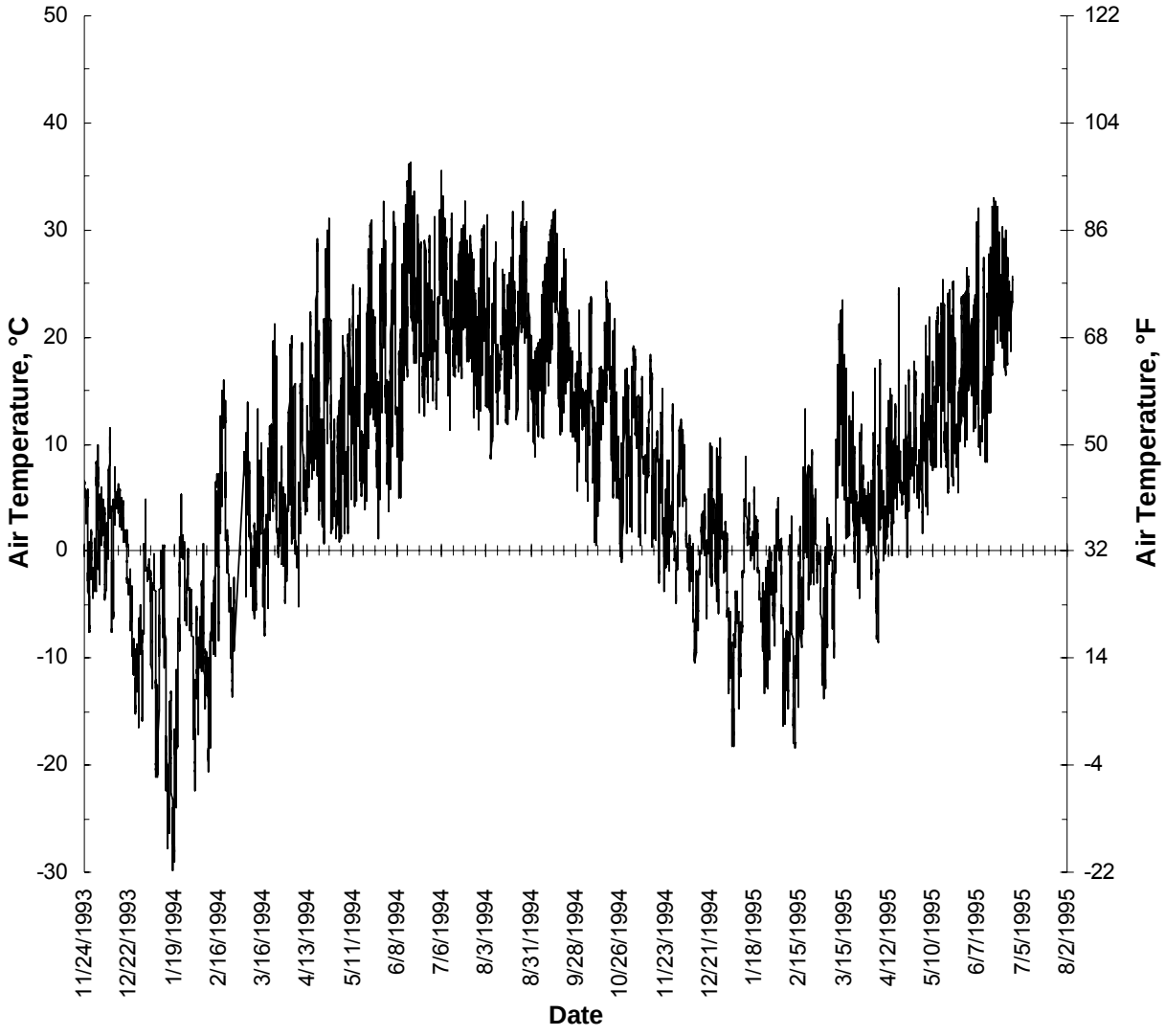

Figure 3-9. Measured shade air temperatures during the monitoring time period.

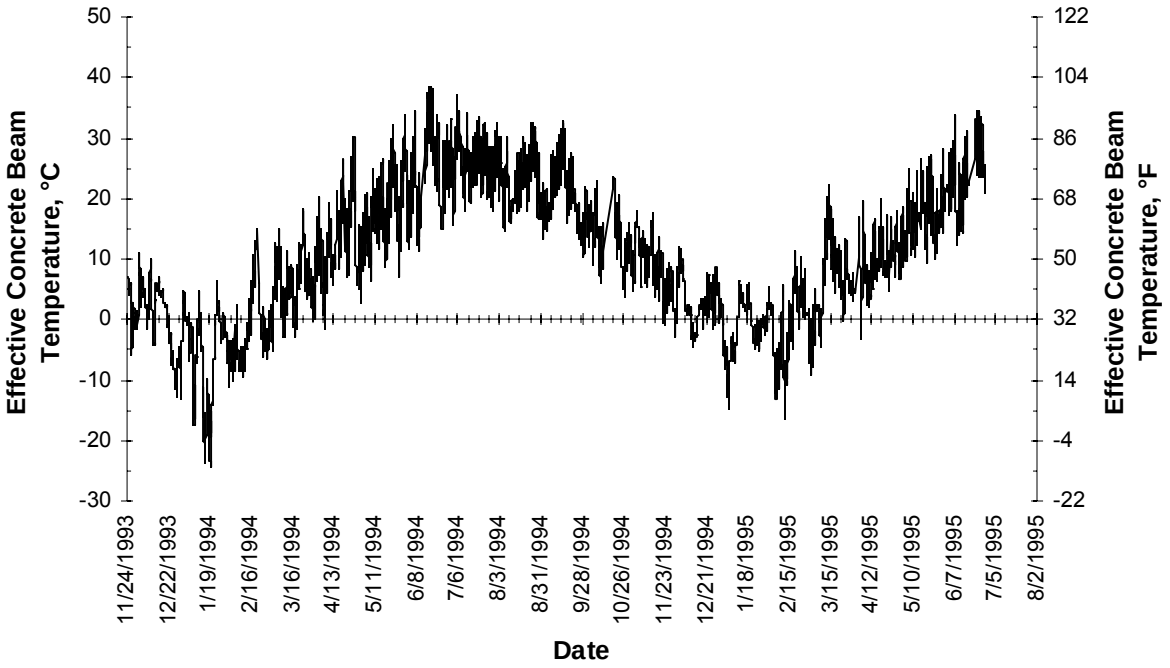

Figure 3-10. Variations in the effective concrete beam temperatures over the monitoring time period.

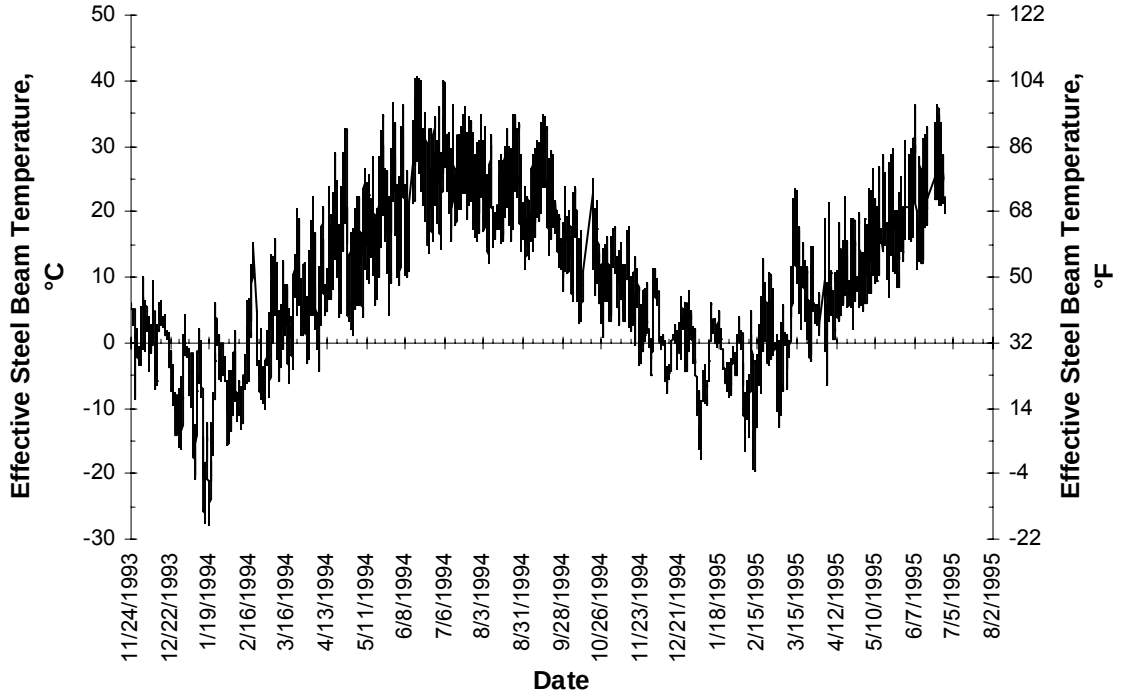

Figure 3-11. Variations in the effective steel beam temperatures over the monitoring time period.

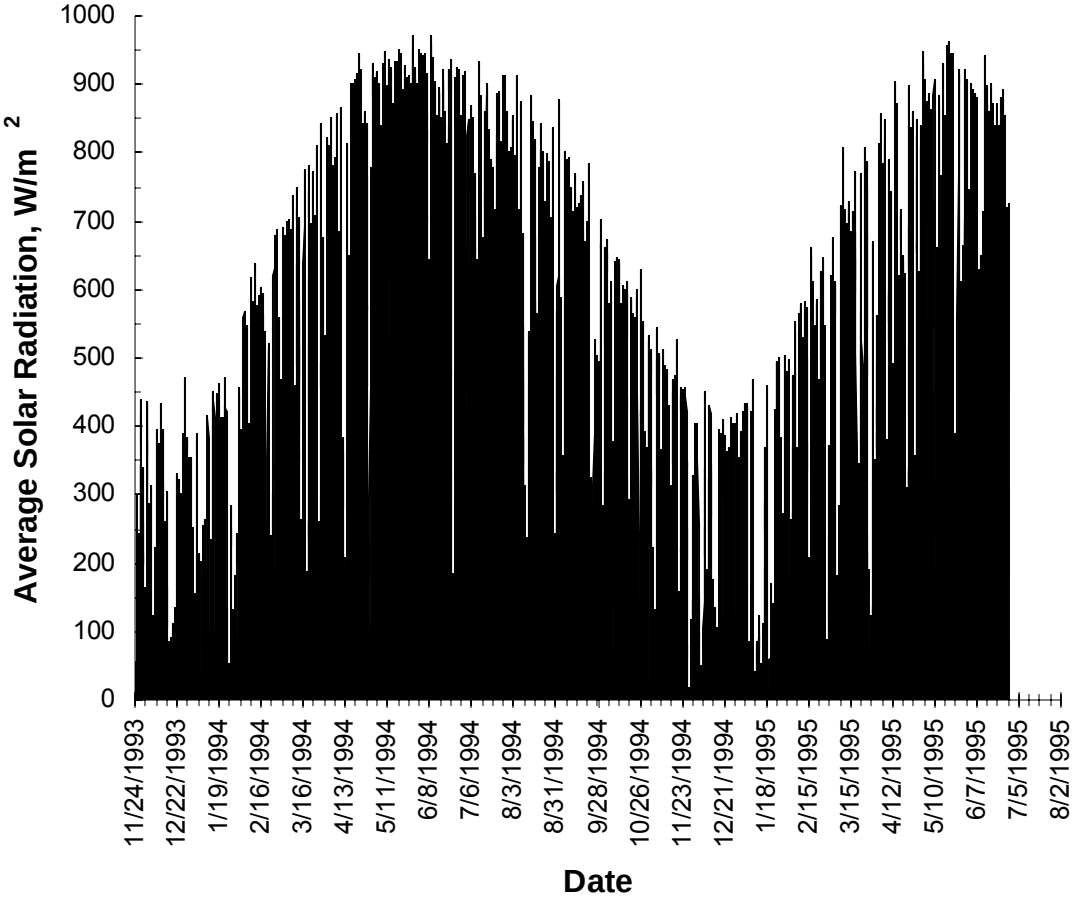

Figure 3-12. Variations in average solar radiation over the monitoring time period.

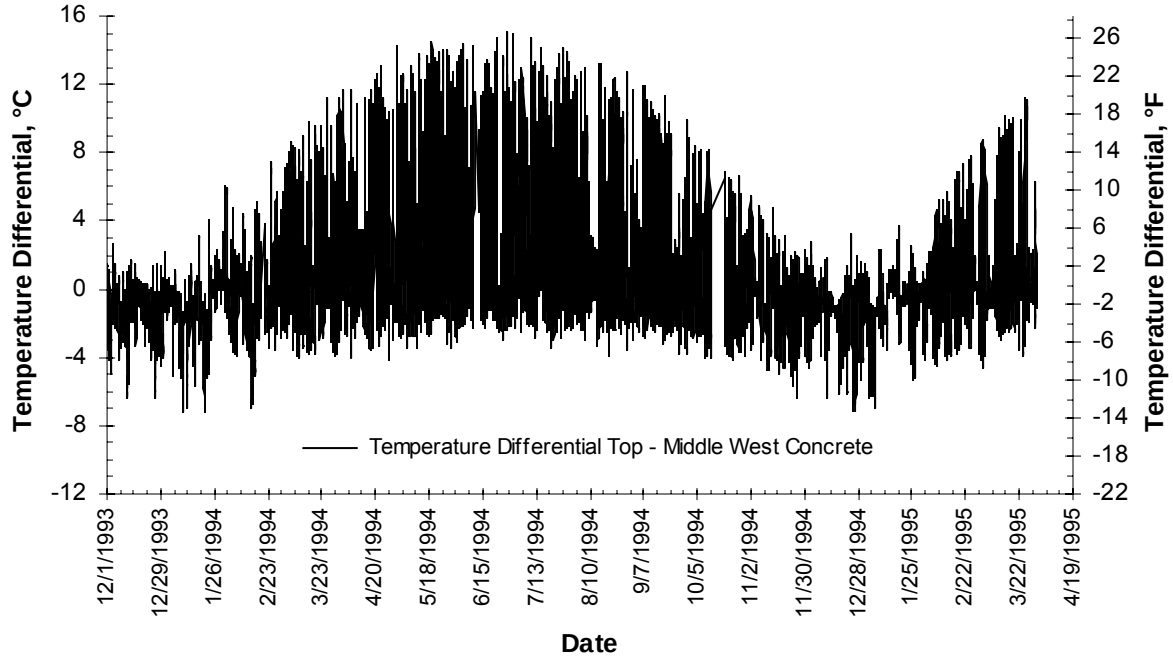

Figure 3-13. Measured temperature differentials for the west span of the concrete beam.

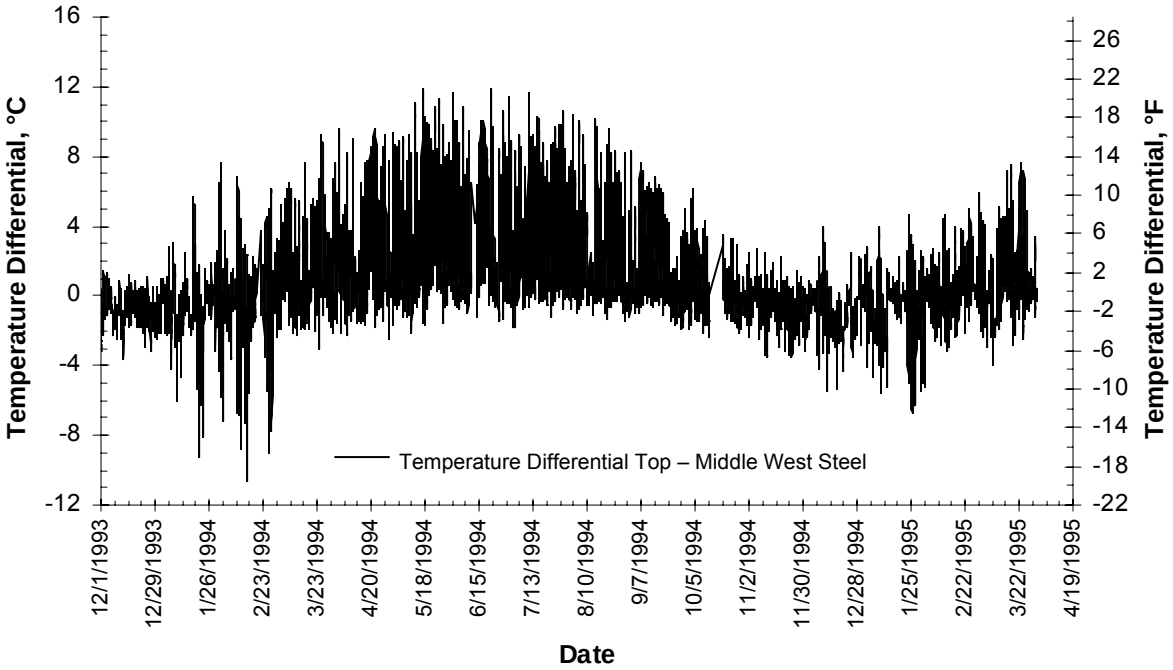

Figure 3-14. Measured temperature differentials for the west span of the steel beam.

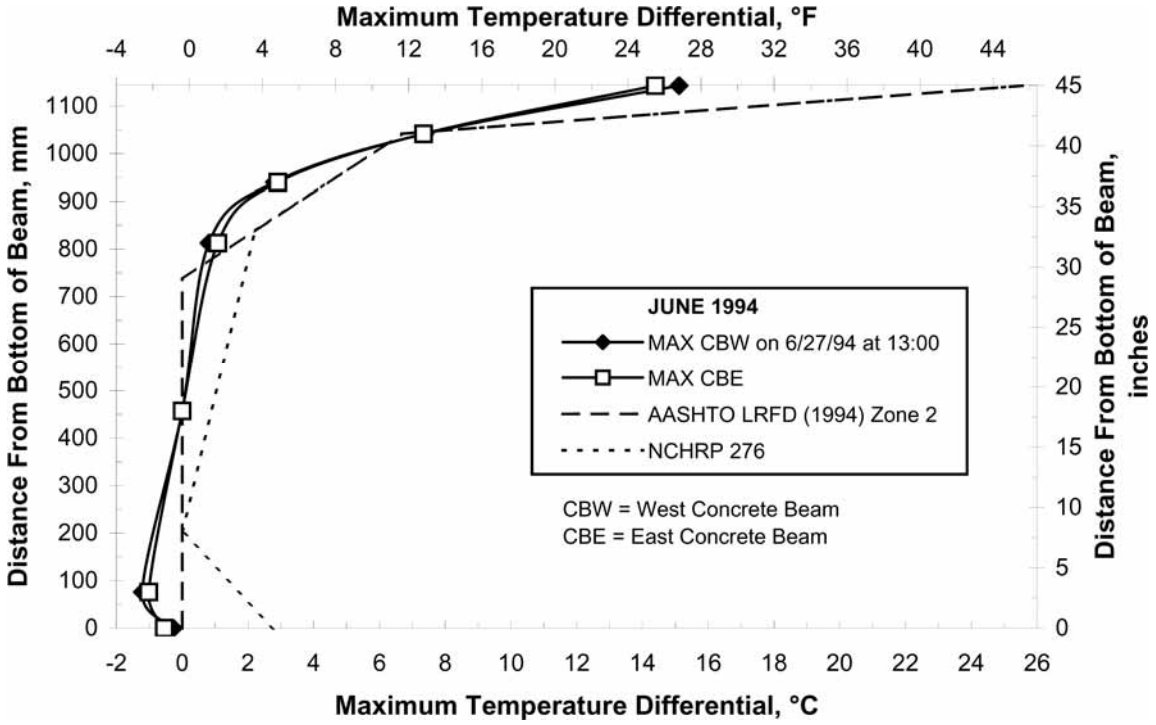

Figure 3-15. Temperature distribution at the time of maximum temperature differential for the concrete beam.

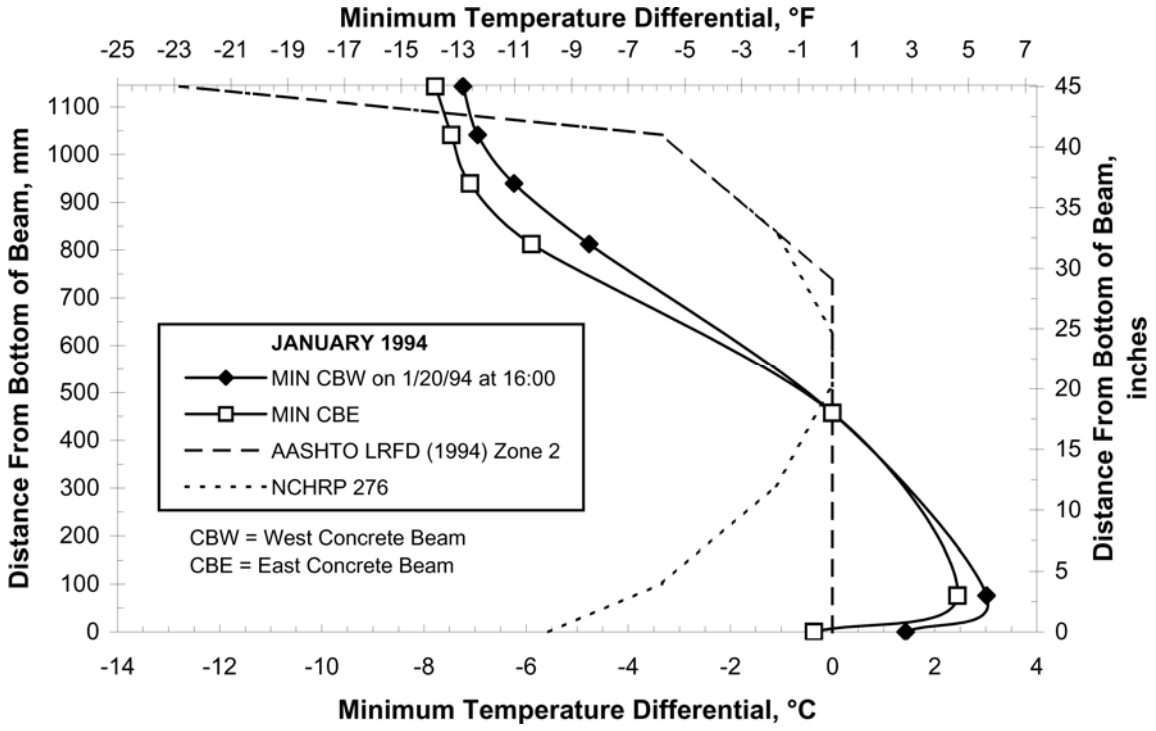

Figure 3-16. Temperature distribution at the time of minimum temperature differential for the concrete beam.

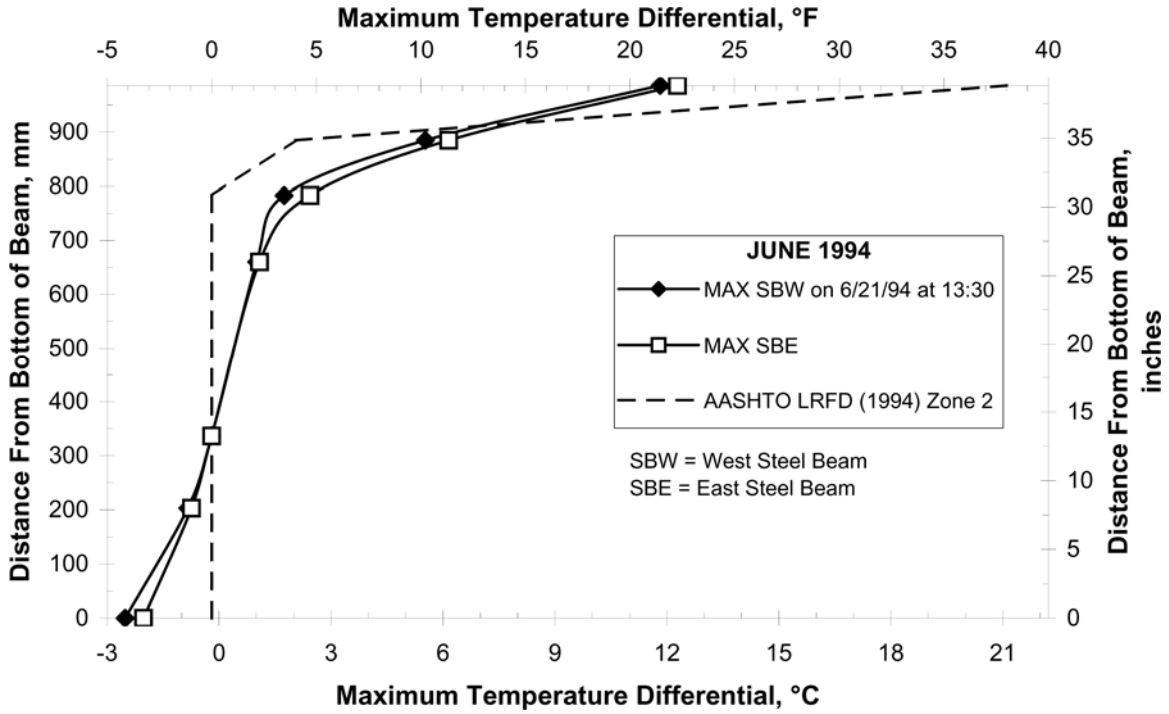

Figure 3-17. Temperature distribution at the time of maximum temperature differential for the steel beam.

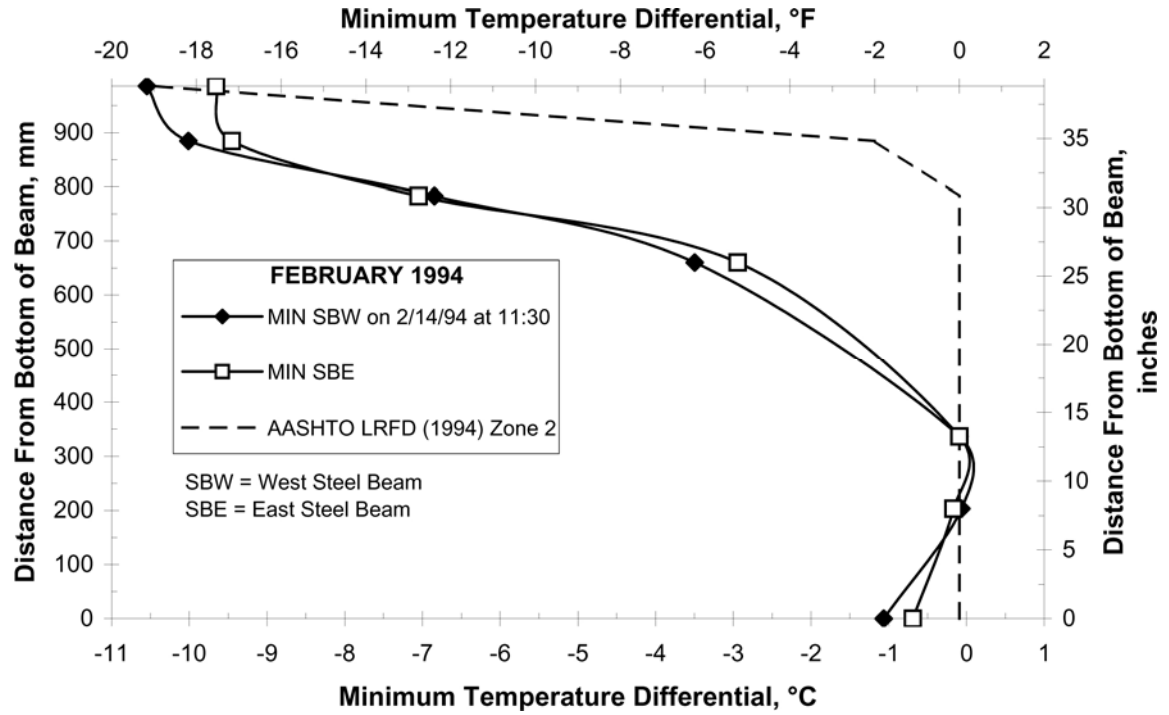

Figure 3-18. Temperature distribution at the time of minimum temperature differential for the steel beam.

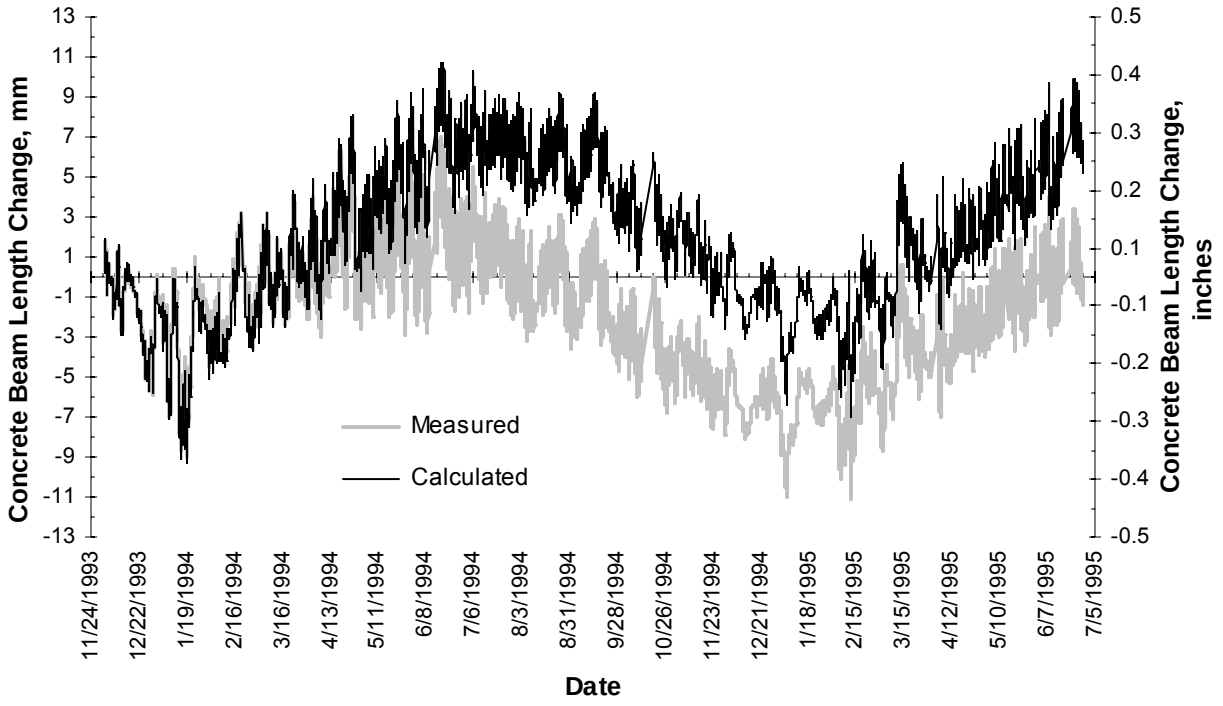

Figure 3-19. Comparison of measured and calculated length changes in concrete beam.

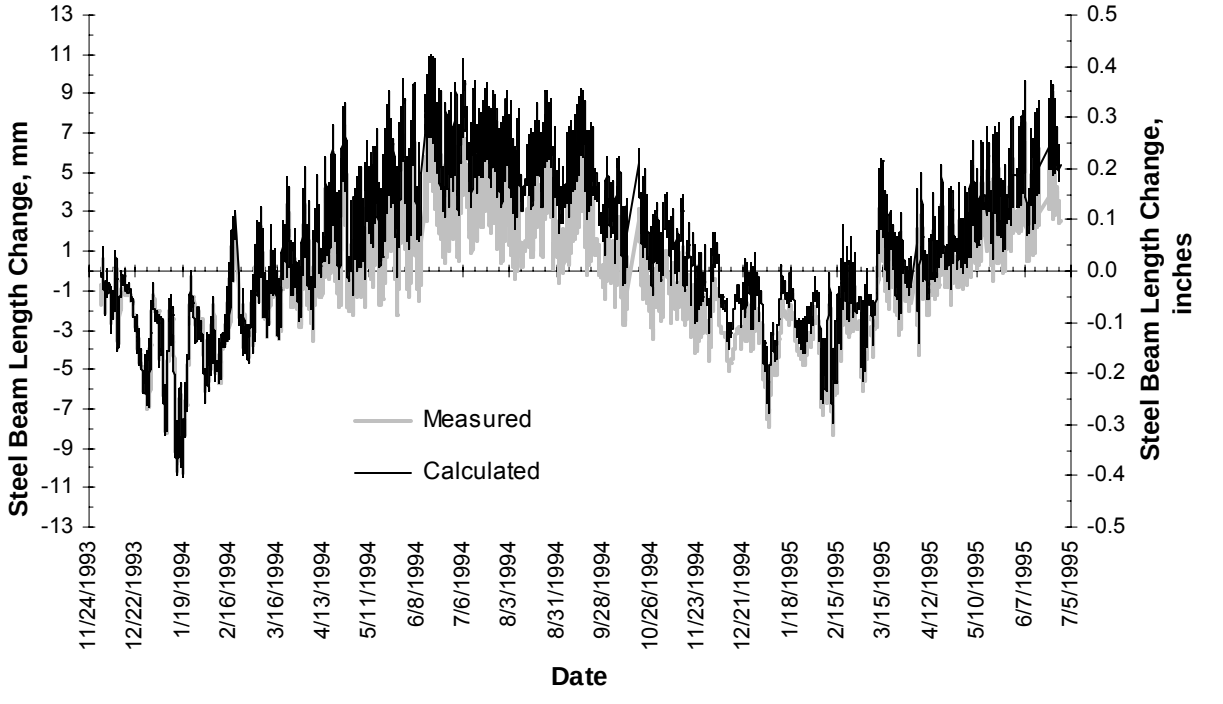

Figure 3-20. Comparison of measured and calculated length changes in steel beam.

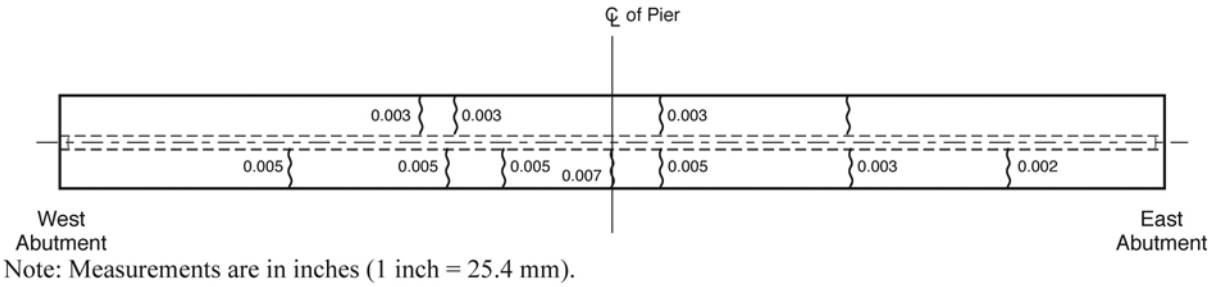

Note: Measurements are in inches (1 inch = 25.4 mm).

Figure 3-21. Cracking of the deck slab over the steel beam.

Figure 3-22. Cracking of diaphragm over center pier in concrete beam.

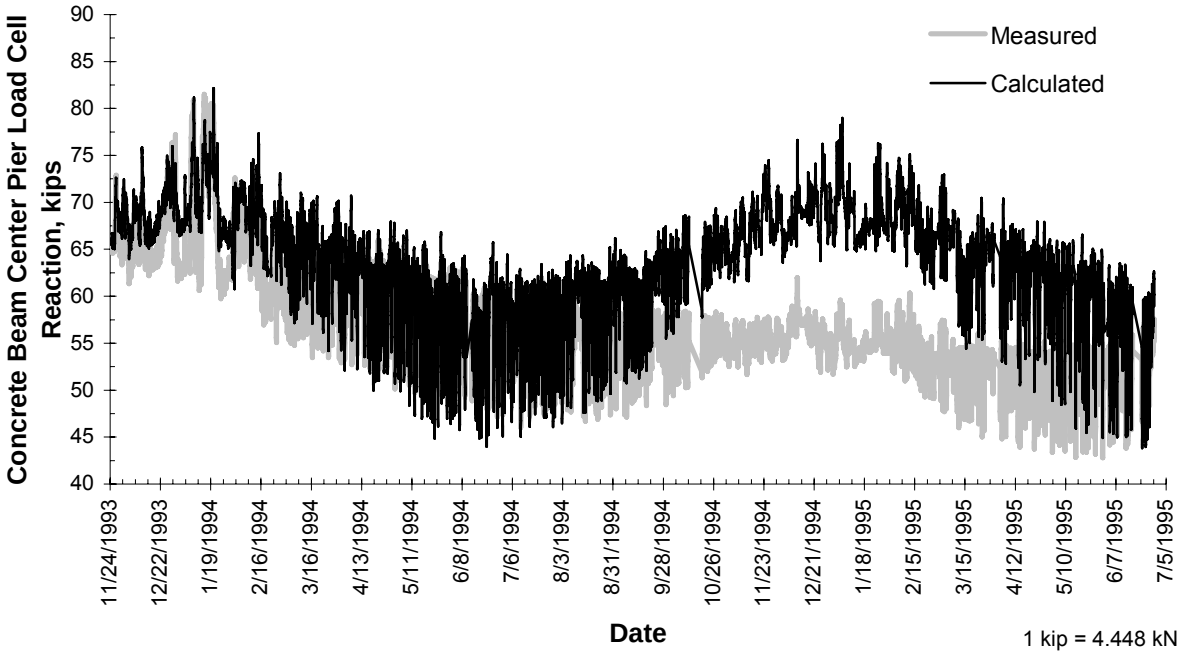

Figure 3-23. Variations in measured and calculated center pier reactions in concrete beam.

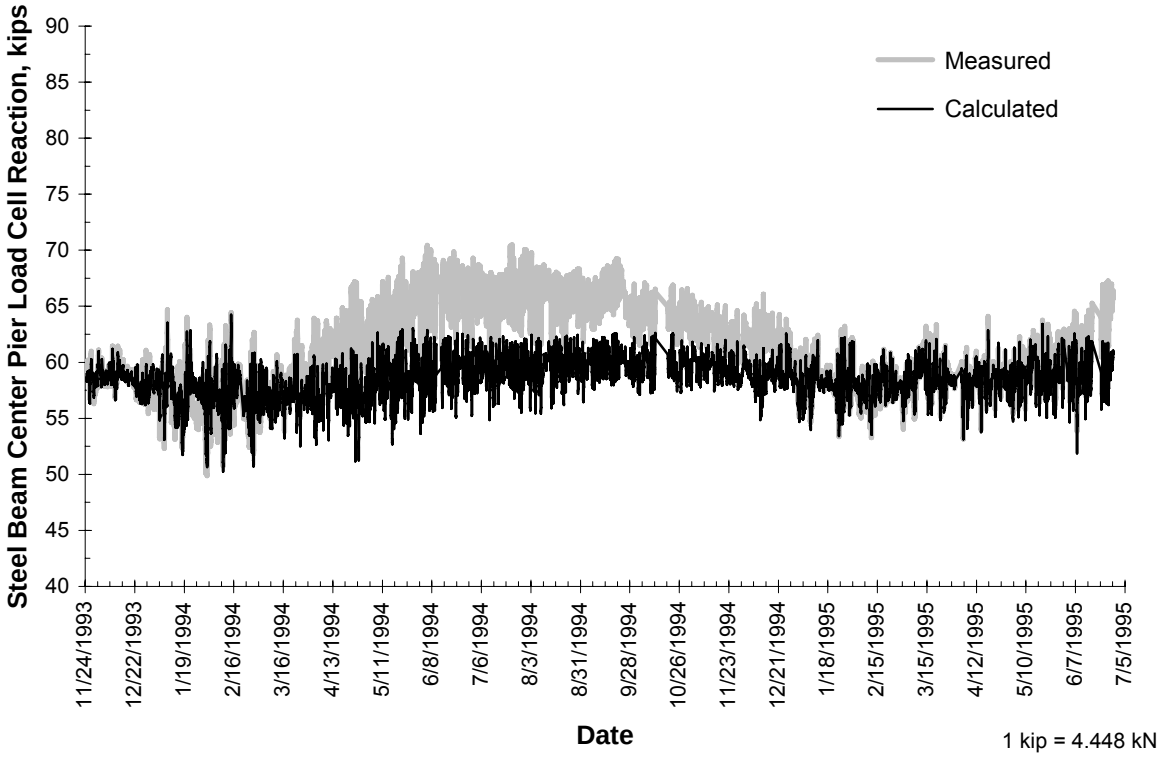

Figure 3-24. Variations in measured and calculated center pier reactions in steel beam.

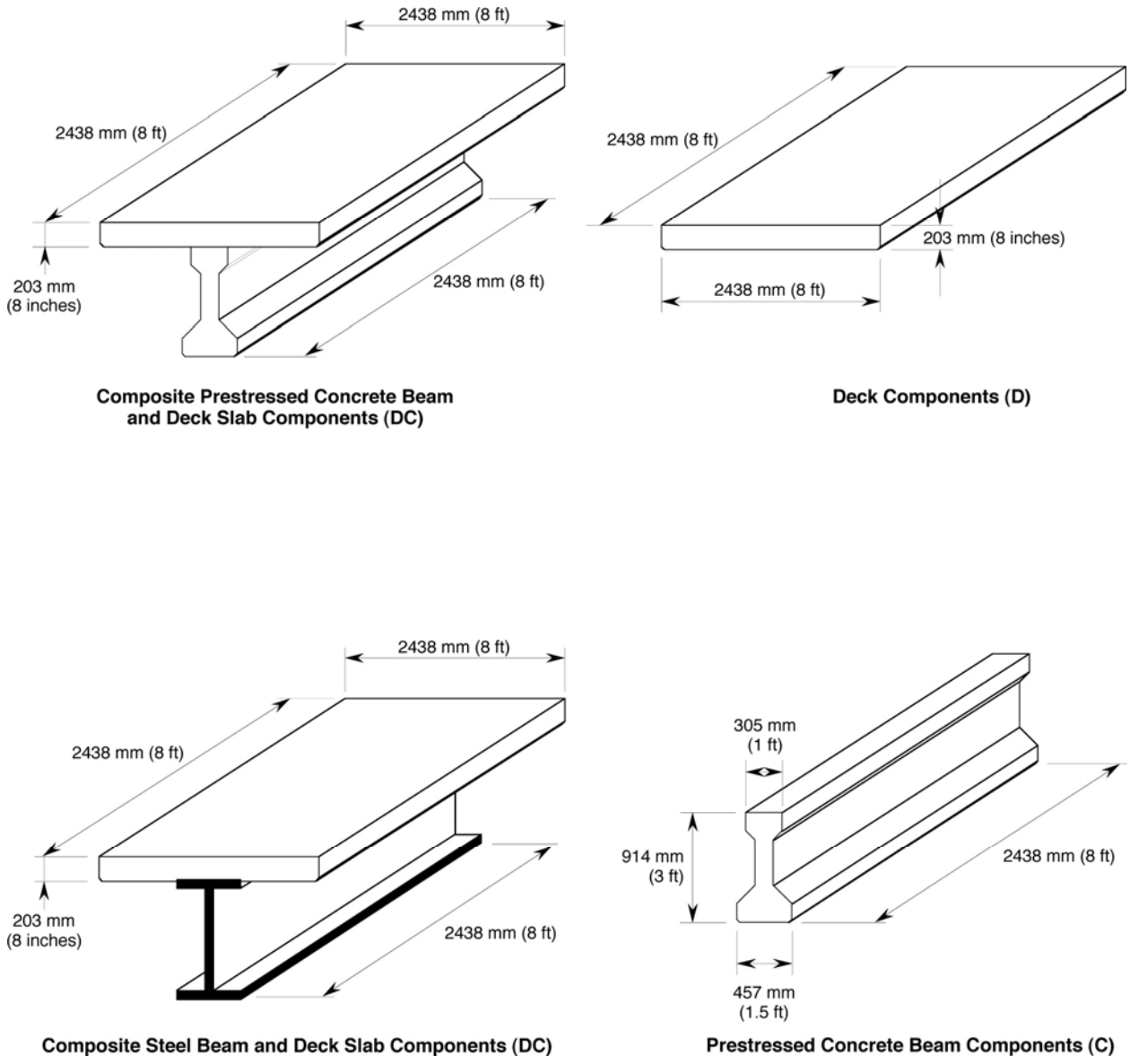

Figure 3-25. Component test specimens.

a. Slab elements.

b. Slab and PS/C beam elements.

Figure 3-26. Component specimens placed outdoors.

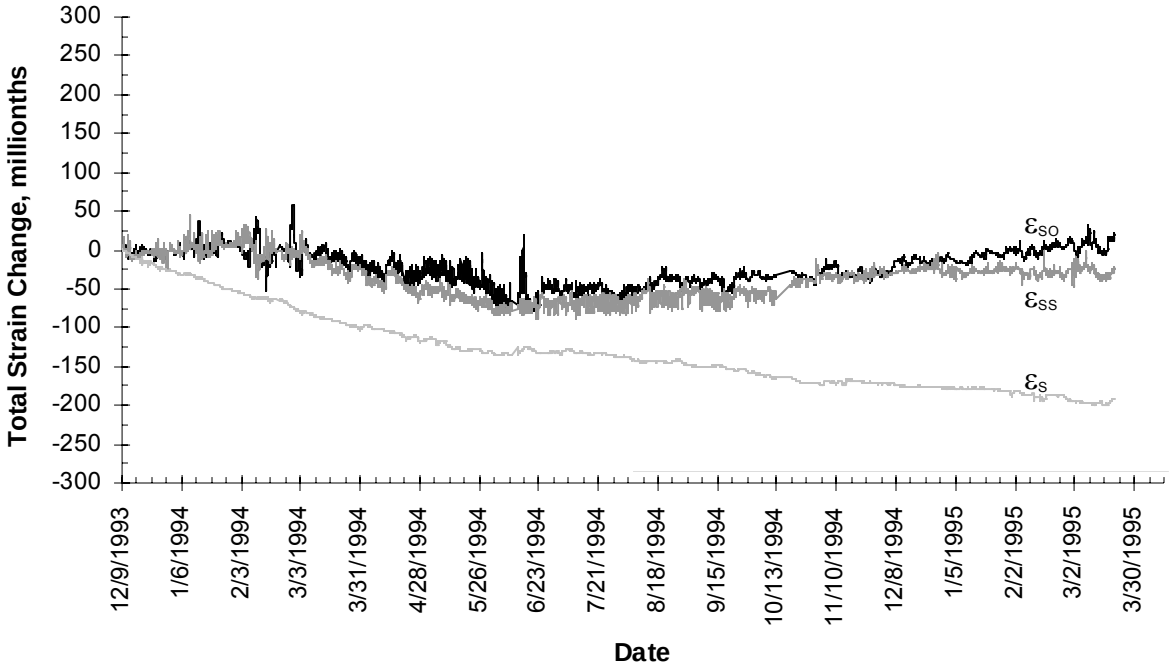

Figure 3-27. Indoor and outdoor (in the shade and in the sun) shrinkage strains for deck components.

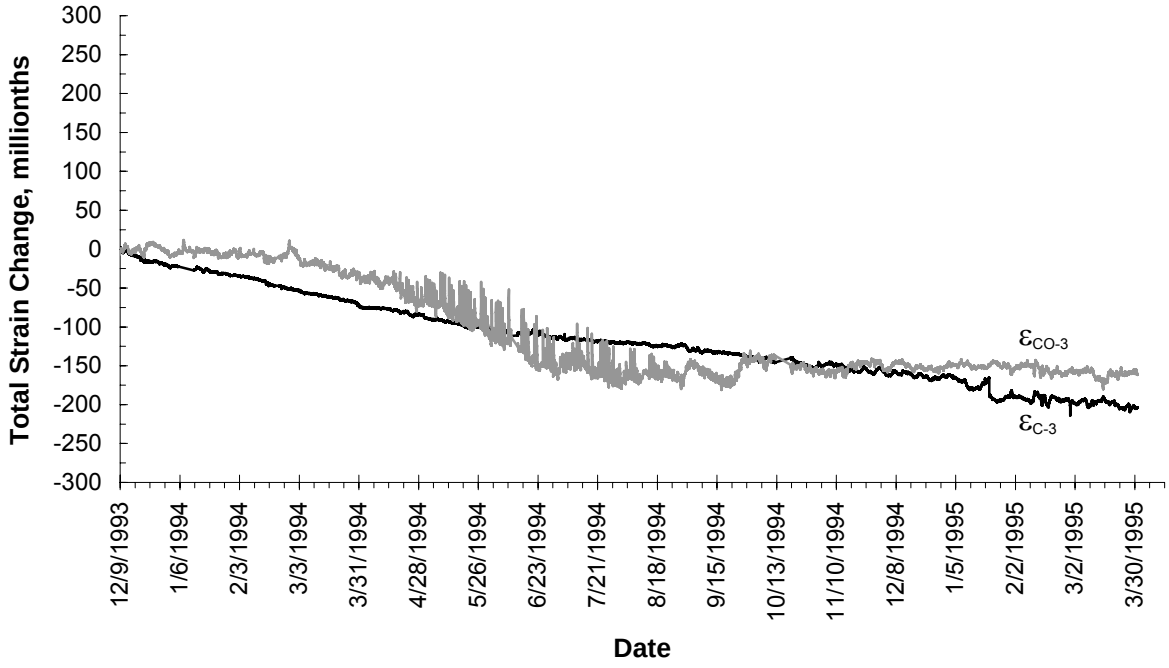

Figure 3-28. Indoor and outdoor (in the shade) creep strains for deck components.

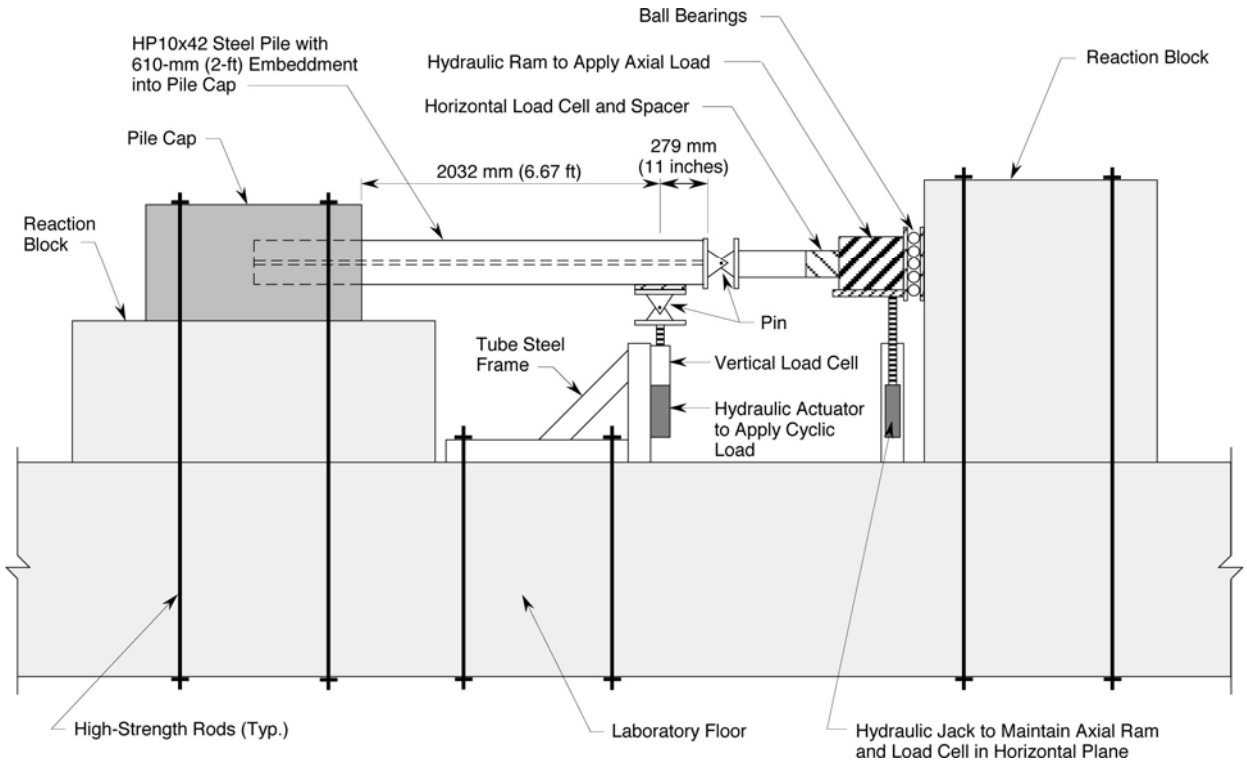

Figure 3-29. Test setup for steel pile.

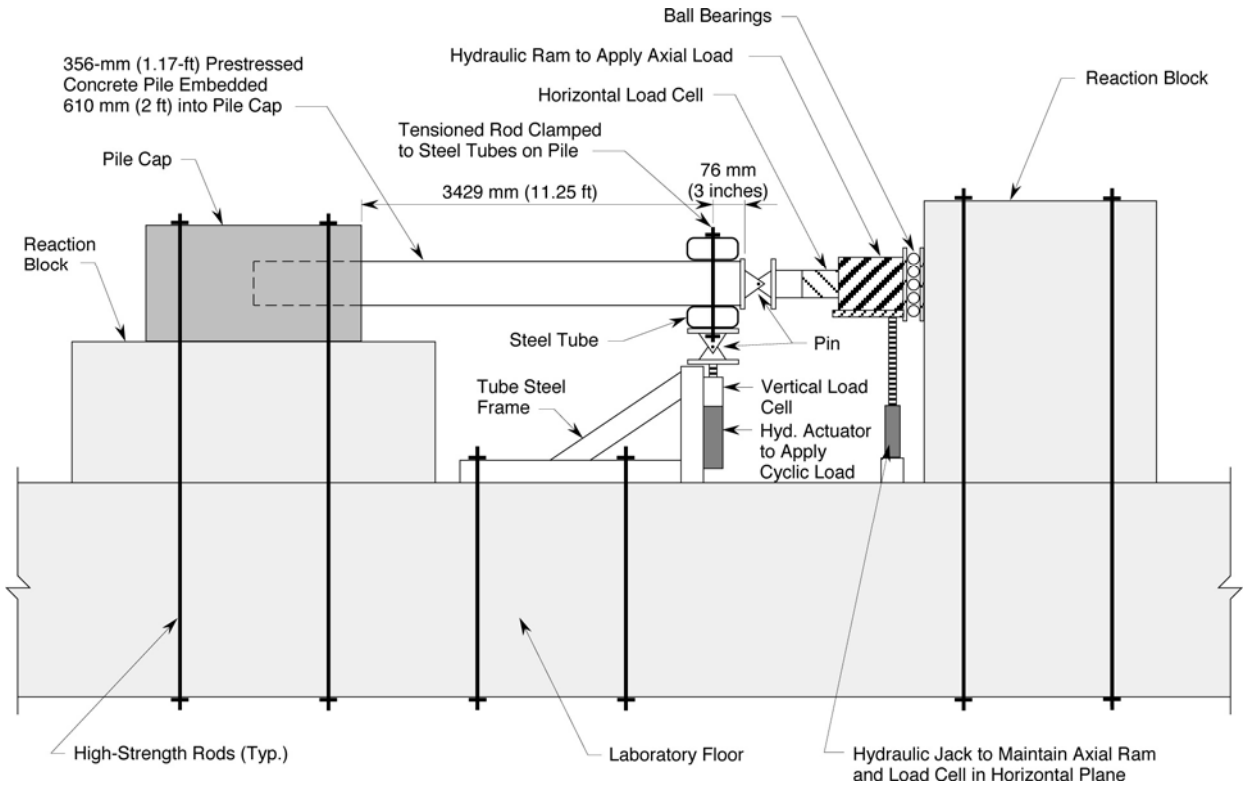

Figure 3-30. Test setup for concrete pile.

Figure 3-31. Local buckling of steel-pile flange at the conclusion of testing.

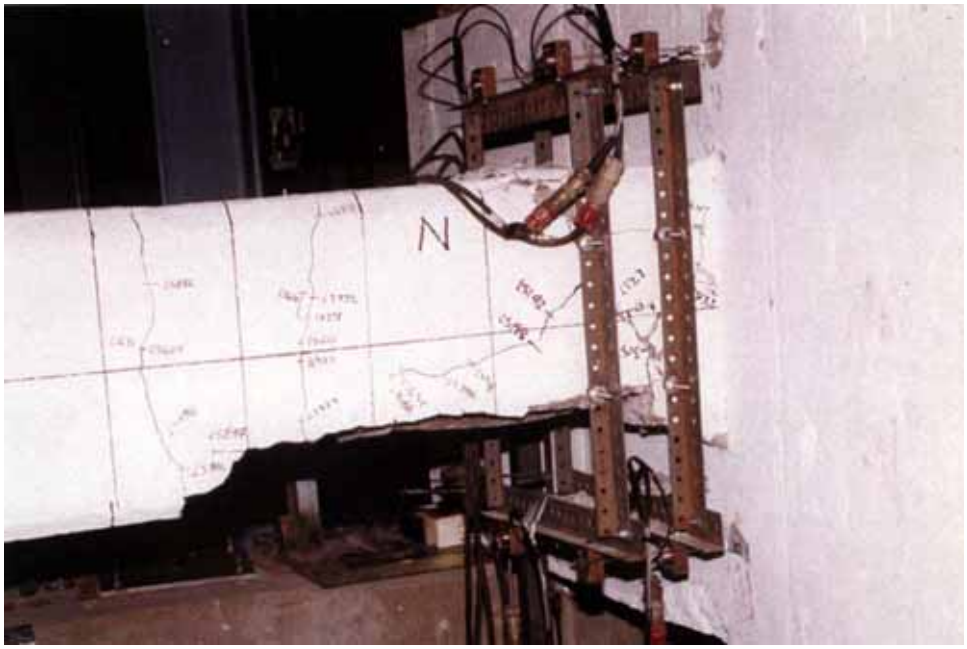

Figure 3-32. Damage to prestressed concrete pile at the conclusion of testing.

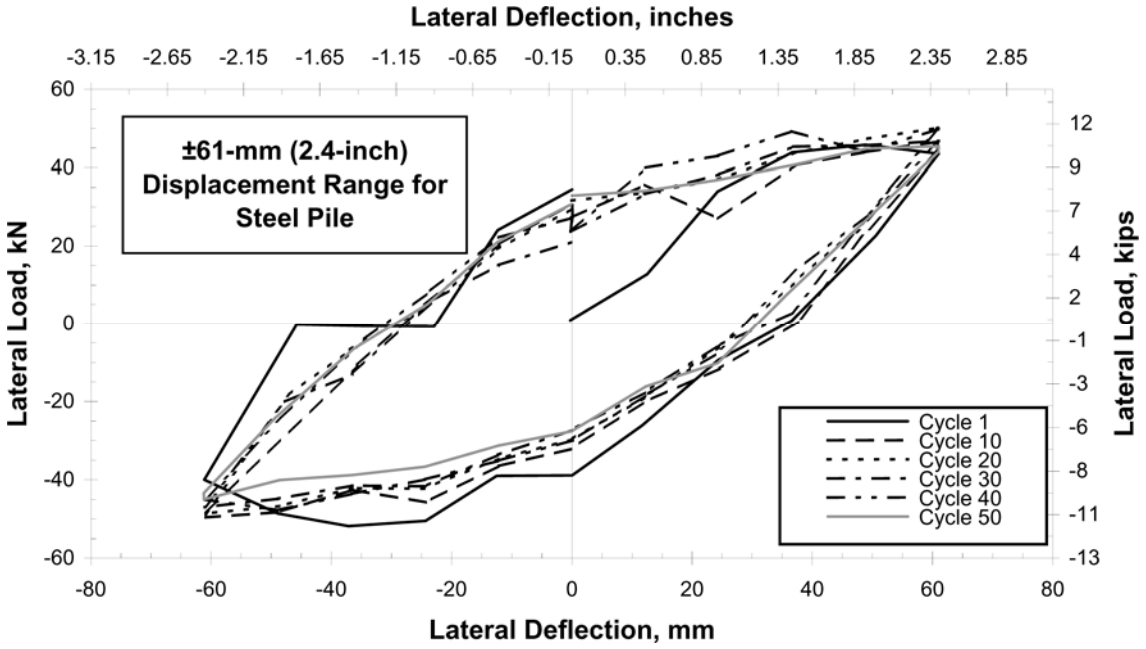

Figure 3-33. Lateral load-deflection response in steel pile ±61-mm (2.4-inch) range.

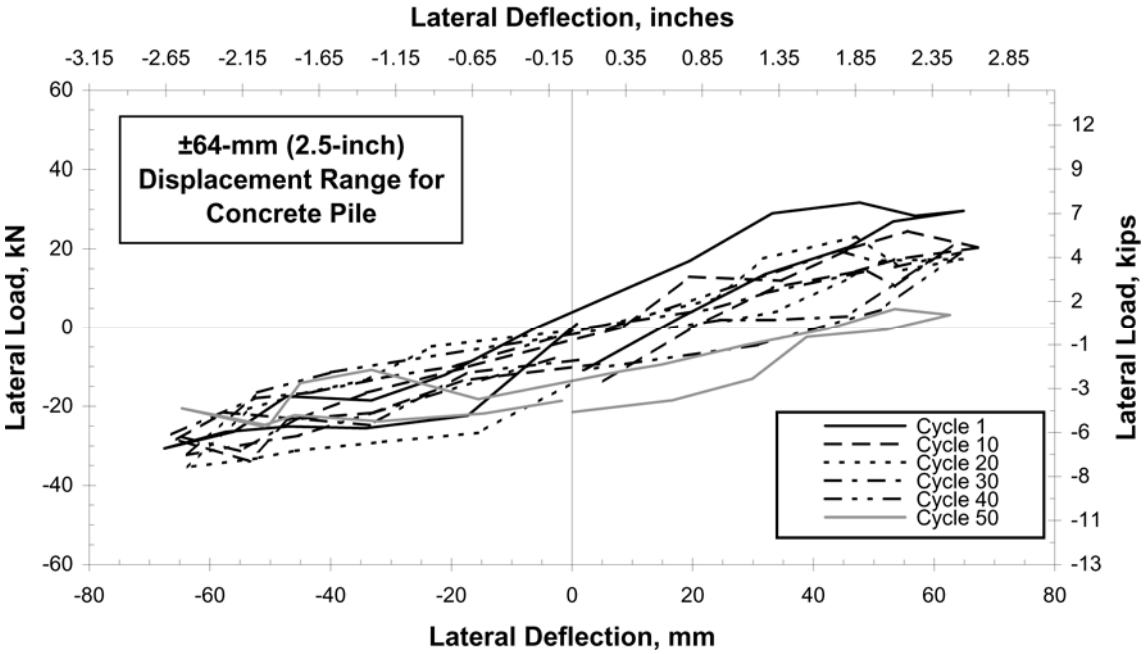

Figure 3-34. Lateral load-deflection response in concrete pile +64-mm (2.5-inch) range.

Figure 3-35. Bridge 2—cracking of diaphragm over pier.

Figure 3-36. Bridge 2—cracking at interface of girder and pier diaphragm.

Figure 3-37. Bridge 10—cracking in bottom flange near north abutment.

Figure 3-38. Bridge 7—efflorescence at construction joint.

Figure 3-39. Bridge 6—washout under the abutment.

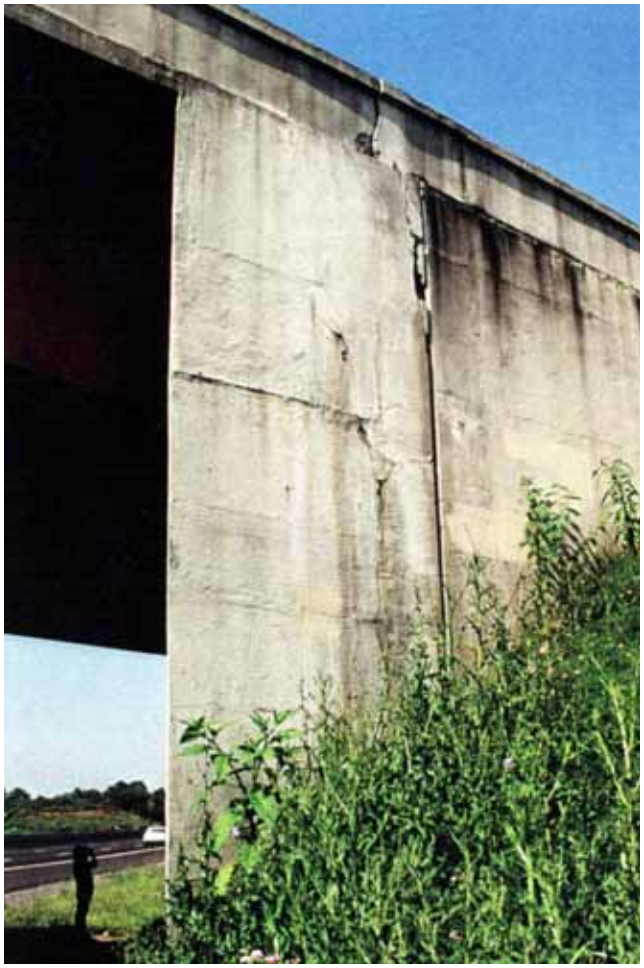

Figure 3-40. Bridge 8—north face of west abutment.

a. Flexural cracks visible on the pier.

b. Closeup of flexural cracks on the pier.

Figure 3-41. Bridge 12—flexural cracks on the south face of the first pier (north end).

Figure 3-42. Bridge 10—cracking in slope pavement.

Figure 3-43. Bridge 5—interface of asphalt pavement and abutment wall without the use of an approach slab.

Figure 3-44. Bridge 1—opening between edge of approach slab and back face of abutment.

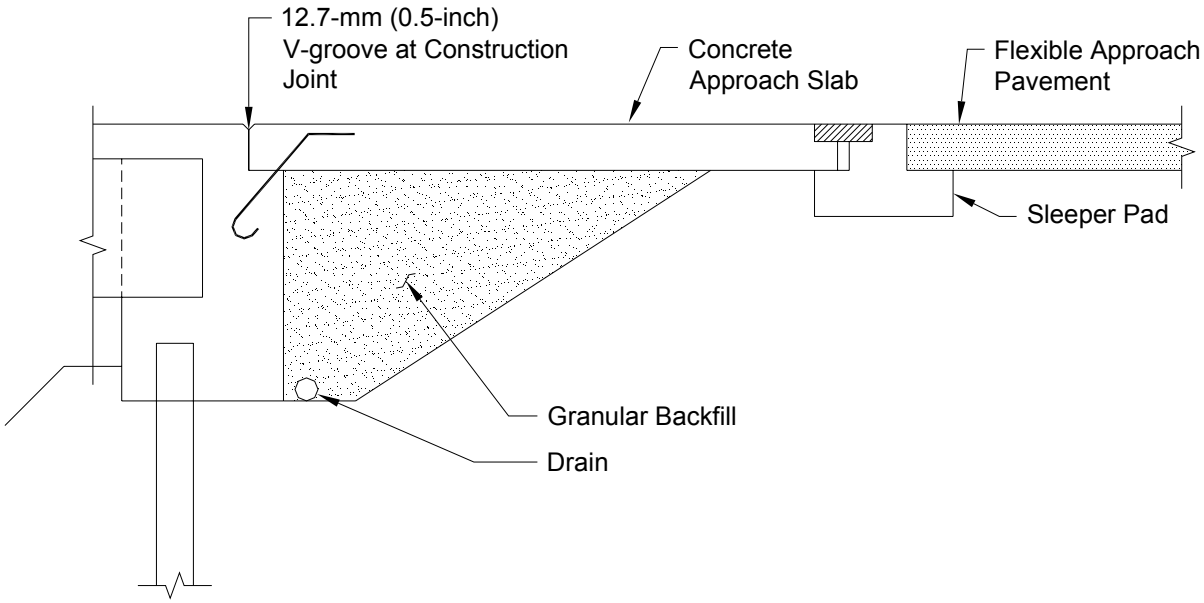

Figure 3-45. Approach slab arrangement.

Figure 3-46. Bridge 7—patching at the end of approach slab.

Figure 3-47. Bridge 10—patching at the end of approach slab (north side).

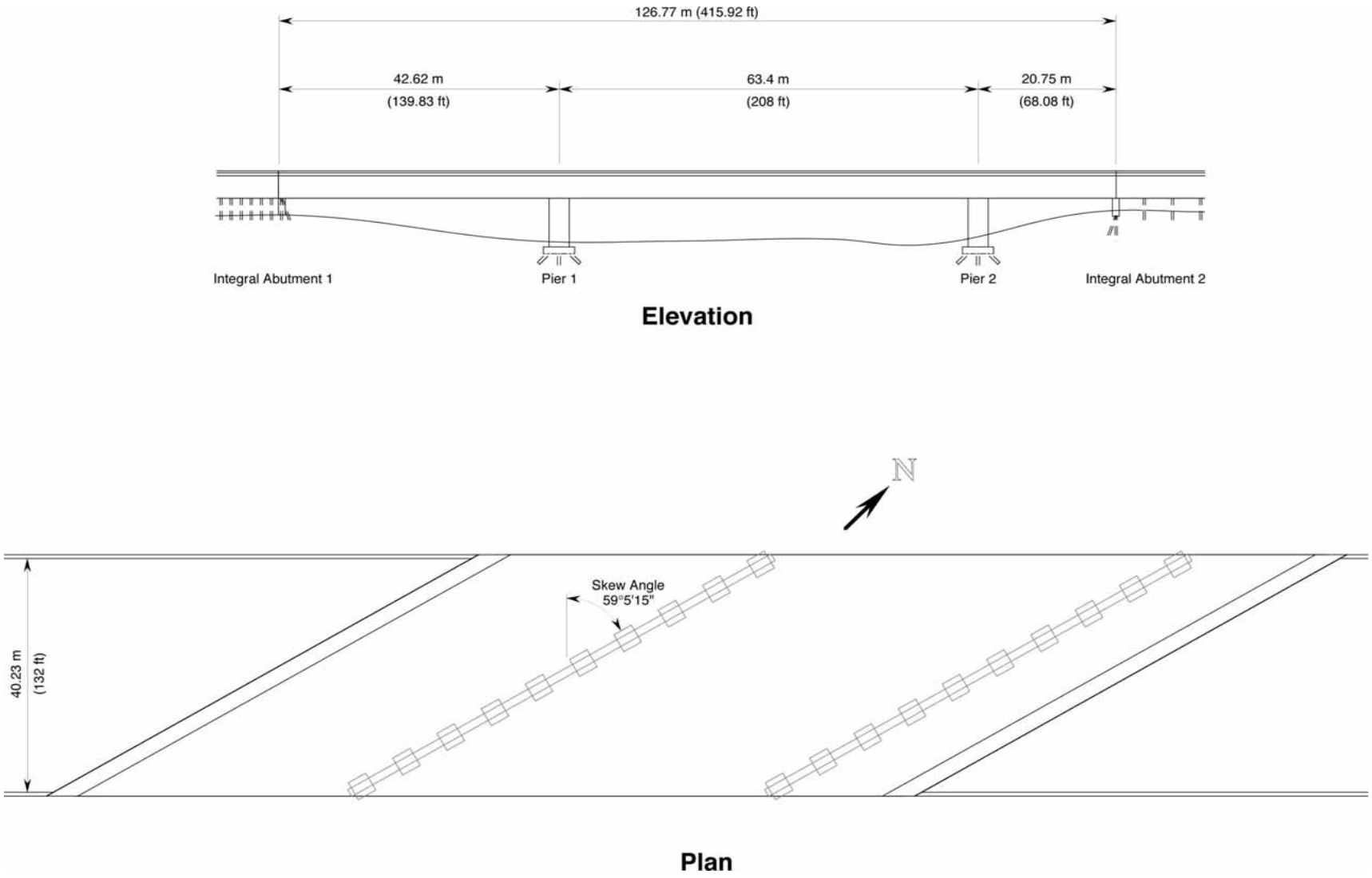

Figure 3-48. Plan and elevation views of the instrumented bridge in Tennnessee.

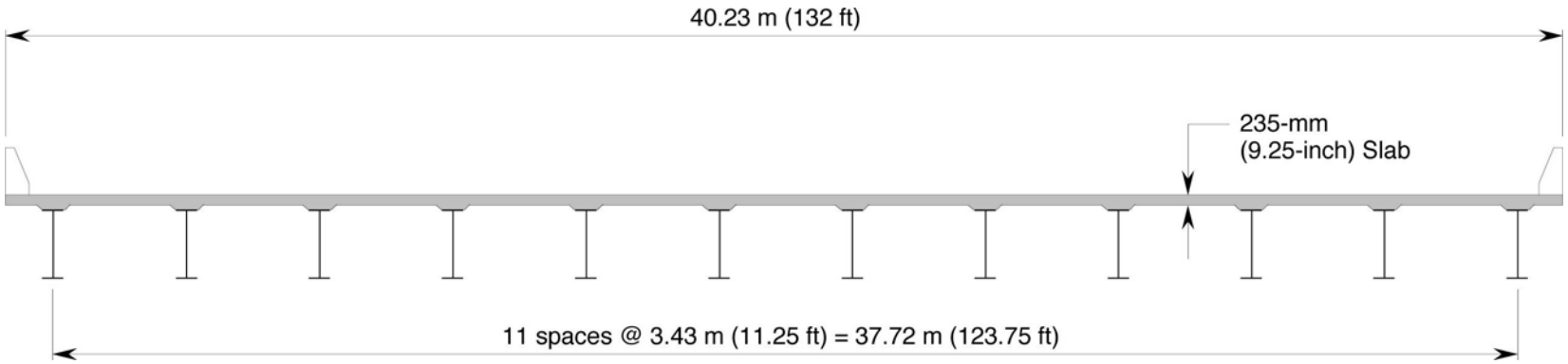

Figure 3-49. Cross-sectional view of the instrumented bridge.

Table 3-1. Material property test information (Task F.1).

Test No.	Specimen Set	Age of Concrete at Beginning of Test, Days	Age of Concrete at Creep Loading, Days	Date of Beginning of Test	Date of End of Test	No. of Days Since Application of Creep Load	Test Duration, Hours
1	A	43	39	9/04/93	9/09/93	3	76
2	A	49	39	9/10/93	9/14/93	10	89
3	A	192	39	1/31/94	2/04/94	153	90
4	B	204	187	2/12/94	2/17/94	17	128
5	B	210	187	2/18/94	2/21/94	23	63.5
6	A	371	39	7/29/94	7/31/94	332	39
7	B	418	187	9/14/94	9/15/94	231	30
8	C	433	382	9/29/94	9/30/94	51	36
9	C	434	382	9/30/94	10/02/94	52	36.5

Table 3-2. Task F.1–details of test specimens and derivation of strain components.

Specimen ID	Location, Indoors/ Outdoors	Exposure, Sun/Shade	Moisture Movement, Sealed/ Not Sealed	Compressive Stress (Creep), MPa (lbf/inch^2)	Measured Strains				
					ε_s	ε_c	ε_t	ε_{se}	ε_{ce}
C1	Indoors	Shade	Not Sealed	0	✓				
C2	Outdoors	Shade	Sealed	0			✓		
C3	Outdoors	Shade	Not Sealed	0	✓		✓	✓	
C4	Outdoors	Shade	Not Sealed	6.89 (1000)	✓	✓	✓	✓	✓
C5	Indoors	Shade	Not Sealed	6.89 (1000)	✓	✓			

Table 3-3. Strain values for specimens C1 through C5.

Strain Value	Description	Combination of Specimen Test Results Required to Extract Value
ε_s	Laboratory Shrinkage Strain	C1
ε_c	Laboratory Creep Strain	C5-C1
ε_t	Temperature Strain	C2
ε_{se}	Environment-Dependent Shrinkage Strain	C3-C1-C2
ε_{ce}	Environment-Dependent Creep Strain	(C4-C3)-(C5-C1)
ε_{so}	Outdoor Shrinkage Strain	C3-C2
ε_{co}	Outdoor Creep Strain	C4-C3

Table 3-4. Summary of test data for Task F.1.

	$\Delta\varepsilon_t$	$\Delta\varepsilon_{se}/\Delta\varepsilon_t$	$\Delta\varepsilon_{ce}/\Delta\varepsilon_t$
Test 1	-19.2	-0.063	-0.141
	96.4	-0.123	-0.012
	-74.8	-0.047	-0.009
	53.0	0.085	-0.051
	-82.5	-0.091	-0.038
	54.8	-0.141	-0.006
	-71.0	-0.072	-0.004
Test 2	-101.4	-0.135	-0.039
	124.1	-0.039	-0.042
	-37.2	0.043	-0.051
	104.1	0.035	-0.061
	-42.4	-0.014	0.033
Test 3	53.0	0.070	-0.064
	-115.7	-0.061	-0.016
	88.2	-0.094	-0.011
	81.4	0.085	-0.058
	-116.9	0.074	-0.029
	98.4	0.031	-0.033
	-40.6	-0.015	0.062

	$\Delta\varepsilon_t$	$\Delta\varepsilon_{se}/\Delta\varepsilon_t$	$\Delta\varepsilon_{ce}/\Delta\varepsilon_t$
Test 4	40.5	0.121	0.083
	-40.3	-0.017	-0.045
	74.0	0.130	-0.112
	-73.3	0.074	-0.162
	175.6	0.066	-0.077
	-91.0	0.076	-0.103
	68.4	0.132	-0.136
	-126.9	0.058	-0.134
	144.2	0.064	-0.116
	-58.0	0.064	-0.205
Test 5	37.2	-0.003	-0.008
	-39.7	0.035	-0.008
	23.5	0.230	-0.034
	-167.4	-0.024	-0.028
Test 6	-44.7	0.110	-0.260
	112.3	-0.029	-0.116
	-69.2	-0.072	-0.129
Test 7	74.2	-0.038	-0.058
	-91.8	-0.064	0.036
	88.3	-0.072	-0.049
Test 8	-14.7	-0.143	-0.102
	116.8	-0.086	-0.031
	-92.1	0.010	-0.103
	132.2	-0.059	-0.039
Test 9	-96.7	-0.123	-0.099

Note: Shaded data were not included in analyzed information shown in table 3-5.

Table 3-5. Summary of results.

Test Set	Test No.	$\Delta\varepsilon_{se}/\Delta\varepsilon_t$			$\Delta\varepsilon_{ce}/\Delta\varepsilon_t$		
		Minimum	Maximum	Average	Minimum	Maximum	Average
A	Tests 1 & 2	-0.135	0.035	-0.067	-0.061	-0.004	-0.029
A	Test 3	-0.094	0.085	0.007	-0.058	-0.011	-0.029
B	Tests 4 & 5	-0.024	0.132	0.072	-0.162	-0.028	-0.109
A	Test 6	-0.072	-0.029	-0.051	-0.129	-0.116	-0.123
B	Test 7	-0.072	-0.038	-0.058	-0.058	0.036	-0.024
C	Tests 8 & 9	-0.123	0.010	-0.065	-0.103	-0.031	-0.068
A,B	All Winter Tests	-0.094	0.132	0.047	-0.162	-0.011	-0.078
A,B,C	All Except Winter	-0.135	0.035	-0.063	-0.129	0.036	-0.050
A,B,C	All Tests	-0.135	0.132	-0.014	-0.162	0.036	-0.062

Table 3-6. Maximum total moments in concrete beam during load tests.

	Simply Supported (Calculated)						Actual (Based on Load Cell Measurements)*						Difference (%)
	M_{dss}		M_{lss}		M_{ss}		M_d		M_l		M		
	kN-m	kip-ft	kN-m	kip-ft	kN-m	kip-ft	kN-m	kip-ft	kN-m	kip-ft	kN-m	kip-ft	
Winter/Sunny 2/04/94	442.5	326.4	693.5	511.5	1136.0	837.9	307.2	226.6	605.1	446.3	912.3	672.9	19.7
Winter/Cloudy 2/28/94	442.5	326.4	653.2	481.8	1095.7	808.2	455.0	335.6	530.4	391.2	985.4	726.8	10.1
Spring/Sunny 5/12/94	442.5	326.4	622.3	459.0	1064.8	785.4	562.7	415.0	528.6	389.9	1091.3	804.9	-2.5
Spring/Cloudy 5/26/94	442.5	326.4	631.7	465.9	1074.1	792.3	443.8	327.3	526.1	388.0	969.8	715.3	9.7
Summer/Sunny 8/17/94	442.5	326.4	622.3	459.0	1064.8	785.4	580.3	428.0	523.8	386.3	1104.0	814.3	-3.7
Summer/Cloudy 9/15/94	442.5	326.4	619.7	457.1	1062.2	783.5	468.6	345.6	563.2	415.4	1031.8	761.0	2.9
Fall/Sunny 11/16/94	442.5	326.4	621.5	458.4	1064.0	784.8	493.7	364.1	556.2	410.2	1049.8	774.3	1.3
Fall/Cloudy 11/21/94	442.5	326.4	630.8	465.3	1073.3	791.6	515.6	380.3	558.5	411.9	1074.1	792.2	-0.1

Notes:

M_{dss} = calculated dead load moment at point A (approximately 40 percent of the span), assuming simply supported condition (zero continuity)

M_{lss} = calculated maximum live load moment at point A, assuming simply supported condition (zero continuity)

M_{ss} = calculated total moment at point A, assuming simply supported condition (zero continuity) = $M_{dss} + M_{lss}$

M_d = dead load moment at point A, using the actual load cell readings and a weight per unit length of 18.695 kN/m (1.281 kips/ft)

M_l = maximum live load moment at point A, using the actual load cell readings (at the support near point A)

M = total moment at point A = $M_d + M_l$

Difference, % = $100x(M_{ss} - M)/M_{ss}$

* Actual includes effects of dead load, live load, and all secondary effects present at the time of testing.

Table 3-7. Maximum total moments in steel beam during load tests.

	Simply Supported (Calculated)						Actual (Based on Load Cell Measurements)*						Difference (%)
	M_{dss}		M_{lss}		M_{ss}		M_d		M_l		M		
	kN-m	kip-ft	kN-m	kip-ft	kN-m	kip-ft	kN-m	kip-ft	kN-m	kip-ft	kN-m	kip-ft	
Winter/Sunny 2/04/94	327.6	241.6	684.4	504.8	1012.0	746.4	146.0	107.7	549.6	405.4	695.7	513.1	31.3
Winter/Cloudy 2/28/94	327.6	241.6	644.6	475.4	972.1	717.0	156.5	115.4	526.1	388.0	682.5	503.4	29.8
Spring/Sunny 5/12/94	327.6	241.6	644.6	475.4	972.1	717.0	156.5	115.4	526.1	388.0	682.5	503.4	29.8
Spring/Cloudy 5/26/94	327.6	241.6	654.6	482.8	982.2	724.4	90.3	66.6	530.4	391.2	620.7	457.8	36.8
Summer/Sunny 8/17/94	327.6	241.6	666.1	491.3	993.7	732.9	91.4	67.4	542.2	399.9	633.6	467.3	36.2
Summer/Cloudy 9/15/94	327.6	241.6	653.9	482.3	981.5	723.9	41.1	30.3	550.1	405.7	591.1	436.0	39.8
Fall/Sunny 11/16/94	327.6	241.6	638.0	470.6	965.6	712.2	79.7	58.8	525.2	387.4	605.0	446.2	37.3
Fall/Cloudy 11/21/94	327.6	241.6	640.4	472.3	967.9	713.9	117.1	86.4	521.6	384.7	638.7	471.1	34.0

Notes:
M_{dss} = calculated dead load moment at point A (approximately 40 percent of span), assuming simply supported condition (zero continuity)
M_{lss} = calculated maximum live load moment at point A, assuming simply supported condition (zero continuity)
M_{ss} = calculated total moment at point A, assuming simply supported condition (zero continuity) = $M_{dss} + M_{lss}$
M_d = dead load moment at point A, using the actual load cell readings and a weight per unit length of 13.841 kN/m (0.948 kips/ft)
M_l = maximum live load moment at point A, using the actual load cell readings (at the support near point A)
M = total moment at point A = $M_d + M_l$
Difference, % = $100x(M_{ss} - M)/M_{ss}$
* Actual includes effects of dead load, live load, and all secondary effects present at the time of testing.

Table 3-8. Deck component tests.

Deck Component	Location, Indoors/ Outdoors	Exposure, Sun/ Shade	Moisture, Drying/ Sealed	Deck Prestressing, Yes/No	Measured Strains							
					ε_s	ε_c	ε_t	ε_{tr}	ε_{se}	ε_{sr}	ε_{ce}	ε_{cr}
D1	Indoors	Shade	Drying	No	✓							
D2	Indoors	Shade	Drying	Yes	✓	✓						
D3	Outdoors	Shade	Sealed	No			✓					
D4	Outdoors	Sun	Sealed	No			✓	✓				
D5	Outdoors	Shade	Drying	No	✓		✓		✓			
D6	Outdoors	Sun	Drying	No	✓		✓	✓	✓	✓		
D7	Outdoors	Shade	Drying	Yes	✓	✓	✓		✓		✓	
D8	Outdoors	Sun	Drying	Yes	✓	✓	✓	✓	✓	✓	✓	✓

Table 3-9. Strain value for deck components D1 through D8.

Strain Value	Description	Combination of Specimen Test Results Required to Extract Value
ε_s	Laboratory Shrinkage Strain	D1
ε_c	Laboratory Creep Strains Caused by Prestressing	D2-D1
ε_t	Temperature Strains	D3
ε_{tr}	Temperature Strains Caused by Solar Radiation	D4-D3
ε_{se}	Environment-Dependent Shrinkage Strains	D5-D3-D1
ε_{sr}	Shrinkage Strains Caused by Solar Radiation	(D6-D5)-(D4-D3)
ε_{ce}	Environment-Dependent Creep Strains	(D7-D5)-(D2-D1)
ε_{cr}	Creep Strains Caused by Solar Radiation	(D8-D6)-(D7-D5)

Table 3-10. Field survey of jointless bridges in Tennessee (May 24–26, 1995).

Bridge No.	Location	Type	Description
1	S.R. 6 bypass over S.R. 6 (Highway 31E) in Hendersonville, Sumner County	Steel-Box Girder	
2	Vietnam Veterans Dr. (S.R. 6 bypass) over Drakes Creek in Hendersonville, Sumner County	PS/C Beams	
3	Ramp B over S.R. 6 in Sumner County	Steel-Plate Girder	Curved and Skewed
4	I-40 over S.R. 136 in Putnam County	Side-by-Side PS/C Box Beams	Retrofit
5	I-40 eastbound over Falling Water River in Putnam County	PS/C-Beams	Retrofit
6	S.R. 1 over Piney Creek (Ray Baird Memorial Bridge)	Arch	Retrofit
7	I-40 westbound over Ramp 3D and 22nd St. in Knox County	Steel-Plate Girder	Curved
8	Ramp 2D over I-40 in Knox County	Steel-Plate Girder	Curved and Skewed
9	I-40 over Ramp 2B in Knox County	Steel-Plate Girder	Curved and Skewed, Instrumented Bridge
10	Deep Springs Rd. over I-40 and Dumplin Creek in Jefferson County	R/C Multicell Box Girder	5.6 Percent Grade
11	S.R. 137 over S.R. 1 in Sullivan County	Steel-Box Girder	Dual (Parallel) Single-Span, Curved

Table 3-10. Field survey of jointless bridges in Tennessee
(May 24–26, 1995) (continued).

Bridge No.	Location	Type	Description
12	Kingsport Bridge, S.R. 137 over Holston River in Sullivan County	PS/C Multiple Box Beams	Bridge Jointed at Abutments Only
13	I-40 over U.S.11W (S.R. 1) in Knox County	Steel-Plate Girder	Retrofit
14	New bridge construction on I-40 near Nashville	PS/C Bulb-T	New Construction
15	New bridge construction on I-40 near Nashville	Steel-Plate Girder	New Construction

4. SUMMARY OF ANALYTICAL INVESTIGATION

The analytical program consisted of studies of the following six areas, to help provide a scientific basis for design:

1. Abutment soil-structure interaction.
2. Pier behavior.
3. Longitudinal bridge movement.
4. Secondary continuity forces.
5. Skewed bridge behavior.
6. Construction sequences.

In general, the analytical research is used to evaluate the response of the jointless bridge, and of its components, to various design parameters.

4.1 OBJECTIVES AND SCOPE

4.1.1 Objectives

The general objectives of the analytical work included:

1. Resolving uncertainties in the behavior of jointless bridges in cases where current analytical methods and empirical data are sufficient to accurately represent the actual behavior of those bridges.
2. Defining areas that need further experimental work to resolve uncertainties in jointless-bridge behavior.

Based on the literature review and the previous discussion of uncertainties in chapter 2, the following specific objectives for the project were developed:

1. Determine criteria that limit the length of jointless bridges for integral and seat-type abutments including abutments supported on spread footings.
2. Identify the effect of longitudinal length changes on superstructure stresses.
3. Determine the significance of continuity moments from temperature gradients, creep, and shrinkage.
4. Develop design criteria for piers.

5. Determine the effects of different construction sequences including retrofitting.
6. Identify limitations and special considerations for skewed and curved bridges.
7. Develop more uniform (and standard) design criteria and methods for new and retrofitted jointless bridges.

4.1.2 Scope

The analytical work involved computer simulations for sensitivity studies and for parametric studies of the major factors influencing the behavior and response of jointless bridges. The analytical work was accomplished within the following scope:

1. Perform analyses of abutment soil-structure interaction. These involved an evaluation of passive soil pressure versus lateral movement of abutments, considering various conditions and determination of abutment pile capacities for steel H-piles, PS/C piles, and concrete-filled pipe piles.
2. Perform analyses for pier response to lateral movement. The analyses included assessment of foundation response, and considered both pile-supported and spread-footing foundations. Also, pier response was evaluated for various loading conditions.
3. Perform a Monte Carlo study to assess potential variability in the expected movements of piers and abutments. The analyses developed databases for the evaluation of the variability of concrete coefficients of thermal expansion, concrete creep and shrinkage, concrete modulus of elasticity, soil stiffness, and average daily temperatures during the construction season. Statistical parameters from the databases were used to determine 98 percent confidence intervals for the expected maximum movement of jointless bridges.
4. Perform a study of effective annual temperature response. The study involved evaluation of temperature range and determination of anticipated bridge movements. A parametric study was included to help understand the effects of various variables on the thermal movements of jointless bridges.
5. Determine secondary continuity forces attributable to effective temperature gradients in bridge superstructures. A parametric study was done here as well to evaluate the thermal response and the response caused by creep and shrinkage.

6. Analyze skewed bridges to assess their expected transverse movement over the effective annual temperature range and to determine the effects of skew on secondary continuity moments.

7. Study the effect of different construction sequences on the behavior of jointless bridges. The study involved a review of a state-of-the-art survey of current practices and a parametric analysis of various conditions. Newly constructed and retrofitted bridges were included in the study.

8. Develop proposed design guidelines for determining the effective temperature range and the expected bridge movement; selecting the abutment type; and designing the abutments, piers, and approach slabs. In addition, design considerations for secondary continuity forces were developed.

9. Present the results of the analytical program in a comprehensive report. Detailed discussions of assumptions, analyses, and results are provided in separate sections for each of the aforementioned analytical studies.

Although analyses of curved jointless bridges were beyond the scope of this study, that is recommended as a topic for future research.

The following sections of this chapter describe the work accomplished and summarize the findings for each of the areas of interest in the analytical studies. A detailed description of the analytical work is given in the analytical report..[15]

4.2 ABUTMENT-SOIL INTERACTION

The specific objectives of the abutment study were to:

1. Investigate the relationships for longitudinal movement versus passive soil pressure, for stub and full-height abutments supported on either piles or spread footings.

2. Assess the effects of combined axial load and lateral deformation of piles for stub abutments as a potential limiting criterion for bridge length.

4.2.1 Soil Pressure Versus Lateral Movement

The nonlinear soil-structure interaction finite element computer program CANDE[19] was used to study the abutment/soil interaction for longitudinal movement of abutments. Figure 4-1 shows the analytical model for the baseline condition of the parametric study. The baseline condition included granular soil compacted at 80 percent of Standard

Proctor maximum density. The backfill soil was assumed to be cohesive soil at 95 percent of maximum density. The nonlinear modified Selig soil model[20] was typically used to model backfill and in situ soil. The steel pile was modeled using nonlinear beam elements with an equivalent cantilevered length.[2] Results of the analyses from CANDE were compared with experimental work by P.W. Rowe, et al.,[21] and with field studies of a bridge with an integral backwall.[22] Comparisons indicated that the computer analyses gave reasonable approximations of actual soil pressure response.

The purpose of this study was to assess the significance of various parameters for the passive soil pressure response to longitudinal movement of integral abutments caused by bridge expansion. The parameters investigated included stiffness of backfill, type of abutment-girder connection (integral versus semi-integral), configuration (slope and width) of backfill behind abutment wall, rotational stiffness of girders connected to abutments, orientation of abutment piles, height of abutment, type of abutment (full-height versus stub abutment), foundation type (spread footings versus piles), stiffness of wall abutment, and type of beam (steel versus precast PS/C). In addition, there was an investigation of an abutment arrangement that may be used to retrofit existing jointed bridges to be integral abutment bridges, which allows the breastwall to slide and rotate with respect to the footing.

The following is a summary of findings and conclusions based on the analyses, literature review, and available test data for soil pressure versus abutment lateral movement:

1. The Rankine passive pressure represents a reasonable estimate for full passive pressure at large movements.

2. The soil pressure and abutment movement data by G.W. Clough and J.M. Duncan[11] presented in the *Manual for the Design of Bridge Foundations*, NCHRP Report 343[23] (and included in chapter 5 of this report in figure 5-11), represents a reasonable upperbound to determine the portion of full passive Rankine pressure to be used as a design passive pressure at the expected maximum abutment movement. This finding is based on a comparison with analytical studies and on a comparison with full-scale tests, including a full-scale model,[24] and the integral bridge that was monitored as part of this project and described in section 3.6 of this volume.

3. The starting point for calculating maximum design passive pressure should be, conservatively, at the point of maximum contraction (from creep, shrinkage, and thermal strain) of the bridge superstructure. This recommendation is based on

observation of test data[25] indicating that, as contraction permits the soil pressure to decrease to the minimum active pressure, the granular soil will follow the contracting abutment wall and will recompact. The recompaction is sufficient to shift the soil pressure and abutment movement curve so that passive pressure starts to build immediately upon thermal reexpansion.

4. A review of the literature and current practices indicates opposing philosophies about the degree of compaction in the backfill soil adjacent to the abutment. One concept is to use loose granular backfill to minimize passive pressure forces. The opposite concept is to use highly compacted backfill, which is based on the observation that voids beneath the approach slab and settlement of the approach slab are a common problem with abutments. Tests on a large-scale abutment specimen[25] indicated that voids under the approach slabs develop as a result of contraction beyond the initial starting point, even with 97 percent relative compaction of the backfill adjacent to the abutment. Therefore, there does not appear to be an advantage to using higher compaction.. Also, it is difficult to attain a high degree of compaction adjacent to the abutment backwall.

5. Parametric computer analyses indicate that the passive pressure can be significantly decreased by using relatively uncompacted backfill and/or by increasing the horizontal length of the backfill zone behind the abutment. The calculated resultant passive soil reaction decreased by a factor of approximately 2.5, with a decrease in compaction from 90 percent to 80 percent. Also, with backfill at 80 percent compaction, the calculated resultant passive pressure decreased by a factor of approximately 2 when the slope of the backfill/in situ soil interface was changed from 45° to 30° (from horizontal). However, extending the backfill zone behind the abutment increases the length needed for the approach slab to span the backfill region and/or increases the settlement of the approach slab.

6. An example of the calculated distribution of soil pressure over the height of the abutment wall is shown in figure 4-2(a). The shape of the pressure distribution depends on the rotation of the abutment wall, but typically shows a large increase in pressure at the base of the abutment. The concentration of pressure at the base increased with a decrease in rotation. The rotation of the abutment depends on the relative bending stiffness of the superstructure and the rotational stiffness of the soil/pile/abutment interaction, and it is difficult to calculate. However, based on

the calculated soil pressure distribution with relatively large superstructure stiffness, the pressure distribution shown in figure 4-2(b) is recommended for the design of stub abutments on piles. The pressure distribution shown in figure 4-3 is recommended for abutments on spread footings, and the pressure distribution shown in figure 4-4 is recommended for full-height abutments.

4.2.2 Abutment Pile Capacity

Vertical load capacity of an abutment pile is a function of the abutment movement associated with a bridge's longitudinal expansion or contraction. A nonlinear, pile-soil interaction finite element program has been developed at Iowa State University to study behavior and develop design criteria for pile-supported stub abutments in integral abutment bridges.[26] The results of computer analysis indicated that, in very stiff clay, the vertical load capacity of H-piles may be reduced by about 20 percent for a horizontal displacement of 25.3 mm (1 inch) and 50 percent for 50.8 mm (2 inches) of horizontal displacement. However, analytical work was limited to steel H-piles, and the research did not include limitation of lateral movement caused by the ductility capacity of other types of piles, such as precast PS/C and concrete-filled pipe piles that are of interest for use in integral abutments. Therefore, this project included a parametric study of the vertical load capacity of various types of piles as a function of horizontal movement. The analytical criteria included the ductility capacity of the pile and its strength and stability.

The analytical approach selected for this study was based on the simplified model developed by Abendroth, et al.[2] Three criteria for determining abutment pile capacity were incorporated in this model. The first criterion was based on the geometric stability of the pile (elastic or inelastic buckling as a function of its vertical load and moment associated with lateral movement). The second criterion was related to material strength (usually governs in case of short or stubby piles). The third criterion was based on the rotational capacity of the pile (a ductility issue related to local hinging of the pile). The calculations associated with these three pile capacity criteria were based on an equivalent cantilever length of the pile. The equivalent cantilever length can be determined for either fixed or pinned conditions between the top of the pile and the bottom of the abutment.

A parametric study was performed to determine vertical load capacity versus lateral displacement for fixed-head piles. The parameters included pile type, pile size, soil stiffness, pile length, and the use of predrilled holes. Pile types were steel H-pile, PS/C pile, and concrete-filled pipe pile. For each pile type, three different sizes were analyzed. Also, three different soil stiffnesses—0.69 MPa, 3.45 MPa, and 6.21 MPa (100 lbf/inch^3,

500 lbf/inch^3, and 900 lbf/inch^3)—were used to represent soft, moderate, and stiff soil conditions, respectively.[27] The parametric study also involved piles installed in 1.88-m-(6-ft-) deep predrilled holes and others installed in soil without predrilled holes.

The rotational capacity of steel H-piles was based on a ductility criterion presented by Abendroth, et al.[2] The criterion included local buckling of the H-section flanges. The rotational capacity of the PS/C piles and concrete-filled pipe piles was determined from a moment-curvature relationship calculated up to the maximum moment capacity of the pile cross sections. For the PS/C piles, concrete compressive strain was limited to 0.003. The limiting moment and curvature for the concrete-filled pipe pile were based on a compressive strain limit of 0.01 in the confined fill concrete. The curvature of the pile cross section was integrated over the pile length to determine the rotational capacity and the associated displacement capacity.

The results of the parametric study are typically in the form of ultimate vertical load capacity versus lateral displacement of piles. A comparison was made with the maximum assumed design vertical load obtained from AASHTO specifications,[28] considering no lateral displacement and no soil data available. Examples of the results of analyses are shown in figures 4-5 through 4-7. The analyses were terminated either when the ductility limit was reached or when 100 mm (4 inches) of deflection were reached.

The data presented in figures 4-5 through 4-7 indicate that displacement capacities increase as soil stiffness decreases and as section size increases. The results of analyses for H-piles shown in figure 4-5 are based on weak-axis bending. Based on surveys of State DOT practices, it appears that many States prefer to orient H-piles for weak-axis bending under longitudinal movement, while other States prefer to use strong-axis bending. The rationale for weak-axis bending is that the flexibility of the pile is greater and the pile can therefore accommodate larger movements. However, the deformation capacity of the pile depends not only on the pile flexural stiffness, but on the combined pile and soil system stiffness. As the pile stiffness increases, the soil is affected to increasing depths. The effective cantilever length in bending therefore increases, tending to decrease the overall stiffness of the pile-soil system.

Analyses presented in chapter 5 of the analytical report demonstrate that bending about the strong axis results in a larger displacement at first yield than bending about the weak axis.[15] For an HP10x42, the ratio of yield displacement for strong-axis bending to yield displacement for weak-axis bending is approximately 1.7. It should be noted, however,

that while strong-axis bending provides a larger displacement capacity, design forces for the pile-to-pile-cap connection are increased.

The data presented in figures 4-5 through 4-7 are based on analytical studies with theoretical ductility limitations. Verification testing was conducted for a steel H-pile and a PS/C pile, as discussed in section 3.4 of this volume. The testing was carried out to investigate the effects of repetitive large inelastic displacement cycles on the ductility limitations.

The steel H-pile test specimen demonstrated slight local buckling of the flanges during the tenth cycle at the deformation limit, which corresponded to the ductility criterion presented by Abendroth, et al.[2] However, the pile was able to sustain the load capacity through 50 cycles at this level of deformation without further deterioration of the section. Therefore, the test results indicated that the ductility criterion was appropriate.

The PS/C pile test specimen demonstrated severe cracking and spalling during cycling of the deformation limit, based on the ductility criterion used in the analytical study. Although the section continued to sustain significant bending moment and the applied axial load, the amount of damage observed was unacceptable from a serviceability viewpoint. Therefore, it is recommended that displacement limits for PS/C piles based on the allowable stress limitations as initially presented by Abendroth, et al.,[2] unless steps are taken to control cracking in the vicinity of the interface between the pile and the abutment, such as details to effect a pinned connection between the pile and the abutment wall as proposed by Kamel, et al.[18]

The experimental plan for this project did not include testing of concrete-filled pipe piles. However, concrete-filled steel tubular columns have been tested by others.[29] This testing indicated that axially loaded columns maintained yield loading to strains significantly beyond the 0.01 strain limit assumed in the analyses in this study. In the case of thin-walled circular columns subjected to inelastic cyclic load reversals, the columns exhibited high ductility with stable loops. The maximum load can be determined by local buckling of the steel tube when the aspect ratio (diameter to wall thickness) is greater than 39. However, the local buckling probably occurs after crushing of the core concrete.

The following is a summary of the findings and conclusions based on the analyses, literature review, and available test data for piles in integral abutments:

1. Vertical load capacity of an abutment pile is a function of the abutment's horizontal movement associated with bridge expansion or contraction. Vertical load capacities decrease when displacements increase.

2. Longitudinal displacement capacity increases as pile flexural stiffness increases and/or soil stiffness decreases. An increase in the ratio of pile stiffness to soil stiffness increases the effective cantilevered length of the pile. Therefore, the curvature demand associated with a particular lateral displacement is spread over a longer length and the ductility demand at that displacement is decreased. Based on these analyses, situating an H-pile for bending about the strong axis with abutment movement will allow larger displacement.

3. The steel H-pile test specimen demonstrated that slight local buckling of the flanges occurred during the tenth cycle of lateral displacement of the inflection point of 61 mm (2.4 inches). This displacement is the calculated deformation limit corresponding to the ductility criterion presented by Abendroth, et al.[2] Therefore, the test results indicated that the ductility criterion proposed by Abendroth et al., was appropriate. Also, the pile was able to sustain the load capacity through 50 cycles at this level of deformation without further deterioration of the section. Therefore, this criterion is recommended for the design of H-piles as described in chapter 5.

4. The analyses indicated that concrete-filled pipe piles have very large displacement capacities and generally lose a lower percentage of vertical load capacity at large displacements. Although no pipe piles were tested in the experimental program for this project, testing of concrete-filled steel tubular columns has shown a high degree of ductility with stable loops.[29] A conservative design approach would include limiting the maximum strain to 0.01 and the maximum aspect ratio of pile diameter to wall thickness to 39.

5. Analytical studies indicated that PS/C piles would have significant displacement capacity if ductile behavior based on a maximum compressive strain limit is assumed. However, testing indicated that a PS/C pile would suffer severe cracking and spalling if cycled at a deformation limit based on the ductility criteria used in the analytical study. Therefore, it is recommended that displacement limits for PS/C piles be based on the allowable stress limitation as initially presented by Abendroth, et al.[2]

4.3 PIER STUDY FOR EFFECTIVE STIFFNESS

Typically, either integral or semi-integral piers are used for jointless bridge superstructures. As used in this study, an integral pier includes a shear and moment connection between the pier cap and the superstructure, whereas a semi-integral pier includes only a shear connection. Bridge movement is accommodated by the flexibility of the piers. However, there are some uncertainties about the effective stiffness of the piers and the resulting pier forces attributed to the superstructure movement. The primary uncertainties are related to the effects of creep and cracking, and the soil-structure response of the foundation.

Tennessee DOT (TDOT) Structures Memorandum 045 includes recommendations for use of a reduced long-term modulus of elasticity of 6,900 MPa (1.0 x 10^6 lbf/inch^2) for concrete, to account for the potential effects of creep.[30] In addition, Memorandum 045 recommends, reducing by a factor of two, the moments and shear forces calculated assuming a fixed-foundation condition, to account for some footing rotation. Although jointless bridges designed using these recommendations are apparently performing well, these are nevertheless empirical rules and are principally based on experience rather than rigorous structural analysis.

Therefore, a study of the response of piers to longitudinal bridge movement was done. The specific objectives of this pier study were to (1) examine the influence of the soil-structure interaction on the horizontal response of the pier to longitudinal movement of the superstructure; (2) examine the effects of combined axial loading and horizontal deformation on piers, considering creep and concrete cracking; and (3) develop some design criteria for piers.

4.3.1 Foundation Response

The rotational stiffness of the foundation is an important factor in the response of piers to longitudinal deck movement. Foundation type and size, and soil stiffness, influence the rotational stiffness. Therefore, , an examination of the range of rotational stiffness based on soil and foundation type was done for a representative bridge.

Four foundations were designed for the same pier loading. Three of these foundations were spread footings: one each on medium stiff clay, stiff clay, and rock. The fourth footing was a bearing pile foundation. The spread footings were designed based on typical allowable bearing pressures for the type of soil assumed. Therefore, the size of these footings varied. The pile foundation was designed based on allowable pile loads.

Finite element models were developed for the spread footing using the computer program CANDE.[19] The footings were subjected to vertical loading and moment to determine a rotational stiffness at the base of the wall or columns. These analyses indicated that the moment-rotation behavior was essentially linear and the rotational stiffnesses were consistent with the simplified analysis presented by J. Zederbaum.[31] Rotational stiffness, K_θ, using Zederbaum's approach, is based on the elastic behavior of an ideal earth prism of a depth equal to one-third of the footing width, b, and can be determined as:

$$K_\theta = \frac{3E_s I_f}{b} \tag{4-1}$$

where,

E_s = modulus of elasticity of the soil
I_f = moment of inertia of the foundation base
b = footing width.

The rotational stiffness of the pile foundation was based on an elastic approach presented by A.A. Witecki and V.K. Raina.[32]

4.3.2 Pier Response

The structural stiffness of the pier wall or columns is another important factor in estimating the restraining forces associated with longitudinal thermal movement of a bridge superstructure. Pier stiffness is a function of the slenderness ratio (i.e., height to thickness), concrete properties, applied vertical loads, inelastic behavior (i.e., creep and cracking of concrete), and the type of connection at the top of the pier (i.e., integral versus semi-integral or pinned piers). Integral piers will transfer both moment and shear forces at the top, whereas semi-integral piers will transfer shear forces only.

To assess the effects of various parameters on the restraining moment at the base of the pier, a parametric study was conducted using the finite element program PBEAM.[33] The analyses incorporated time-dependent creep, shrinkage, and cracking of the concrete in a time-history analysis by imposing sinusoidal annual temperature movement at the top of the pier over a 3-1/2 year period. A total of 12 pier models were analyzed in the parametric study. Table 4-1 presents the values of the various parameters in each of the 12 cases. The parameters included foundation rotational stiffness, pier height, amount of axial load, creep coefficient, age of the concrete at loading, and the magnitude of the peak lateral movement at the top of the pier. In one analysis, the top of the pier was restrained with a rotational spring simulating an integral connection with the

superstructure. In all other analyses, a pinned connection was used. Two analyses were conducted for each set of parameters, including an analysis with inelastic creep, shrinkage, and cracking, and an analysis assuming, completely elastic uncracked behavior.

Table 4-2 presents the results for each case, including the ratio of inelastic moment to elastic moment and the percentage of lateral movement at the top of the pier accounted for by foundation rotation. The results of the analyses indicated:

1. For the range of parameters used in this study, the foundation rotation accounted for 20 percent to 79 percent of the lateral movement at the top of the pier. This percentage essentially increases as the relative inelastic stiffness of the pier increases.

2. The primary factors affecting the contribution of bending in the pier to the lateral movement at the top of the pier are cracking and the slenderness of the pier (height-to-thickness ratio). The baseline case (Case 1) with a 6.1-m (20-ft) height and a peak lateral displacement of 51 mm (2 inches) attained an inelastic moment of approximately 64 percent of the moment calculated for the completely elastic model. Figure 4-8 shows a plot of elastic moment and inelastic moment for 3 years of cyclic movement for this baseline case.

   For Case 2, cycling the 6.1-m- (20-ft-) high pier at 102 mm (4 inches) of peak lateral displacement instead of 51 mm (2 inches) of displacement (i.e., more cracking in the pier) decreased the inelastic moment to approximately 52 percent of the completely elastic moment. For Case 3, an increase in the height of the pier to 9.2 m (30 ft) (i.e., an increase in slenderness) increased the inelastic moment to 80 percent of the calculated completely elastic moment.

3. Comparison of Cases 5 and 7 with Case 1 indicates that concrete creep and the age of the concrete at loading had a relatively insignificant effect on the results.

4. Axial stress in the pier affects the cracking moment and, therefore, the effective stiffness. Figure 4-9 shows the results of analyses for Cases 1, 6, and 10 with three different levels of axial stress in the pier. The calculated peak inelastic moment was 64 percent, 82 percent, and 92 percent of the completely elastic moment for vertical loads of 0.53, 1.58, and 3.15 kN/mm, respectively.

The inelastic behavior of concrete is a significant factor in reducing flexural stiffness and, therefore, the design forces for piers supporting integral bridges. The results of the

parametric study performed on pier models indicate that the ratio of inelastic moment to elastic moment varied from 0.52 to 0.96. The lower value of the moment ratio corresponds to increased cracking, and the level of axial stress has a significant effect on the level of cracking.

To estimate the reduced stiffness of the pier caused by the inelastic behavior, the lateral deflection of each pier resulting from the rotation of the soil-foundation system was determined and subtracted from the total deflection induced at the top of the pier. The net deflection is the result of the flexural behavior of the pier, taking into account the inelastic response of the concrete. The flexural deflection was then used with inelastic moment data from the PBEAM analyses to obtain the reduced (equivalent) stiffness of the pier.

The above data was used to determine a relationship for the effective moment of inertia, I_e, for the pier:

$$I_e = \left(\frac{M_{cr}}{M_a}\right)^{\alpha} I_g + \left[1 - \left(\frac{M_{cr}}{M_a}\right)^{\alpha}\right] I_{cr} \qquad (4\text{-}2)$$

in which,

M_a = calculated elastic moment based on assumed bridge movement

I_g = moment of inertia of gross concrete section about the centroidal axis, neglecting reinforcement

I_{cr} = moment of inertia of cracked section transformed to concrete

α = exponent to be derived for best fit with the data

M_{cr} = cracking moment, which can be calculated as follows:

$$M_{cr} = \left(\frac{P}{A} + f_r\right)\frac{I_g}{y} \qquad (4\text{-}3)$$

where,

P = applied vertical load

A = cross-sectional area of concrete, neglecting reinforcement

y = half-depth of pier section

f_r = modulus of rupture of concrete

= $0.62\sqrt{f'_c}$ (MPa)

$= 7.5 \sqrt{f'_c}$ (lbf/inch^2)

f'_c = compressive strength of concrete.

This approach is analogous to the effective moment of inertia for flexural members in the American Concrete Institute (ACI) 318-02 building code requirements.[34] However, the piers are combined flexural and compression members. Therefore, the effects of axial load, P, are included in equation 4-3 for calculation of the cracking moment, M_{cr}. In addition, the exponent α was evaluated to provide the best correlation with data determined from PBEAM analyses. An exponent α of 1.25 was found to provide the best correlation. A correlation coefficient of 81 percent was obtained. The following equation is, therefore, recommended to estimate the equivalent moment of inertia (I_e) for the pier:

$$I_e = \left(\frac{M_{cr}}{M_a}\right)^{1.25} I_g + \left[1 - \left(\frac{M_{cr}}{M_a}\right)^{1.25}\right] I_{cr} \leq I_g \qquad (4\text{-}4)$$

Equations 4-1 and 4-4 can be used in an iterative procedure to determine the pier forces for a given movement at the top of the pier. Section 5.4 of this volume presents a methodology to accomplish this, and also methods to estimate a point of fixity within the bridge and methods to estimate the maximum expected movement at the tops of each pier.

It should be noted that use of an integral pier with a moment connection between the pier cap and the superstructure can induce significantly higher restraint forces in the pier as compared to the use of a semi-integral pier. Figure 4-10 shows the results of Case 8, simulating an integral pier, with the baseline Case 1 simulating a pinned-top pier. The maximum moment induced in the integral pier at 51 mm (2 inches) of peak deflection was approximately 40 percent higher than the moment induced in the semi-integral pier.

A summary of the results of the analyses for pier behavior are as follows:

1. Foundation rotation contributed to a significant portion of the longitudinal movement at the top of the pier. For the range of parameters used in the study, the foundation rotation accounted for 20 percent to 79 percent of this movement. Foundation rotational stiffness can be adequately estimated using existing elastic analyses approaches.

2. The primary factors affecting the contribution of bending in the pier to the longitudinal movement at the top of the pier are the slenderness of the pier

(height-to-thickness ratio) and cracking. Axial stress in the pier affects the cracking moment and, therefore, the effective stiffness. Concrete creep and the age of the concrete at loading had a relatively insignificant effect on the results. Based on the parameters in the pier study, equation 4-4 provides a recommended effective moment of inertia to account for cracking and axial stress in the piers.

3. Use of an integral pier with a moment connection between the pier cap and the superstructure will induce significantly higher restraint forces in the pier as compared to the case of using a semi-integral pier with a pinned connection. Since pier stiffness has a negligible effect on the total bridge movement, the stiffer connection does not decrease the expected movement at the top of the pier. Using an integral pier eliminates the need for the elastomeric bearing pads and details to accommodate rotation between the pier cap and the superstructure. Also, integral piers eliminate the mass of the pier cap for seismic design and provide increased clearance. However, the details for a semi-integral pier are simple compared to detailing a moment connection at the top of the pier.

4.4 EXPECTED BRIDGE MOVEMENT

A major focus of this study is on the effect of longitudinal bridge movement on jointless bridges. A bridge will expand and contract because of seasonal variations in temperature, but it will only contract as a result of concrete creep and shrinkage strains. Piers and abutments must be designed to accommodate the expected movement, and the superstructure must be capable of carrying the forces induced by the stiffness of the piers and abutments.

To study the effect of longitudinal bridge movement, an important first step is the determination of the expected movement. The factors involved include an effective temperature range, including seasonal and diurnal components; coefficients of thermal expansion, creep, and shrinkage; and the restraint from piers and abutments. The overall variability of these factors causes uncertainty in the determination of bridge movements. Therefore, the specific objectives of the bridge movement study were to:

1. Define the appropriate temperature ranges for bridge design, which would depend on the location and the type of bridge.

2. Determine the expected abutment and pier support movements and the potential variability of that movement, depending on bridge type; the resistance from support structures; and the effects of creep and shrinkage in the concrete.

Once these objectives were attained, this information would provide the basis for an analysis of jointless bridges subjected to longitudinal movement. The objectives of this analysis were to:

1. Develop an increased understanding of the behavior and response of a jointless bridge subjected to annual temperature change.
2. Identify critical locations within the bridge structure during this cyclic temperature variation.

4.4.1 Effective Temperature Range

The effective bridge temperature, also referred to as the mean or average bridge temperature, is the temperature that governs the overall longitudinal movement of the superstructure. Determining effective bridge temperature is a complex problem influenced by many factors such as shade temperature, solar radiation, wind speed, material properties, surface characteristics, and section geometry. Many of these factors are highly variable and are not necessarily related. A number of researchers have had limited success in attempting to relate one of these environmental factors, namely shade temperature, to the effective bridge temperature.[5]

Emerson developed a relationship between instantaneous shade air temperature and effective bridge temperature by first developing a relationship between the mean shade temperature and the effective bridge temperature.[5] She found that a 48-hour mean shade temperature correlated well with the effective temperatures of concrete bridges and that a 24-hour mean shade temperature correlated well with the effective temperatures of steel-stringer bridges. The use of mean shade temperatures minimized the random nature of most of the variables affecting bridge temperature. Emerson then related the mean shade temperatures to the instantaneous shade temperatures, based on meteorological data recorded throughout the United Kingdom. Emerson's approach was subsequently incorporated into British Standard (BS) 5400 to predict the minimum and maximum effective bridge temperatures based on geographical distribution of the minimum and maximum shade temperatures.

Imbsen applied and extended Emerson's approach to effective bridge temperatures in NCHRP Report 276.[7] The design guidelines in the NCHRP Report 276 are the basis for the temperature data in the current *AASHTO Guide Specifications for Thermal Effects in Concrete Bridge Superstructures*.[35] To cover the larger range of minimum and maximum shade temperatures experienced within the United States, Imbsen extrapolated

Emerson's mean and effective bridge temperature relationships. However, the isotherms in NCHRP Report 276 only represent *normal* daily minimum and maximum values instead of the extreme values of shade temperatures. Imbsen compared normal daily minimum and maximum shade temperatures with minimum and maximum extreme temperatures and found agreement within 3 °C (6 °F). However, these minimum and maximum extreme temperatures were apparently the averages of the extreme values on a particular day over a 30-year period and do not appear to represent reasonable extreme shade temperatures. As an example, D.D. Girton measured effective maximum temperature ranges of 64 °C (115 °F) and 65 °C (117 °F) over a 2-year period for a concrete bridge and a composite steel bridge, respectively, located in Iowa.[36] Using appendix A of NCHRP Report 276, an effective bridge design temperature of approximately 39 °C (70 °F) was determined for the concrete bridge and 50 °C (90 °F) was determined for the composite steel bridge.

This discrepancy led to a study to determine more appropriate minimum and maximum shade temperatures, depending on the location within the United States. A variety of climatological references were evaluated, including:

1. *Climatic Atlas of the United States*, U.S. Department of Commerce, Ashville, NC, June 1968.[37]
2. "Daily Normals of Temperature, Precipitation, and Heating and Cooling Degree-Days, 1961–1990," *Climatography of the United States*, No. 84, National Climatic Data Center, Ashville, NC.[38]
3. *Climatic Atlas of the United States*, Harvard University Press, Cambridge, MA, 1954.[39]
4. *ASHRAE Fundamentals Handbook*, Chapter 24: Weather Data, American Society of Heating, Refrigerating, and Air-Conditioning Engineers (ASHRAE), New York, NY, 1993.[40]

References 1 and 2 contain normal daily minimum and maximum shade temperatures and also the absolute extreme temperatures recorded. The *normal* daily minimum and maximum values were the basis of the isothermal map data depicted in Imbsen[7] and are not considered to represent the range of values that can commonly occur. The absolute extreme values seemed excessive for design purposes. However, Harvard's *Climatic Atlas of the United States* depicts isothermal maps of the lowest and highest temperatures experienced in a normal year, and the ASHRAE handbook contains tabularized data of

outdoor air temperatures (used for the design of heating and cooling systems for buildings) based on 99 percent confidence intervals. During a normal summer, there would be about 30 hours at or above the ASHRAE maximum, and during a normal winter, there would be approximately 22 hours at or below the ASHRAE minimum temperatures. References 3 and 4 were evaluated further to determine if they yielded reasonable extreme values for minimum and maximum shade temperatures based on geographical location.

Table 4-3 is a comparison between maximum measured bridge movement and calculated bridge movement based on the various minimum and maximum shade temperature sources, and site movement and temperature data available for four bridges. Both Harvard's *Climatic Atlas* and the ASHRAE weather data are compared to site-measured minimum and maximum shade temperatures and the temperature values depicted by Imbsen's isothermal maps. In all cases, the minimum and maximum shade temperatures are converted to effective bridge temperatures through the application of Emerson's relationships, including the extrapolations in NCHRP Report 276. Calculated bridge movement is then equal to the product of the effective temperature range, length, and coefficient of linear expansion. The two Iowa bridges are covered in an Iowa DOT report[36]; the Tennessee bridge is covered in TDOT Report No. 77-27-2[41]; and the North Dakota bridge is discussed in a North Dakota State University research project.[42]

The comparison in table 4-3 reveals that the isothermal map data in NCHRP Report 276 significantly underpredict the anticipated bridge movements, while site-measured minimum and maximum shade temperatures provide the closest agreement with measured bridge movement (except in the case of the Kingsport Bridge). The errors from using either Harvard's *Climatic Atlas* or the ASHRAE weather data was generally less than the error from using the NCHRP Report 276 data. Calculated bridge movements based on the various sources differ from the measured bridge movements by the following percentages:

	RANGE AVERAGE
Site-Measured	4–15% 9%
Climatic Atlas	1–16% 10%
ASHRAE	0–22% 12%
NCHRP Report 276	12–40% 25%

Emerson also found closer agreement between measured and calculated bridge movements when using site-measured shade temperatures, usually measured directly beneath the bridge, as opposed to using data from meteorological stations.[(5)] It is important to note that, in general, all of the climatic sources underpredict the measured bridge movement even though the measured movements may not represent extremes for these bridges, because they were measured only over a 1- to 3-year interval.

However, both Harvard's *Climatic Atlas* and the ASHRAE weather data provide more appropriate minimum and maximum shade temperatures than does the NCHRP Report 276. Both the *Climatic Atlas* data and the ASHRAE weather data were statistically derived from detailed records from the National Climatic Data Center (NCDC) of the National Oceanic and Atmospheric Association (NOAA), the U.S. Air Force, and the U.S. Navy. However, the ASHRAE data are based on more recent weather data. In addition, with an extensive listing of 755 individual stations throughout the United States, the data are easier to apply, particularly in the mountainous western region, than are the data from the isothermal maps. As a result, it is recommended that the ASHRAE weather data, used in part to create the tables in appendix A, be used to determine minimum and maximum shade temperatures based on the intended bridge location. From these values, minimum and maximum effective bridge temperatures can be determined through application of Emerson's relationships, including the extrapolations in NCHRP Report 276.

In reviewing Emerson's work, however, it was found that the study, which had been conducted in Great Britain, lacked temperature data for above 28 °C (82 °F) and below -12 °C (10 °F). Furthermore, nonlinear relationships applied to the data above and below these values did not appear justified because of this lack of available data. Therefore, a study was conducted to examine temperature data from 10 cities throughout the United States, representing a range of climatic conditions with greater temperature ranges. Plots and subsequent regression analyses for data relating 24- and 48-hour mean shade temperatures to the maximum and minimum shade temperatures revealed the following:

1. Only a small difference existed between the 24- and 48-hour relationships, indicating that either value could be applied.
2. A linear relationship appeared justified at all locations throughout the range of data, with a correlation of 0.97 with all cities combined.

Based on the study, the following relationships are recommended to determine the 24-hour mean temperatures corresponding to the minimum and maximum shade temperatures taken from the appendix A tables:

$$T_{24}_{min} = 1.035\ T_{min}_{shade} + 4.75\ °C\ (7.43\ °F) \quad (4\text{-}5)$$

$$T_{24}_{max} = 0.977\ T_{max}_{shade} - 5.44\ °C\ (9.05\ °F) \quad (4\text{-}6)$$

where,

T_{24}_{min} = 24-hour mean shade temperature determined from the minimum shade temperature

T_{24}_{max} = 24-hour mean shade temperature determined from the maximum shade temperature

The next step in this approach was similar to Emerson's work for the minimum effective bridge temperature, but varied slightly for the maximum effective bridge temperature. For minimum effective bridge temperatures, the effective bridge temperatures were measured at 6 a.m. in the two-span test bridges described in chapter 3 of this volume. These measured effective bridge temperatures were then related to a 24-hour mean shade temperature. An essentially uniform thermal distribution exists within a bridge beam at that time, which agreed with Emerson's work. For maximum effective bridge temperatures, the thermocouple located at the midheight of the beams was measured at

the time of maximum thermal gradient (approximately 1 p.m.) and then related to a 24-hour mean shade temperature. This thermocouple reading represents a reasonable approximation of the maximum effective bridge temperature, accounting for all of the diurnal effects except direct solar radiation. The data indicated that a linear relationship existed for both the minimum and maximum effective bridge temperatures. For concrete, the relationships were as follows:

$$T_{\underset{eff}{min}} = 0.963T_{\underset{min}{24}} + 0.17\ °C\ (1.49\ °F) \quad (4\text{-}7)$$

$$T_{\underset{eff}{max}} = 0.988T_{\underset{max}{24}} + 2.81\ °C\ (5.45\ °F) \quad (4\text{-}8)$$

For steel, the relationships were as follows:

$$T_{\underset{eff}{min}} = 1.004T_{\underset{min}{24}} - 2.24\ °C\ (4.16\ °F) \quad (4\text{-}9)$$

$$T_{\underset{eff}{max}} = 1.113T_{\underset{max}{24}} + 6.09\ °C\ (7.34\ °F) \quad (4\text{-}10)$$

where,

$T_{\underset{eff}{min}}$ = minimum effective bridge temperature

$T_{\underset{eff}{max}}$ = maximum effective bridge temperature, excluding direct solar effects.

The final component to be obtained is the direct solar effect. Comparisons of various proposed thermal gradients with data accumulated from the test girders indicated that the positive temperature gradients in the AASHTO LRFD specifications provide reasonable upperbounds to solar radiation differentials.[43] An additional uniform temperature increment, $\Delta\overline{T}$, caused by direct solar radiation can be calculated from these gradients through application of the following equations:

$$\varepsilon_{t_{avg}} = \frac{\sum_{i=1}^{m} \alpha_i \Delta T_i A_i E_i}{\sum_{i=1}^{m} A_i E_i} \quad (4\text{-}11)$$

$$\bar{\alpha} = \frac{A_d E_d \alpha_d + A_g E_g \alpha_d}{A_d E_d + A_g E_g} \quad (4\text{-}12)$$

$$\Delta \bar{T} = \frac{\varepsilon_{t_{avg}}}{\bar{\alpha}} \quad (4\text{-}13)$$

where,

$\varepsilon_{t_{avg}}$ = average thermal strain in cross section

α_i = coefficient of thermal expansion in subsection i

α_d = coefficient of thermal expansion of deck concrete

α_g = coefficient of thermal expansion of girder material

$\bar{\alpha}$ = effective coefficient of thermal expansion of a composite cross section

E_i = modulus of elasticity in subsection i

E_d = modulus of elasticity of deck

E_g = modulus of elasticity of girders

ΔT_i = diurnal increment of temperature in subsection i

A_i = cross-sectional area of subsection i

A_d = cross-sectional area of the deck

A_g = cross-sectional area of the girder.

This solar increment, $\Delta \bar{T}$, is a function of the solar zone, beam type, and cross section. However, a study of PS/C and steel cross sections with a range of deck thicknesses and beam spacings indicates a $\Delta \bar{T}$ equal to 0.26 T_1 for concrete and 0.18 T_1 for composite steel, where T_1 is the positive solar incremental temperature at the top surface of the deck from the AASHTO LRFD specifications.[43] For the range of beam/deck parameters studied, $\Delta \bar{T}$ ranged from 0.18 to 0.28 T_1 for concrete and 0.14 to 0.19 T_1 for composite steel. Proposed values for $\Delta \bar{T}$ solar based on this study are presented in table 4-4. The proposed values of 0.26 T_1 for concrete and 0.18 T_1 for composite steel are based on a 95 percent probability that they represent upperbound values. Any error in using these

values is relatively small compared to the overall effective temperature range, including seasonal and other diurnal effects.

Combining the above relationships for minimum and maximum shade temperatures versus 24-hour mean shade temperature, 24-hour mean shade temperature versus effective bridge temperature, and direct solar effects, equations can be developed to predict the minimum and maximum effective bridge temperatures based on the minimum and maximum shade temperatures. For concrete, the relationships are as follows:

$$T_{\underset{eff}{min}} = 1.00\, T_{\underset{shade}{min}} + 5\ °C\ (9\ °F) \quad (4\text{-}14)$$

$$T_{\underset{eff}{max}} = 0.97\, T_{\underset{shade}{max}} - 2\ °C\ (3\ °F) + \Delta \overline{T}_{solar} \quad (4\text{-}15)$$

For composite steel, the relationships are as follows:

$$T_{\underset{eff}{min}} = 1.04\, T_{\underset{shade}{min}} + 2\ °C\ (3\ °F) \quad (4\text{-}16)$$

$$T_{\underset{eff}{max}} = 1.09\, T_{\underset{shade}{max}} - 0\ °C\ (3\ °F) + \Delta \overline{T}_{solar} \quad (4\text{-}17)$$

where,

$T_{\underset{eff}{min}}$ = minimum effective bridge temperature

$T_{\underset{eff}{max}}$ = maximum effective bridge temperature

$T_{\underset{shade}{min}}$ = minimum shade temperature from the ASHRAE weather data based on bridge location (see appendix A)

$T_{\underset{shade}{max}}$ = maximum shade temperature from the ASHRAE weather data based on bridge location (see appendix A)

$\Delta \overline{T}_{solar}$ = uniform temperature change from direct solar radiation based on girder type and bridge location (see table 4-4).

Application of the above relationships to the bridges studied in table 4-3 indicates that this approach provides closer agreement with the measured bridge movement, as shown in table 4-5.

4.4.2 Determination of Maximum Longitudinal Movement

Bridges expand and contract because of temperature changes and time-dependent volume changes associated with concrete creep and shrinkage. In jointless bridges, it is important to estimate the maximum expansion and contraction at each end of a bridge to determine the longitudinal displacement expected for the abutment piles. It is also important to predict the movement at each pier and the joint width needed between the approach slab and the pavement. Another important movement is the maximum total thermal movement at each end resulting from the total effective temperature range. As discussed in section 4.2 of this volume, the starting point to determine the maximum passive pressure should conservatively be at the maximum contraction. The maximum passive pressure is related to the end movement, with expansion for the full effective temperature range.

The length change for a PS/C bridge can be calculated through use of typical design values for the coefficient of thermal expansion combined with creep and shrinkage strains from ACI 209R-92.[44] However, the overall variability of these factors adds uncertainty to the calculated end movements. Although a coefficient of thermal expansion for concrete is typically assumed to be 9.9 to 10.9 millionths/°C (5.5 to 6.0 millionths/°F), it is known that this value can range from approximately 5.4 to 12.6 millionths/°C (3.0 to 7.0 millionths/°F).[45] Also, the variability of creep, shrinkage, and modulus of elasticity of concrete is known to be significant.[46] In addition, resistance to length change from abutments and piers, combined with the variability of the restraint (primarily caused by the variability of the soil), leads to unequal movement at each end of a bridge and uncertainty as to the magnitude of the movement at each end. Finally, the effective setting temperature of the bridge and the age of the PS/C girders at completion of the superstructure are typically unknown, making the relative magnitude of expansion and contraction and the starting point for creep and shrinkage calculations uncertain.

Monte Carlo studies were conducted to investigate the effects of the variability of the parameters and to provide guidance in formulating recommendations for design calculations. Two standard four-span bridge models were selected for these Monte Carlo studies. The first model was a PS/C bridge that was modified to simulate various conditions. The second model included steel wide-flange stringers. The Monte Carlo studies (or simulations) used a spreadsheet for calculation of bridge movements, to generate a large number (typically 2,000) of runs using the statistical variation of material parameters affecting the movement. Within each run, a computer program randomly selected values for the coefficient of thermal expansion, temperature at construction,

creep and shrinkage parameters of concrete, modulus of elasticity of concrete, and soil stiffness, based on statistical distributions of the values of these parameters. The variations in calculated bridge end abutment movements were then used to determine a 98 percent confidence interval for the maximum calculated movements. The PS/C bridge model was modified to simulate a cast-in-place concrete bridge. Another modification to this model incorporated the J.H. Emanual and J.L. Hulsey method[47] of calculating the coefficient of thermal expansion of concrete. The prestressed bridge model was analyzed to estimate the maximum total thermal expansion after full contraction. Further details of the Monte Carlo studies are presented in chapter 7 and appendix B of the analytical report.[15]

Table 4-6 presents the values of the magnification factors, referred to as Γ factors, for the various conditions based on the results of the Monte Carlo studies. These Γ factors are intended to modify the calculated values to account for uncertainty in the calculations. Case 1 includes magnification factors for the maximum expected movement from the assumed "as constructed" condition. A primary factor affecting the magnitude of these magnification factors is the uncertainty of the construction temperature. The Γ values for total movement account for uncertainty in the calculation of the overall change in the length of the bridge. However, because of uncertainty about the stiffness of the abutments and piers, the Γ's for the calculation of the movement at each end are somewhat larger.

Case 2 addresses reexpansion after full contraction. Case 3 is a modification of Case 1(a), using a more certain coefficient of thermal expansion estimate based on the methodology from Emanual and Hulsey for calculating the coefficient of thermal expansion of concrete.[47] The results of the analysis for the coefficient of thermal expansion of concrete following the Emanual and Hulsey model indicated that calculated end movements should be increased by Γ factors of 2.05 for maximum expansion and 1.45 for maximum contraction. The Γ values calculated in this simulation are greater than the values calculated in the Case 1(a) condition. This is attributable to the difference in calculating design thermal movements rather than to the variability of computer-predicted movements. The coefficient of thermal expansion design value of 10.8 millionths/°C
(6.0 millionths/°F) recommended by AASHTO and used in the Case 1(a) study is conservatively high when compared to the average of the database developed for the Monte Carlo study. The average for the coefficient of thermal expansion of concrete in the database described in appendix B of the analytical report is 8.8 millionths/°C

(4.9 millionths/°F).[15] Therefore, the conventional design calculated value of movement using 10.8 millionths/°C (6.0 millionths/°F) apparently already includes some margin of safety. It should be noted, however, that the absolute values of the bridge movements calculated by the simulation using the Emanual and Hulsey model are lower than those calculated in the baseline condition. This is expected since the Emanual and Hulsey database had a lower coefficient of variation. Therefore, it is recommended to use the Emanual and Hulsey model to estimate the value of the coefficient of thermal expansion of concrete, if sufficient information regarding the concrete composition is available to the designer.

Section 5.2.2 of this volume presents procedures for using these Γ factors in determining the maximum end movements of jointless bridges. It is assumed that the bridge has unknown construction timing and that no specific data on material properties are available. It should be noted that similar procedures can be used to estimate the maximum expected joint movement in jointed bridges.

4.4.3 Response to Effective Annual Temperature Change

There were analyses of jointless bridges subjected to longitudinal movement carried out to develop a better understanding of their behavior and response to annual temperature changes and to identify potentially critical locations within these structures. These analyses utailized two-dimensional models of PS/C, reinforced concrete, and composite steel bridges, and were intended to study:

1. Creep and shrinkage for concrete bridges and the concrete deck of composite steel bridges.
2. Cracking in the concrete.
3. Nonlinear end-restraint stiffnesses from abutment piles, the approach slab, and passive soil pressure.
4. Lateral support stiffnesses at piers.
5. Time-history analyses over several years, superimposing sinusoidal annual uniform temperature change effects on creep and shrinkage effects.

Actual bridges were used for the analyses, based on *Standard Plans for Highway Bridges, Volumes IV and IV(A)*.[48] The plans were modified to conform to typical jointless bridge details and layouts. Analyses included both a short-span and a long-span

structure for each bridge type. The computer program PBEAM,[33] verified through comparison with previously measured bridge movement data, was used to model the various bridges and included all of the desired analysis features discussed above. Various combinations of starting temperatures, cycling, creep, shrinkage, and bridge details were investigated to cover a broad range of bridge behaviors and responses. Both chapter 7 and appendix C of the analytical report contain detailed results of these analyses.[15] Appendix C of the analytical report is also included as appendix C of this volume.

In general, the results of the analyses indicated that bridge contraction is more critical than bridge expansion. As a jointless bridge contracts, tension forces accumulate within the structure because of restraint from the abutments and piers, with the abutments usually providing the majority of the restraint. These tension forces will tend to decrease the flexural capacity of the bridge girders. The tension forces also induce additional stresses at joints within the structure, such as the deck/abutment connections, pier diaphragms in PS/C bridges, and splices in steel beams.

Analyses of bridge contraction indicated the following conclusions, relative to all three bridge types:

1. Longitudinal movement of the bridge is essentially unchanged by abutment and pier restraint as compared to its free displacement.
2. The total restraint provided by the abutment is the sum of the pile restraint and approach slab restraint from sliding friction, and except for relatively short bridges (total length, not individual span length), thermal movement alone results in the abutment piles yielding.
3. Yielding of the abutment piles and dragging of the approach slab represent an upperbound on the abutment restraint forces and are statically determinate.
4. The positive end-restraint moment, caused by eccentricity of the pile from the beam centroid, is significant for the beam-to-abutment connections, but diminishes rapidly along the bridge length, resulting in a relatively small negative moment at the first interior support.
5. Piers are typically softer than abutments and therefore contribute only a small amount to the overall tension, unless they are unusually short and stubby. 9/16/06

These conclusions are very important because they indicate that increasing the overall bridge length will not significantly increase the overall tension within a jointless bridge,

except for the nominal increases in restraint that come from the additional piers with a longer bridge. Also, the restraint forces are statically determinate, and the abutment restraint moment, although an important consideration for design of the beam-to-abutment connection, has a relatively minor impact at other locations within the bridge.

Conclusions specific to PS/C bridge contraction include:

1. Longitudinal contraction caused by creep and shrinkage exceeds that caused by cyclic temperature variations for realistic bridge casting temperatures.
2. Secondary continuity moments caused by creep and shrinkage at intermediate piers significantly exceed moments caused by abutment end restraint.
3. Live load moments at piers significantly exceed moments caused by abutment end restraint.
4. The absence of a positive-moment connection at piers will increase stresses within the deck reinforcement at the diaphragm. However, the majority of this tension is caused by bending from relative creep and shrinkage between the girder and the deck and not from the abutment and pier restraint.

Conclusions specific to composite steel bridge contraction include:

1. Secondary continuity moments at piers, caused by concrete deck shrinkage, significantly exceed moments caused by abutment end restraint.
2. Dead load and live load moments at piers significantly exceed moments caused by abutment end restraint.

Conclusions specific to reinforced concrete bridge contraction include:

1. Secondary continuity moments at piers, caused by relative shrinkage within the cross section, are relatively minor and are on the same order of magnitude as moments caused by abutment end restraint.
2. Dead load and live load moments at piers significantly exceed moments caused by abutment end restraint.

Another study of PS/C bridges included an investigation of live load continuity at piers. A series of analyses were completed, which included creep, shrinkage, cracking, cyclic uniform temperature change, and live load application for both a jointless and a jointed bridge. Except for the abutment restraint, all other aspects of the two bridges were identical. In PS/C bridges constructed as simply supported for dead load and made

continuous for live load, the effective continuity for live load depends on the relative age of the beams when the slab is cast and the age of the bridge when live load is applied.[49] Therefore, to bound the behavior in the study, one set of analyses applied late-age live load to an early-age slab cast deck, and the other set of analyses applied early-age live load to a late-age slab cast deck. A comparison of the results for the two bridges revealed that the abutment and pier restraint had a minimal effect on the degree of continuity. Relative creep and shrinkage between the slab and the girder dominated the response and the degree of continuity at the intermediate piers.

Although bridge expansion is not as critical a mode of behavior as bridge contraction, there are nevertheless vital issues to be addressed regarding bridge expansion and the behavior of jointless bridges. As a jointless bridge expands, compression forces accumulate within the structure because of restraint from the abutment and piers, with the abutment providing the vast majority of the restraint. Bridge expansion induces significant passive soil pressures at the abutment in addition to the pile and approach slab restraint already encountered during bridge contraction. At full Rankine passive pressures, the total abutment compressive restraint force is approximately five times greater than the tensile restraint force during bridge contraction. However, in general, this compressive force is beneficial to bridge capacity, both within the spans and at joints within the structure. Furthermore, even though the restraint force with expansion is increased by five times compared to contraction, the end-restraint moment is increased only three times compared to the moment developed during contraction. The resultant soil pressure resisting expansion has a smaller eccentricity than the shear in the abutment support pile resisting contraction.

To study the effects of bridge expansion, there were bounding analyses done on the six sample jointless bridges. These analyses assumed that the soil behind the abutment will fill in behind the bridge as it contracts. Over time, the soil will become recompacted, as discussed in section 4.2. Maximum overall bridge lengths were based on assuming a minimum bridge starting temperature of 13 °C (55 °F), limiting pile movement to a practical extreme of 102 mm (4 inches) during the initial contraction period, and contracting the bridge to its minimum effective bridge temperature. At this point, the soil is assumed to have been recompacted behind the abutment, and the bridge is allowed to expand through its full thermal range, which is 64 °C (116 °F) for the bridges studied. The structural capacity of each bridge is checked for the forces generated during this expansion, including the increased pile reactions caused by the end-restraint moment.

Stresses along each bridge were checked against the allowable values from the AASHTO *Standard Specifications for Highway Bridges*.[16] At some locations, stresses caused by the expansion were compared directly to the allowable values since dead and live load stresses are essentially zero. One location that exhibits these characteristics is the beam section at the abutment. This connection is typically assumed to be pinned under gravity loads. At other locations, stresses caused by the expansion were compared to 25 percent of the allowable values based on table 3.22.1A of the AASHTO *Standard Specifications*, which includes a 25 percent increase in the allowable stresses when including thermally induced forces with gravity loads. The capacity check also included calculations for buckling/instability of the bridge girders under these large compressive forces, including the P-delta effects. In general, for all six bridges studied, stresses from these bounding analyses were less than the allowable AASHTO values. However, two topics that require close examination under conditions of bridge expansion are (1) the buckling/instability of the steel bottom flange in the composite steel bridges and (2) the punching shear at the girder/abutment interface for all bridge types.

4.4.4 Transverse Movement in Skewed Bridges

A skewed bridge has the longitudinal axis at an angle other than 90° with the piers and abutments. The skew angle , θ , is shown in figure 4-11. With skewed bridges, the soil passive pressure developed in response to thermal elongation has a component in the transverse direction, as illustrated in figure 4-11. Within certain limits of skew, soil friction on the abutment will resist the transverse component of passive pressure. However, if the soil friction is insufficient, either significant transverse forces or significant transverse movements, depending on the transverse stiffness of the abutment, could be generated.

Because of the potential problems and uncertainties with the response of skewed integral abutments, many State DOTs limit the skew in this type of bridge. A typical limit for the maximum skew angle for the jointless bridges used by many States is 30°. However, maximum skew angle limits in various States range from 0° to no limit.[50] There is a need to define a rational basis for limiting and/or accommodating skew angles for bridges with integral abutments. Therefore, an analytical study was carried out to investigate transverse movement in skewed bridges.

The objectives of this study on skewed bridges were to:

1. Demonstrate the relationship between the skew angle and abutment-soil friction for limiting skew. When the skew angle is below some limit, there is no need for special consideration for the transverse forces or transverse movement.
2. For bridges where it is required transverse movement be limited, demonstrate the relationship of the magnitude of forces required to guide integral or semi-integral abutments to minimize transverse movement in bridges with large skew angles.
3. For bridges where transverse movement is acceptable, develop a relationship between the skew angle and the expected transverse movement for a typical integral stub abutment having no special design features to restrain this movement.
4. Compare analytical results with field data for a skewed bridge that was monitored as part of the experimental portion of this project.
5. Perform a sensitivity study to demonstrate the relationship between transverse movement and longitudinal expansions for various skew angles and ratios of bridge length to width.
6. Perform a sensitivity study to investigate the effects of skew on secondary continuity response.

This work was accomplished by developing equilibrium and compatibility equations for end abutment forces and, in the case of a typical stub abutment, solving these equations for varying skew angles and bridge length-to-width ratios.

4.4.4.1 *Skew Angle Limit for Limiting Transverse Effects*

Figure 4-12 shows the relationship between the passive soil pressure (P_p) response to thermal expansion and the soil/abutment interface friction (F_{af}) assuming no rotation of the superstructure. For rotational equilibrium:

$$F_{af}\,(L \cos\,\theta) = P_p\,(L \sin\,\theta) \tag{4-18}$$

$$F_{af} = P_p \tan\,\delta \tag{4-19}$$

where,

$\tan\,\delta$ = friction factor for interface of formed concrete and soil.

Substituting equation 4-19 into 4-18:

$$\tan \delta = \frac{\sin\theta}{\cos\theta} = \tan \theta$$
$$\delta = \theta \qquad (4\text{-}20)$$

Therefore, the bridge superstructure will be held in rotational equilibrium until the skew angle, θ, exceeds the angle of backwall friction, δ. Integral abutments are typically backfilled with granular material. NCHRP Report 343, *Manual for the Design of Bridge Foundations*, lists a friction angle of 22° to 26° for formed concrete against clean gravel, gravel sand mixtures, and well-graded rock fill with spalls.[23] Based on the data, 20° represents a reasonably conservative skew angle below which special consideration for transverse forces or transverse movement will not be needed.

4.4.4.2 *Forces Required to Resist Transverse Movement*

With larger skew angles, either the integral abutment can be designed to resist the transverse force generated by the soil passive pressure in an attempt to keep the abutment movement predominantly longitudinal, or the abutment can be detailed to accommodate the transverse movement. Figure 4-13 shows the relationship for rotational equilibrium, including lateral resistance of the abutment, F_a, and the wall/soil interface friction, F_{af}. For rotational equilibrium:

$$(F_a + F_{af})\,(L \cos \theta) = P_p\,(L \sin \theta)$$
$$F_{af} = P_p \tan \delta \qquad (4\text{-}21)$$

$$F_a = P_p\,(\tan \theta - \tan \delta) \qquad (4\text{-}22)$$

Figure 4-14 shows the relationship between F_a and P_p, assuming the interface friction angle, δ, to be 20°. As shown in figure 4-14, the force required to resist transverse movement is a significant portion of the passive soil pressure response, P_p. It should be noted that P_p is not necessarily the full passive pressure response, but can be determined for the end movement using the Clough and Duncan relationships[11] shown in figure 5-11. The end movement to be considered for Δ/H in figure 5-11 is the end movement normal to the abutment, $\Delta\ell_n$. As illustrated in figure 4-15, this end movement is:

$$\Delta\ell_n = \Delta\ell \cos \theta \qquad (4\text{-}23)$$

where $\Delta\ell$ is the maximum expected end movement for thermal reexpansion from the starting point of full contraction for the full range of effective bridge temperatures as discussed in section 4.2 of this volume.

From figure 4-15, it can be seen that, as the skew angle, θ, increases, $\Delta\ell_n$ reduces with respect to $\Delta\ell$. This relationship helps offset the increase in F_a/P_p with increasing θ. However, F_a will still be a sizeable portion of P_p.

For relatively short bridges in locations with small effective temperature ranges, it may be feasible to design the abutment substructure to resist F_a. It should be understood though that, for whatever is used to develop F_a (batter pile and/or lateral passive soil resistance), lateral movements are required to develop the resistance, F_a. Therefore, details anticipating some transverse movement should be used. The expected movements are a function of the relative stiffnesses of resistance to P_p and F_a. It should also be noted that adding battered piles to an integral abutment for lateral load will also increase the stiffness in the longitudinal direction, which induces more demand on the superstructure and connections between the deck and abutments.

To avoid the effects of increased abutment stiffness for guiding skewed bridges, M.P. Burke has proposed a semi-integral abutment, shown in figure 4-16, with an end diaphragm sliding with respect to a fixed abutment.(51) This concept reduces the restraint on the superstructure to just the passive pressure on the backside of the end diaphragm and the resistance of the bearings. However, moveable bearings are required both for vertical support and horizontal support to guide the end movement. The bearings for horizontal support and the abutment substructure should be designed for the force F_a to resist the passive pressure response on the backside of the end diaphragm. Figure 4-17 depicts a two-span, semi-integral abutment bridge with a skew angle of 45°.(52) This bridge was constructed in 1969 with semi-integral abutments. The semi-integral construction included an integral end diaphragm that moves with the superstructure and that both slides longitudinally on and is guided transversely by relatively stiff abutments. Figure 4-18 shows cracking in the abutment wall near an acute corner of the superstructure, presumably caused by transverse forces related to soil pressures.(52) An alternative approach is to use a stub abutment without any special design features to resist transverse movement, but to detail the bridge to accommodate the transverse movement, as discussed in the following section.

4.4.4.3 *Expected Transverse Movement With Typical Stub Abutment*

To investigate the relationship between skew angle and expected transverse movement for a typical integral stub abutment, a set of relationships were derived based on the equilibrium and compatibility of end abutment forces in the plane of the bridge superstructure. For this analysis, the superstructure is assumed to act as a rigid body with

rotation, β, about the center of the deck (for a longitudinally symmetrical bridge), as illustrated in figure 4-19. The rotation occurs to accommodate the thermal end movement, $\Delta\ell$. Forces considered in response to this movement include soil pressure on the abutment and wingwalls, wall/soil interface friction on the abutment, and pile forces normal to and in line with the abutment and wingwalls.

The relationships between these forces and the components of abutment movement are defined in appendix B of this volume. The relationships derived were used to calculate the expected transverse movement and longitudinal restraint forces in girders for the skewed bridge instrumented as part of the experimental program described in section 3.6 of this volume. The results calculated from the derived relationships were in good agreement with the experimental data as described in chapter 9 of the analytical report.[15] Therefore, these relationships were used to further investigate transverse movement and longitudinal restraint in skewed bridges.

To demonstrate the effects of skew angle on expected transverse movement and longitudinal restraint forces, analyses were carried out using the spreadsheet program and the equations in table B-1 in appendix B. Variables used included skew angle and length-to-width ratio for the bridge. The abutment for the instrumented bridge is a fairly typical type of stub abutment used in Tennessee and was used as the baseline structure for the analyses.

A primary variable in this study is length-to-width (L/W) ratio. The instrumented baseline bridge is relatively wide compared to the length, and the L/W ratio for this bridge is 3.15. To demonstrate sensitivity to the bridge L/W ratio, the analyses were repeated for bridge widths that were 2/3 of the width and 1/3 of the width of the instrumented baseline bridge; this corresponds to L/W ratios of 4.73 and 9.45, respectively. The abutment piles were reduced from 18 to 12 piles for an L/W of 4.73, and to 9 piles for an L/W of 9.45.

The length of the wingwalls required for skewed abutments to support the sloping soil is a function of the skew angle as follows:

$$\ell_w \cong \frac{h_{abut}}{s\cos\theta} \tag{4-24}$$

where,

θ = skew angle
h_{abut} = height of the abutment

s = slope of the embankment away from the abutment.

Therefore, in these analyses, the length of the wingwalls from the baseline bridge with a 59° skew angle was shortened for the smaller skew angles as a function of θ from equation 4-24, assuming h_{abut}/s as a constant. The number of piles under the wingwall was reduced from three to two for the abutments, with a ℓ_w <66 of the length of the wingwalls for the 59° skewed bridge. Therefore, two piles were used to support wingwalls with skew angles of 40° or less.

The results of these analyses for the ratio of transverse movement to longitudinal $\Delta_{t1}/\Delta\ell$, for a $\Delta\ell$ of 25.4 mm (1.0 inch), are shown in figure 4-20. The transverse movement, Δ_{t1}, is the transverse movement of the acute corner of the bridge (obtuse corner of the wingwall/abutment), as further described in appendix B. This is the corner that experiences the largest transverse movement because of the skew angle.

The results in figure 4-20 demonstrate the increase in the transverse movement with increasing skew angle. The data in figure 4-20 also demonstrate the increase in transverse movement with decreasing L/W ratio. It should be pointed out the change in L/W was accomplished in the analyses by decreasing the width, W, and keeping the length, L, constant. Also the length of the wingwall at each skew angle was constant. Therefore, the results in figure 4-20 predominantly demonstrate the effects of increasing the ratio of the length of the wingwalls, ℓ_w, to the length of the abutment wall, ℓ_{abut}. The data in figure 4-20 show that increasing the wingwall length relative to the abutment wall length (which includes increasing the number of wingwall piles relative to the number of abutment wall piles) can significantly decrease the transverse movement. However, the wingwalls and abutment have to be designed to transmit the restraint forces on the wingwalls into the superstructure.

Figure 4-21 shows the resulting total longitudinal restraint force for these analyses and demonstrates the decrease in longitudinal restraint with increasing skew angle. For the full-width bridge with a L/W ratio of 3.15, the longitudinal restraint at a skew angle of 60° is approximately 60 percent of the longitudinal restraint at θ = 25°. For the larger L/W ratio of 9.45, the ratio of the longitudinal restraint at θ = 60° is approximately 70 percent of the restraint at θ = 25°. This demonstrates the increase in restraint resulting from the increase in the resistance to lateral moment caused by the larger ratio of wingwall length to abutment length.

Since the baseline abutment used in these analyses is a relatively high stub abutment (with an abutment height of 3.96 m [13.0 ft] and with the strong axis of the pile resisting movement normal to the abutment versus weak-axis bending for movement parallel to the abutment), the data in figure 4-20 represent a reasonably large estimate for the transverse movement of skewed abutments. Although there is significant uncertainty about actual soil and pile stiffness, the maximum expected end movement, $\Delta\ell$, determined as discussed in section 4.4.2, includes a multiplier to account for uncertainty. Therefore, it is suggested that designers use the data in figure 4-20 to approximately estimate the expected transverse movement in skewed integral abutments caused by restraint of longitudinal thermal expansion. In addition, the relationships between longitudinal restraint force and skew angle shown in figure 4-21 can be used to estimate the relative decrease in restraint forces in a skewed bridge. Also, the transverse movements can be used to estimate the transverse restraint forces on the wingwall caused by passive soil load and pile resistance, and to estimate longitudinal and transverse movements of the abutment piles for biaxial bending considerations. All of the other components of movement and forces can be determined from Δ_{t1} and $\Delta\ell$, using the relationships in appendix B. For more accurate estimates, the equations in table B-1 of appendix B can be used to analyze specific skewed abutments (and/or can be modified for other pile orientations).

It should be noted that the transverse movement, Δ_{t1}, discussed above is the movement of the acute corner of the bridge deck related to the rigid body rotation of the superstructure caused by abutment passive restraint of longitudinal thermal expansion, $\Delta\ell$. There will also be transverse thermal expansion of the abutment. This transverse thermal expansion will be limited as compared to the longitudinal expansion, because the temperature change is moderated by the fact that abutment breastwalls are exposed to ambient air temperature on one side only and the abutment is not appreciably exposed to solar radiation. Therefore, depending on the width of the bridge and the skew angle, the transverse thermal expansion may or may not add significant additional transverse movement to the abutment wingwalls. This additional transverse movement would add to Δ_{t1} and subtract somewhat from Δ_{t2}. To estimate this transverse thermal expansion of the abutment, it is suggested that the temperature range be determined from the difference between the maximum 24-hour mean temperature, $T_{24\,max}$, from equation 4-6 and the mean temperature during construction. The mean temperature during construction and the maximum shade temperature used in equation 4-6 are determined from the data in appendix A for the specific location of the bridge. This temperature range can be used

with one-half the bridge width, W/2, to estimate the additional transverse movement at Corner 1 to be added to the movement Δ_{t1} and subtracted from Δ_{t2} from the rigid body rotation when determining transverse soil forces and pile movements for the wingwalls. Since this transverse expansion will tend to counteract the transverse movement Δ_{t2}, it is suggested that the resulting restraint forces on Wingwall 2 be determined with and without the transverse thermal expansion component, to examine and design for the more severe condition.

To detail the abutments for the transverse movement of the corners, all interfaces of the integral abutment with other components such as the approach pavement, barrier walls, pavement for slope protection, and drainage components, should be detailed to accommodate this movement. In addition, relatively flexible connections to piers should be considered in the direction parallel to the pier caps. The analyses described in section 4.4.2 indicated that, for right bridges, the restraint forces from the piers into the superstructure resulting from longitudinal expansion, have relatively minor effects. This is for movement perpendicular to the pier cap. Foundation rotation and cracking in the pier (cantilevered from the foundation) contribute to a relatively flexible pier response for this direction of movement. The foundation and pier structure stiffness will probably be more significant for movement parallel to the pier cap. Therefore, it is recommended that the connection between the bottom of the superstructure and the pier caps be flexible in this direction. (This approach, however, may not be appropriate for the purposes of seismic design.) In this case, design of the diaphragms should consider the piers' restraint of the rigid body rotations that result from passive abutment restraint of longitudinal thermal expansion.

4.5 SECONDARY CONTINUITY FORCES

Secondary continuity forces result from the continuous nature of jointless bridges. A major uncertainty with these bridges is in determining the effects of diurnal temperature variations. In addition, a number of other effects contribute significantly to secondary continuity moments. These include concrete creep, shrinkage, and heat of hydration during construction; variation in the coefficients of thermal expansion between the girder and the deck; and seasonal moisture changes in the concrete that cause shrinkage reversals. All of these factors contribute to longitudinal stresses within a continuous bridge structure. In some instances, these factors are additive, while in others, they oppose one another. The magnitude of these effects to be considered in design, and the critical combinations to be considered, are uncertain.

Calculated elastic thermal gradient stress caused by the combined internal restraint and secondary continuity moments can be very high, particularly when combined with other secondary effects. There have not, however, been many cases of distress related to these secondary stresses. Previous research indicates that there may be some stress relief related to short-term thermal creep and shrinkage.[6,10] In addition, cracking and yielding will diminish the stresses caused by the secondary effects.

Chapter 3 describes laboratory studies and outdoor, environmentally exposed studies, which were carried out in the experimental part of this project to investigate the potential for short-term thermal creep to relieve differential thermal strains. These studies indicated that short-term thermal creep does not have a significant effect. Therefore, it was necessary to examine the effects of temperature gradient in combination with other restraint stresses, while also considering cracking and yielding, to establish the significance of temperature gradiants on jointless bridges.

The following section summarizes the analytical methods, the results of parametric studies, and recommendations regarding the impact of secondary continuity forces on jointless bridges.

This study is described in more detail in chapter 8 of the analytical report.[15]

The objectives of this work on secondary continuity forces were to:

1. Determine the significance of bridge superstructure component stresses caused by the various sources of secondary moment.
2. Determine which combinations of secondary effects, if any, should be considered during design.
3. Provide proposed design guidelines for consideration of secondary moments when their potential effects are significant.

The objectives were accomplished within the following scope of work:

1. A study to determine effective thermal gradients for analyses to evaluate secondary thermal continuity moments.
2. The development of simplified analytical methods to account for concrete cracking and reinforcement yielding, where appropriate, in analyses of steel and PS/C bridges.

3. A comparison of analytical results to the results from the full-scale tests which are described in chapter 3.
4. Parametric studies for positive and negative secondary moment effects for both steel and PS/C bridge girders.
5. A presentation of the analytical work summary and conclusions, and of preliminary design guidelines, for investigating secondary moments.

The following sections describe parametric studies of steel and PS/C bridges. Initial analyses were typically for the elastic and uncracked (gross section) condition. Where analyses of the uncracked section indicated the potential for significant secondary stresses, there were further analyses conducted to consider the effects of concrete cracking and reinforcement yielding. Stresses were judged as significant or not by comparison with allowable values from AASHTO's *Standard Specifications for Highway Bridges*.[16] Calculated stresses were typically compared to 125 percent of the allowable values based on table 3.22.1A in the *Standard Specifications* publication, which included a 25 percent increase in allowable stress when thermally induced forces were included with gravity loads. This evaluation of the significance of the stresses calculated, however, included the understanding that secondary effects are typically self-limiting because they dissipate with cracking and yielding. In a ductile system, differential inelastic strains caused by temperature, creep, and shrinkage typically do not significantly affect the strength of the system. In the analyses described in the following sections of this chapter, there are two potentially critical situations defined for service-level stresses from the combined primary and secondary effects, which may affect the strength of the system:

1. Negative secondary moments increase the compressive stress in the bottom flange of steel girders and may cause lateral torsional buckling when the bottom flange is inadequately braced to develop yield stress.
2. The addition of positive secondary moments may cause cracking in the bottom of prestressed girders.

The above two situations, although occurring under service-level loads, can affect strength. Lateral torsional buckling of the compressive flange in the negative-moment region of a steel girder can be considered a strength failure. For PS/C girders, cracking under service-load conditions may eventually lead to fatigue failure. Although the studies described in this chapter deal with service-level stresses, chapter 5 presents

considerations for using the results of these studies in the AASHTO LRFD design approach.

4.5.1 Effective Thermal Gradient

There has been significant research performed to define temperature distributions through bridge decks and girders (see references 7, 9, and 53 through 56). When determining which temperature distribution is most appropriate, the question of accuracy versus complexity needs to be weighed.

The two critical parameters of a temperature gradient are the maximum temperature differential and the distribution of this differential throughout the depth of the cross section.

Table 4-7 contains data on nine bridges monitored for temperature differentials with the AASHTO LRFD positive gradients,[43] at various locations within the United States. The list contains four composite steel bridges and five PS/C bridges (three I-beam and two segmental box structures). The 1998 AASHTO LRFD positive gradients either exceed or are within 1 °C (2 °F) of the maximum measured differential for all but one of the bridges. (The PennDOT segmental box girder bridge exceeded the code-specified maximum differential by nearly 25 percent.) For the majority of the cases, the maximum measured positive differential was between 60 percent and 100 percent of the 1998 AASHTO LRFD value.

Chapter 3 presents temperature gradient data from the test girders that were part of this study, at the time of maximum temperature differential. The 1998 AASHTO LRFD gradients have been superimposed on the same plots for comparison. Although the measured peak values are only 60 percent of the 1998 AASHTO LRFD values, the general shape of the measured positive temperature gradients compares reasonably well with the code-specified gradients for both the precast concrete and the steel beams. It would appear that the 1998 AASHTO LRFD gradients offer a possible overly conservative upperbound estimation of the actual thermal gradients in both precast and steel bridge members. However, as determined in the experimental program, other secondary continuity effects, such as differences in the coefficient of thermal expansion between the deck and the girder, augment the effects of the temperature gradient. The combined effects are such that calculations for the steel girder using the 1998 AASHTO LRFD positive gradient to determine the redistribution of the reactions caused by the secondary effects were in reasonable agreement with the measured redistribution of the reactions. Also, it is important to note that the monitoring periods for the field-measured

temperature differentials listed in table 4-7 were limited, ranging from only 1 to 2 years. It is definitely possible that fairly extreme environmental conditions did not occur with some of those bridge girders during those periods. Therefore, the 1998 AASHTO LRFD positive temperature gradients were used in the following analyses that considered secondary continuity forces.

For negative temperature gradients, the shape of the measured temperature distributions in the experimental study was significantly different from that with the 1994 AASHTO LRFD distribution.[1] At the measured peak negative temperature differentials, the measured distribution was relatively uniform through the deck, whereas the AASHTO LRFD distribution has a steep gradient through the deck. A comparison of measured data with the 1994 AASHTO LRFD distribution is shown in figure 3-16 of this volume.

Note that the 1994 edition of the AASHTO LRFD specifications[1] is referenced here because the analyses described in this report were conducted prior to the 1998 edition.[43] Negative gradients were reduced from the 1994 edition to the 1998 edition. As seen in figure 3-16, the differential measured from the top of the concrete to the midpoint of the beam is significantly smaller than the 1994 AASHTO LRFD negative gradient. However, the shape of the temperature distribution is also quite different. With the measured, more uniform temperature in the deck, the tensile forces in the deck may actually be greater than the 1994 AASHTO LRFD steep gradient. In the initial analyses for the negative secondary continuity effects described in the following section, uncracked section analyses with the 1994 AASHTO LRFD negative gradient indicated that cracking of the deck concrete is likely. In addition, deck cracking occurs from the combined effects of the negative temperature gradient, locked-in heat of hydration strain, shrinkage strain, and a differential strain caused by the difference in the coefficients of thermal expansion of the deck and girder. Therefore, in subsequent analyses, a simplified analytical procedure was developed that included the effects of deck cracking, based on a uniform inelastic contraction strain in the deck concrete.

4.5.2 Composite Steel Bridge Girders

The following section discusses the investigation of secondary continuity forces in composite steel jointless bridges. Positive and negative secondary moments are caused by the restraint to bowing provided by the piers within the continuous bridge. In addition, longitudinal internal restraint stresses (or eigenstresses) are caused by the response of the cross section to nonlinear strain distributions over the depth of the girders. Positive and negative secondary stresses, including stresses caused by secondary moments and

internal restraint (eigenstresses), are investigated separately; the methods of analysis, results of parametric studies, and recommendations regarding each are presented in the following discussion.

4.5.2.1 *Positive Secondary Moments*

Strains within a continuous bridge cross section subjected to a nonlinear temperature gradient are a function of two components: internal restraint strains and continuity strains. Internal restraint strains result from the difference between the unrestrained free temperature strains and the actual final restrained strain profile. The final restrained strain profile is typically assumed to be linear based on one-dimensional beam theory and the Navier-Bernoulli hypothesis that initially plane sections remain plane after bending. The internal restraint that occur because of restraint within the cross section, are shown graphically in figure 4-22. If the nonlinear temperature gradient of figure 4-22(b) is applied to the cross section of figure 4-22(a), and if each individual fiber of the cross section is allowed to move freely, the strain profile of figure 4-22(c) will result. However, the final strain profile is assumed to be linear, as shown in figure 4-22(d). The difference between the free strain profile and the final strain profile, shown by the shaded portion of figure 4-22(e), is the internal restraint strain.

These restraint strains can be calculated for a section without external axial and flexural restraints, from equations developed by M.J.N. Priestley.[55] Priestley's equations for average strain and curvature, as modified for an irregular cross section, consist of the following:

$$\varepsilon_{t_{avg}} = \frac{\int \alpha_y \Delta t_y b_y E_y \, dy}{\int b_y E_y \, dy} \tag{4-25}$$

$$\phi = \frac{\int \alpha_y \Delta t_y b_y E_y \, y \, dy}{\int b_y E_y \, y^2 \, dy} \tag{4-26}$$

where,

$\varepsilon_{t_{avg}}$ = strain at the neutral axis of the cross section caused by the imposed nonlinear temperature variation along the depth and referred to as average strain in the cross section

ϕ = curvature of the cross section caused by the imposed nonlinear temperature variation along the depth

α_y = coefficient of thermal expansion as a function of depth, $\alpha_y = F(y)$

Δt_y = change in temperature of the cross section as a function of depth (the applied thermal gradient), $\Delta t_y = F(y)$

b_y = width of cross section as a function of depth, $b_y = F(y)$

E_y = modulus of elasticity as a function of depth, $E_y = F(y)$

y = distance from neutral axis of cross section.

If the cross section is divided into n discrete subsections, and a transformed cross section is used through application of a modular ratio, the equations simplify to:

$$\varepsilon_{t_{avg}} = \frac{\sum_{i=1}^{n} \alpha_i \Delta t_i A_i}{A_c} \qquad (4\text{-}27)$$

$$\phi = \frac{\sum_{i=1}^{n} \alpha_i \Delta t_i A_i y_i}{I_c} \qquad (4\text{-}28)$$

where,

α_i = coefficient of thermal expansion in subsection i

Δt_i = change in temperature in subsection i

A_i = cross-sectional area of transformed subsection i

y_i = distance from neutral axis of cross section to subsection i

A_c = cross-sectional area of the entire composite transformed section

I_c = moment of inertia of the entire composite transformed section.

The average strain and curvature are shown graphically in figure 4-23. The restraint strains are then calculated as the difference between the final strain profile and the free strain profile, also shown in figure 4-23, through application of the following equation:

$$\varepsilon_{r_y} = \varepsilon_{t_{avg}} + \phi y - \alpha_y \Delta t_y \quad (4\text{-}29)$$

where,

ε_{r_y} = restraint strain as a function of depth

$\varepsilon_{t_{avg}}$ = average strain

ϕ = curvature

y = distance from neutral axis

α_y = coefficient of thermal expansion as a function of depth

Δt_y = change in temperature as a function of depth (the applied thermal gradient).

However, the above calculations assume a cross section without external axial and flexural restraints. For a simple-span bridge, the curvature resulting from the imposed thermal gradient, calculated from either equation 4-26 or 4-28, will result in a bowing of the section along the span. Only the internal restraint strains as discussed previously are present in the cross section because of the imposed nonlinear temperature variation. For a two-span continuous bridge, on the other hand, the same bowing is restrained by the center support. This external restraint gives rise to additional forces acting on the cross section. These additional forces are often referred to as secondary continuity forces because they result from the continuous nature of the structure.

The magnitude and distribution of the secondary continuity forces, and the corresponding continuity strains, are a function of the bridge cross section and the number and relative length of each span comprising the bridge. For example, the two-span bridge shown in figure 48-24(a) is subjected to a positive thermal gradient. The interior redundant support is removed, and the girder is allowed to bow upward, as shown in figure 4-24(b). The curvature, ϕ, is then calculated from either equation 4-26 or 4-28, and the corresponding deflection, δ, is calculated from the second moment area theorem as $\phi L^2/8$, where L is equal to the total length of the bridge, or a+b. To restore the interior support, a force, P, must be applied at the location of the previously removed redundant support, which will result in a deflection equal and opposite to that caused by the initial bowing, as shown in figure 4-24(c). The magnitude of this force can be calculated by setting the deflection for a concentrated load at midspan of a simple-span beam equal to the curvature deflection, δ, or $PL^3/48E_c I_c = \phi L^2/8$. Solving for P yields a value of $6E_c I_c \phi/L$, where E_c and I_c are the modulus of elasticity and moment of inertia, respectively, of the composite

transformed section. The corresponding midspan moment (moment at the center support) is then equal to PL/4 or ($6E_c I_c \phi/L$) L/4, which simplifies to 1.5 $E_c I_c \phi$, and the complete secondary continuity moment diagram is as shown in figure 4-24(d).

The same approach can be used to derive secondary continuity moments for any span and support condition combination. The term $E_c I_c \phi$ is often referred to as the restraint moment, M_r, since it is the result of the internal cross-section restraint of the section when subjected to a nonlinear thermal gradient. Various span combinations will result in secondary continuity moments ranging from a minimum of 1.0 to a maximum of 1.5 times this restraint moment. By the principle of superposition, the total thermal strains are then the combination of the internal restraint strains, as calculated from equations 4-25 through 4-29, and the continuity strains, as calculated from the one-dimensional beam theory for the continuity moments resulting from the specific support conditions of the bridge in question. Thermal stresses are then calculated directly from the thermal strains.

A parametric study of composite steel girders was performed to assess the impact of the positive diurnal component of environmental thermal loading, which occurs primarily in the form of a nonlinear temperature gradient. Beam sections used for the analyses were selected, in part, based on *Standard Plans for Highway Bridges, Volume IV(A)*.[48] Sections were selected based on the composite rolled steel beam drawings, W36x135 through W36x230, and on the composite welded steel girder drawings, FHWA 1 through FHWA 4. The plans were modified, where required, to conform with typical jointless bridge details and layouts and to include the variety and range of the parameters studied. In addition, two sections, T1 and T2, used in a previous study of integral abutment bridges were used in this study. The analyses encompassed a broad range of beam cross sections, beam spacings, span lengths, number of spans, and concrete deck thicknesses. The parameters are listed in table 4-8. The analyses were based on an uncracked concrete deck and a steel beam section. The assumption of an uncracked concrete deck represents an upperbound on the response to the thermal gradients. Furthermore, a positive thermal gradient will tend to close existing cracks and will result in primarily uncracked behavior. This fact was apparent during live load application tests on the test bridges, as described in section 3.3. Tests during periods of high solar radiation (sunny days) displayed load-deflection behavior consistent with an uncracked deck cross section, while tests during periods of low solar radiation (cloudy days) displayed load-deflection behavior consistent with a partially cracked deck section.

Analyses were completed to examine the total stress state of a bridge subjected to gravity, thermal, and shrinkage loading. The critical stress was determined to be compressive stress in the deck at midspan of the center span for a three-span bridge. Concrete deck thickness was designed based on girder spacing. For all of the various combinations of decks and girders, span lengths were determined so that steel girder stresses would be at AASHTO's allowable stress limits for the combination of dead load plus live load. The deck stresses were then calculated from the corresponding live load. The steel girder was assumed to have a yield strength of 345 MPa (50,000 lbf/inch^2), which represented an upperbound for the determination of the deck's compressive stress under service live load. Again, calculated stresses were compared to allowable values because thermal strains are primarily a serviceability issue.

Thermal gradient stresses were determined from combined internal restraint strains and continuity moments for the positive 1998 AASHTO LRFD thermal gradients.[43] In addition, restraint stresses from overall thermal expansion of the bridge were included. The results from the bounding expansion analyses discussed in section 4.4.3 formed the basis for the restraint stresses resulting from the annual temperature change. Although the conditions of maximum longitudinal expansion and maximum positive thermal gradient are not coincident, the difference is not significant and it will represent an absolute upperbound for thermal stresses. Also, a minimum deck shrinkage of 90 millionths was included based on observations of the study's test girders.

Table 4-9 contains the results of the parametric study. Deck compressive stresses are listed for live load, thermal plus shrinkage gradient, and thermal longitudinal restraint, with the total stress value given in the last column. This total value was compared to the AASHTO allowable concrete compressive strength, including the 25 percent increase when including thermal and shrinkage effects with gravity loading. A concrete compressive strength of 28 MPa (4,000 lbf/inch^2) was assumed for the deck as a reasonable lowerbound and results in a maximum allowable stress of 14 MPa (2,000 lbf/inch^2) for the load combination considered. For all combinations of parameters studied, the total stress state is less than the maximum allowable AASHTO value. Therefore, the results of this parametric study indicate that explicit calculations to consider positive secondary moments and associated eigenstresses in composite continuous steel bridges are unnecessary.

4.5.2.2 *Negative Secondary Moments*

As was done for positive secondary moments, a parametric study of composite steel members was completed to assess the impact of the negative diurnal component of environmental thermal loading, which occurs primarily in the form of a nonlinear temperature gradient. Cross sections identical to those used in the parameter study of positive secondary moment were investigated for this study of negative secondary moments. As such, the analyses encompassed a broad range of beam cross sections, beam spacings, span lengths, number of spans, and concrete deck thicknesses. Restraint and continuity strains were calculated as previously discussed in section 4.5.2.1. The continuity moment diagrams were calculated for two-, three-, four-, and multispan bridge layouts. Beyond four spans, the continuity moment diagrams do not vary appreciably.

Initial analyses were based on an uncracked /concrete deck and steel beam section. The assumption of an uncracked concrete deck represents an upperbound for the response to thermal gradients. The results of these initial parametric analyses for negative 1994 AASHTO LRFD thermal gradients,[1] combined with a minimum of 90 millionths of uniform deck shrinkage, indicated that deck cracking was likely. For all conditions investigated, the deck stress exceeds the modulus of rupture for concrete with a compressive strength of 28 MPa (4,000 lbf/inch^2), with values ranging from 0.18 to 1.60 MPa (26 to 232 lbf/inch^2) above the AASHTO recommended value of 3.27 MPa (474 lbf/inch^2).[16] Furthermore, the analyses included only 90 millionths of deck shrinkage, which represents a lowerbound. In addition, other factors that were not included in the above analyses but that will significantly increase deck and beam stresses, include the heat of hydration of the deck and the variation of the coefficients of thermal expansion between the deck and the beam.

Cracking of the concrete deck is highly probable when all of the factors that contribute to negative secondary moments are included in the analysis. This fact is evident in the decks of numerous composite steel bridges, including this study's test bridge (described in section 3.3), and is well documented in NCHRP's Report 380, *Transverse Cracking in Newly Constructed Bridge Decks*[57] as well as in other research studies on deck cracking. Therefore, two critical load conditions are analyzed. The first corresponds to the beam stress, with the deck contracted relative to the beam to a peak contraction strain immediately prior to deck cracking. This condition represents a worst-case scenario for the uncracked section, which apparently most composite steel bridges experience at some stage during the life of the bridge. The critical stress resulting from this condition is in

the bottom flange of the steel girder at the pier of a two-span continuous structure. Equations were developed to calculate the corresponding girder stress at the point immediately prior to deck cracking, regardless of the cause. This approach eliminates the uncertainty inherent in many of the factors that contribute to negative secondary moments. The second critical load condition considers adding live load to the secondary effects after deck cracking.

In addition to thermal gradient stresses, restraint stresses from overall thermal expansion of the bridge were added to both load conditions. The results from the bounding expansion analyses discussed in section 4.4.3 formed the basis for the restraint stresses resulting from the annual temperature change. The conditions of maximum longitudinal expansion and maximum negative thermal gradient are not coincident; therefore, there was a study completed on the temperature gradient and longitudinal expansion data from the test bridges to ascertain a reasonable combination of these effects. Based on this study, it was determined that approximately two-thirds of the maximum expansion could occur at the time of maximum negative gradient.

For the first condition corresponding to the negative secondary effects immediately prior to deck cracking, deck and beam stresses can be calculated for the condition of a uniform inelastic strain in the deck, from equations developed by D.E. Branson.[58] The equations are applicable to a simply supported member and include the eigenstress component. Referred to as the composite section method, the equations consist of the following:

$$f_c = - \left[\frac{Q}{A} + \frac{Qe}{S'_c} \right] \frac{1}{n} + E_c \varepsilon_f \tag{4-30}$$

$$f_s = - \frac{Q}{A'} + \frac{Qe}{S'_s} \tag{4-31}$$

where,

f_c = stress in the top of the deck

f_s = stress in the bottom of the beam

Q = $E_c A_{deck} \varepsilon_f$

E_c = deck modulus of elasticity

A_{deck} = cross-sectional area of the deck

ε_f = free strain in the deck caused by the negative thermal gradient, shrinkage, heat of hydration, etc.

n = E_s/E_c, modular ratio

E_s = girder modulus of elasticity

A' = composite cross-sectional area with deck transformed to an equivalent steel area

S'_c = composite section modulus to top of deck with deck transformed to an equivalent steel area

S'_s = composite section modulus to bottom of beam with deck transformed to an equivalent steel area

e = distance from deck centroid to composite centroid.

Equations 4-30 and 4-31 can be modified to calculate the girder stress when the deck just reaches the cracking stress by dividing equation 4-30 by E_c to obtain the final deck strain, setting this value equal to the cracking strain, and solving for ε_f as:

$$\varepsilon_f = \frac{\varepsilon_{cr}}{\left[1 - \frac{A_{deck}}{nA'} - \frac{A_{deck}e}{nS'_c}\right]} \quad (4\text{-}32)$$

where,

ε_{cr} = cracking strain in the deck, equal to 0.62 $\sqrt{f'_c}$ / E_c, MPa (7.5 $\sqrt{f'_c}$ / E_c, lbf/inch^2).

The girder stress at cracking of the deck is then calculated from equation 4-31.

However, equations 4-31 and 4-32 need to be modified to include the continuity effects for multispan conditions. The calculation of the continuity effects as a function of the bridge cross section and the number and relative length of each span comprising the bridge is discussed in detail in section 4.5.2.1. Applying those relationships to equations 4-31 and 4-32 by modifying the restraint moment term to include a continuity moment term results in the following equations:

$$\varepsilon_f = \frac{\varepsilon_{cr}}{\left[1 - \frac{A_{deck}}{nA'} + m\left(\frac{A_{deck}e}{nS'_c}\right)\right]} \quad (4\text{-}33)$$

$$f_s = - \frac{E_c A_{deck} \varepsilon_f}{A'} - m\left(\frac{E_c A_{deck} \varepsilon_f e}{S'_s}\right) \quad (4\text{-}34)$$

where,

m = support condition multiplier, equal to 0.5 for a two-span girder, 0.2 for a three-span girder, 0.27 at the first interior support of a multispan girder, and 0.0 at all other interior supports of a multispan girder.

All other variables are as previously defined.

Stresses at the bottom of the beam over the pier for a two-span continuous structure calculated from equations 4-33 and 4-34, combined with applicable dead load stresses, are shown in tables 4-10 and 4-11 for yield strengths of 248 and 345 MPa (36,000 and 50,000 lbf/inch^2), respectively. To include dead load stresses, span lengths were determined such that steel beam stresses were at the maximum allowable for dead plus live load. A 3.7-m (12-ft) beam spacing was selected as being representative of the parametric analysis results. The stresses were subsequently compared to AASHTO's allowable steel stress, including the 25 percent increase when including secondary effects with gravity loading. For the Grade A36 beams (table 4-10), stresses range from 113 percent to 152 percent of allowable, with three of the five members exceeding the 125 percent limit. For the Grade A572 beams (table 4-11), stresses range from 96 percent to 123 percent of allowable, with all five members below the 125 percent limit.

The second critical load condition for negative secondary effects includes adding live load. Since the above stresses are calculated based on uncracked sections for secondary effects that take the deck just to the cracking strain, adding live load will initiate cracking in the deck and a subsequent redistribution of forces, particularly since cracking will relieve a significant portion of the deck temperature and shrinkage inelastic strains. Therefore, relationships similar to equations 4-33 and 4-34 were derived to calculate the steel girder stress resulting from the secondary effects after cracking has occurred in a portion of the deck. The analyses accounting for live load and secondary effects with deck cracking are described in chapter 8 and appendix D of the analytical report.[15] Appendix D of the analytical report is also included as appendix D of this summary. The results were combined with previous analyses to consider the following load combinations (LC):

$$\text{LC 1:} \quad f_S = f_{S_{DL}} + f_{S_{LL}} \quad (4\text{-}35)$$

$$\text{LC 2:}\quad f_S = f_{S_{DL}} + f_{S_{gradient}} + f_{S_{longitudinal}} \tag{4-36}$$

$$\text{LC 3:}\quad f_S = f_{S_{DL}} + f'_{S\,LL} + f'_{S\,gradient} + f_{S_{longitudinal}} \tag{4-37}$$

where,

f_S = steel girder stress

$f_{S_{DL}}$ = steel girder stress caused by dead load from an elastic gross-section analysis

$f_{S_{LL}}$ = steel girder stress caused by live load from an elastic gross-section analysis

$f_{S_{gradient}}$ = steel girder stress prior to deck cracking under secondary effects sufficient to induce deck cracking, calculated from equation 4-34

$f_{S_{longitudinal}}$ = steel girder stress caused by the restraint of longitudinal expansion, equal to the external axial restraint force divided by the girder and deck transformed cross-sectional area, with a value of 0.67 of the full restraint force when combined with maximum gradient effects

$f'_{S\,LL}$ = steel girder stress caused by live load from an analysis that accounts for deck cracking

$f'_{S\,gradient}$ = steel girder stress after deck cracking under secondary effects sufficient to induce deck cracking.

Analyses for LC 1 and LC 2 are based on an uncracked section, while analyses for LC 3 are based on a cracked section.

LC 1 is the primary combination for the design of the composite cross section and is compared to 100 percent of the AASHTO allowable design stress. LC 2 and LC 3 include secondary effects and are compared to 125 percent of the AASHTO allowable design stress.

The results of all previous parametric studies were combined in accordance with equations 4-36 and 4-37. Table 4-12 presents the results as the percentage of calculated steel girder stress to allowable steel girder stress. As previously discussed, all of the actual bridge sections were designed such that LC 1 would result in a steel girder stress equal to 100 percent of the allowable design value. The results indicate that Grade A36

steel girders reach the 125 percent limit at smaller spacings than the Grade A572 steel girders. However, there are significant girder spacings for which explicit calculations to consider negative secondary moments and associated eigenstresses are not necessary in composite steel sections. The cutoffs are approximately 2.1 m (7 ft) for the Grade A36 steel girders and 2.7 m (9 ft) for the Grade A572 steel girders.

Calculations for LC 3, which account for deck cracking and redistribution of secondary and live load effects, can be complex. However, the calculations can be simplified without a noticeable loss of accuracy by modifying LC 3 (equation 4-37) as follows:

$$f_S = f_{S_{DL}} + \alpha\,(f_{S_{LL}}) + \beta\,(f_{S_{gradient}}) + f_{S_{longitudinal}} \qquad (4\text{-}38)$$

where $f_{S_{LL}}$ and $f_{S_{gradient}}$ are calculated using uncracked section analyses.

The constants α and β are factors that account for the redistribution of stresses caused by cracking. Parametric studies were carried out to examine the values of α and β for a range of beam sizes and spacings. As described in chapter 8 of the analytical report, the parametric studies indicated that values of 0.80 for α and 0.60 for β result in a minimal loss of accuracy.[15] Therefore, the load combinations to be considered are now defined as follows:

$$\text{LC 1:}\quad f_S = f_{S_{DL}} + f_{S_{LL}} \qquad (4\text{-}39)$$

$$\text{LC 2:}\quad f_S = f_{S_{DL}} + f_{S_{gradient}} + f_{S_{longitudinal}} \qquad (4\text{-}40)$$

$$\text{LC 3:}\quad f_S = f_{S_{DL}} + 0.8\,f_{S_{LL}} + 0.6\,f_{S_{gradient}} + f_{S_{longitudinal}} \qquad (4\text{-}41)$$

where all variables are as previously defined. This simplification results in the need for only elastic gross-section analyses.

4.5.3 Prestressed Concrete Bridge Beams

The following section discusses the investigation of secondary continuity forces in PS/C jointless bridges. Factors such as positive diurnal temperature gradients, beam creep, and variation in the coefficients of thermal expansion between the beam and the deck result in positive secondary moments and longitudinal eigenstresses. Conversely, negative diurnal

temperature gradients, deck shrinkage, and the heat of hydration result in negative secondary moments and longitudinal eigenstresses. These positive and negative secondary moments are caused by the restraint to bowing provided by the piers in continuous bridges with moment connections at the piers. The longitudinal eigenstresses, however, are caused by internal restraint of the cross section in response to nonlinear strain distributions. Positive and negative secondary moment responses, including eigenstresses, are investigated separately, followed by presentation of the methods of analysis, the results of parametric and sensitivity studies, and recommendations regarding each.

4.5.3.1 *Positive Secondary Moments*

Positive secondary moments are affected by beam creep and differential shrinkage between the beam and the deck, by positive diurnal temperature gradients, by variation in the coefficients of thermal expansion between the beam and the deck, and by deck heat of hydration. As described in chapter 8 of the analytical report, an analytical approach was developed to include the effects of the following factors:[15]

1. Creep and shrinkage of the girder and deck.
2. Temperature distribution through the cross section, including diurnal effects, deck heat of hydration, and variation in the coefficients of thermal expansion between the girder and deck.
3. Potential for concrete cracking and yielding of the positive-moment reinforcement in the diaphragm at the pier.

The results of the analyses and the comparison with data from the test girder in this study indicate that a reasonable estimate of continuity moments and the resulting reactions can be obtained using the procedure outlined in chapter 8 of the analytical report.[15] However, the results also indicate that accurate creep and shrinkage parameters, along with the heat of hydration effects, are necessary to reliably predict the actual continuity moments and the associated reactions. The analytical results also demonstrated the effects of cracking in relieving continuity moments and reactions; however, in doing so, the cracking also induced high strains in the positive-moment continuity connection (over the pier).

The analytical method was used to study the sensitivity to various factors of positive continuity moments in PS/C jointless bridges. An AASHTO Type IV cross section and Precast/Prestressed Concrete Institute (PCI) BT-72 cross section were selected for the

study for two reasons. The first reason is that these sections had been investigated extensively by Oesterle, et al., in NCHRP Report 322..[49] The second reason is that they represent a relatively heavy cross section, the AASHTO Type IV, and a relatively light cross section, the PCI BT-72.

Table 4-13 lists the variables considered in the sensitivity study. Ultimate creep coefficients of 1.625 and 3.25 were used to match the values used in the NCHRP study. The lower coefficient (1.625) is similar to the value used in the analysis of the test bridge in this study (1.78). Ultimate shrinkage strains of 100 millionths and 600 millionths were used, with the lower value reflecting the effect of the environment on shrinkage, based on observations of component testing in this study, and the higher value reflecting standard laboratory test specimens, based on the NCHRP study. A beam age of 17 days was assumed at the time of deck casting. This assumed beam age represents a condition with continuity established with a relatively early-age beam, the most critical condition for development of positive continuity moments. Positive-moment continuity reinforcement was varied in the range of 129 to 4,645 mm^2 (0.2 to 7.2 $inches^2$), identical to the NCHRP study. An initial temperature difference of 7.8 °C (14 °F) was assumed between the deck and the beam because of the heat of hydration. This value was based on this study's test bridge results. Temperature gradients were based on the 1998 AASHTO LRFD specifications,[43] and gravity loading consisted of a 1.44-kN/m^2 (30 lbf/ft^2) superimposed dead load.

A series of analyses were completed on the PCI BT-72 cross section to examine the effects of varying the amount of positive-moment continuity reinforcement over the pier. The baseline structure consisted of four equal-length spans of 39.6 m (130 ft), each with a 2.4-m (8-ft) beam spacing. Upperbound concrete properties were assumed, with an ultimate creep coefficient of 3.25 and an ultimate shrinkage strain of 600 millionths.

Figure 4-25 contains the results of the analyses with four different amounts of positive-moment continuity reinforcement (129, 774, 2,323, and 4,645 mm^2 [0.2, 1.2, 3.6, and 7.2 $inches^2$]) superimposed on the results of an analysis that does not incorporate concrete cracking in the model. The results indicate two important findings: (1) cracking reduces the magnitude of the restraint moment, and (2) the amount of reinforcement significantly affects the response to positive moment. For instance, above 2,323 mm^2 (3.6 $inches^2$), the behavior is essentially unchanged by adding extra steel reinforcement.. However, at some level below 2,323 mm^2 (3.6 $inches^2$), the reinforcement will yield and limit the restraint moment to the yield moment for that amount of reinforcement, as

shown by the plots for 129 and 774 mm^2 (0.2 and 1.2 $inches^2$) of positive-moment continuity reinforcement. For the lowest reinforcement amount (129 mm^2), the yield moment is less than the cracking moment. As a result, the positive continuity moment drops off after cracking occurs. Because the behavior is deformation-controlled, the sudden drop-off in moment capacity does not lead to a brittle failure mode. Similar results were obtained for the AASHTO Type IV cross section with a 2.4-m (8-ft) beam spacing and four equal span lengths of 30.5 m (100 ft) each.

Observations of the test bridge, as described in section 3.4, indicated that positive continuity moments are significantly affected not only by creep and shrinkage in the girder and deck, but also by temperature gradients caused by daily and seasonal temperature changes and by residual stresses resulting from the heat of hydration in the deck. Also of note is the low level of shrinkage strain actually observed because of the environmental effects. Data from the test girder demonstrated that all of these factors can be additive and that the positive-moment reinforcement provided in the diaphragm reached and most likely exceeded the yield stress under the combination. As such, the following analyses were performed to illustrate the relative influence of each factor on the positive continuity moments for PS/C jointless bridges. The AASHTO Type IV and PCI BT-72 cross sections were analyzed for two ultimate shrinkage values—100 millionths to represent the environmental effects and 600 millionths to represent standard laboratory test specimens—and for a creep coefficient value of 1.625. As previously described, the baseline structure consisted of four equal-length spans of 30.5 m and 39.6 m (100 ft and 130 ft) for the AASHTO Type IV and PCI BT-72 cross sections, respectively. Both bridges had a 2.4-m (8-ft) beam spacing. Positive-moment continuity reinforcement was selected to provide a yield moment capacity equal to 25 percent of the cracking moment at midspan, resulting in a steel area of 400 mm^2, two D16 bars (0.62 $inch^2$, two No. 5 bars) for both sections.

The positive continuity moments resulting from the AASHTO LRFD positive temperature gradient and the deck heat of hydration calculated over the center pier of the four-span bridges were determined based on an elastic analysis with uncracked sections. The results are shown in table 4-14 for the AASHTO Type IV cross section.

Table 4-14 also contains the peak creep and shrinkage continuity moments, the superimposed dead load moment over the pier, the cracking moments based on a modulus of rupture equal to $0.33\sqrt{f'_c}$, MPa ($4\sqrt{f'_c}$, $lbf/inch^2$) and to $0.62\sqrt{f'_c}$, MPa ($7.5\sqrt{f'_c}$,

lbf/inch^2), and the positive continuity reinforcement yield moment, M_y. The data contained in the tables indicate the following:

1. Temperature gradient moments are large relative to moments caused by other factors (generally larger than moments caused by creep and shrinkage).
2. Moments caused by the heat of hydration are on the same order of magnitude as those caused by creep and shrinkage.
3. In all cases, the total positive continuity moment is greater than the initial cracking moment and the yield moment. Therefore, the moments based on an elastic uncracked section analysis could not be fully developed and would be limited to the yield moment value.

The same general trend was evident with the PCI BT-72 sections.

Connections are made in the diaphragm and deck concrete for this type of construction so that the beams, which are simply supported for dead load, are made continuous for live load. Structural capacity for live load can be gained, particularly with the development of negative moments over the piers. However, by providing a positive-moment connection, the secondary effects will probably cause positive secondary moments and cracking at the bottom of the diaphragms. The magnitude of the positive moment that can develop depends on the amount of positive reinforcement provided and the adequacy of the anchorage of this reinforcement. With application of live load, the positive-moment crack in the bottom of the diaphragm must essentially close before any negative moment can develop over the pier. In other words, the beams will respond as simply supported members under live load until the positive secondary moment is relieved by rotations of the beam ends. If the positive secondary moment is large enough and the positive-moment connection capacity is strong enough, some positive secondary moment may still be present under full live load. This remaining positive secondary moment is superimposed on the positive live load moments with the beams acting as simply supported for live load. In other words, by providing a positive-moment connection at the piers, secondary moments may be induced such that the stress in the bottom of the prestressed beams near midspan, caused by the combined dead load, live load, and secondary effects, may be more tensile than if the spans were left simply supported. This was the case for the study's test bridge as discussed in section 3.4 of this volume.

The live load tests on the test girder illustrate the fact there were no benefits realized (as far as maximum positive service-load moments are concerned) by making the beam

continuous over the pier. Secondary effects from creep, shrinkage, thermal effects, etc., generated additional positive moments in the beam to overcome the benefit from live load continuity. In general, the typically early age of the PS/C at the time of casting of the deck slab ensures that beam creep will dominate the long-term behavior. This, combined with the positive temperature gradient effects, introduces significant positive secondary moments into the beam when enough positive-moment reinforcement is added to the pier diaphragm for continuity.

The previous sensitivity study and the comparisons with the test data revealed that positive continuity moments can be significant and need to be considered in the design of PS/C jointless bridges. However, creep and shrinkage parameters can vary significantly, as found in the data from this study's component test, which revealed the phenomenon of the environment's effects on shrinkage. Diurnal temperature gradients vary significantly throughout the year and are directly affected by the weather. The deck heat of hydration is difficult to accurately quantify prior to construction and is noticeably affected by the weather conditions at the time of casting and by the construction sequence and curing operations. Considerable variation exists in the determination of the coefficients of thermal expansion of the deck and girder concrete. To quantify the role of cracking in relieving part of the secondary moment requires complex calculations. In addition, the age of the beams when the deck and diaphragms are cast is usually unknown unless specific steps are taken to ensure that the beams are at a minimum age prior to establishing continuity. (Note that if the beams are older when the deck and diaphragm are cast, the probability of negative-moment deck cracking over the piers increases. This may have a more adverse effect on the durability of the bridge than does positive-moment cracking in the bottom of the diaphragms.) Therefore, there is a lot of uncertainty about both the magnitude of the various effects contributing to positive-moment continuity and the critical combinations of these effects.

Considering the uncertainty of the factors affecting the potential for positive secondary moment, establishing a simplified procedure to account for these effects was a prime objective. To accomplish this objective, two simplified design philosophies are proposed. The first involves eliminating the positive-moment connections in the bottom of the diaphragm over the piers. This essentially eliminates positive secondary moments, and the girders can be designed as simply supported for service-level stresses from dead and live loads. For ultimate strength design, as long as sufficient reinforcement is provided in the deck and a concrete diaphragm is cast between the ends of the girders so that compression exists when the crack (or control joint) closes, there will be a negative-

moment capacity for extreme loads. This approach eliminates the uncertainty of positive-moment service-level stresses in PS/C girders, but provides a jointless deck and continuous structure for strength design. Consideration of details that allow rotation to occur at the ends of the girders and that connect the piers to the superstructure are discussed below.

The second design philosophy for simplifying procedures to account for positive-moment effects is to design the positive-moment connection to yield prior to developing stresses that could crack the prestressed beams. With this philosophy, the positive-moment connection acts as a fuse to eliminate the uncertainty of the positive secondary moment effects, by designing an upperbound for these effects.

Three design options based on the two philosophies are described in detail in section 5.5 of this volume. A fourth, more complex option is also presented, one based on the calculation of an upperbound estimate of secondary moments.

Concerning the design options for positive secondary moments, two other considerations should be given to the positive-moment connection design. The first relates to the potential for positive cracking moment within the diaphragm connection, even without any positive-moment rebar to produce significant positive secondary moments. Even considering a reduced modulus of rupture of $0.33\sqrt{f'_c}$, MPa ($4.0\sqrt{f'_c}$, lbf/inch^2) for the cold joint at the interface of the girder and diaphragm, the increase in positive moment near the midspan may produce stresses exceeding AASHTO's 125 percent of allowable stress.

Therefore, debonding the lower region of at least one of the two girder ends of the adjacent girders might be considered at the pier diaphragms, to eliminate the cracking moment and to allow the girder end to slide with respect to the diaphragm concrete as the girder end rotates because of creep, thermal gradient effects, and live load. Figure 4-26 illustrates a conceptual approach to accomplish the debonding. However, to our knowledge, this approach is untried, and no actual problems of cracking in this type of bridge have been attributed to the positive cracking moment restraint without positive-moment reinforcement being present.

When positive-moment reinforcement is provided in the bottom of the diaphragms, debonding of the lower region of the diaphragm from one of the girders is not required. However, if debonding is not used, it is recommended that the cracking moment (f_r =

$0.33\sqrt{f'_c}$, MPa [$4\sqrt{f'_c}$, lbf/inch^2]) be used as a minimum secondary moment at the diaphragm when checking the stresses at midspan for 125 percent of allowable stress.

The other design consideration for the positive-moment connection is that the diaphragm is required to transfer the forces generated at the top of the pier caps, resulting from thermal movement, into the superstructure. Typically, semi-integral pier caps are used with a pinned connection at the bottom of the pier diaphragms. Shear (and moment for integral pier caps) needs to be transferred between the top of the pier and the superstructure to tie the pier to the bridge. Therefore, as illustrated in figure 4-26, it is advisable that one of the two girder ends be connected to the diaphragm to transfer this force from the pier cap. The positive-moment connection has to be designed for this pier force. Also as illustrated in figure 4-26, with both end girders tied to the abutments, one of the end girders will have positive-moment connection at both ends. However, the maximum positive restraint moment developed in the end girder is limited to the forces developed in the abutment pile during peak contraction.

When positive-moment reinforcement is used at the diaphragms, the girder section must also be checked near the ends where prestressing is decreased. The reinforcement used to develop the positive-moment connection should be extended sufficiently into the prestressed girders to ensure that the positive restraint moment will not cause excessive cracking in the end regions.

4.5.3.2 *Negative Secondary Moments*

As was done for positive secondary moments, the PS/C girders were studied to assess the impact of the negative diurnal component of environmental thermal loading, which occurs primarily in the form of a nonlinear temperature gradient. The same sections used for the positive secondary moment study, the AASHTO Type IV and the PCI BT-72, were investigated for negative secondary moment study.

Restraint and continuity strains were calculated, as previously discussed in section 4.5.2.1. The continuity moment diagrams were calculated for two-, three-, four-, and multispan bridge layouts. Beyond four spans, the continuity moment diagrams do not vary appreciably. The analyses were initially based on an uncracked concrete deck and concrete girder section. The assumption of an uncracked concrete deck represents an upperbound on the response to thermal gradients.

The results of these initial sensitivity studies for the negative 1994 AASHTO LRFD thermal gradients,[(1)] combined with a minimum of 90 millionths of uniform deck

shrinkage, indicated that deck cracking was likely. For all conditions investigated, the deck stress exceeds the modulus of rupture for concrete with a compressive strength of 28 MPa (4,000 lbf/inch^2), with values ranging from 0.96 to 2.78 MPa (139 to 403 lbf/inch^2) above the 1992 AASHTO recommended value of 3.27 MPa (474 lbf/inch^2).[59] Furthermore, the analyses included only 90 millionths of deck shrinkage, which represents a lowerbound. In addition, other factors not used in the above analyses, but which could significantly increase deck stresses, include deck heat of hydration, variation in the coefficients of thermal expansion between the deck and the girder, and later-age continuity (i.e., casting the deck and diaphragms when the girders are relatively old and a significant portion of creep deformation has already occurred).

When all of the factors that contribute to negative secondary moments are included in the analysis, it is reasonably likely that the concrete deck will crack. This fact is well documented in Portland Cement Association (PCA) Bulletin D46, "Precast-Prestressed Concrete Bridges 5, Creep and Shrinkage Studies,"[60] and NCHRP Report 380, *Transverse Cracking in Newly Constructed Bridge Decks*.[57] Consequently, the investigation proceeded into examining the stress in the deck reinforcement over the piers after cracking has occurred in the deck, regardless of its cause. An analytical approach similar to that applied to steel beams was used to derive equations relating stress in deck reinforcement to the inelastic strain that is sufficient to initiate cracking in the concrete deck. These analyses are described in chapter 8 and appendix D of the analytical report.[15] Appendix D of the analytical report is also included as appendix D of this summary.

The maximum total stress in the deck reinforcement will occur under design live load plus negative secondary continuity effects with a cracked deck over the supports. Table 4-15 combines the results of the live load study with those from the secondary continuity study. Deck reinforcement stresses are presented for the live load conditions of gross-section and cracked-section analyses and for secondary effects. The maximum total stress in the deck reinforcement is based on combining the cracked-section live load analysis with the secondary effects. The data indicate that analyses including secondary continuity effects result in deck reinforcement stresses that are approximately equal to those determined from an elastic, gross-section (uncracked) analysis for live load alone. In other words, relief of live load moment caused by deck cracking approximately equals the maximum increase in negative moment from the secondary effects. Therefore, the negative-moment deck reinforcement can be determined from an elastic, gross-section analysis for live load, and the effects of secondary continuity moments can be ignored.

4.5.4 Reinforced Concrete Bridge Girders

A parametric study of secondary continuity moments in reinforced concrete bridge beams was not carried out. The reason is that, as long as minimum reinforcement ratios are provided for crack control to ensure flexural behavior after cracking, and as long as maximum reinforcement limits are observed to ensure ductile behavior, service-level secondary stresses would not significantly affect the strength or serviceability of the bridge superstructure. In addition, reinforced concrete beams will respond similarly to PS/C girders, but with fewer sources of differential strain between the deck and girders. Primarily, the differential creep in prestressed girders that may contribute to significant positive secondary moments is not present in reinforced concrete girders. Analyses of the restraint of longitudinal movement and the annual temperature change for the reinforced concrete bridges considered in the study and described in section 4.4.3 included secondary moments resulting from relative shrinkage within the cross section. These analyses indicated that the secondary moments are relatively minor. Also, analyses of PS/C girders for negative secondary effects did not indicate a potential for excessive stresses.

Analyses of reinforced concrete bridges included in the study and described in section 4.4.3 indicated that the positive moments caused by abutment restraint to contraction were more significant than the secondary continuity moments. The cracking observed in the bottom flange of Bridge 10, as described in section 3.5 of this volume, demonstrates the effects of the restraint of contraction. Positive-moment cracking near the end integral stub abutment was the most extensive positive-moment cracking observed on this reinforced concrete bridge.

Based on the above observations, it is recommended that reinforced concrete bridge girders be designed for gross-section analyses for dead and live load combined with abutment and pier restraint forces, and that secondary continuity moments can be ignored as long as code requirements for minimum and maximum reinforcement ratios are applied.

4.5.5 Skewed Bridges

The analyses of the secondary continuity effects, as discussed in sections 4.5.2 and 4.5.3, were made for individual beams simulating a response in the longitudinal direction of a right bridge. A skewed bridge with a skew angle of less than 20° is usually considered to behave essentially as a right bridge and, for skews greater than 20°, longitudinal moments caused by live load typically decrease as compared to an equivalent-span right

bridge. However, live load shears for beams in the region of the obtuse corner typically increase.[61] AASHTO LRFD provides correction factors to account for a reduction in live load moment with skew angles greater than 30° and for an increase in shear in the exterior girder near the obtuse corner with skewed bridges with skew angles of 0 to 60°.[43] These factors, however, are based on the effects of skew on lateral distribution of concentrated wheel loads. For equivalent ratios of transverse to longitudinal stiffness, a skewed bridge will redistribute concentrated loads to the beams in a more efficient manner for bending, but will tend to concentrate the reactions in the obtuse corners of the superstructure. It was not clear how this behavior applies to secondary effects such as positive thermal gradient effects that involve the entire deck expanding with respect to all of the beams. Therefore, to investigate the effects of skew on secondary continuity, three-dimensional finite element analyses were carried out for a four-span PS/C bridge with skew angles varying from 0 to 60°, to demonstrate relative response to positive thermal gradients.

Three-dimensional finite element models were generated for the four-span PS/C I-beam bridge detailed in *Standard Plans for Highway Bridges, Vol. IV (A)*.[48] This bridge has four equal spans of 19.5 m (64 ft). Each span has five AASHTO Type III girders with a 227-mm- (9-inch-) thick deck. The beam spacing is 2.67 m (8.75 ft), with a total deck width of 13.0 m (42.58 ft). Cast-in-place diaphragms are included at the piers and at the center of each span. Four linear elastic models were generated using the SAP 2000 computer program, with skew angles of 0°, 20°, 40°, and 60°. Intermediate diaphragms were oriented perpendicular to the stringers. Pier diaphragms are parallel to the piers and abutments. The deck was modeled with triangular-plate elements. The girders and diaphragms were modeled with beam elements. The deck was offset from the beam elements in the vertical direction, equal to the distance between the centers of gravity of the girders and the center of the deck, using rigid links. The deck mesh and beam framing for the bridge model with a skew angle of 20° is shown in figure 4-27. The node at the center of the bridge was constrained for rigid-body translations in the horizontal x-y plane and rotation about the z-axis. Beam and diaphragm nodes were supported in the vertical (z) direction at the piers and abutments. Loading included a uniform temperature increase of 16.7 °C (30 °F) in the deck elements relative to the beam elements.

The resulting deck membrane stresses and axial forces in the beam elements were evaluated for the four bridge models. Figure 4-28 shows the tensile axial forces in the beam elements representing the AASHTO Type III girders,. These axial forces indicate the resultant continuity moment response. The expanded deck is in compression and the

beams are in tension, and the resulting couple related to the eccentricity between the center of the beam and the center of the deck is the continuity moment..

The axial loads in the edge girders and the center girder at the first and center piers are shown in figure 4-28 for reference. However, table 4-16 lists the axial loads for all girders at the midspans and piers. Review of the data in figure 4-28 and table 4-16 indicates the following:

1. Comparison of the *average* beam tensile forces at the center of the exterior and interior spans indicates that the total secondary continuity moment resulting from the differential strain between the deck and the beam is not significantly affected by skew angle (table 4-16). The peak deck stresses and average girder axial forces remain relatively constant among the four analyses. However, there is a redistribution of force from the spandrel beams to the interior beams that is affected by skew angle. This effect is discussed in item 3 below.

2. Two-dimensional calculations assuming one isolated four-span beam with a 2.67-m- (8.76-ft-) wide concrete slab attached indicate a peak deck compressive stress of 2.06 MPa (299 lbf/inch^2) at the first pier, and a beam tension of 1,126 kN (253 kips) at the center of the second span (which will be additive with the dead and live load stresses). The average beam tension from the three-dimensional finite element analyses ranged from 1,061 kN (239 kips) at $\theta = 0°$ to 958 kN (215 kips) at $\theta = 60°$. The average from the three-dimensional analyses is slightly less than that from the two-dimensional analyses. However, there is a variation across the width of the bridge for the three-dimensional analyses that ranges from approximately 8 percent greater than to 18 percent less than the tension indicated by the two-dimensional analyses.

3. The variation in beam tension at midspan that runs transversely across the bridge is related to the restraint of transverse deck expansion and the resultant bowing by the intermediate diaphragms. This restraint of transverse expansion by the diaphragms adds vertical load to the exterior (spandrel) beams and decreases the load on the interior beams. This transverse redistribution is related to the effective stiffness of the intermediate diaphragms, which decreases with increasing skew angle because the diaphragms, being perpendicular to the beams, become discontinuous transverse beams in skewed bridges. Also, with a right bridge (with $\theta = 0°$), the actual transverse redistribution will be significantly reduced by cracking in the diaphragms.

4. From secondary continuity moment analyses at the first and center piers, two-dimensional analyses indicated beam tensions of 1.260 kN (283 kips) and 990 kN (223 kips) at the first and center piers, respectively. The results in table 4-16 for the three-dimensional analyses indicate that the average beam tension at the pier locations ranged from approximately -5 percent to +12 percent of the values from the two-dimensional analyses, with a general trend toward an increase in the average beam tension with increasing skew angle. However, this increase in beam tension at the piers with increasing skew is a local effect caused by the longitudinal component of force in the pier diaphragms (which are not perpendicular to the girders). This effect does not influence PS/C girder tensile stresses in the midspan region, where they are additive with dead and live load stresses. Also, this effect would not occur in composite steel girders with diaphragm bracing perpendicular to the girders at all locations. Therefore, skew should not influence negative thermal gradient effects in composite steel girders.

5. The variation in tension in the beams at the piers that runs transversely across the bridge is related to the restraint of transverse expansion and the resultant bowing by the intermediate diaphragms. The transverse redistribution noted in item 3 above has the reverse effect for tension in the beam over the piers in that it decreases positive secondary moments in the exterior (spandrel) girder at the piers and increases the positive secondary moments on the interior girders. This transverse redistribution decreases with increasing skew angle and would also decrease significantly with cracking in the intermediate transverse diaphragms because of secondary moments in the diaphragms.

The membrane deck stresses and the axial beam forces in figure 4-28 and table 4-16 indicate that there is no appreciable reduction of secondary continuity moments for increasing skew, whereas there is a reduction in live load moments for increasing skew. Analyses for the secondary continuity moments presented in sections 4.5.2 and 4.5.3 were typically done either by comparing the increase in stress caused by secondary effects to 25 percent of the allowable stress or by comparing the total stress caused by the combined dead, live, and secondary effects to 125 percent of the allowable stress as a measure of the significance of the secondary effects. If reduction factors for live load moment are used to size a beam for a skewed bridge, a lighter girder section will result as compared to a right bridge. With no reduction in secondary effects related to skew, the secondary continuity stresses become a larger portion of the total stress. Therefore, the conclusion presented in section 4.5.2 that explicit calculations for the positive secondary

effects of shrinkage and temperature gradient are not necessary in composite steel beams may not apply to bridges skewed more than 30° and designed using live load moment reduction factors. Separate analyses may be required by the designer. Also, the relative beam spacings for which negative secondary continuity effects become critical for composite steel beams may not apply to skewed bridges where $\theta > 30°$ if moment reduction factors for live load are used, and therefore separate analyses may be required.

The concepts recommended to limit the effects of positive secondary moments in PS/C beams in section 4.5.3 should still be valid. These recommendations include either eliminating positive secondary moments by eliminating the positive-moment connections at the piers, or designing the section to accommodate the potential maximum secondary moment that can be generated by the connection. This is determined either by yielding of the connection or by upperbound analyses of the effects that cause positive secondary moments. The maximum positive secondary moments should be applied to the girders without any reduction for the effects of skew.

Conclusions concerning reinforcement of the deck slab for negative secondary continuity effects and the effects of deck cracking in PS/C girders, however, also require reevaluation for bridges with skews greater than 30° if live load moment reduction factors are used to determine the reinforcement for negative moment over the piers.

Figure 4-29 shows the vertical shear in the beam elements representing the AASHTO Type III girders from the three-dimensional finite element analyses. These shear forces are also listed in table 4-17. Review of the data in figure 4-29 and table 4-17 indicates the following:

1. A comparison of *average* shear forces from table 4-17 indicates that the average vertical beam shears caused by the differential thermal gradient are not significantly affected by the skew angle. The *average* shear forces in the beams near the abutments and piers remain relatively constant or decrease somewhat with large skew angles.

2. Two-dimensional calculations that assumed one isolated four-span beam with a deck-slab width equal to the beam spacing, indicated beam shear forces of 48 kN (10.8 kips) at the abutment and exterior-span side of the first pier, and a beam shear of 10.2 kN (2.3 kips) for the interior spans. The average beam shear from the three-dimensional analysis for the exterior span ranged from approximately +2 percent to -15 percent of the maximum shear of 48 kN from the two-dimensional analysis. However, there is a significant variation across the width of

the bridge for the three-dimensional analyses, which ranges between +160 percent to -200 percent of the 48-kN shear from the two-dimensional analysis.

3. The variation in beam shear that runs transversely across the bridge is related to restraint of the transverse deck expansion and the resultant bowing by intermediate diaphragms. This restraint of the transverse expansion by the diaphragms adds vertical load to the exterior (fascia) girders and decreases the load on the interior girders. This transverse redistribution is related to the effective stiffness of the intermediate diaphragms, which become less effective with increasing skew angle.

4. The most significant redistribution of shear load caused by restraint of the transverse thermal expansion of the deck by the diaphragms occurs in a right bridge. The actual redistribution, however, will be significantly reduced by cracking in the diaphragms.

5. The transverse redistribution of beam shear related to the bowing of the diaphragms tends to decrease as the skew angle increases. Also, the shear in the beam near the acute corner of the deck at the abutment remains large, while the shear in the beam near the obtuse corner of the deck at the abutment decreases as the skew angle increases.

The results in figure 4-29 and table 4-17 indicate that skew has a minor effect on the distribution of beam shear caused by the thermal gradient effects. Factors to increase shear in the exterior girder near the obtuse corner for live load in skewed bridges are not appropriate for shear caused by the thermal gradient. A more significant redistribution of beam shear may occur in right bridges because of the restraint of transverse deck expansion by the intermediate diaphragms. This type of redistribution occurs when continuous intermediate diaphragms are used in simply supported or continuous superstructures with or without integral abutments. Cracking in the reinforced concrete diaphragms may limit the magnitude of the transverse redistribution of shear; however, further parametric studies would be needed to evaluate the significance of this effect.

4.6 CONSTRUCTION SEQUENCE

Continuity in bridge construction gives rise to volume-change restraint stresses related to creep, shrinkage, and temperature, as well as negative moments over supports caused by applied live loads. Improvement in durability and in the other performance characteristics

through controlling the cracking caused by these stresses is therefore a major objective in the design of jointless bridges.

Proposed guidelines for concrete bridge deck materials and construction to control transverse cracking in concrete bridge decks in general are presented in NCHRP Report 380.[57] These guidelines address a number of issues, including the effect of construction practices. Among the construction practices and construction-related issues that affect deck cracking are weather at the time of placement, curing, vibration, finishing, construction loads, and concrete placement length and sequence. The following sections review current practices related to construction sequence for jointless bridges. Construction of integral abutments is addressed first, followed by construction of multiple-span continuous superstructures.

4.6.1 Construction Sequence for Integral Abutments

A number of agencies, including New York State Department of Transportation (NYSDOT) and the Ontario Ministry of Transport (MOT), have developed standard procedures for the construction of bridges with integral abutments. The construction sequence generally involves the following steps, as illustrated in figure 4-30:

1. Predrill holes for piles if required by the design, drive piles in predrilled holes, and fill holes with loose sand.
2. Construct abutment footings and wingwalls to the top of the bearing-seat
3. Place beams on supports (or bearings) that allow rotation caused by their deadweight and the weight of the deck.
4. Cast deck slab and the portion of the abutment (end-diaphragm) above the bridge -seat elevation integrally with the beams, as described in section 4.6.2. The ends of the slab and the top portion of the abutment should be placed last to minimize locked-in stresses at the supports. If a retarder is used, the deck and top portion of the abutment can be placed in a single pour.
5. Place backfill behind the abutments after the deck has reached a required strength level. For example, Ontario MOT requires the deck concrete to reach 75 percent of the specified strength, while NYSDOT requires curing for 7 days. Backfill should be placed simultaneously behind both abutments.
6. Cast the approach slab. It is desirable to place concrete for the approach in the early morning so that the bridge superstructure will expand against the approach

slab during the day. This avoids putting the slab into tension until the concrete has gained some strength.

Variations from this sequence may be required to accommodate specific details. For example, if steel beams are supported directly on bearing plates welded to the top of the piles, the abutment can then be placed in a single pour after the connection between the beam and the pile has been made, followed by casting of the deck concrete. At all stages of construction, the stability and integrity of the structure must be maintained.

4.6.2 Construction Sequence for Deck in Multispan Jointless Bridges

As discussed in NCHRP Report 322, restraint moments resulting from differential creep and shrinkage at the supports of simple-span, PS/C girders that are made continuous, are highly dependent on the timing of construction.[49] The primary factor is the girder age at the time continuity is established by construction of the cast-in-place deck and the end diaphragms. However, the sequence of deck and diaphragm construction, either simultaneous or one before the other, also affects the development of restraint moments.

NCHRP Report 322 was based on an NCHRP study that used a questionnaire to determine the typical practice for the sequence of construction for this type of bridge. Thirty-four respondents provided this information. The majority of the responses indicated that the girders were between 10 days and 90 days old at the time of construction. The sequence of placing the concrete for the deck and end diaphragms has an influence on the long-term behavior of the bridge. Nine respondents indicated that bridge decks are typically cast before diaphragms. A common variation consists of casting positive-moment areas of the deck first and then casting pier diaphragms and negative-moment areas of the deck. Sixteen of the respondents typically cast deck and pier-diaphragm concrete simultaneously. Ten respondents typically cast pier-diaphragms before the deck.

Based on the results of structural analysis, Oesterle, et al., concluded that if the deck is cast before the support diaphragms, the positive moment is increased at midspan, but the potential for deck cracking over the supports is decreased.[49] On the other hand, if the diaphragms are cast first, there is a slight decrease in positive moment at midspan, but there is also an increase in the potential for deck cracking over the supports.

Both of these construction sequences, however, had only a minor influence on the development of restraint moments and effective continuity when compared to the effects of the girders' age at the time of establishing continuity. Construction with young girders

will result in a tendency for positive-moment cracking in the diaphragms at the supports. Construction with relatively old girders will increase the potential for deck cracking from the negative moment over the piers.

TDOT and other agencies have adopted a deck-slab placement sequence in which the positive-moment region is placed first, followed by the slab and the diaphragms over the supports. The end diaphragms and the adjacent portion of the deck are usually cast last. The sequence of deck-slab placement is illustrated schematically in figure 4-31. This sequence has apparently resulted in satisfactory performance and is applicable to both steel and PS/C bridges.

There is at least one reported instance where positive-moment cracking observed in the end regions of PS/C girders may have been caused by a construction sequence in which the diaphragms were cast before the deck.[62] If a deck is cast after the diaphragms, the negative moment that is developed over the pier can move the location of the maximum positive-restraint moment from the end diaphragm to a location within the girder. This effect may have contributed to the case cited above, although other factors, such as a stress discontinuity developing at the ends of the bars placed to carry positive moment across the diaphragm, may also have contributed.

Transverse deck cracking from negative moment is a greater durability problem than positive-moment cracking in the diaphragms. Also, positive-moment cracking is probably desirable in the diaphragm if compared to the risk of cracking in the ends of the girders where the prestressing is lower. Therefore, the construction sequence illustrated in figure 4-31, with the positive-moment regions of the deck cast prior to the diaphragms and to the negative-moment regions, is the recommended sequence.

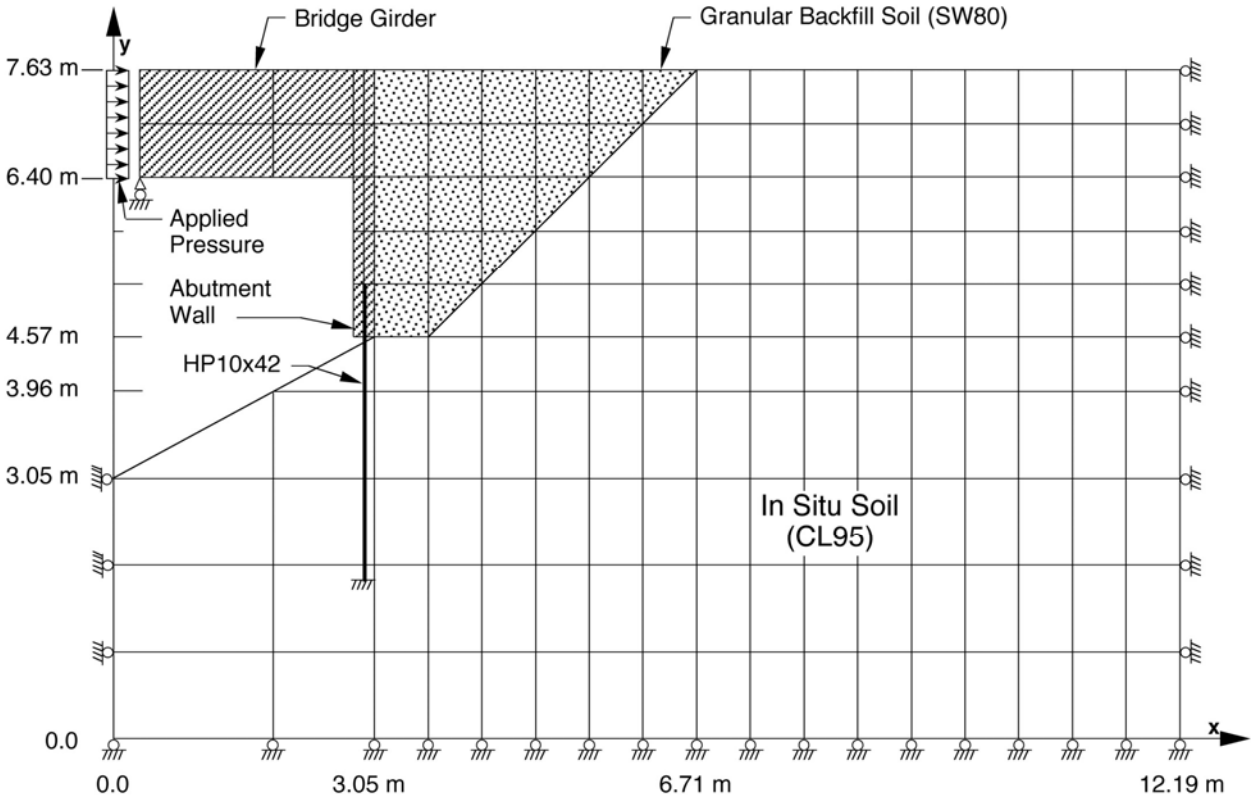

Figure 4-1. Analytical model of baseline condition.

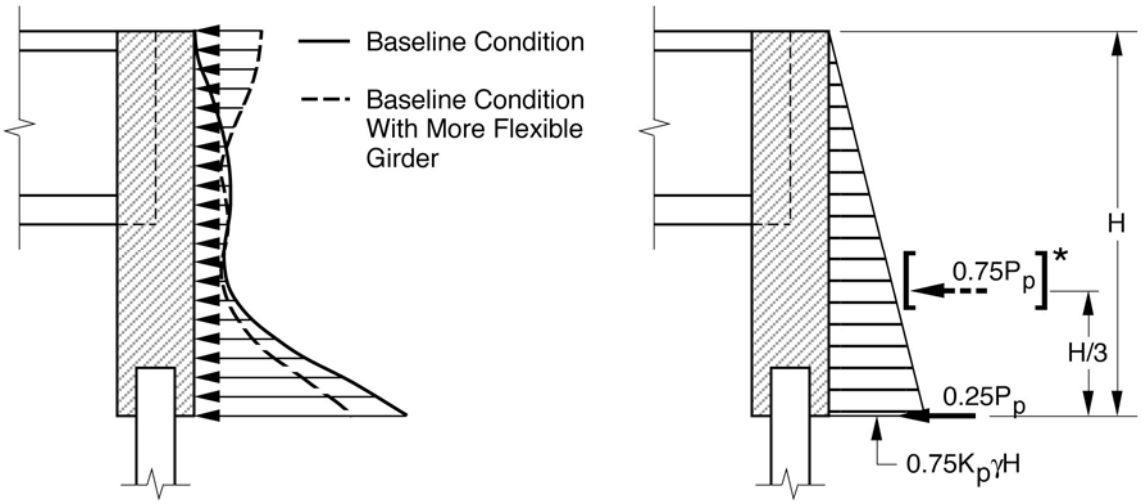

(a). Passive pressure distribution.

(b). Location of passive pressure resultants for design of integral stub abutments.

Figure 4-2. Passive pressure distribtion and location of passive pressure resultants.

* Resultant of triangular distribution.
$P_p = ½ K_p H^2$
K_p = Passive pressure coefficient dependent on wall movement according to Clough and Duncan[11]

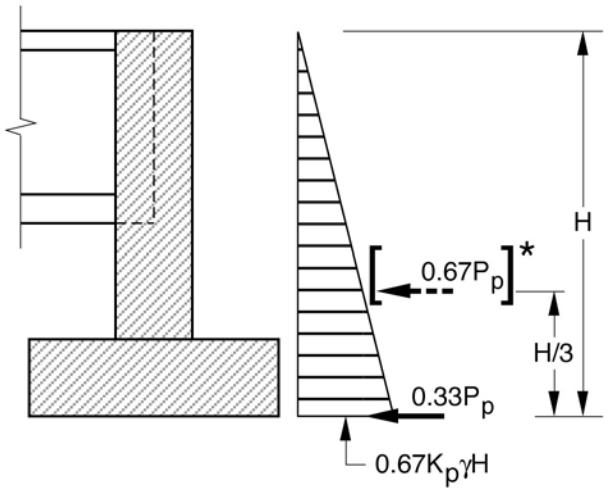

Figure 4-3. Location of passive pressure resultants for design of stub abutments on spread footings.

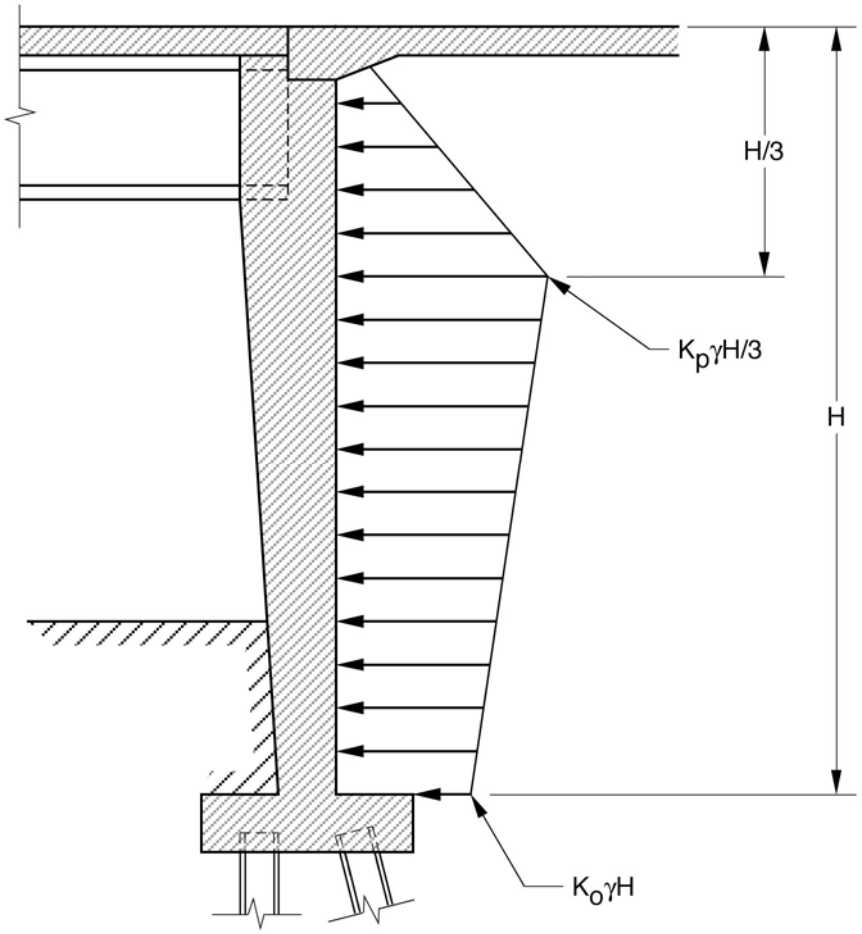

Figure 4-4. Design envelope for full-height wall abutments based on passive and at-rest pressures.

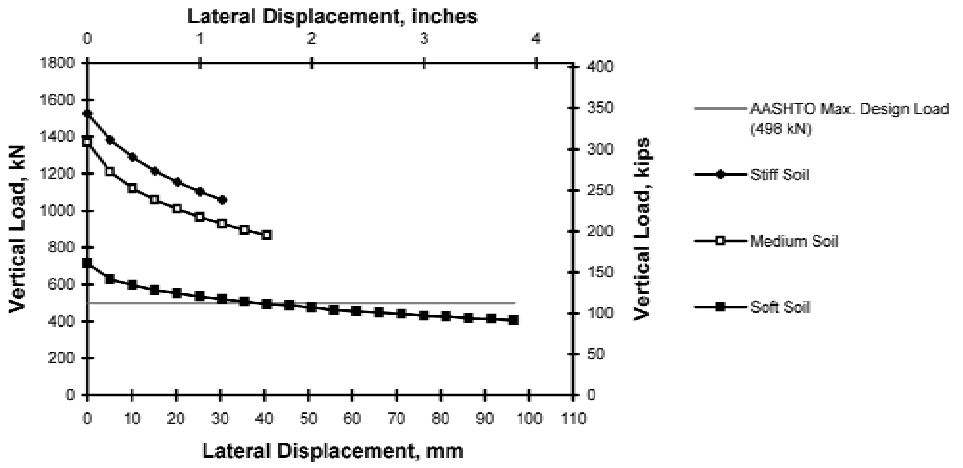

Figure 4-5(a). Ultimate load capacity for HP10x42 (without overdrilled holes).

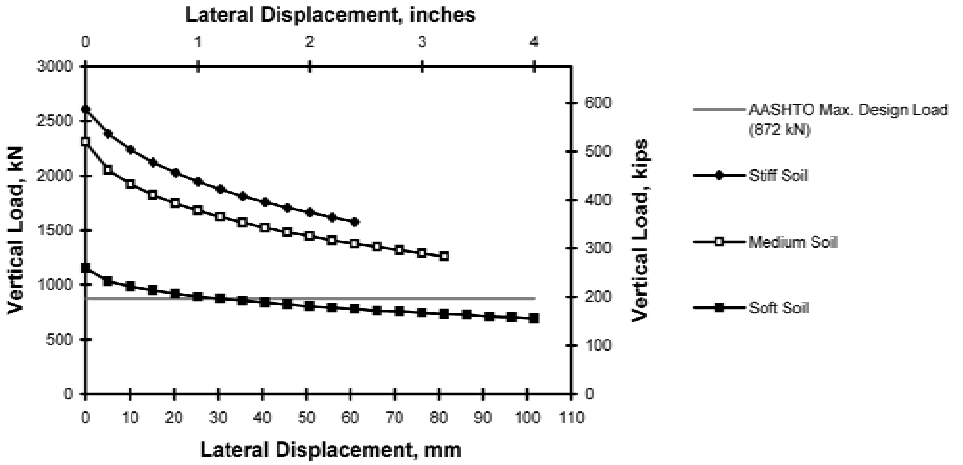

Figure 4-5(b). Ultimate load capacity for HP12x74 (without overdrilled holes).

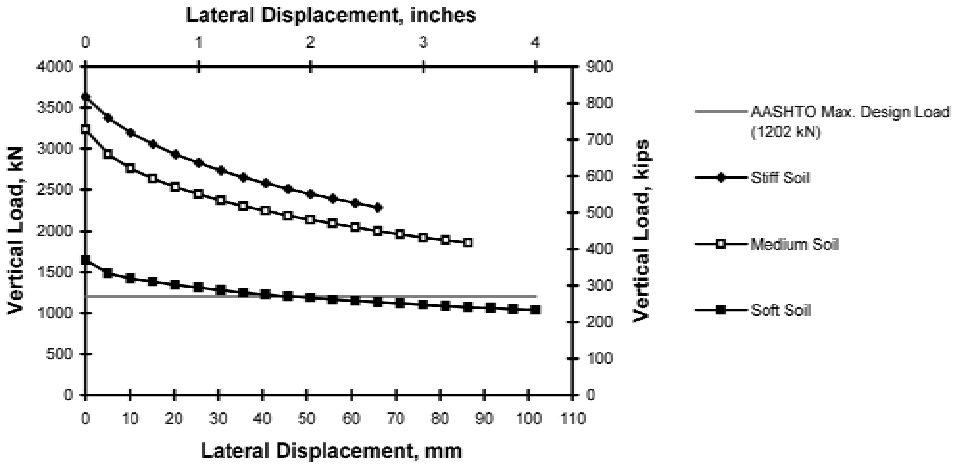

Figure 4-5(c). Ultimate load capacity for HP14x102 (without overdrilled holes).

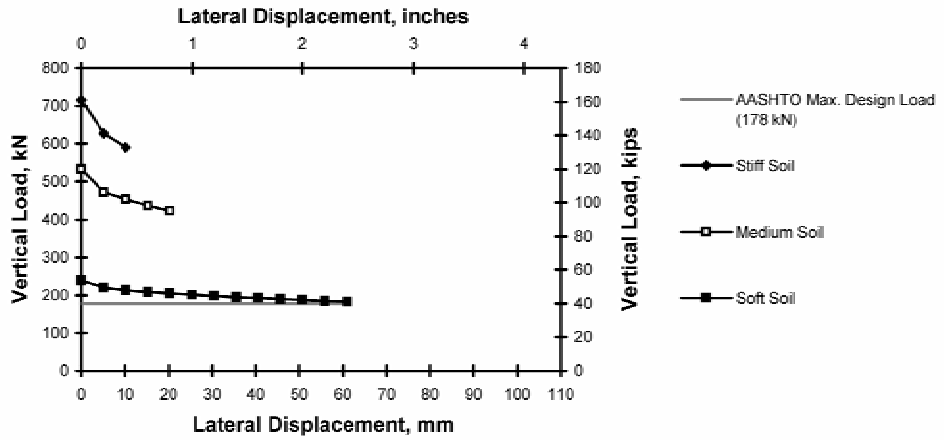

Figure 4-6(a). Ultimate load capacity for 254- by 254-mm (10- by 10-inch) prestressed concrete piles (without overdrilled holes).

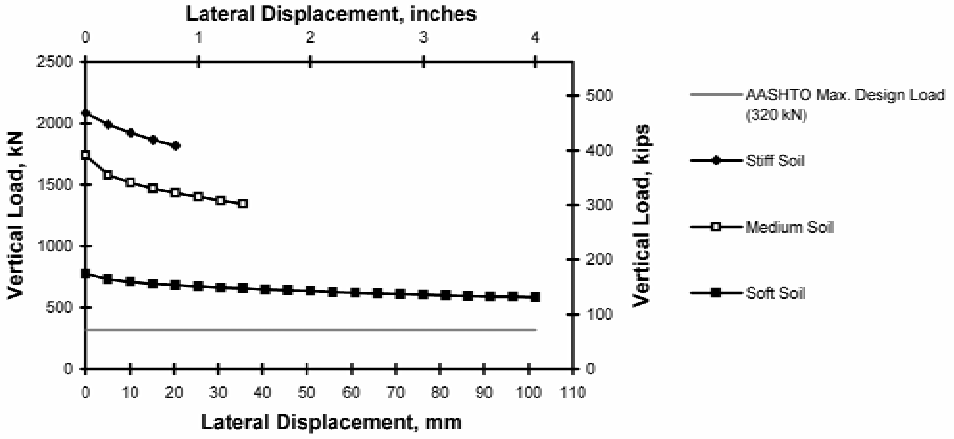

Figure 4-6(b). Ultimate load capacity for 406- by 406-mm (16- by 16-inch) prestressed concrete piles (without overdrilled holes).

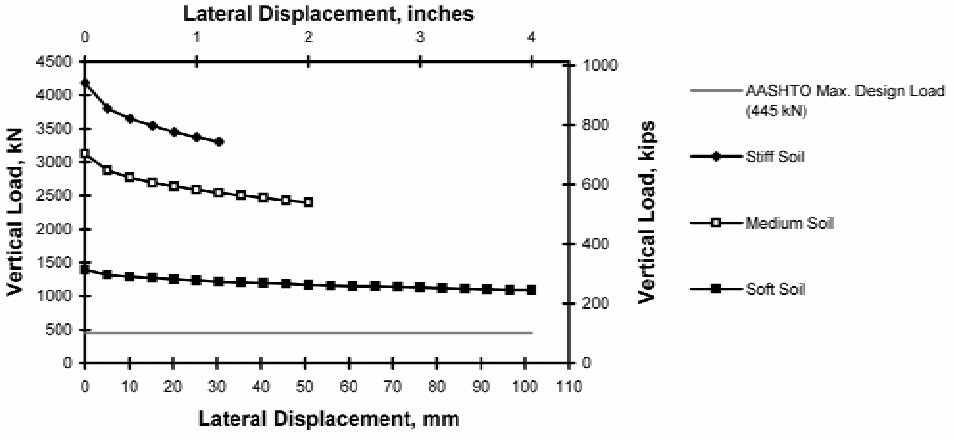

Figure 4-6(c). Ultimate load capacity for 610- by 610-mm (24- by 24-inch) prestressed concrete piles (without overdrilled holes).

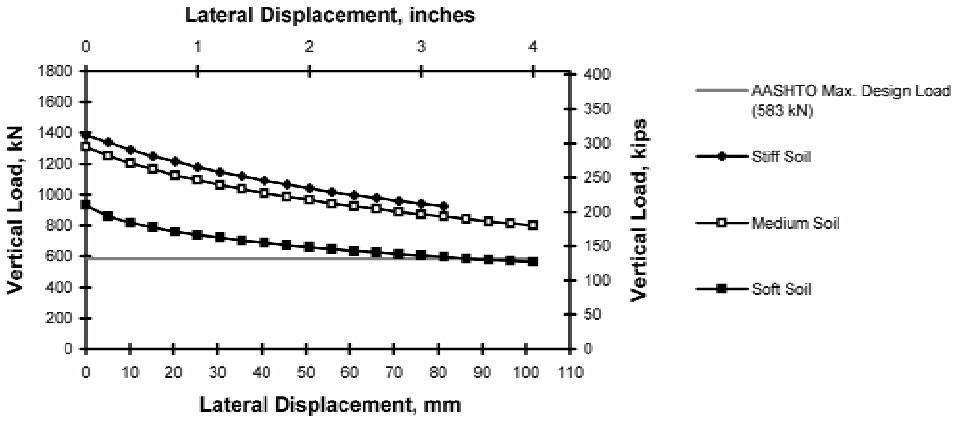

Figure 4-7(a). Ultimate load capacity for PP 10-3/4 (without overdrilled holes).

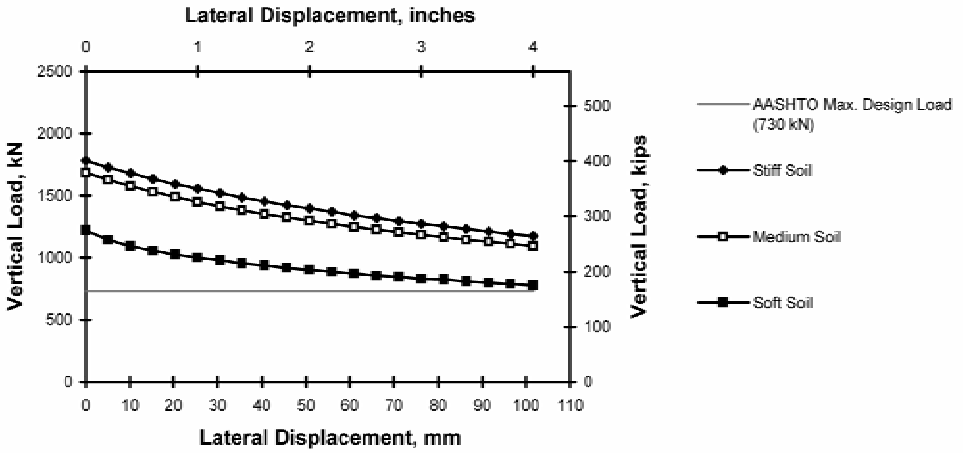

Figure 4-7(b). Ultimate load capacity for PP 12-3/4 (without overdrilled holes).

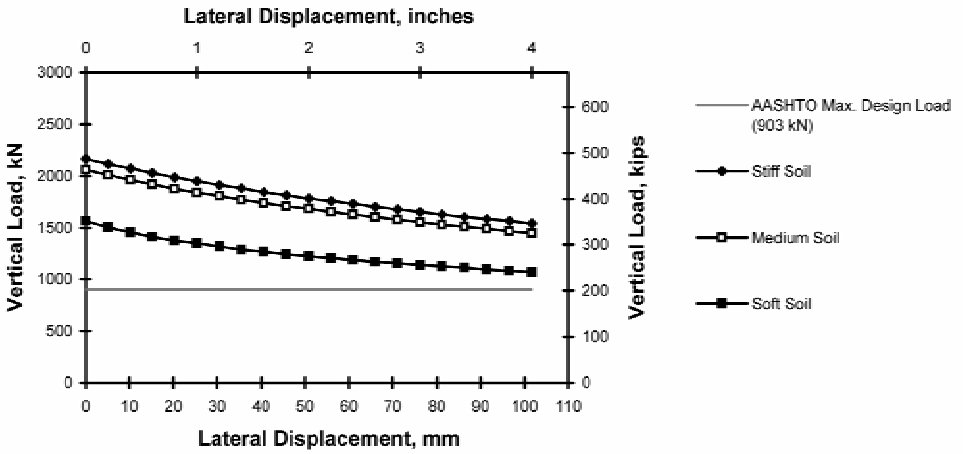

Figure 4-7(c). Ultimate load capacity for PP 16 (without overdrilled holes).

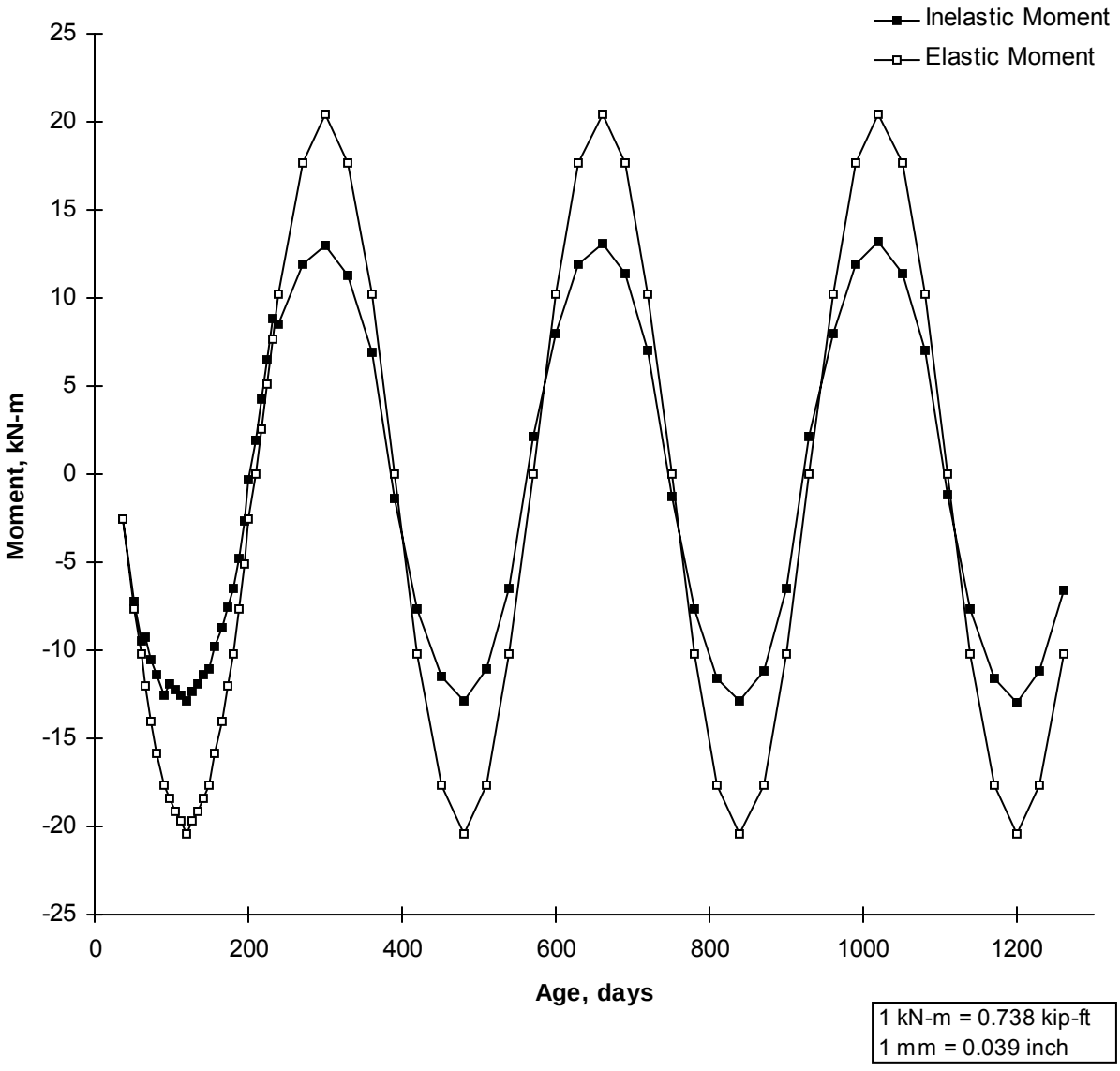

Figure 4-8. History of elastic and inelastic moments (Case 1).

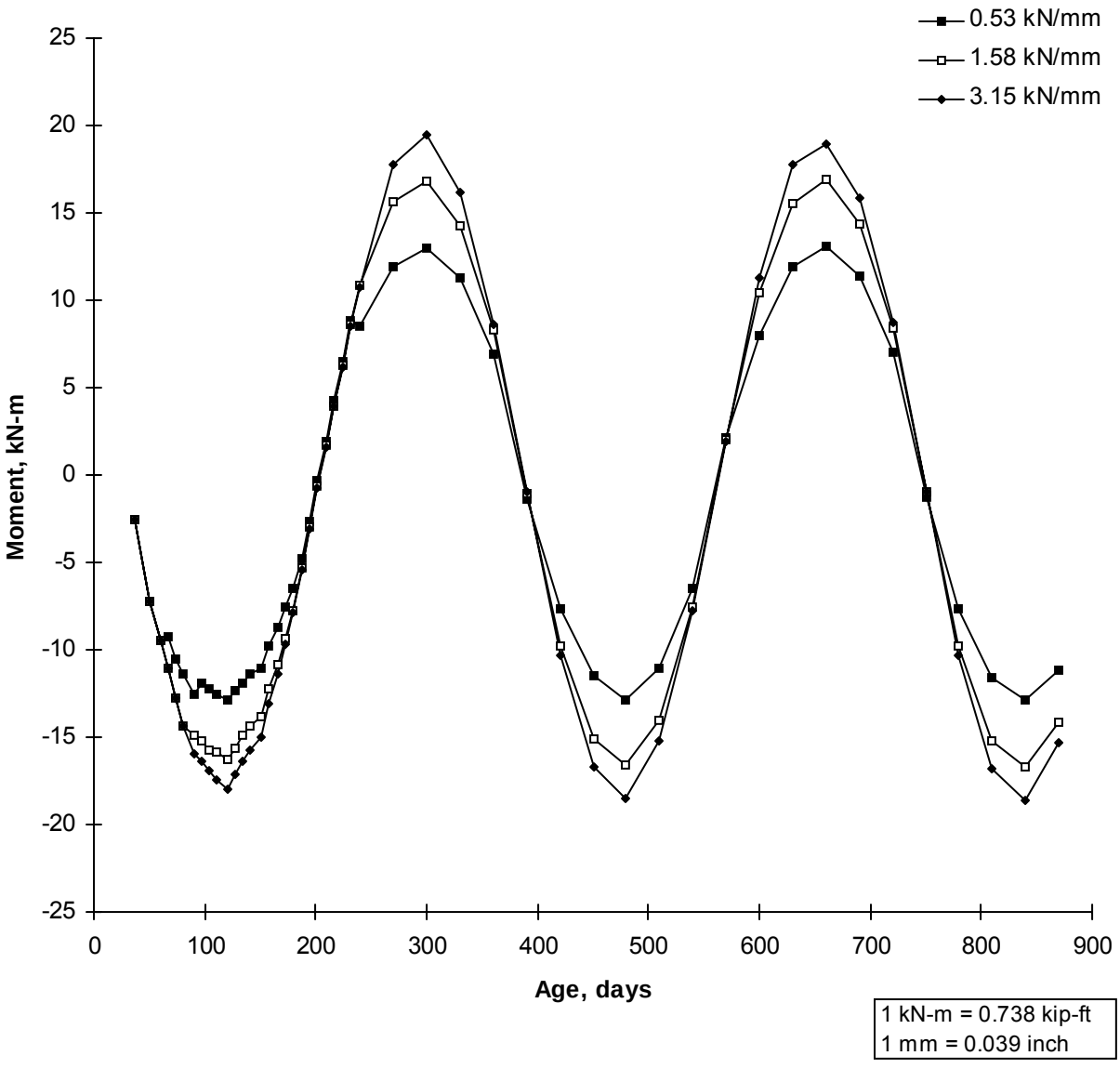

Figure 4-9. Effect of vertical loads.

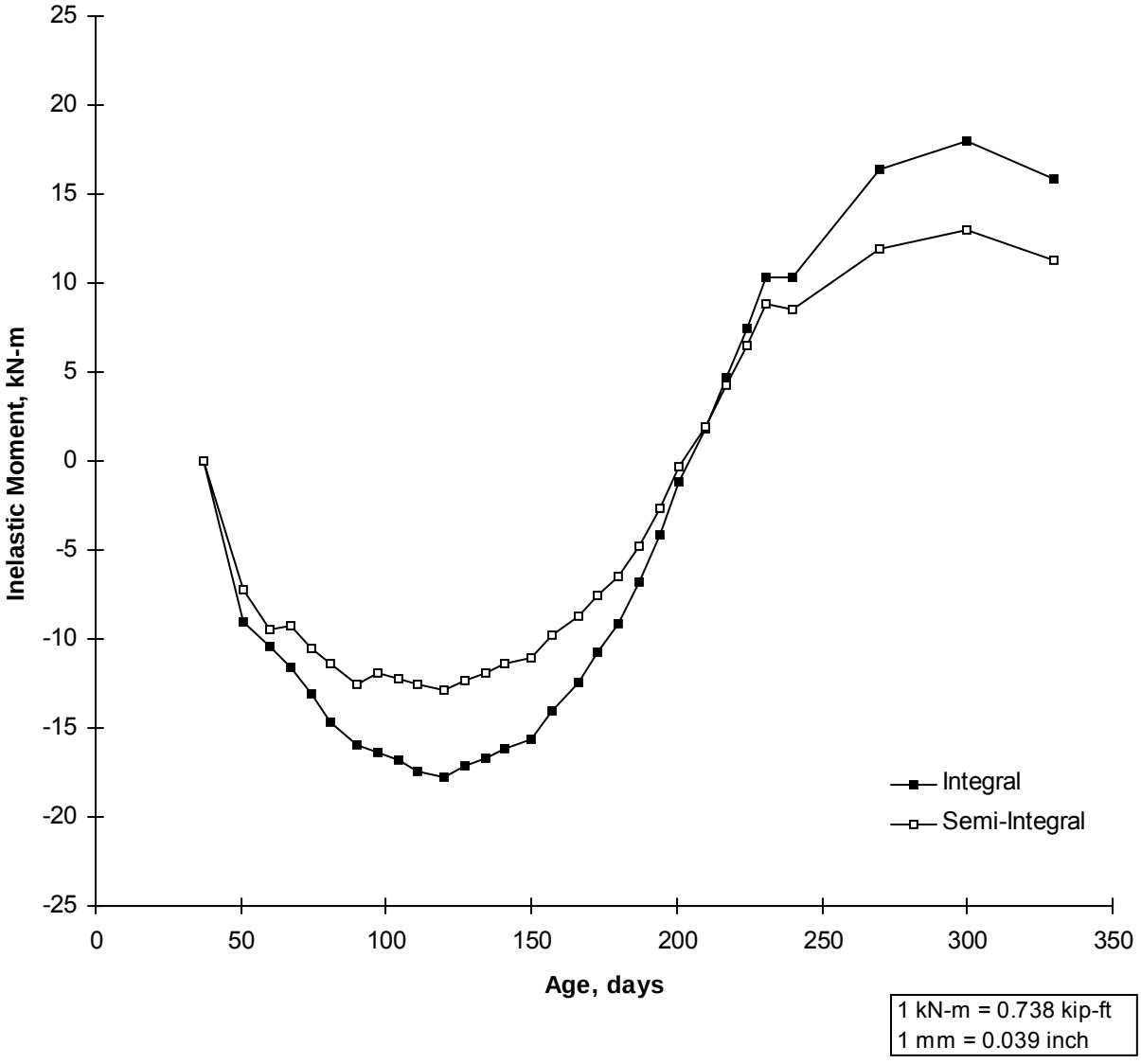

Figure 4-10. Effect of connection to superstructure (Cases 1 and 8).

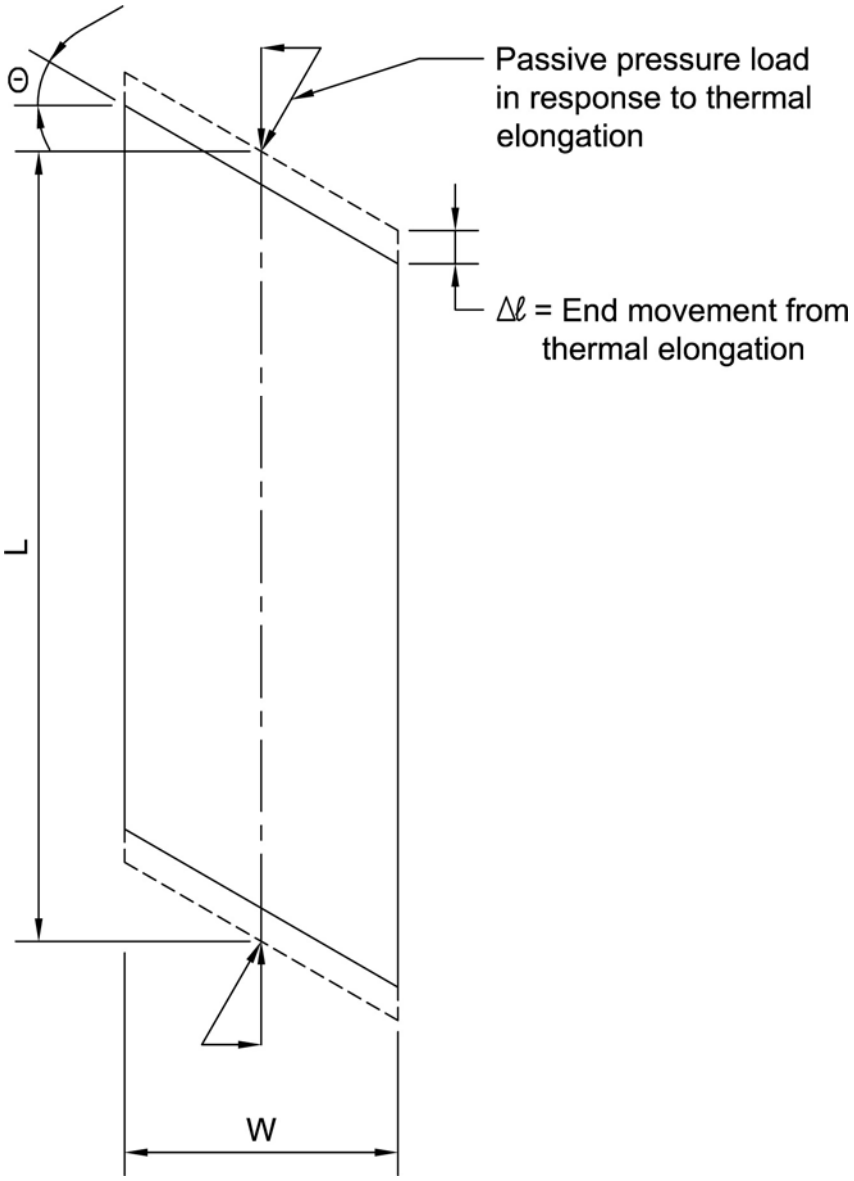

Figure 4-11. Components of abutment-soil passive pressure response to thermal elongation in skewed bridges with integral abutments.

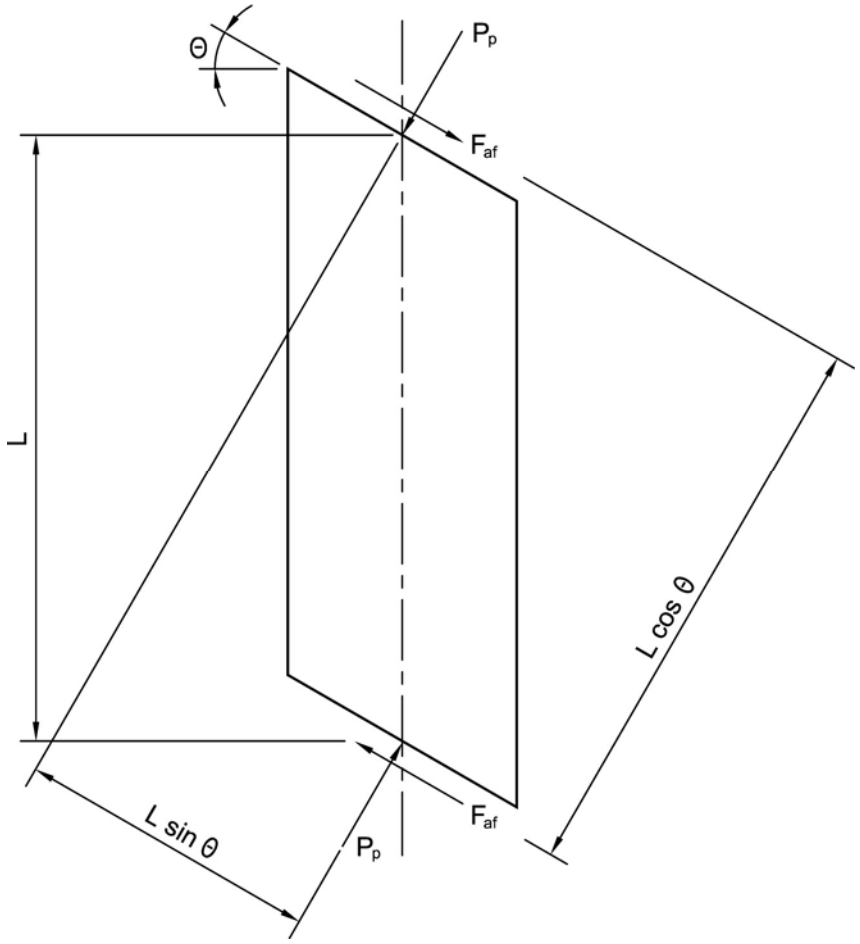

Figure 4-12. Soil pressure load, $P_{p,}$ and soil/abutment interface friction, F_{af}.

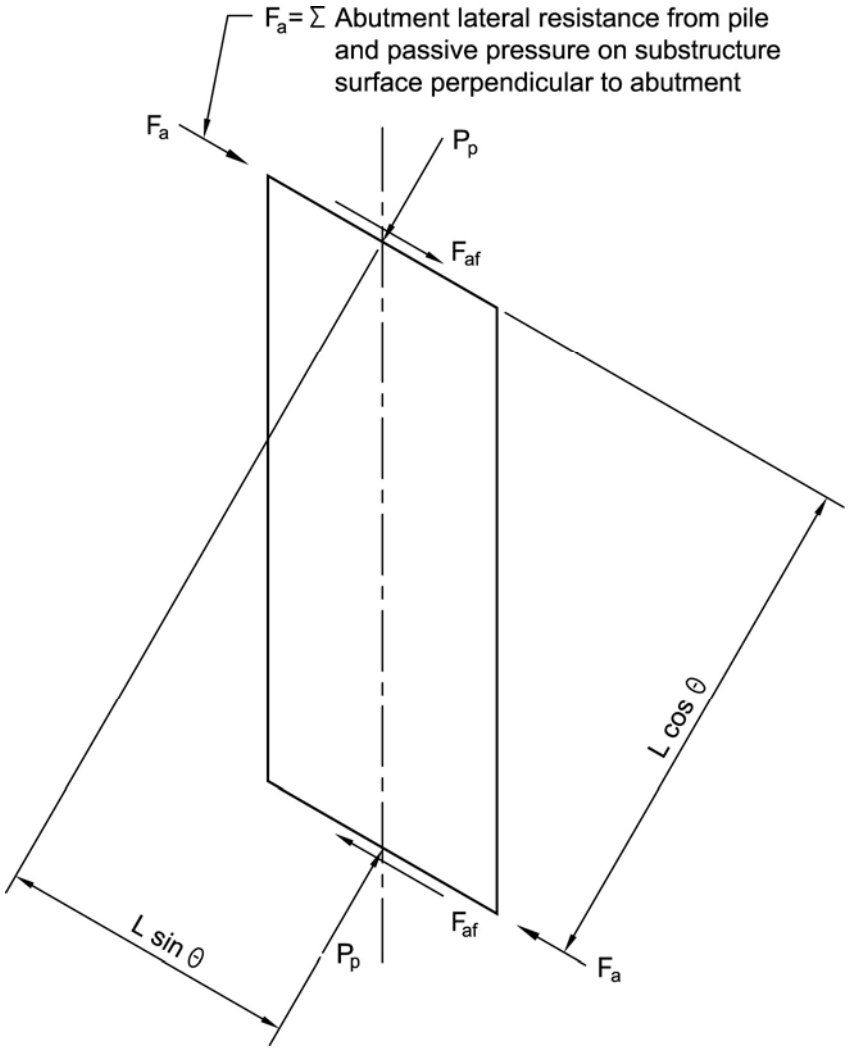

Figure 4-13. Abutment lateral force, F_a, required in combination with interface friction, F_{af}, for rotational equilibrium of heavily skewed bridge.

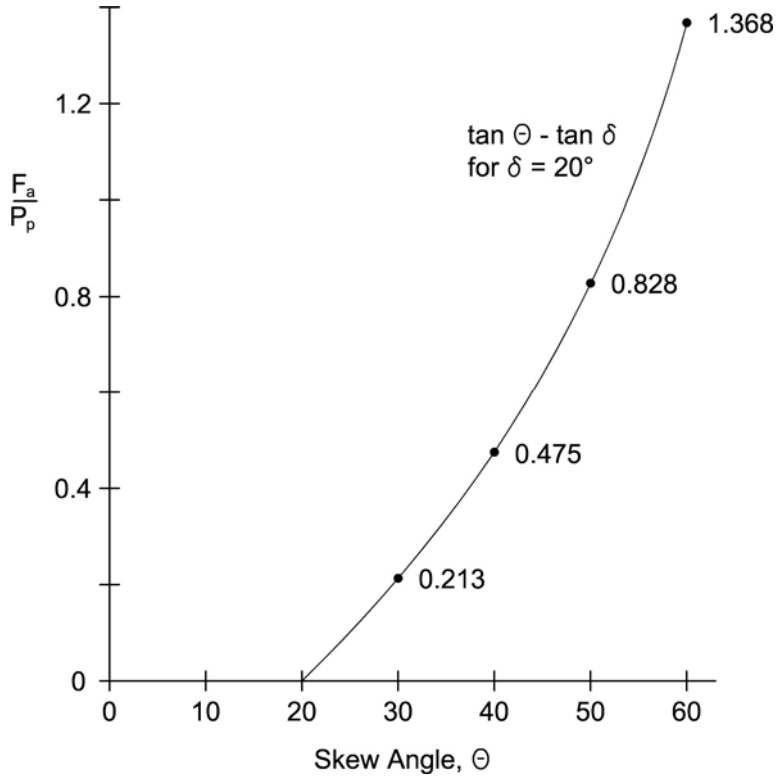

Figure 4-14. Relationship between force required for abutment lateral resistance, F_a, and passive pressure response, P_p, to restrain lateral movement.

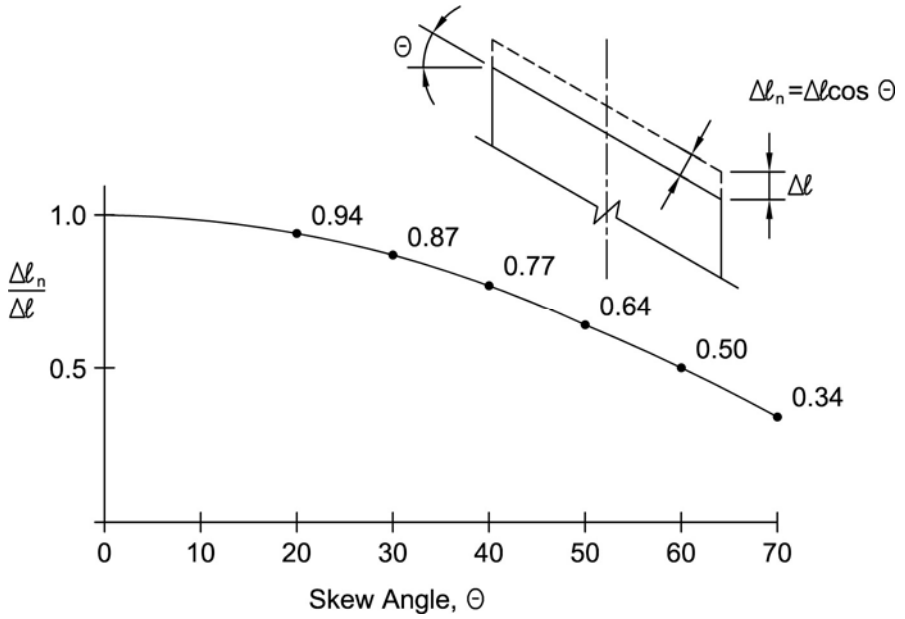

Figure 4-15. Relationship between end normal movement, $\Delta\ell_n$, and end thermal expansion, $\Delta\ell$.

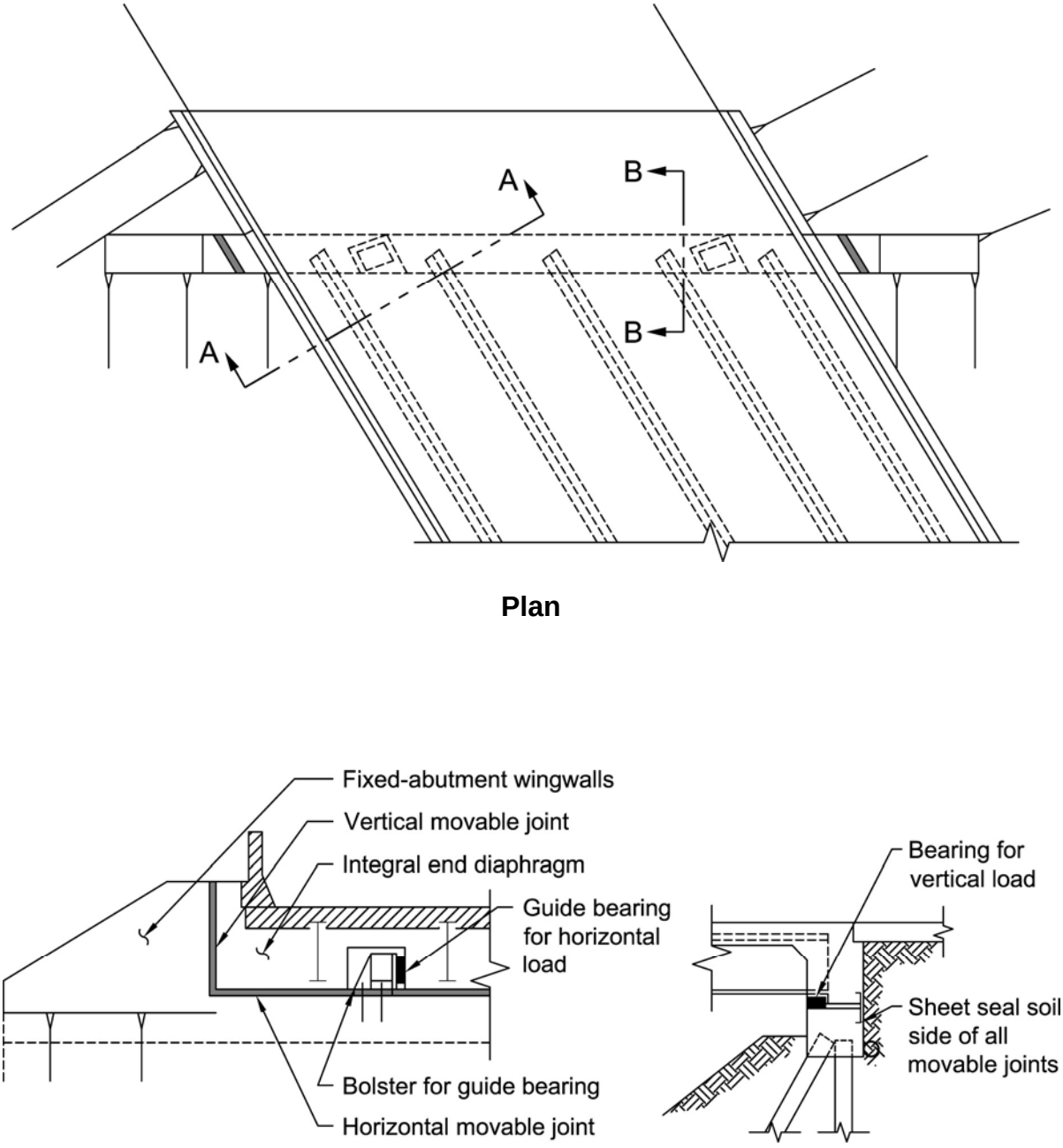

Figure 4-16. Semi-integral abutment with end diaphragm moving and abutment fixed.

Figure 4-17. Two-span bridge with an overall length of 89 m (292 ft), a width of 11.6 m (38 ft), and a 45° skew.[52]

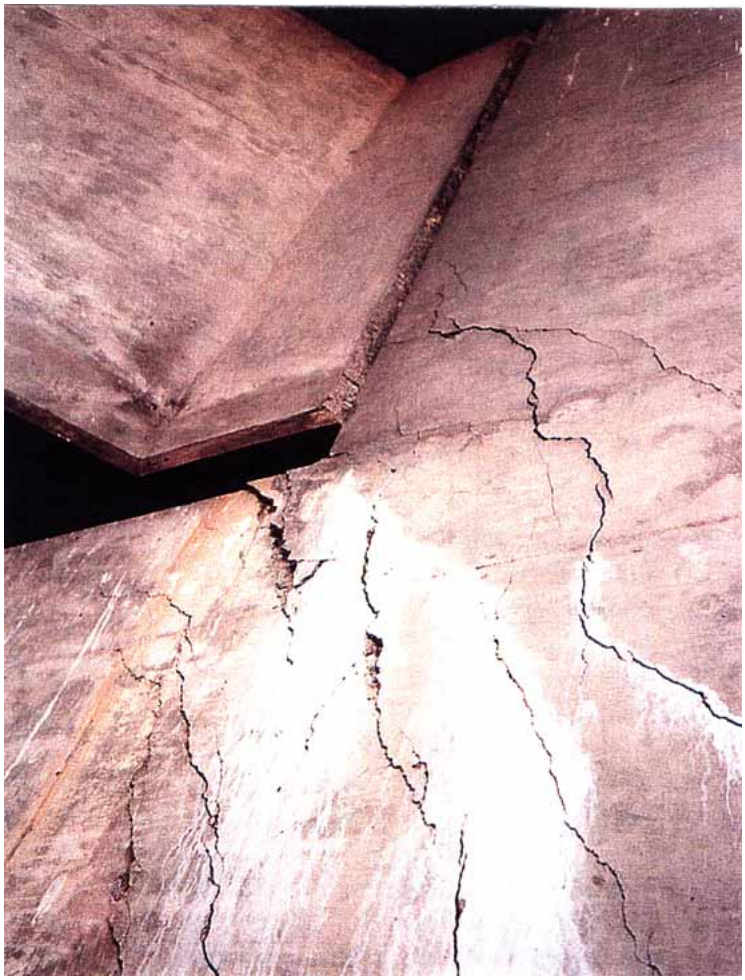

Figure 4-18. Cracking in the abutment wall near an acute corner of the superstructure for the bridge shown in figure 9-2.[52]

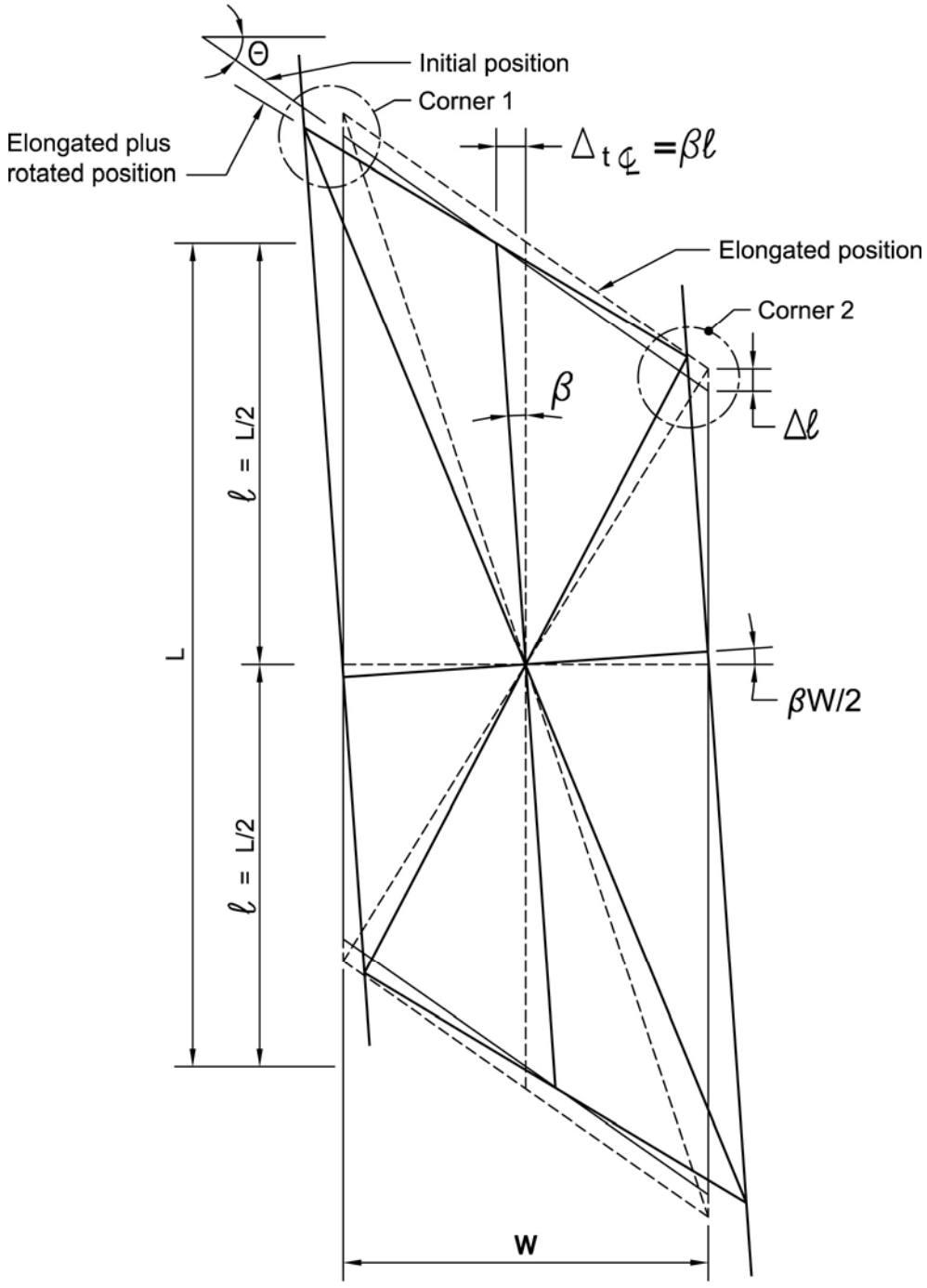

Figure 4-19. Elongation, $\Delta\ell$, and rigid body rotation, β.

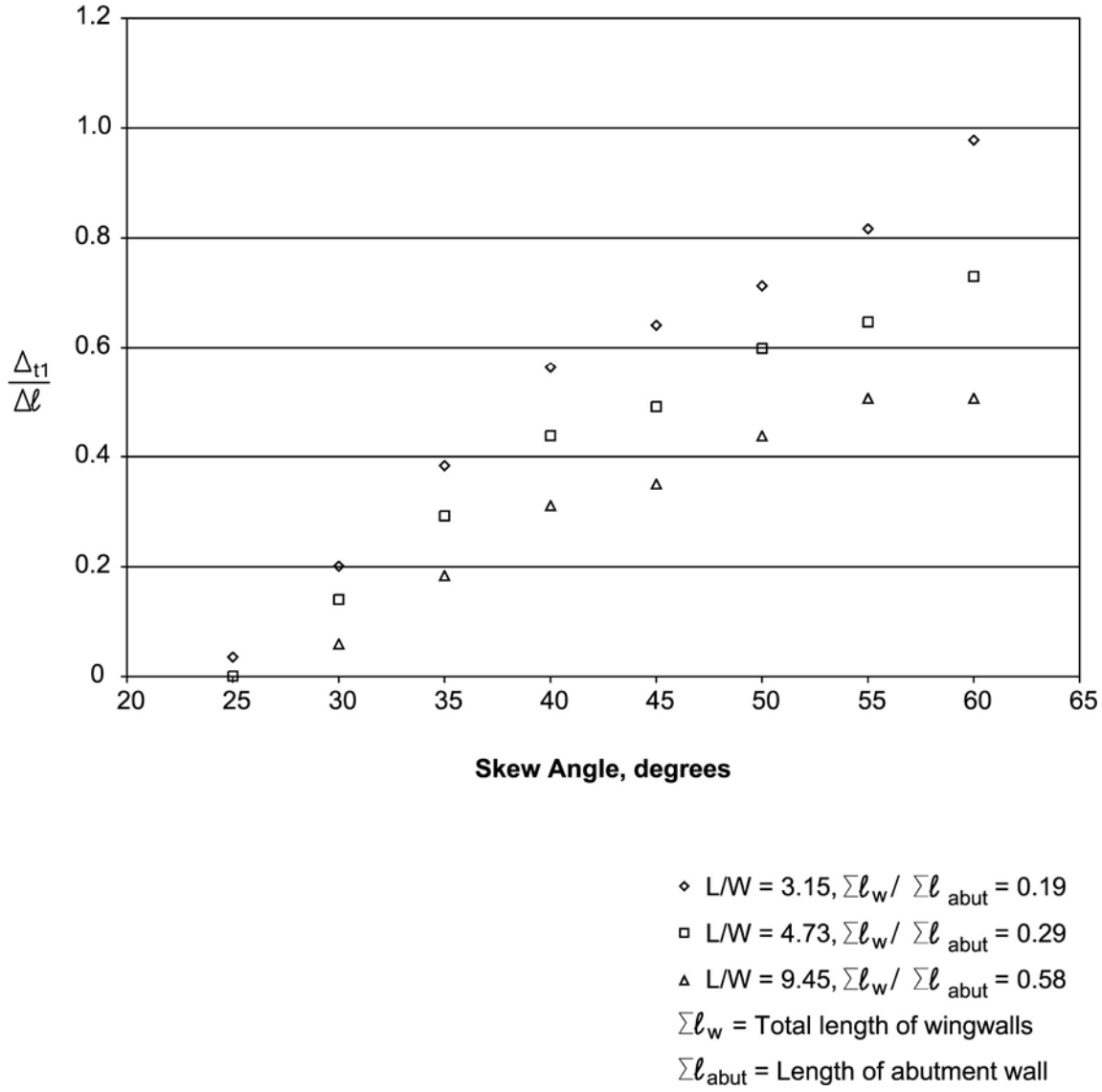

Figure 4-20. Relationship between transverse movement at the acute corner, Δ_{t1}, and thermal expansion, $\Delta\ell$, for an expansion of 25.4 mm (1 inch) with constant-length bridge, L = 126.77 m (415.92 ft), and varying L/W.

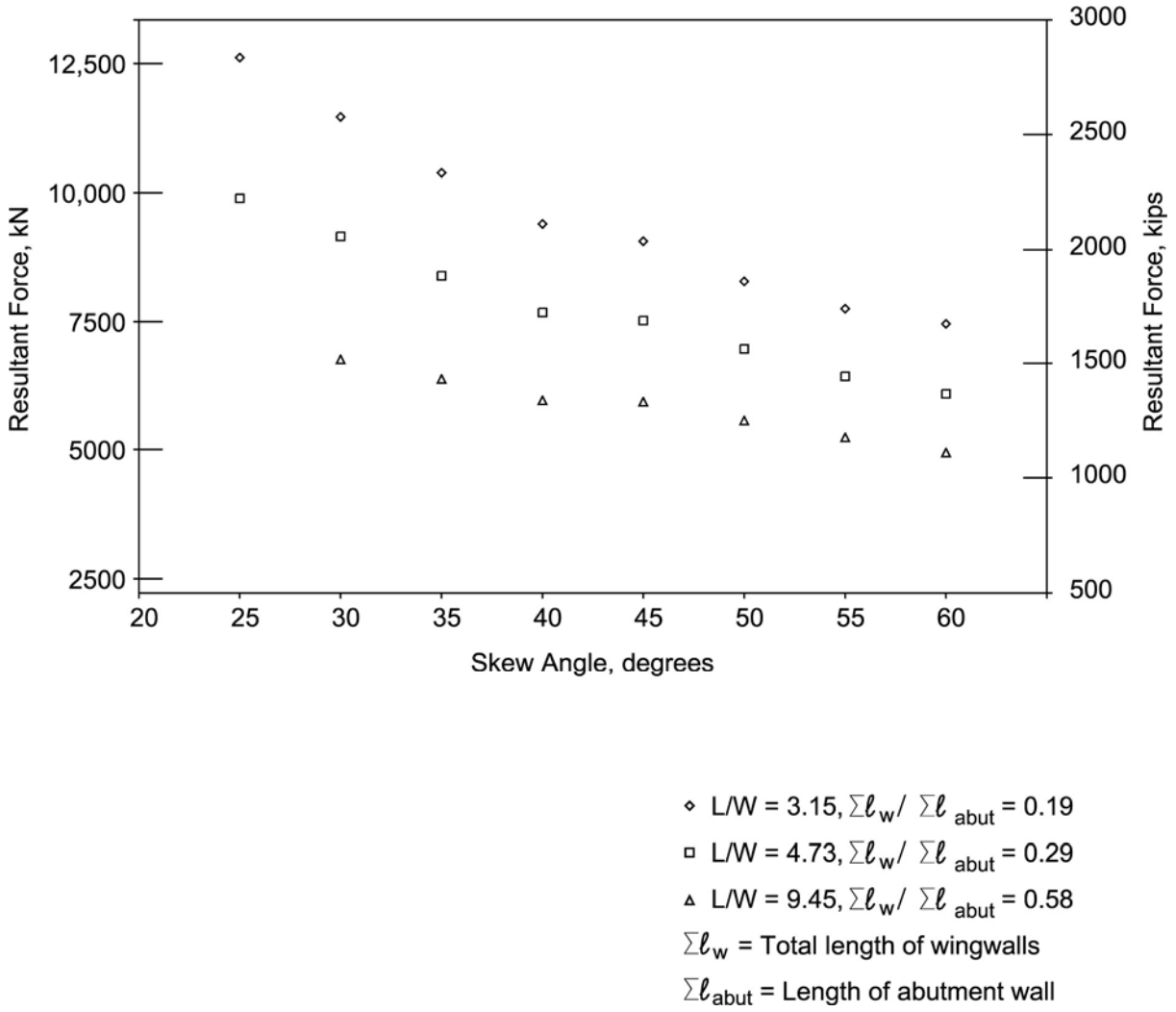

Figure 4-21. Relationship between resultant longitudinal restraint force and skew angle for thermal expansion, $\Delta\ell$, of 25.4 mm (1 inch) with constant-length bridge, L = 126.77 m (415.92 ft), and varying L/W.

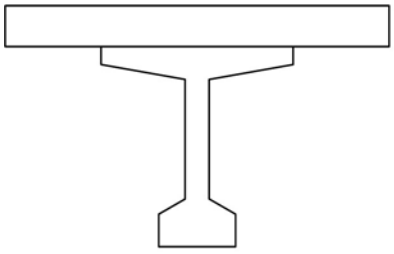

(a) Cross Section.

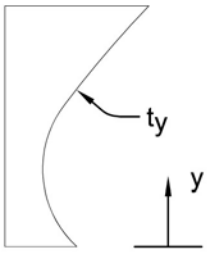

(b) Temperature Gradient.

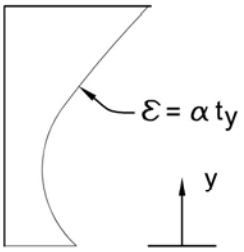

(c) Free Strains.

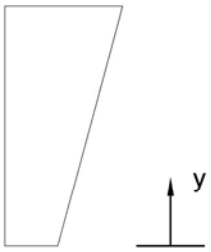

(d) Final Restrained Strain Profile.

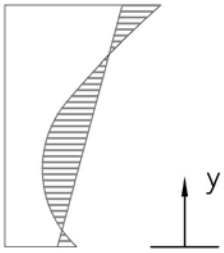

(e) Internal Restraint Strain.

Figure 4-22. Diagram of restraint strains in a cross section.

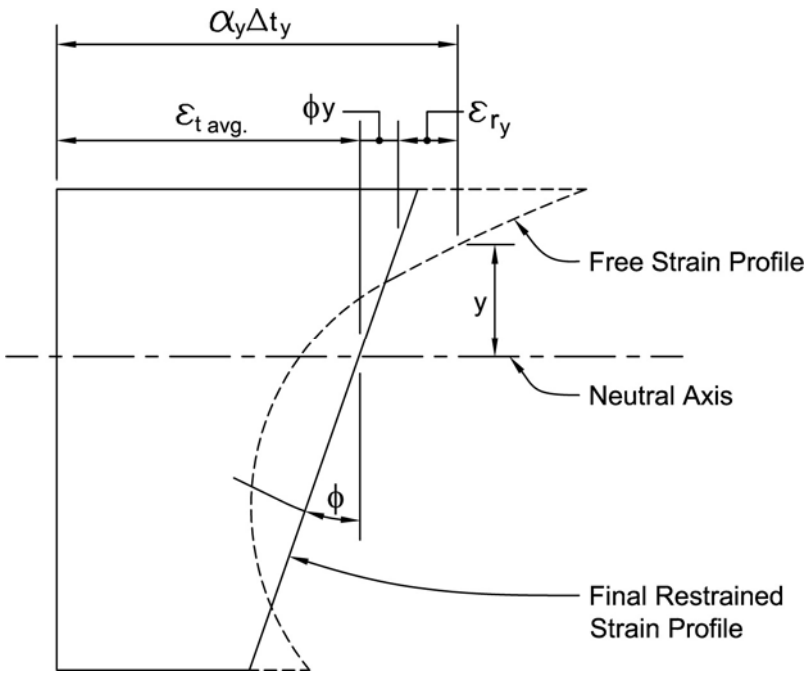

Figure 4-23. Restraint strain components.

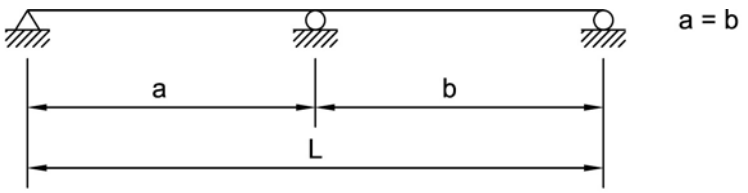

(a) Two span bridge.

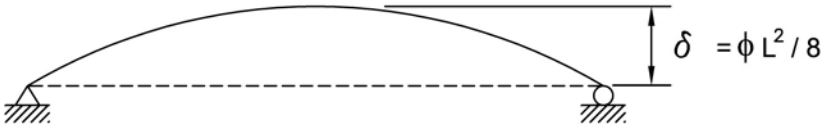

(b) Bowing after removal of redundant support.

(c) Restoration of redundant support.

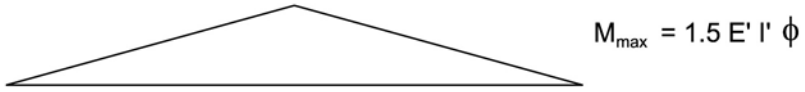

(d) Resultant secondary continuity moment diagram.

Figure 4-24. Two-span bridge secondary continuity moments.

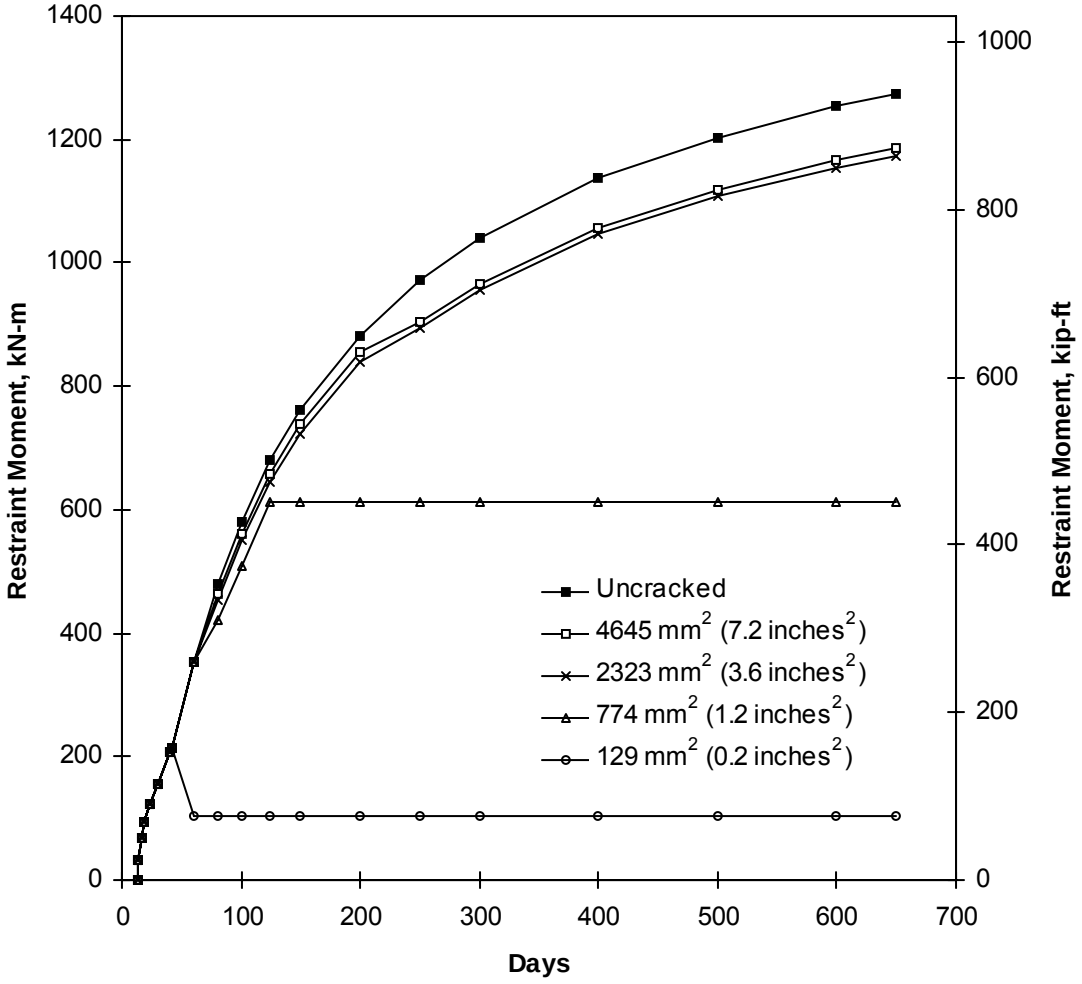

Figure 4-25. Analyses for varying amount of positive-moment continuity reinforcement.

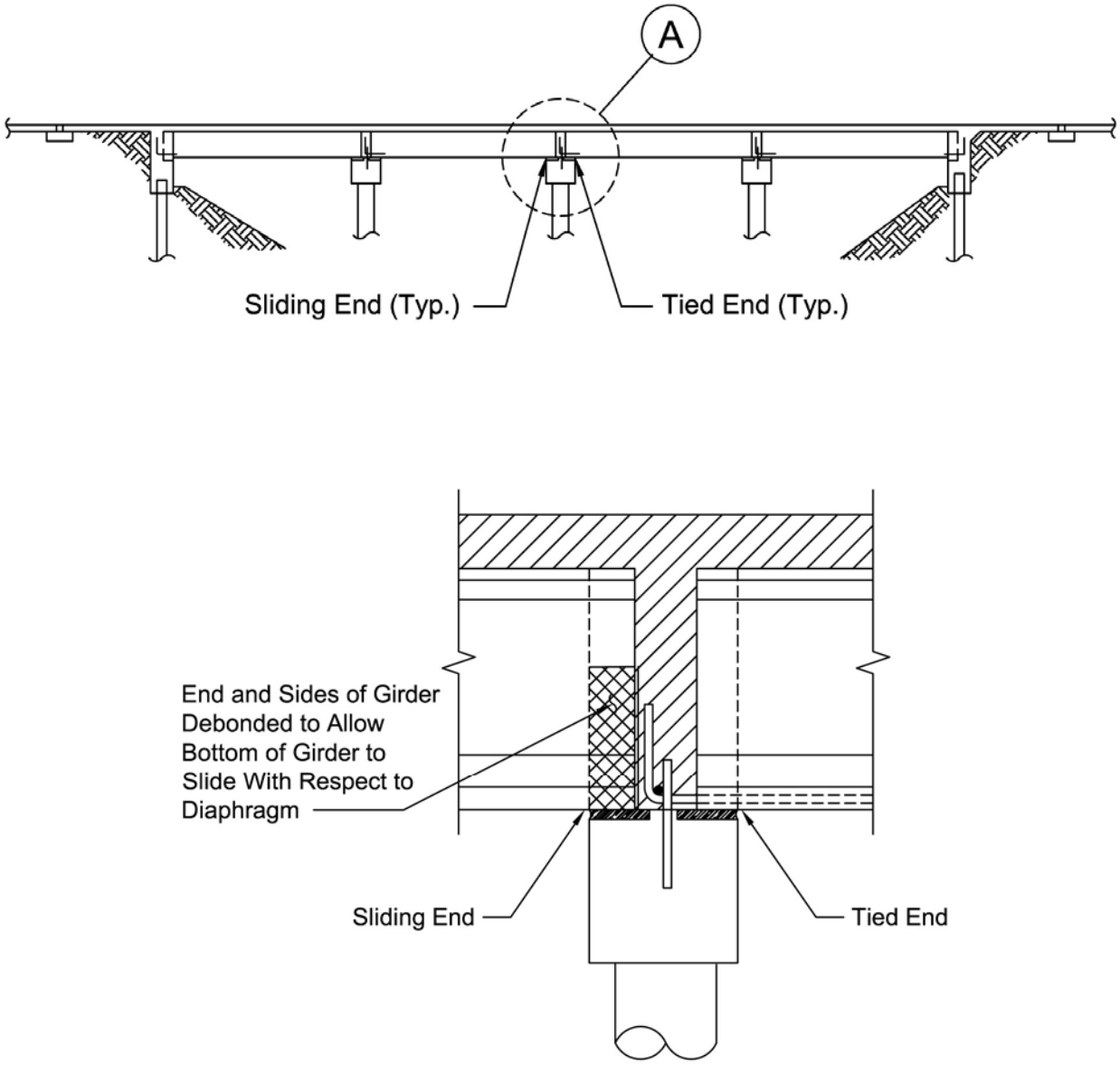

Figure 4-26. Connection of prestressed girders to semi-integral pier cap for Design Option 1.

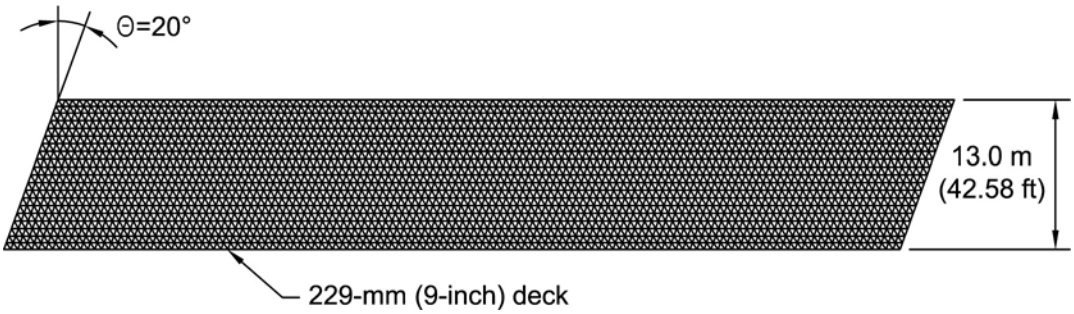

(a) Deck.

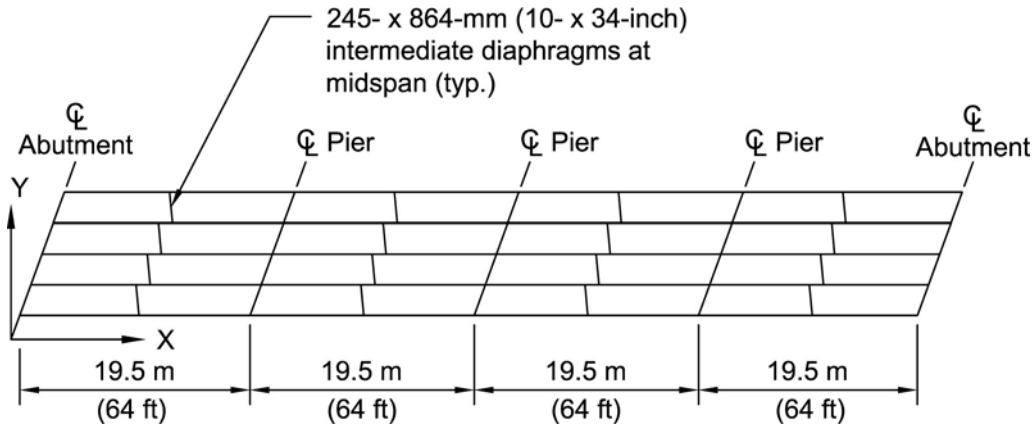

(b) Beams and diaphragm.

Figure 4-27. Finite element model for bridge with a skew angle of 20°.

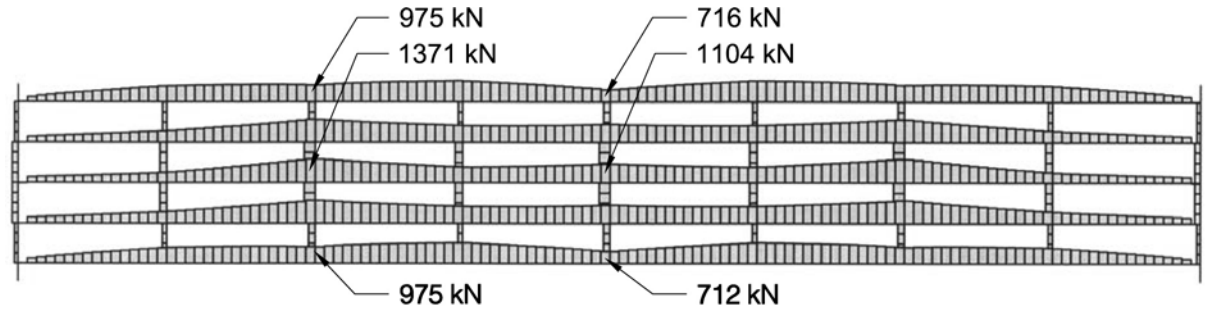

(a) Θ=0°

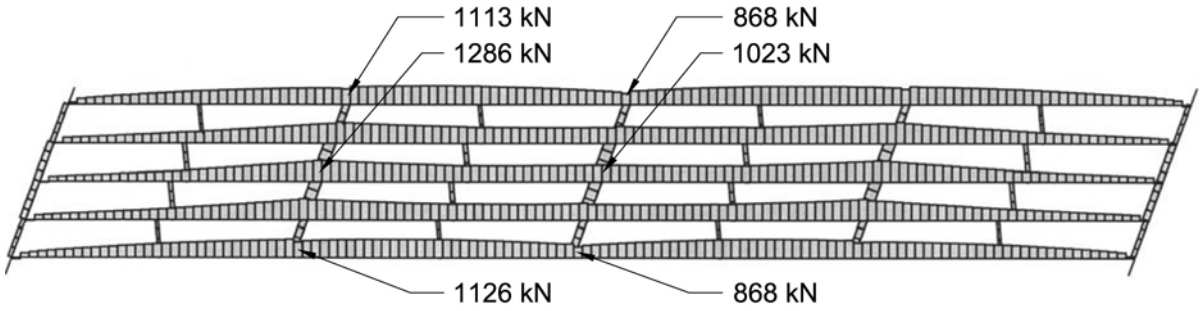

(b) Θ=20°

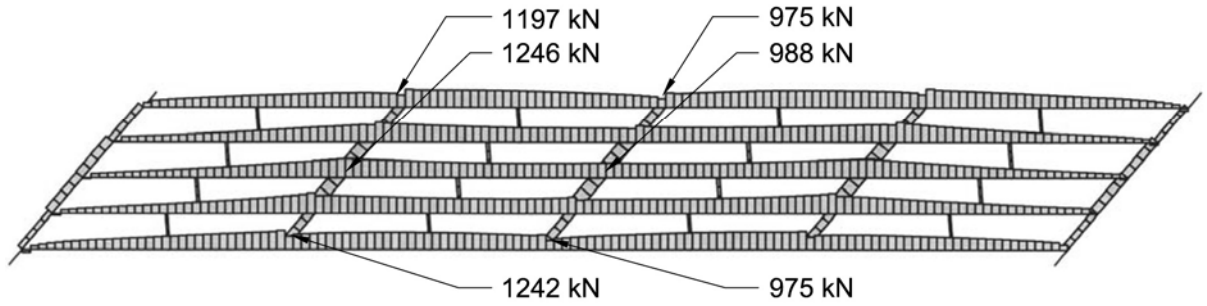

(c) Θ=40°

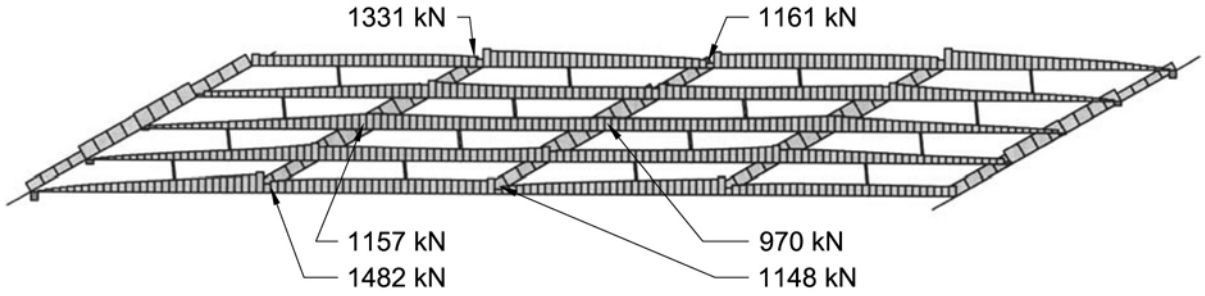

(d) Θ=60°

Figure 4-28. Axial load in beams and diaphragms caused by thermal gradient.

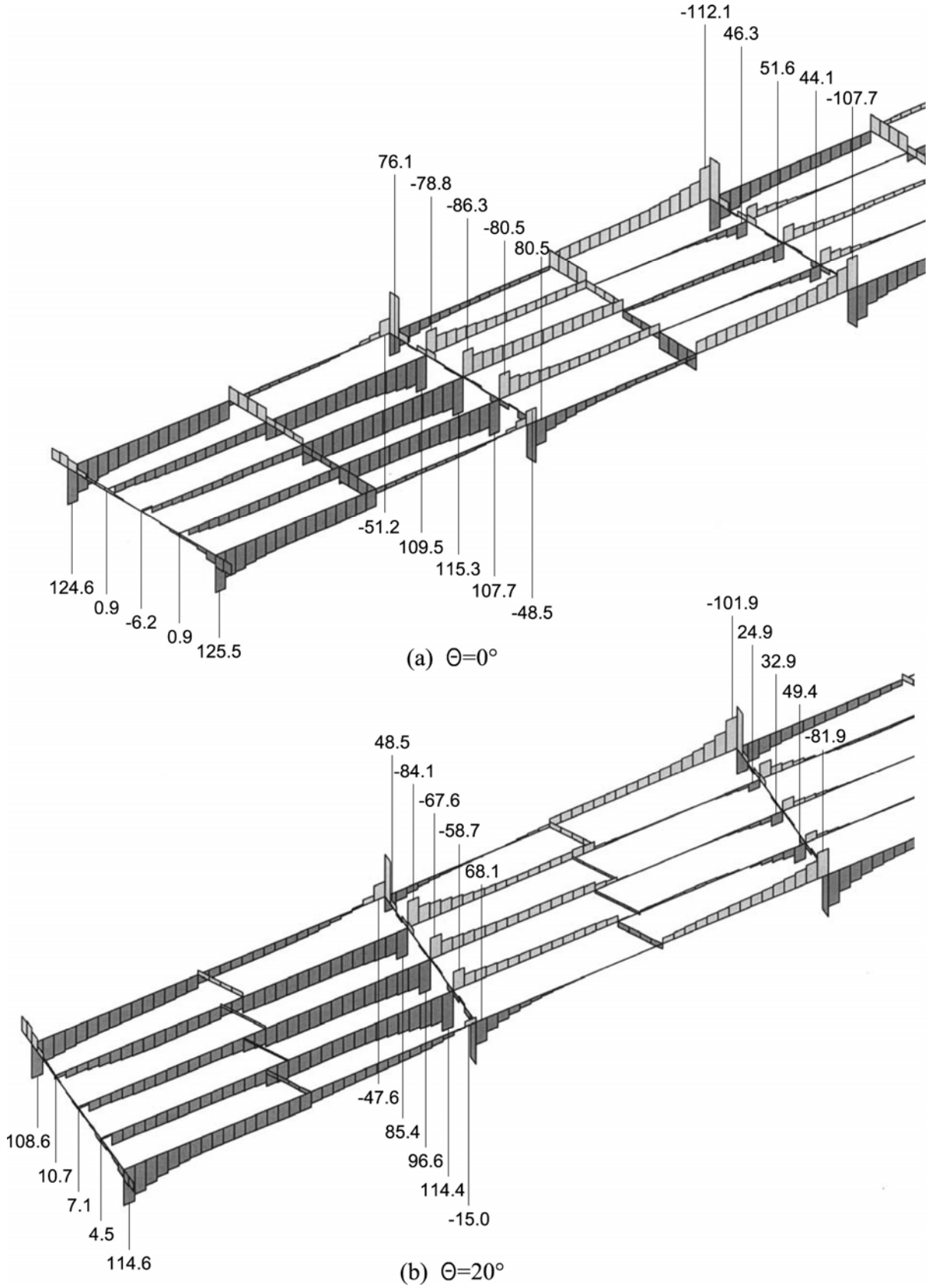

Figure 4-29. Shear forces (in kN) in beams and diaphragms caused by thermal gradient.

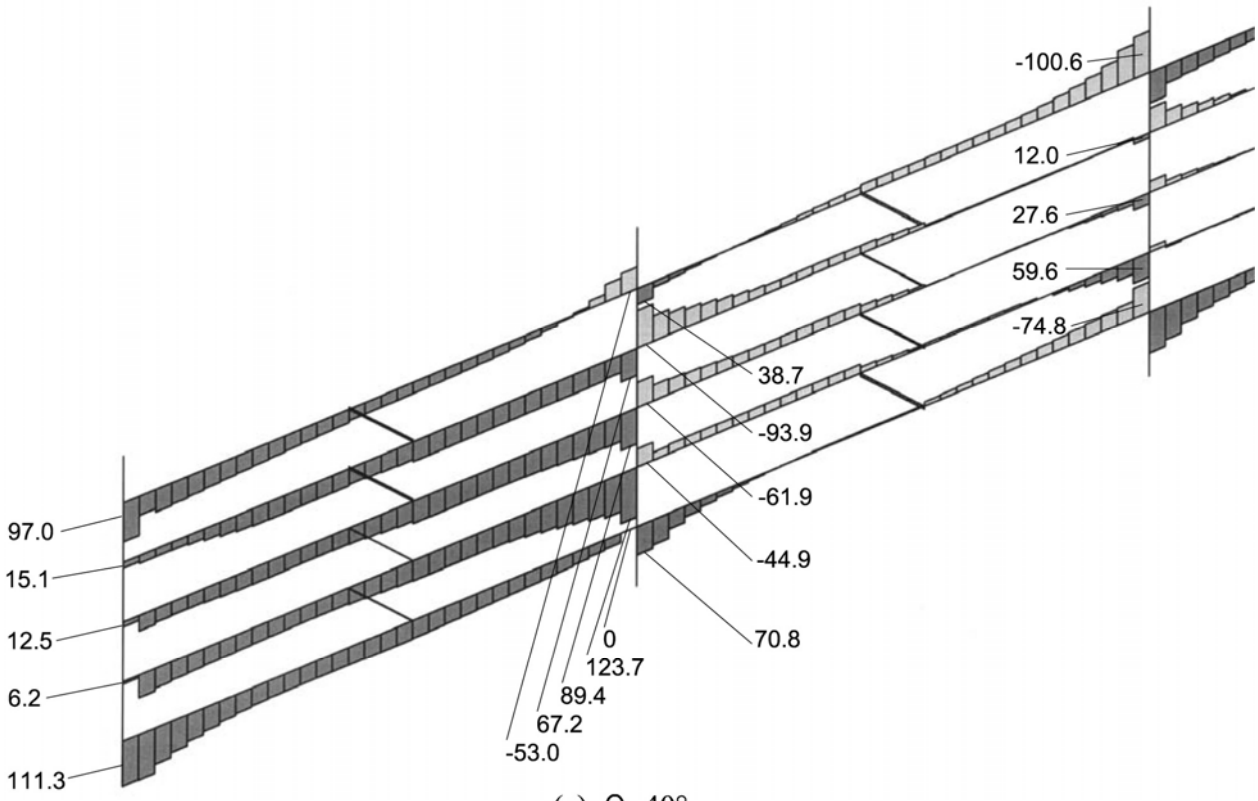

(c) Θ=40°

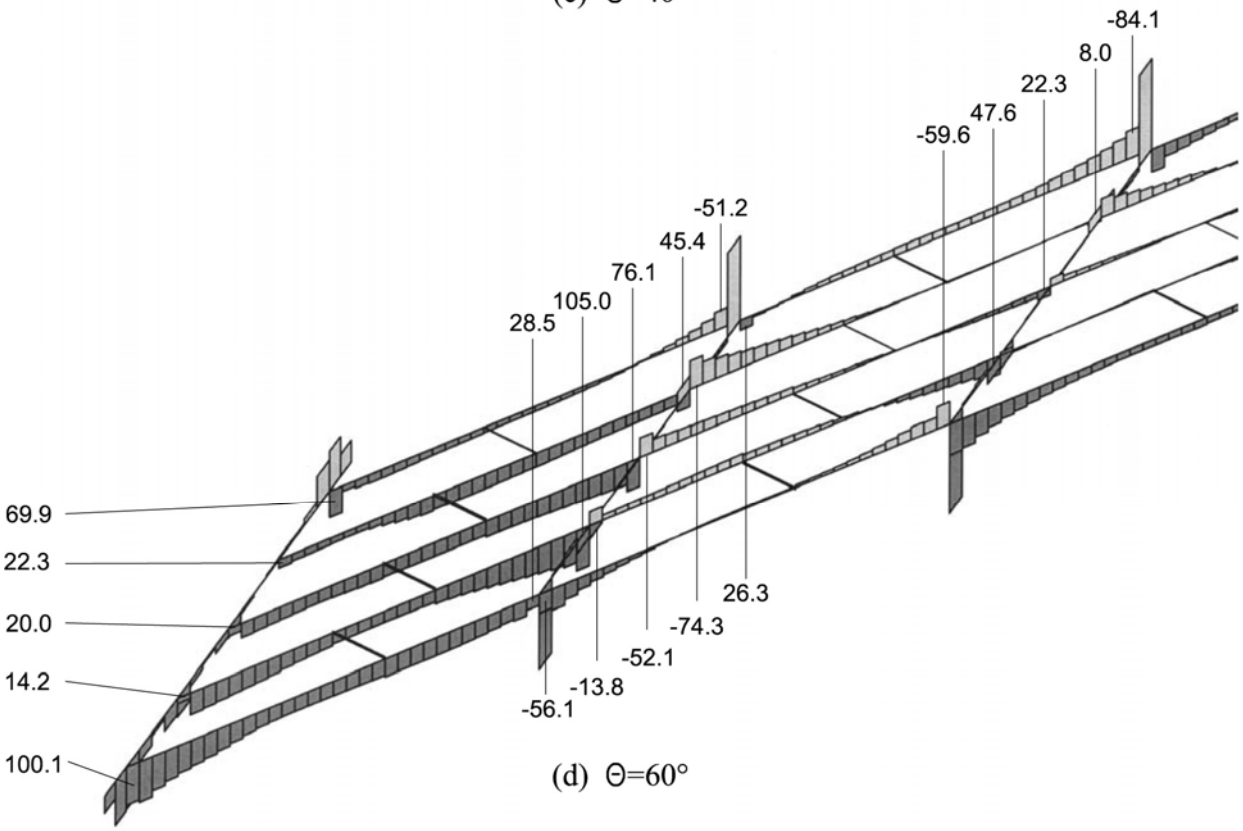

(d) Θ=60°

Figure 4-29. Shear forces (in kN) in beams and diaphragms caused by thermal gradient (continued).

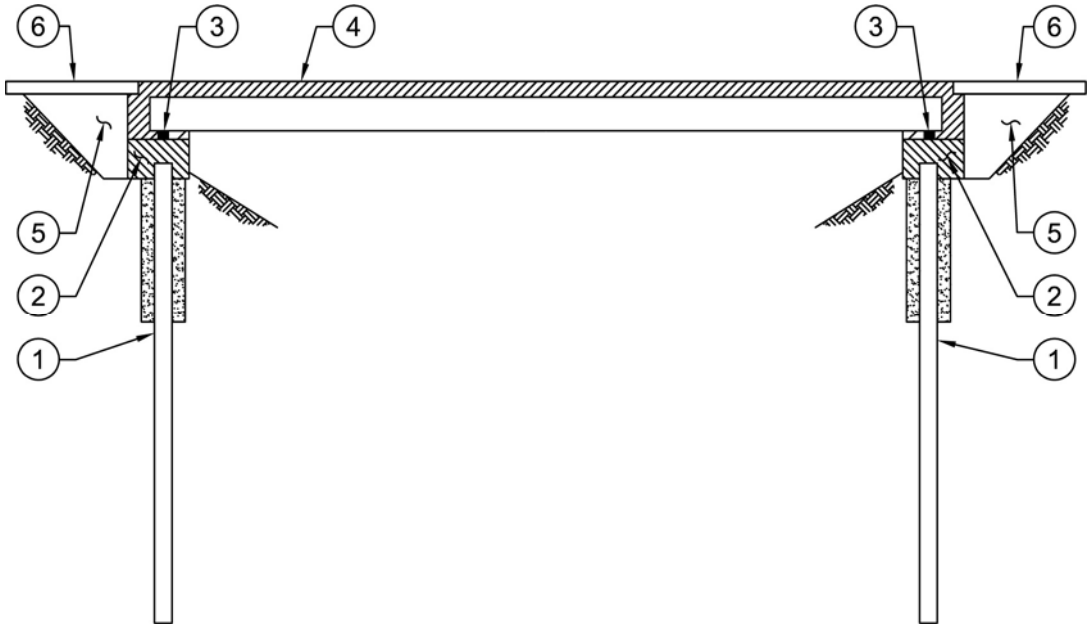

Figure 4-30. Construction sequence for integral abutment bridge.

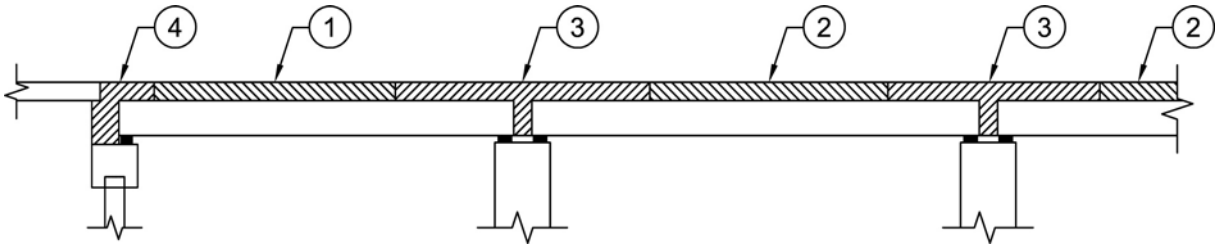

Figure 4-31. Suggested deck concrete placement sequence.

Table 4-1. Values of parameters in pier models.

Case ID	Peak Deflection, mm	Pier Height, m	Foundation Rotational Stiffness kN-m/rad/mm		Ultimate Creep Coefficient	Vertical Load,* $\frac{kN}{mm}$	Age of Concrete at Loading, days
			Bottom	Top			
Case 1, Baseline	51	6.1	160	0	1.3	0.53	30
Case 2	102	6.1	160	0	1.3	0.53	30
Case 3	51	9.2	160	0	1.3	0.53	30
Case 4	51	6.1	53.4	0	1.3	0.53	30
Case 5	51	6.1	160	0	1.7	0.53	30
Case 6	51	6.1	160	0	1.3	1.58	30
Case 7	51	6.1	160	0	1.3	0.53	420
Case 8	51	6.1	160	790	1.3	0.53	30
Case 9	102	9.2	160	0	1.3	0.53	30
Case 10	51	6.1	160	0	1.3	3.15	30
Case 11	102	9.2	53.4	0	1.3	0.53	30
Case 12	102	6.1	160	0	1.3	3.15	30

*Load per unit width of pier cap.

Table 4-2. Results of pier study.

Case ID	Parameter Variables	Inelastic Moment / Elastic Moment	Percentage of Peak Deflection Caused by Foundation Rotation
Case 1	Baseline	0.64	39
Case 2	Peak Deflection	0.52	32
Case 3	Pier Height	0.80	30
Case 4	Foundation Rotational Stiffness	0.96	79
Case 5	Creep Coefficient	0.63	38
Case 6	Vertical Load	0.82	50
Case 7	Concrete Age	0.63	39
Case 8	Integral Connection	0.70	53
Case 9	Peak Deflection Pier Height	0.57	20
Case 10	Vertical Load	0.92	57
Case 11	Peak Deflection Pier Height Foundation Rotational Stiffness	0.83	43
Case 12	Peak Deflection Vertical Load	0.83	45

Table 4-3. Comparison between maximum measured and predicted bridge movements.

	Boone River Bridge	Maple River Bridge	Kingsport Bridge	Cass County Bridge
Bridge Type	Prestressed Concrete	Composite Steel	Prestressed Concrete	Prestressed Concrete
Location	Webster City, IA	Panbury, IA	Kingsport, TN	Fargo, ND
Length, m	98.9	97.6	823.2	137.2
α Concrete, millionths/°C	8.1	9.0	9.0	10.8
α Steel, millionths/°C	N/A*	11.7	N/A	N/A
α Concrete Tested?	Yes	Yes	Yes	No
Minimum Measured Shade Temperature	-32 °C	-29 °C	-17 °C	-24 °C
Maximum Measured Shade Temperature	39 °C	45 °C	34 °C	34 °C
Maximum Measured Movement, mm	49.5	64.8	286.3	74.7
Calculated Movement With Site-Measured Shade Temperatures, mm	44.5	61.7	328.7	71.6
Calculated Movement With Climatic Atlas Shade Temperatures, mm	42.2	60.5	332.7	75.7
Calculated Movement With ASHRAE Shade Temperatures, mm	38.6	55.9	320.3	74.9
Calculated Movement With NCHRP Report 276 Shade Temperatures, mm	30.7	45.0	250.7	61.0

*N/A = not applicable

1 m = 3.28 ft, 1 mm = 0.039 inch, 1 °C = 1.8 °F

Table 4-4. Solar increment values based on girder type and bridge location.

Zone	T_1	Concrete $\Delta\overline{T}$	Composite Steel $\Delta\overline{T}$
1	30 °C	8 °C	6 °C
2	26 °C	7 °C	5 °C
3	23 °C	6 °C	4 °C
4	21 °C	5 °C	4 °C

1 °C = 1.8 °F

Table 4-5. Comparison between measured and predicted bridge movements.

	Boone River Bridge	Maple River Bridge	Kingsport Bridge	Cass County Bridge
Maximum Measured Movement, mm	49.5	64.8	286.3	74.7
Calculated Movement with ASHRAE Shade Temperature and Proposed Equations (4-14 through 4-17), mm	44.5	62.2	340.9	75.4

1 mm = 0.039 inch

Table 4-6. Values of Γ magnification factor.

Case No.	Design Condition	For Bridge Expansion		For Bridge Contraction	
		Total	End	Total	End
1(a)	Conventional Design of Prestressed Bridge	1.50	1.60	1.30	1.35
1(b)	Cast-in-Place Concrete Bridge	1.50	1.60	1.30	1.40
1(c)	Composite Steel Bridge	1.50	1.70	1.45	1.50
2	Reexpansion After Full Contraction	1.10	1.20	—	—
3	Emanual and Hulsey Modification[47] to Case 1(a)	1.85	2.05	1.35	1.45

Table 4-7. Comparison of measured temperature differentials with AASHTO LRFD positive gradients.

Bridge	Location	Type	Monitoring Period, Years	Measured Differential,* °C	AASHTO LRFD Gradient, °C
—	Alaska	Composite Steel	—	19	18
CTL Test	Illinois	Prestressed Concrete	1.5	15	26
CTL Test	Illinois	Composite Steel	1.5	13	21
Boone River	Iowa	Prestressed Concrete	2	17	26
Maple River	Iowa	Composite Steel	2	17	21
Red River	Louisiana	Prestressed Segmental Box	1	16	26
U.S. 190	Louisiana	Prestressed Concrete	—	6	26
—	Missouri	Composite Steel	—	22	21
PennDOT	Pennsylvania	Prestressed Segmental Box	1	28	23

*Difference between the temperature at the top of the concrete deck slab and the minimum temperature in the section.

Table 4-8(a). Parameters considered in the study.

Parameter	Value
Rolled Beams	W36x135 to W36x230
Plate Girder Shapes	FHWA 1, 2, 3, and 4, Types T1 and T2
Number of Spans	two, three, four, and multispan
Girder Spacings	1.2 m to 4.8 m
Concrete Deck Thicknesses	178 mm to 270 mm

Table 4-8(b). Plate girder shapes.

	Flange		
Section	Top	Bottom	Web
FHWA 1	305 mm x 13 mm (12 x 0.5 inches)	305 mm x 19 mm (12 x 0.75 inches)	13 mm x 1.7 m (0.5 x 67 inches)
FHWA 2	305 mm x 13 mm (12 x 0.5 inches)	406 mm x 22 mm (16 x 0.88 inches)	13 mm x 1.7 m (0.5 x 67 inches)
FHWA 3	305 mm x 18 mm (12 x 0.69 inches)	406 mm x 29 mm (16 x 1.13 inches)	16 mm x 1.7 m (0.63 x 67 inches)
FHWA 4	305 mm x 30 mm (12 x 1.19 inches)	406 mm x 38 mm (16 x 1.5 inches)	16 mm x 1.7 m (0.63 x 67 inches)
T1	305 mm x 30 mm (12 x 1.19 inches)	406 mm x 13 mm (16 x 0.5 inches)	16 mm x 1.7 m (0.63 x 67 inches)
T2	305 mm x 13 mm (12 x 0.5 inches)	305 mm x 22 mm (12 x 0.88 inches)	16 mm x 1.7 m (0.63 x 67 inches)

Table 4-8(c). Concrete deck thickness.

Girder Spacing, m (ft)	1.22─2.13 (4─7)	2.44 (8)	2.74 (9)	3.05 (10)	3.35 (11)	3.65 (12)	3.96 (13)	4.27 (14)	4.57 (15)	4.88 (16)
Deck Thickness, mm (inches)	178 (7)	191 (7.5)	203 (8)	216 (8.5)	222 (8.75)	229 (9)	241 (9.5)	248 (9.75)	254 (10)	267 (10.5)

Table 4-9. Maximum concrete deck compressive stresses for gravity, thermal, and shrinkage loading.

Section	Maximum Concrete Deck Compressive Stress, MPa			
		Thermal and Shrinkage		
	Live Load	Gradient	Longitudinal	Total
W36x135 at				
1.2-m spacing	6.58	4.25	1.23	12.06
2.4-m spacing	4.99	4.43	1.54	10.96
3.7-m spacing	3.97	4.83	1.49	10.29
4.9-m spacing	3.53	5.17	1.37	10.07
W36x160 at				
1.2-m spacing	6.84	4.24	1.12	12.20
2.4-m spacing	5.30	4.42	1.46	11.18
3.7-m spacing	4.21	4.81	1.43	10.45
4.9-m spacing	3.68	5.16	1.34	10.18
W36x182 at				
1.2-m spacing	7.03	4.23	1.05	12.31
2.4-m spacing	5.67	4.41	1.39	11.47
3.7-m spacing	4.27	4.80	1.39	10.46
4.9-m spacing	3.83	5.14	1.31	10.28
W36x210 at				
1.2-m spacing	7.20	4.22	0.97	12.39
2.4-m spacing	5.82	4.40	1.32	11.54
3.7-m spacing	4.54	4.79	1.34	10.67
4.9-m spacing	3.92	5.13	1.28	10.33
W36x230 at				
1.2-m spacing	7.58	4.21	0.92	12.71
2.4-m spacing	6.04	4.39	1.27	11.70
3.7-m spacing	4.87	4.78	1.31	10.96
4.9-m spacing	4.11	5.12	1.25	10.48

1 MPa = 145.03 lbf/inch^2

Table 4-10. Maximum steel girder compressive stresses for dead and secondary loading, A36 grade steel, 3.7-m spacing.

Section	Maximum Steel Girder Compressive Stress, MPa			
		Secondary Loading		
	Dead Load	Gradient	Longitudinal	Total
W36x135	59.3	139.3	8.3	206.9
W36x182	60.0	107.6	7.6	175.2
W36x230	60.0	87.6	6.9	154.5
FHWA 2	66.9	121.4	10.3	198.6
FHWA 4	69.6	82.7	9.0	161.3

Table 4-11. Maximum steel girder compressive stresses for dead and secondary loading, A572 grade steel, 3.7-m spacing.

Section	Maximum Steel Girder Compressive Stress, MPa			
		Secondary Loading		
	Dead Load	Gradient	Longitudinal	Total
W36x135	86.2	139.3	8.3	233.8
W36x182	89.6	107.6	7.6	204.8
W36x230	87.6	87.6	6.9	182.1
FHWA 2	97.2	121.4	10.3	228.9
FHWA 4	100.7	82.7	9.0	192.4

Table 4-12. Percentage of calculated steel girder stress to allowable steel girder stress.

Section	Percentage of Calculated to Allowable Steel Girder Stress							
	1.2-m Girder Spacing				3.1-m Girder Spacing			
	Load Combination 2		Load Combination 3		Load Combination 2		Load Combination 3	
	A36	A572	A36	A572	A36	A572	A36	A572
W36x135	91	82	116	109	143	118	147	131
W36x160	88	80	113	108	131	111	139	126
W36x182	85	79	114	108	123	106	134	122
W36x230	81	78	109	105	113	97	126	116
FHWA 2	91	84	113	107	137	116	139	126
FHWA 4	86	81	109	105	119	101	126	116

Table 4-13. Variables considered in the sensitivity study.

Variable	Value
Ultimate Creep Coefficient	1.625, 3.25
Ultimate Shrinkage Strain	100 millionths , 600 millionths
Girder Age at Continuity	17 days
Positive Moment Continuity Reinforcement	129 mm^2 to 4645 mm^2
Heat of Hydration Effect	8 °C
Temperature Gradients	AASHTO LRFD
Superimposed Dead Load	1.44 kN/m^2

Table 4-14. Center pier moments for AASHTO Type IV girders.

Center Pier Moments	Ultimate Deck Shrinkage	
	100 millionths	600 millionths
AASHTO Temperature Gradient	1597 kN-m	1597 kN-m
Deck Heat of Hydration	-457 kN-m	-457 kN-m
Creep and Shrinkage	1017 kN-m	517 kN-m
Subtotal	2157 kN-m	1657 kN-m
Superimposed Dead Load	-393 kN-m	-393 kN-m
Total	1764 kN-m	1264 kN-m
M_{cr_1} ($f_r = 4\sqrt{f'_c}$)	472 kN-m	472 kN-m
M_{cr_2} ($f_r = 7.5\sqrt{f'_c}$)	883 kN-m	883 kN-m
M_y	313 kN-m	313 kN-m

Table 4-15. Combination of live load and secondary effects.

Section	Deck Reinforcement Ratio	Deck Reinforcement Stress, MPa			
		Live Load Analyses			
		Gross Section	Cracked Section	Secondary Effects	Total*
AASHTO IV	0.0100	228.6	181.1	34.5	215.6
AASHTO IV	0.0133	184.3	147.8	33.7	181.5
AASHTO IV	0.0166	143.1	116.3	32.8	149.1
BT-72	0.0117	211.7	178.6	31.9	210.5
BT-72	0.0156	169.5	144.4	31.2	175.6
BT-72	0.0195	135.9	117.0	30.3	147.3

* Total deck reinforcement stress is based on combining the cracked-section live load analysis with the secondary effects.

Table 4-16. Axial force in beams caused by the thermal gradient.

Location	Beam*	Axial Force, kN**			
		Skew Angle			
		0°	20°	40°	60°
At Center of Exterior Span	1	935	868	859	854
	2	685	716	739	757
	3	623	676	699	690
	4	690	707	712	681
	5	939	854	837	846
	Average	774	764	769	766
At First Pier	1	975	1113	1197	1331
	2	1317	1313	1331	1304
	3	1371	1286	1246	1157
	4	1317	1317	1343	1308
	5	975	1126	1242	1482
	Average	1191	1231	1272	1316
At Center of Interior Span	1	1210	1113	1068	970
	2	975	988	979	912
	3	921	970	979	926
	4	983	1001	1001	930
	5	1215	1135	1113	1050
	Average	1061	1041	1028	958
At Center Pier	1	716	868	975	1161
	2	1055	1055	1090	1144
	3	1104	1023	988	970
	4	1055	1055	1090	1135
	5	712	868	975	1148
	Average	928	974	1024	1112

* Beam 1 is near obtuse corner of deck at left abutment and Beam 5 is near the acute corner.

** Positive number indicates tension.

Table 4-17. Shear force in beams caused by the thermal gradient.

Location	Beam*	Shear Force, kN**			
		Skew Angle			
		0°	20°	40°	60°
At Abutment	1	124.6	108.6	97.0	69.9
	2	0.9	10.7	15.1	22.3
	3	-6.2	7.1	12.5	20.0
	4	0.9	4.5	6.2	14.2
	5	125.5	114.8	111.3	100.1
	Average	49.1	49.1	48.4	45.3
At Exterior-Span Side of First Pier	1	-51.2	-47.6	-53.0	-51.2
	2	109.5	85.4	67.2	45.4
	3	115.3	96.6	89.4	76.1
	4	107.7	114.4	123.7	105.0
	5	-48.5	-15.6	0	28.5
	Average	46.6	46.6	45.5	40.8
At Interior-Span Side of First Pier	1	76.1	48.5	38.7	26.3
	2	-78.8	-84.1	-93.0	-74.3
	3	-86.3	-67.6	-61.9	-52.1
	4	-80.5	-58.7	-44.9	-13.8
	5	80.5	68.1	70.8	56.1
	Average	-17.8	-18.8	-18.1	-11.6
At Side of Center Pier	1	-112.1	-101.9	-100.6	-84.1
	2	46.3	24.9	12.0	8.0
	3	51.6	32.9	27.6	22.3
	4	44.1	49.4	59.6	47.6
	5	-107.7	-81.9	-74.8	-59.6
	Average	-15.6	-15.3	-15.2	-13.2

* Beam 1 is near obtuse corner of deck at left abutment and Beam 5 is near the acute corner.

** Positive number indicates tension.

5. DESIGN RECOMMENDATIONS

5.1 INTRODUCTION

The overall objectives of this jointless bridge project were to develop a greatly expanded knowledge of the behavior of jointless bridges and to provide a scientific basis for their design. The work performed to achieve these objectives is summarized in chapters 3 and 4 of this volume and is presented in detail in this project's experimental report and analytical report.[14-15] This chapter presents design recommendations based on the work carried out in this project and a review of the literature. This chapter proposes procedures for:

1. Determination of expected bridge movement.
2. Design of abutments, including piles, pile-to-pile-cap connections, wingwalls, and beam-to-abutment connections.
3. Pier design.
4. Design considerations for the effects of secondary continuity forces.
5. Design of approach slabs.
6. Considerations for details to accommodate bridge movement.

The recommendations in this chapter are not intended to be all-inclusive guidelines for designing jointless bridges with integral abutments. They are intended as design procedures and considerations to supplement or modify current practices in areas perceived to have a significant degree of uncertainty, or where there is a less than full understanding of behavior.

5.2 DETERMINATION OF EXPECTED MOVEMENT

The first step in designing a jointless bridge is the determination of expected bridge movements. Without expansion joints, the piers, abutments, and approach slabs must be designed and detailed to accommodate the bridge's thermal movements, creep and shrinkage movements. The maximum length and skew angle for jointless bridges are only limited by the ability of the piles to tolerate the expected movements and by the ability of the details at the pier caps, abutments, and approach slabs to accommodate those movements. Therefore, a reasonable upperbound estimate of the movement This determination of expected movement includes establishing the effective temperature

range, and calculating the maximum movement based on temperature range, creep and shrinkage effects, and restraint by the substructure.

The 1998 AASHTO LRFD code specifies, in the absence of more precise information, uniform temperature ranges for steel of −18 °C to 49 °C (0 °F to 120 °F) for moderate climates and −34 °C to 49 °C (−30 °F to 120 °F) for cold climates.[43] For concrete, the specified temperature ranges are −12 °C to 27 °C (10 °F to 80 °F) for moderate climates and −18 °C to 27 °C (0 °F to 80 °F) for cold climates. From the data presented in the experimental report[14] and in chapter 4 of this volume, AASHTO guidelines are usually too conservative for steel bridges and not conservative for concrete structures.

Also, AASHTO LRFD indicates that the setting temperature should be taken as the actual air temperature averaged over the 24-hour period immediately preceding the setting event. For jointless bridges, the setting event occurs when the longitudinal continuity is established by tying the bridge deck to the integral abutments. This setting temperature, however, would be unknown to the designer. In addition, other uncertainties, as discussed in section 4.4.2 of this volume, are involved in the calculation of the expected movement.

The following are recommendations to more precisely determine the effective bridge temperature range and to use the data to predict maximum bridge movement while accounting for uncertainties about the actual bridge response. The background for these recommendations is included in chapter 7 of the analytical report.[15]

5.2.1 Determination of the Range of Effective Temperature

The effective bridge temperature, as used here, is the average temperature in the structure, which governs the overall longitudinal movement of the bridge superstructure. The following procedures for the range of the effective bridge temperature are based on:

- Minimum and maximum shade air temperatures determined from the ASHRAE data[40] and included in the tables in appendix A of this volume.
- Relationships between 24-hour mean shade air temperatures and the minimum and maximum air shade temperatures.
- Relationships between the minimum and maximum effective bridge temperatures (excluding the solar effects) and the 24-hour mean shade air temperatures.
- Additional uniform temperature increment, $\Delta\overline{T}$, caused by direct solar radiation.

To determine the range of the effective bridge temperatures:

1. Obtain the minimum and maximum shade temperatures from the State weather database in appendix A, for the weather stations nearest the bridge, and interpolate as needed. The introduction in appendix A indicates adjustments for elevation change.

2. Determine the solar zone for the bridge location from figure 3.12.3-1 in the 1998 AASHTO LRFD specifications,[43] and the corresponding solar increment, $\Delta\overline{T}_{solar}$, from table 4-4 of this volume.

3. Calculate the minimum and maximum effective bridge temperatures from the following relationships:

   For concrete bridges:

$$T_{\underset{eff}{min}} = 1.00\, T_{\underset{shade}{min}} + 5\ °C\ (9\ °F) \tag{5-1}$$

$$T_{\underset{eff}{max}} = 0.97\, T_{\underset{shade}{max}} - 2\ °C\ (3\ °F) + \Delta\overline{T}_{solar} \tag{5-2}$$

   For composite steel bridges:

$$T_{\underset{eff}{min}} = 1.04\, T_{\underset{shade}{min}} + 2\ °C\ (3\ °F) \tag{5-3}$$

$$T_{\underset{eff}{max}} = 1.09\, T_{\underset{shade}{max}} - 0\ °C\ (3\ °F) + \Delta\overline{T}_{solar} \tag{5-4}$$

   where,

   $T_{\underset{eff}{min}}$ = minimum effective bridge temperature

   $T_{\underset{eff}{max}}$ = maximum effective bridge temperature

   $T_{\underset{shade}{min}}$ = minimum shade temperature from the weather data, based on bridge location (see appendix A)

   $T_{\underset{shade}{max}}$ = maximum shade temperature from the weather data, based on bridge location (see appendix A)

   $\Delta\overline{T}_{solar}$ = uniform temperature change from direct solar radiation, based on girder type and bridge location (see table 4-4).

5.2.2 Determination of Maximum Movements

5.2.2.1 *Determination of Longitudinal End Movements*

The following procedures are recommended to determine end movements in the longitudinal direction while accounting for the uncertainty of calculations. Magnification factors, Γ's, to account for the level of uncertainty based on the Monte Carlo study discussed in section 4.4.2, are listed in table 4-6 of this volume. It is assumed that the date and temperature when the deck was cast are unknown and that no specific data on the material properties of the concrete are available other than 28-day compressive strength, f'_c.

To determine the maximum end movements of a prestressed concrete bridge:

1. From the weather database in appendix A, determine the mean construction temperature for locations nearest the bridge, and interpolate to determine a mean construction temperature for the bridge location. Alternatively, determine a mean construction temperature from data for stations in the same part of the country with similar minimum and maximum shade temperatures to those determined for the bridge location from Step 1 in section 5.2.1 above.

2. To calculate end movements:

    a. Determine the minimum and maximum effective bridge temperatures from equations 5-1 and 5-2, respectively.

    b. Use typical design values of 10.8 millionths/°C (6.0 millionths/°F) for the coefficient of thermal expansion of concrete, values for creep and shrinkage from ACI 209R-92,[44] and 4,700 $\sqrt{f'_c}$, MPa (57,000 $\sqrt{f'_c}$, lbf/inch^2) for the modulus of elasticity of concrete.

    c. Use the procedure presented by Zederbaum[31] to determine the point of zero movement or the point of fixity within the bridge based on the stiffness of the piers and the abutments. This procedure and its application are explained in section 5.4 of this volume. This lateral stiffness of the piers can be determined as described in section 5.4 of this volume, and the use of the Clough and Duncan data[11] discussed in section 5.3.3 is recommended, to determine the passive restraint for integral abutments. The equivalent cantilever method or the computer program COM624P,[17] as described in section 5.3.1, can be used to estimate the lateral stiffness of the abutment piles. Since the responses

of the piers and abutments are nonlinear, the stiffnesses should be based on a preliminary estimate of the end movements. It should be noted, however, that for a symmetrical bridge, the point of fixity would be at the longitudinal center of the bridge.

d. The following equations are used to determine the strain values for a prestressed concrete bridge. Changes in length are determined by multiplying the strain by the total initial length:

$$\varepsilon_{th} = \alpha \, \Delta T \tag{5-5}$$

$$\varepsilon_{sh} = \varepsilon_{sh_{girder}} + \frac{\varepsilon_{sh_{deck}} - \varepsilon_{sh_{girder}}}{1 + \dfrac{(EA)_{girder}}{(EA)_{deck}}} \tag{5-6}$$

$$\varepsilon_{cr} = \varepsilon_{cr_{girder}} \left[\frac{1}{1 + \dfrac{(EA)_{girder}}{(EA)_{deck}}} \right] \tag{5-7}$$

$$\Delta \ell = \Gamma \varepsilon_{total} \ell \tag{5-8}$$

where,

ε_{th} = thermal strain
ε_{sh} = shrinkage strain
ε_{cr} = creep strain
α = coefficient of thermal expansion
E = modulus of elasticity
A = cross-sectional area
ℓ = length from calculated point of fixity to end of bridge. Note that, for a nonsymmetrical bridge, two different lengths are involved.
Γ = magnification factor to account for uncertainty

$$\varepsilon_{total} = \varepsilon_{th} - \varepsilon_{sh} - \varepsilon_{cr} \text{ for expansion} \tag{5-9}$$

$$\varepsilon_{total} = -\varepsilon_{th} - \varepsilon_{sh} - \varepsilon_{cr} \text{ for contraction} \tag{5-10}$$

$\Delta\ell$ = maximum end movement.

3. Maximum expansion typically occurs shortly after construction. For this maximum expansion (Case 1[a] expansion in table 4-6), use the temperature differential between the maximum effective bridge temperature and the mean construction temperature for thermal expansion, and a time span equal to one-quarter of the construction season for creep and shrinkage contraction with the beams assumed to be 90 days old when the deck is cast. Based on the Monte Carlo studies, the calculated end movements should be increased by a Γ factor of 1.60 (see table 4-6) to account for the uncertainties that are described in section 4.4.3, with a 98 percent confidence that the movement will be less than that calculated.

4. For maximum contraction after several years of service (Case 1[a] contraction in table 4-6), use the temperature differential between the minimum effective bridge temperature and the mean construction temperature for thermal contraction, and ultimate creep and shrinkage values with the beams assumed to be 10 days old at the time of casting of the deck. Based on the Monte Carlo studies, the calculated end movement should be increased by a Γ factor of 1.35 (see table 4-6) to account for uncertainties, with a 98 percent confidence that the movement will be less than that calculated.

5. For maximum thermal reexpansion from a starting point of full contraction (Case 2 in table 4-6), the full range of effective bridge temperatures should be used without any creep or shrinkage movement. The resulting calculated end movements should be multiplied by a Γ factor of 1.20 (see table 4-6) to account for uncertainties in the calculation.

For reinforced concrete bridges, similar procedures can be used to determine the maximum expansion and contraction end movements. However, shortening caused by creep is not a factor. Calculated end movements for reinforced concrete bridges should be increased by the Γ factors, shown with Case 1(b) in table 4-6, of 1.60 for maximum expansion and 1.40 for maximum contraction. A Γ factor of 1.20 can be used for Case 2, which is maximum thermal reexpansion from a starting point of full contraction. Note that the magnitudes of the multipliers, Γ's, for Cases 1(a) and 1(b) are significantly larger

than the multiplier, Γ, for Case 2 because of the uncertainty and variability of the construction temperature.

For composite steel bridges, the procedures used to estimate the maximum end movements are also similar to the procedures outlined above for the prestressed concrete bridges, except that a modulus of elasticity of 20×10^4 MPa (29×10^6 lbf/inch^2) and a coefficient of thermal expansion of 11.7 millionths/°C (6.5 millionths/°F) should be used for the steel girders. These values are recommended by AASHTO for structural steel. The results of the Monte Carlo study for composite steel bridges indicated that calculated end movements should be increased by the Γ factors for Case 1(c) of 1.70 for maximum expansion and 1.50 for maximum contraction. A Γ factor of 1.2 can be used for Case 2, which is the maximum thermal reexpansion from a starting point of full contraction.

If sufficient information regarding the composition of the concrete is available to the designer, a more accurate value for the coefficient of thermal expansion of concrete can be obtained by using the Emanual and Hulsey model[47] to estimate the value of the coefficient of thermal expansion of concrete. Calculated end movements using the more accurate Emanual and Hulsey coefficient of thermal expansion of concrete should be increased by Γ factors for Case 3 (table 4-6) of 2.05 for maximum expansion and 1.45 for maximum contraction. These Γs are greater than the values calculated for the conditions with Cases 1(a) or 1(b). This is caused by the difference in calculating the design thermal movements rather than the variability of the predicted movements. The coefficient of thermal expansion design value of 10.8 millionths/°C (6.0 millionths/°F) recommended by AASHTO and used for Cases 1(a) and 1(b) is conservatively high when compared to the figure for the average of the database in appendix B of the analytical report.[15] The average coefficient of thermal expansion for concrete in the database, which is described in appendix B of the analytical report[15], is 8.8 millionths/°C (4.9 millionths/°F). Therefore, the conventional design calculated value of movement already includes some margin of safety.

Note that when using the Emanual and Hulsey model[47] to estimate α, the concrete for the deck slab is commonly different than the concrete for the beam. Therefore, an effective coefficient of thermal expansion, α_e, for the composite section can be calculated as:

$$\alpha_e = \frac{(\alpha EA)_{girder} + (\alpha EA)_{deck}}{(EA)_{girder} + (EA)_{deck}} \quad (5\text{-}11)$$

The end movements, determined from Case 1 for maximum expansion and maximum contraction, are recommended for use in determining a design range of abutment movements. The larger of these two movements should be used for comparison with the limiting pile displacement, Δ, when designing abutment piles as described in section 5.3.1.

The end movements, $\Delta\ell$, determined from Case 2 for maximum reexpansion from a starting point of full contraction, should be used to determine passive soil pressure on the abutment, as further discussed in section 5.3.3. In addition, the end movements determined for Cases 1 and 2 should be used to obtain the forces on the abutment piles to use in designing the connection between the piles and footing, and in designing the abutment breastwall, as described in sections 5.3.2 and 5.3.3. Note that the pile may not yield under the initial expansion from Case 1, which is typically a smaller movement, but may do so with Case 1 contraction or with the reexpansion from Case 2, as shown in the example in figure 5-1.

It should also be noted that the above procedures can be used to estimate design joint movements in bridges with expansion joints. In those cases, however, calculating the point of fixity would be much simpler.

5.2.2.2 *Determination of Transverse End Movements*

As described in section 4.4.4, a bridge with a skew angle, $\theta > 20°$, may theoretically rotate in the plane of the superstructure because of the transverse component of the passive soil pressure resisting thermal expansion. Therefore, in heavily skewed bridges, there will be a transverse component of the abutment movement associated with longitudinal thermal expansion unless specific measures are taken to attempt to restrain the movement. The maximum transverse movement will occur at the acute corner of the bridge deck, Δ_{t1}, for Corner 1, as seen in figure 4-19. For a typical stub abutment on HP10 x 42 piles, data from figure 4-20 can be used for a rough estimate of this expected movement. The $\Delta\ell$ used with the data in figure 4-20 should be based on Case 2, which is the maximum expected reexpansion after full contraction. For the effect of the wingwalls, interpolate between the data in figure 4-20, based on the ratio of the effective lengths of the wingwalls to the length of the abutment. The effective length of a wingwalls is the longitudinal component of the wingwall. For more accurate estimates of transverse movement associated with rotation caused by the restraint of longitudinal expansion, the equations in table B-1 of appendix B of this volume, modified as needed for other pile or

wingwall orientations, can be used to analyze specific skewed abutments. It should be noted that the equations in table B-1 of appendix B are still an approximate solution, in that the biaxial bending effects in the pile for combined bending about the strong and weak axes are uncoupled and treated independently. Also, the responses of the abutment piles to longitudinal movement and superstructure rotation are treated independently and superimposed as if the responses were linear. These approximations simplify the solution and are reasonable considering the unknowns in the actual soil and pile response. If desired, nonlinear finite element analyses could be used to increase precision.

The transverse movement of the obtuse corner of the bridge deck, Δ_{t2}, for Corner 2 in figure 4-19 can be determined from the estimated Δ_{t1} (above) as follows:

$$\Delta_{t2} = \Delta_{R2} \cos \alpha_2 \tag{5-12}$$

where,

$$\Delta_{R2} = \beta \left[\left(\frac{W}{2} \right)^2 + \left(\ell - \frac{W}{2} \tan \theta \right)^2 \right]^{0.5} \tag{5-13}$$

$$\beta = \frac{\Delta_{R1}}{\left[\left(\frac{W}{2} \right)^2 + \left(\ell + \frac{W}{2} \tan \theta \right)^2 \right]^{0.5}} \tag{5-14}$$

$$\Delta_{R1} = \frac{\Delta_{t1}}{\cos \alpha_1} \tag{5-15}$$

$$\alpha_1 = \tan^{-1} \left[\frac{W}{2 \left(\ell + \frac{W}{2} \tan \theta \right)} \right] \tag{5-16}$$

$$\alpha_2 = \tan^{-1} \left[\frac{W}{2 \left(\ell - \frac{W}{2} \tan \theta \right)} \right] \tag{5-17}$$

ℓ = length of bridge along longitudinal axis from the point of fixity to the end of the bridge at the abutment

W = width of bridge perpendicular to the longitudinal axis

θ = skew angle.

In addition to transverse movement, Δ_{t1}, caused by the rotation of the superstructure, there will also be transverse thermal expansion. This movement will be small for bridges with three lanes or less. However, to estimate this thermal expansion, Δ_{te}, determine the difference between the maximum 24-hour mean temperature and the mean construction temperature, and use this with the bridge width, W, as follows:

$$T_{\underset{max}{24}} = 0.977\, T_{\underset{shade}{max}} - 5.44\ °C\ (9.05\ °F) \tag{5-18}$$

$$\Delta T = T_{\underset{max}{24}} - T_{mc} \tag{5-19}$$

$$\Delta_{te} = 1.6\ (\alpha \Delta T)\frac{W}{2} \tag{5-20}$$

where,

$T_{\underset{shade}{max}}$ = maximum shade temperature from tables in appendix A

T_{mc} = mean construction temperature from tables in appendix A

α = 10.8 millionths/°C (6.0 millionths/°F).

The factor of 1.6 in equation 5-20 is taken from table 4-6 to account for the uncertainty of the calculated expansion in reinforced concrete.

The transverse movement Δ_{te} should be added to Δ_{t1} at the acute corner (bridge-deck side) to determine transverse soil forces and pile forces for the design of the wingwall, as will be discussed in section 5.3.4. Because the transverse expansion Δ_{te} will tend to counteract the transverse movement Δ_{t2} at the obtuse corner (bridge-deck side), it is recommended the resulting forces on this wingwall be evaluated both with and without $\Delta_{te,}$ to examine and design for the more severe condition.

The transverse movements for skewed bridges should also be used to detail the abutments at all interfaces with other components, such as the approach pavement, barrier walls, the pavement for slope protection, and drainage components.

5.3 DESIGN OF ABUTMENTS

5.3.1 Design Procedure for Flexible Piles Supporting Integral Abutments: Equivalent Cantilever Method

A typical arrangement for an integral abutment on piles is shown in figure 5-2. Abutment piles should be designed for vertical forces from dead and live loads. In addition, the integral abutment will induce additional vertical loading on its piles because of negative moments generated by the passive soil pressure and horizontal pile forces, as described later in section 5.3.3.1. Also, with continuous bridges, secondary moments caused by the differential strain between the deck and the girders generate a redistribution of dead load that may be significant enough to be considered in the design of the pile, as discussed later in section 5.5.2. The objective of the design concepts presented in this section is to accommodate longitudinal movement of integral abutments through pile bending while retaining adequate vertical-loading capacity in the pile.

Detailed investigations at Iowa State University[26] and by Abendroth, et al.,[2] which involved full-scale and model pile tests and nonlinear finite element analyses of the pile-soil system, resulted in an equivalent cantilever method for the analysis and design of piles under integral abutments. A simplified design procedure was found to be conservative compared to the nonlinear finite element analysis results. The finite element model was verified by comparison with pile test results.

In the design procedure presented by Abendroth, et al., [2] the soil-pile interaction problem is simplified by replacing the soil-pile system with an equivalent cantilever in air. The length of the equivalent cantilever varies, depending on whether the value of interest is elastic buckling capacity, maximum moment in the pile, or horizontal stiffness. The cantilever idealization is illustrated in figure 5-3, where ℓ_e is the equivalent pile embedment length and ℓ_u is the pile length above ground (typically the pile length in an overbored hole). Equivalent lengths are presented in figure 5-4 for both fixed and pinned conditions at the pile cap. The equivalent length, ℓ_e, is given in terms of the ratio ℓ_e/ℓ_c, where ℓ_c is a critical depth below which lateral displacements and bending moments are considered to be insignificant. This length is given by:

$$\ell_c = 4\sqrt[4]{\frac{EI}{k_h}} \tag{5-21}$$

where,

EI = flexural stiffness of the pile

k_h = lateral stiffness of the soil (force/length squared).

In equation 5-21, k_h is the effective spring stiffness per unit length of the pile. Representative values of k_h for clay and sand are given in table 5-1.

Table 5-1. Values of k_h for clay and sand.[26]

Soil Type		k_h (kips/ft^2)
Clay	Soft	72 or 58.x *
	Stiff	580 or 190 + 41X
	Very Stiff	2200 or 750 + 610X
		Use the smaller of the two values
Sand	Loose	8.0x
	Medium	27x
	Dense	72x

x = soil depth (ft)
1 ft = 0.305 m, 1 kip/ft^2 = 47.88 kN/m^2

Values of ℓ_e/ℓ_c are given in figure 5-4 ℓ_u/ℓ_c, ranging from 0 to 4.

For layered soils, an equivalent uniform soil lateral stiffness, k_e, can be obtained using the following procedure:

1. Assume a value for k_e

$$\text{Calculate } \ell_o = 2\sqrt[4]{\frac{EI}{k_e}} = \ell_c/2 \tag{5-22}$$

2. To equate the work of the equivalent uniform soil layers, the following linearly displaced shape is assumed: $y = \Delta_g\left(1 - \frac{x}{\ell_o}\right)$, where Δ_g is the lateral displacement at ground level.

$$\int_o^{\ell_o} \frac{k_e y^2}{2}\,dx = \int_o^{\ell_o} \frac{k_h(x) y^2 dx}{2} \tag{5-23}$$

$$\text{i.e., } k_e = \frac{\int_o^{\ell_o} k_h(x)\left(1-\frac{x}{\ell_o}\right)^2 dx}{\int_o^{\ell_o}\left(1-\frac{x}{\ell_o}\right)^2 dx}$$

3. Repeat Steps 1 and 2 with the new value of k_e and continue until the solution converges.

The converged value of k_e can be used in place of k_h in equation 5-21 to compute ℓ_c. Equivalent cantilever lengths can then be obtained from the charts in figure 5-4. The embedded pile length ℓ must be greater than ℓ_c.

Another way to account for the layered soil involves using the computer program COM624P.[17] Section 5.3.4 of the analytical report provides an example demonstrating the use of COM624P to calculate an equivalent cantilever length.[15] In this example, the equivalent cantilever calculated by COM624P was found to be 8 percent to 17 percent less than the equivalent length calculated by the foregoing method,[26] resulting in a stiffer pile system that produces greater forces for a given pile displacement. Once the equivalent cantilever lengths have been established, the pile can be checked as a structural member using either elastic analysis (Alternative 1) or inelastic analysis (Alternative 2).

5.3.1.1 *Alternative 1: Elastic Analysis*

The axial force and moment developed in the pile because of the dead load, live load, and longitudinal movement can be determined by structural analysis. The effects of passive pressure developed in the abutment because of the longitudinal movement should be included in the analysis.

The moment developed at the top of the pile because of displacement, Δ, is given by:

$$M = \frac{D_i\, EI\, \Delta}{L^2} \tag{5-24}$$

where,

D_i = 6 for fixed end

D_i = 3 for pinned end

L = total length of equivalent cantilever for moment

= $\ell_e + \ell_u$

The pile section can be checked for combined axial load and moment using the following interaction equations and the appropriate equivalent cantilever length for buckling:

$$\frac{P}{P_{cr}} + \frac{C_m M}{M_p\left(1 - \frac{P}{P_e}\right)} \leq 1 \tag{5-25}$$

$$\frac{P}{P_y} + \frac{M}{M_p} \leq 1 \tag{5-26}$$

where,

P = vertical load applied to pile head

P_{cr} = critical buckling load

P_e = Euler elastic buckling load

P_y = yield load

C_m = moment gradient coefficient = 0.85[26]

M = bending moment applied to pile head

M_p = plastic moment strength of pile

A = pile area.

For elastic analysis, the critical buckling load P_{cr} is equal to the Euler buckling load given as:

$$P_{cr} = P_e = \frac{\pi^2 EA}{\left(\frac{kL}{r}\right)^2} \tag{5-27}$$

where,

kL/r = the slenderness ratio

EA = the axial rigidity of the pile.

The effective length factor (k) should be based on the assumption that the pile is braced against sideways since the passive pressure in the soil at the abutment prevents a sideways buckling mode from occurring.

5.3.1.2 *Alternative 2: Inelastic Analysis*

In this approach, yielding is permitted and the ductility capacity of the pile is checked. This method is only recommended for steel H-piles or concrete-filled pipe piles. Applying first-order plastic theory, a solution is obtained by neglecting stresses resulting from longitudinal displacement. The strains induced by the longitudinal displacement are, however, considered through satisfying a ductility requirement. Using this design alternative, an upperbound end moment caused by the vertical pile load is determined from the equilibrium of the deflected equivalent cantilever as:

$$M = D_2 P \Delta \tag{5-28}$$

where,

D_2 = 1/2 for fixed end

= 1 for pinned end.

This value of end moment is used in checking for the combined axial load and bending moment using equations 5-25 and 5-26 above. For inelastic analysis, the critical buckling load P_{cr} is given as:

$$P_{cr} = F_y A \left[1 - \frac{F_y}{4\pi^2 E} \left(\frac{kL}{r} \right)^2 \right] \tag{5-29}$$

where,

F_y = yield stress of the pile.

The ductility limit is satisfied if:

$$\Delta \leq \Delta_p \left(D_3 + 2.25\, C_i \right) \tag{5-30}$$

where,

Δ_p = displacement corresponding to formation of plastic hinge

$$= \frac{M_p L^2}{D_i EI}$$

D_3 = 0.6 for fixed end, 1.0 for pinned end

D_i = 6 for fixed end, 3 for pinned end

C_i = rotation capacity reduction factor as defined below

M_p = $F_y Z$

Z = plastic section modulus

EI = flexural rigidity.

For the H-pile:

$$C_i = 1 \text{ for compact section } \left(\frac{b_f}{2t_f} \le \frac{65}{\sqrt{F_y}} \right)$$

$$= \frac{19}{6} - \frac{b_f \sqrt{F_y}}{60 t_f} \text{ for } \left(\frac{65}{\sqrt{F_y}} < \frac{b_f}{2t_f} < \frac{95}{\sqrt{F_y}} \right) \qquad (5\text{-}31)$$

$$= 0 \text{ for noncompact section } \left(\frac{b_f}{2t_f} \ge \frac{95}{\sqrt{F_y}} \right)$$

where b_f and t_f are the width and thickness of the flange, respectively.

For concrete-filled pipe pile:

$$C_i = 1.0 \text{ with } \frac{h}{t} \le 39$$

where,

h = outside diameter of the pipe

t = wall thickness.

Concrete-filled pipe piles are expected to be significantly more ductile than the H-piles. However, since specific testing of pipe piles to demonstrate the limits for ductility was not performed, $C_i = 1$ is conservatively recommended at this time, considering that a compact concrete-filled pipe pile is at least as ductile as a compact-section H-pile. The limit of h/t = 39 is based on testing of concrete-filled steel tubular columns.[29] In these tests, when h/t was larger than 39, the maximum load was determined by local buckling of the steel tube. No recommendations are provided for h/t > 39 at this time because of lack of test data.

To provide a margin of safety against reaching the ductility limit, the displacement (calculated using the Alternative 2 approach for H-piles and concrete-filled pipes) Δ_p in tion 5-30 is replaced by Δ_b, which is the reduced displacement corresponding to an allowable stress F_b in the pile:

$$\Delta_b = \frac{F_b S L^2}{D_i E I} \tag{5-32}$$

where S is the elastic-section modulus.

Assuming $F_b/F_y = 0.6$ and $Z/S = 1.15$, the ratio $F_b S/F_y Z$ is analogous to a resistance factor of $0.6/1.15 \cong 0.5$ applied to the nominal displacement ductility capacity or a factor of safety of $1/0.5 = 2$ against reaching the ductility limit.

The proposed limiting displacement for the design using the Alternative 2 approach is therefore:

$$\Delta \leq \Delta_b \, (D_3 + 2.25 \, C_i) \tag{5-33}$$

A detailed example illustrating the application of the design method is presented in L.F. Greimann, et al.[26] In this design example, the pile structural capacity is checked against the allowable stress design provisions of the AASHTO standard specifications for both Alternative 1 and Alternative 2.[28] In Alternative 2, the reduced ductility capacity should be checked against the nominal temperature displacement, $\Delta\ell$, that was determined as described in section 5.2.2. By permitting inelastic action in the pile, Alternative 2 allows a longer bridge length than Alternative 1 for a given pile system, as demonstrated in Greimann's design example.

5.3.1.3 *Load Transfer to Soil*

In addition to structural capacity, the pile should be checked for its capacity to transfer load to the supporting soil. For friction piles, a portion of the length near the top of the pile should be neglected because lateral movement of the pile near the ground surface reduces or destroys the frictional capacity of the pile. The length ℓ_n to be neglected can be determined from the charts given in figure 5-5 for a range of y_{max}/Δ values.[26] The term y_{max} is the maximum lateral pile displacement below which the frictional resistance of the pile is assumed not to be affected by lateral movement and can be taken as 2 percent of the pile diameter (or depth). The term Δ in figure 5-5 is the lateral displacement at the top of the pile.

5.3.1.4 *Design Options*

If the calculated limiting displacement, Δ, (from equation 5-33) for a trial abutment pile arrangement is smaller than the determination of the required expected movement, as described in section 5.2, the following options are available:

1. Try a larger size pile, or switch from a weak-axis bending to a strong-axis bending pile orientation. Increasing the flexural stiffness of the pile with respect to the soil will increase the limiting displacement, Δ. It should be noted, however, that as the pile section is increased, the plastic hinging moment Mp will increase. Therefore, the design requirements may increase for the pile-to-pile-cap connection, the reinforcement in the abutment, and the beam-to-abutment connection, as described in the following section of this chapter.

2. Drill oversized or counterbored holes with loose granular fill. Oversized holes are drilled prior to driving the pile and then backfilled after the piles have been installed. Oversized holes are typically 0.6 m (2 ft) in diameter and 2.5 to 3 m (8 to 10 ft) deep. A study by P.S. Yang, A.M. Wolde-Tinsae, and L.F. Greimann indicated that oversized holes should be at least 1.2 m (4 ft) deep and that there is no significant reduction in pile capacity up to a 100-mm (4-inch) lateral deflection.[63] A design example with predrilled holes is given in the Iowa State University report.[26]

3. Use a jointless bridge with expansion joints at the end abutments. The 825-m-(2,700-ft-) long Holston River Bridge described in section 3.5 demonstrates that a very long jointless bridge can be successfully constructed using this concept.

4. Use a semi-integral abutment as described in section 5.3.6 and illustrated in figure 5-19 of this volume. A semi-integral abutment allows rotation and/or translation of the superstructure with respect to the pile cap. A semi-integral abutment that allows rotation between the pile cap and the bridge superstructure essentially produces a pinned-head condition for the pile. The limiting displacement for pinned-head piles will be larger than for fixed-end piles in an integral abutment. However, vertical load capacity will decrease more rapidly with increasing lateral displacement in a pinned-head pile.

   A semi-integral abutment that allows translation between the pile cap and the bridge superstructure can use a rigidly supported pile cap, as illustrated in figure 5-18 of this volume, and removes the lateral displacement capacity of the pile from the design considerations. Maximum end-abutment movement becomes a function of the details that allow the sliding to occur between the abutment wall and the pile cap.

   With either type of semi-integral abutment, bearings and details to accommodate the articulation and translation add to the complexity and expense of the construction and may require more maintenance.

5.3.2 Pile-to-Pile-Cap Connection

The pile-to-pile-cap connection for an integral abutment should develop the moment capacity of the pile and the shear associated with the longitudinal displacement of the pile cap. Figure 5-6 shows the moments and shears developed in the displaced pile, assuming that the full plastic moment capacity of the pile, M_p, is developed.

The pile moment M_p can be developed in the pile cap by bearing stresses f_{cb} between the pile and the concrete, as illustrated in figure 5-7. As described by E.P. Wasserman and J.H. Walker,[64] the depth of the stress block can be taken as:

$$a_p = 0.85\left(\frac{\ell_{pe}}{2}\right) \tag{5-34}$$

where ℓ_{pe} is the embedment length of the pile inside the cap.

Setting the resisting couple equal to the pile moment capacity gives:

$$M_p = C_M D' = a_p \, b \, f_{cb2} \, (\ell_{pe} - a_p) \tag{5-35}$$

$$f_{cb2} = \frac{M_p}{a_p b(\ell_{pe} - a_p)}$$

$$f_{cb1} = f_{cb2} + \frac{V}{a_p b} \tag{5-36}$$

$$f_{cb1} = \frac{M_p}{a_p b(\ell_{pe} - a_p)} + \frac{V}{a_p b}$$

where,

C_M = bearing force developed between the face of the pile and the concrete over a length a_p

D' = distance between the center of the compressive stress zones on the top and bottom of the embedment, as shown in figure 5-7

b = flange width, b_f (for the pile situated for strong-axis bending, or

d = pile section depth (for weak-axis bending).

Based on research reported by E.G. Burdette, et al.,[65] Wasserman and Walker suggested a limit of $f_{cb1} \sim 1.9 \, f'_c$ for the concrete-bearing capacity on a pile embedded in a concrete pile cap.[64]

Figure 5-7 shows the forces on the pile from the reactions within the concrete. These pile forces must also be carried through the height of the pile cap and across the construction joint as illustrated in figure 5-8. A general approach to the design of the pile cap to transfer the pile moment and shear across the pile cap construction joint can be developed using a strut-and-tie model as outlined in the 1998 AASHTO LRFD specifications.[43] Figure 5-9(a) shows an example of a strut-and-tie model to transfer the pile moment and shear from the pile to the construction joint. It is recommended that these forces be transferred in a local region of the pile cap around each pile. A proposed width of the local region is illustrated in figure 5-8, section AA. It should be noted that the pile-to-pile-cap connection and moment capacity across the construction joint must be developed for the pile moment capacity acting in either direction.

Figure 5-9(b) shows soil loads on the abutment pile cap because of the passive soil pressure. The design for these loads is discussed in the following section.

5.3.3 Abutment Wall Design

5.3.3.1 *Stub Abutments Supported on Flexible Piles*

Figure 5-10 shows the forces acting on a pile-supported abutment wall because of thermal expansion. Passive pressure is developed in the soil behind the wall and moment and shear are developed at the top of the pile because of the bending of the pile. The maximum passive pressure force, P_p, is determined from:

$$P_p = \frac{1}{2} K_p \gamma H^2 \tag{5-37}$$

where K_p is the passive pressure coefficient, K, determined for the abutment movement, $\Delta\ell$, from Case 2 (reexpansion after full contraction), as determined in section 5.2.2. Note that K_p is not necessarily the *maximum* K_p associated with full passive pressure. It is recommended that K_p be determined from the wall movement versus the wall height relationships shown in figure 5-11.[(11)]

A review of the literature and current practices indicated opposing philosophies for the degree of compaction for the backfill soil adjacent to the abutment. One approach is to use loose granular backfill to minimize passive pressure forces. The opposite approach is to use highly compacted backfill since voids beneath the approach slab and the settlement of the approach slab are a common problem with integral abutments. Tests on a large-scale abutment specimen indicated that even with 97 percent relative compaction of the backfill, voids develop under the approach slabs as a result of contraction beyond the initial starting point.[(25)] Therefore, there does not appear to be an advantage to using high compaction with the backfill; high compaction is also difficult to attain behind the backwall.

Parametric computer analyses indicated that the passive pressure can be significantly decreased by using relatively uncompacted backfill or by increasing the horizontal length of the backfill prism behind the abutment. The passive soil reaction decreased by a factor of approximately 2.5 when the relative compaction decreased from 90 percent to 80 percent. The calculated passive pressure also decreased by a factor of approximately 2 when the slope of the backfill/in-situ soil interface changed from 45° to 30° (from horizontal). However, the use of lower compaction, with or without a larger horizontal

length of backfill prism, will probably result in increased settlement of the approach slab. Also, the analyses discussed in section 4.4.3 of this volume demonstrate that the typical bridge can accommodate the forces developed by passive soil pressure with 90 percent relative compaction (Standard Proctor) without detrimental effects. The moderate 90 percent compaction will probably result in less settlement of the approach slab than would loose fill and can be more readily achieved than 95 percent or 97 percent compaction. Also, it is suspected that a moderately compacted soil versus a heavily compacted soil would reduce the likelihood for approach slab uplift and lateral bulging of side-embankment soil. This behavior was observed by V.R. Schaefer and J.C. Koch in testing of a full-scale abutment during the expansion phase of cyclic testing, with an abutment backfill that started at 97 percent compaction.[25] Therefore, it is recommended that well-graded granular soil with a moderate compaction of approximately 90 percent (Standard Proctor) be placed behind the abutment, provided that structural approach slabs are used (as discussed in section 5.6). Following this recommendation, the curve for medium-dense sand in figure 5-11 may be used to determine soil pressure behind the abutment. Pile forces are determined from the equivalent cantilever or by using COM624P, as described in section 5.3.2, for the movements that are described in section 5.2.2.

For bridges with a skew angle greater than 20°, abutment movements would probably include a transverse component. Soil pressure normal to the backside of the abutment wall can be determined based on the normal movements Δ_{n1} and Δ_{n2}, as described in appendix B. Movements for pile forces can be determined based on the normal and parallel abutment movements Δ_{n1}, Δ_{p1}, Δ_{n2}, and Δ_{p2}, which are described in appendix B. These movements can be estimated based on a determination of Δ_{t1}, as discussed in section 5.2.2.2, and equations B-1 and B-2 in appendix B.

The summations of the soil pressures and the pile forces in the longitudinal direction of the bridge are in equilibrium with a reaction H_G and moment M_G developed in the deck-girder system. The summations of soil pressures and pile forces transverse to the bridge are in equilibrium with in-plane shear forces in the deck.

The abutment wall should be designed for vertical and horizontal bending and also for punching shear that results from the force in the girder. The critical section for punching shear is at the perimeter of the bottom region of the girder. The design requirements for moment transfer at the slab-to-column connections, according to ACI 318-02, section 11.12.6, are recommended for checking shear in the abutment wall around the girders.

The critical section for vertical bending in the abutment wall is at the construction joint below the beam bearings, where the moment resulting from passive soil pressure below the construction joint adds to the moment from the piles. It is recommended to use local reinforcement in the vicinity of each pile for the pile forces as illustrated in figure 5-8. However, the cantilever moment resulting from the passive pressure, shown in figures 5-9(b) and 5-10, is distributed over the length of the backside of the abutment and is resisted by the bridge beams. For skewed bridges, the moments at the construction joint are determined from the pile and soil forces normal to the abutment wall.

Because of the concentrated beam reactions, it is recommended that the vertical reinforcement for this moment from the soil pressure be distributed so that 75 percent of the bars are within 25 percent of the beam spacing on either side of the beam and the remainder is spread across the middle 50 percent of the beam spacing. It is also recommended that, for crack control purposes, the center-to-center spacing of this flexural reinforcement, s, does not exceed the following limits:

$$s \le \frac{540}{f_s} - 2.5c_c \quad \text{(inches)} \tag{5-38}$$

$$s \le 12\left(\frac{36}{f_s}\right) \quad \text{(inches)} \tag{5-39}$$

where,

c_c = clear cover from the nearest surface in tension

f_s = calculated stress (kips/inch^2) at service load (f_s may be taken as 60 percent of the specified yield).

The above relationships for maximum spacing of flexural reinforcement are provisions in ACI 318-02, section 10.6.4. These provisions simplify the requirements for the distribution of flexural reinforcement for crack control without severely penalizing increased cover thickness, as did the previous z-factor approach.[66]

The abutment wall should also be checked for torsion caused by the eccentricity of the passive pressure force relative to the resultant force in the beams. If the piles are offset from the beams, the pile moment and shear also contribute to torsion in the abutment wall.

Under thermal expansion and the force system shown in figure 5-10, a negative end moment is developed in the beam. This moment increases the vertical reaction in the pile and should be considered in pile design, as discussed in section 5.3.1.

When the bridge contracts because of thermal, creep, and shrinkage strains, the soil pressure is reduced to a pressure between the at-rest and active pressures as the abutment moves away from the soil. When this soil pressure reduces the effect of the other loads, it is recommended that active soil pressure be used. When this soil pressure adds to the other loads, at-rest pressure should be used.

Along with contraction, shear and moment in the pile produce a positive moment at the beam ends, as illustrated in figure 5-12. Also, if backfill soil bears against the front face, pressure from this soil will add to the positive moment. It is recommended that local reinforcement be provided in the vicinity of each pile to transfer the pile forces across the construction joint between the pile cap and the abutment wall. Also, additional vertical reinforcement should be distributed along the length of the front face of the abutment to minimize cracking at the construction joint. The field survey of jointless bridges presented in section 3.5 indicated that cracking and efflorescence were commonly observed on the face of integral abutments at this construction joint, particularly directly below the beams. Therefore, it is recommended that at least minimum reinforcement for flexural members, according to the 1998 AASHTO LRFD specifications, section 5.7.3.3.2, be provided across the construction joint near the forward face of the abutment for 25 percent of the beam spacing on each side of the beams. It is also recommended that at least minimum reinforcement for slabs, according to the 1998 AASHTO LRFD specifications, section 5.10.8, be provided for the remainder of the construction joint. Local reinforcement in the vicinity of each pile in these areas is considered to be part of the minimum reinforcement. Furthermore, the spacing limitations in equations 5-38 and 5-39 above are recommended for this reinforcement.

5.3.3.2 *Abutments Supported on Spread Footings*

Integral abutments are usually supported on a single row of piles to provide flexibility. Also, piles are typically used to minimize settlement of the abutment and differential settlement within the superstructure. However, in many situations, spread footings are appropriate for integral abutments, such as when rock or competent soil is close to the surface, and for single-span bridges. In addition, there is some evidence that differential settlement may not be significantly increased by the use of spread footings. With respect to differential settlement within the superstructure, L.K. Moulton, et al., and Hearn

indicated there is essentially no difference in the settlement magnitude between the abutments on piles and the abutments on spread footings.[67-68] Therefore, it should be possible to use spread footings under integral abutments for multispan bridges. However, there is very little experience with the actual use of spread footings for integral abutments. Hence, it is recommended that experience be gained by starting with relatively short bridges, and then progressing to longer structures.

There are two proposed approaches to designing abutments on spread footings. The first approach is to use a relatively shallow abutment in situations where rock is very close to the surface or where spread footings are used on competent soil that is near the surface. With a shallow abutment, the end movements caused by thermal, creep, and shrinkage strains can be accommodated by sliding of the footing. When rock is deeper or it is desirable to place the spread footing on deeper soil, movements of the integral abutment may be accommodated by bending in a relatively flexible abutment stem.

The following recommendations pertain to abutments supported by relatively shallow spread footings, in situations where end movement may be accommodated by sliding:

1. For footings founded on rock, a layer of granular fill should be used (on top of a leveling layer of fill concrete, as needed) between the footing and rock to facilitate sliding. Do not key the footing into rock.

2. For footings founded on embankments, steps should be taken to minimize abutment settlement, such as allowing the maximum time feasible for the embankment to settle before completing construction, or establishing superstructure continuity or preloading the embankment to accelerate settlement.

3. Design forces for the spread-footing abutment are shown in figure 5-13. The passive pressure coefficient K_p can be determined from figure 5-11, similar to an abutment on piles. However, the recommended passive pressure distribution is altered, as shown in figure 5-13, because the extension of the footing tends to concentrate increased soil pressure near the bottom of the foundation. Design forces also include friction on the bottom of the footing that should be figured using a normal force that includes additional vertical load resulting from the negative moment on the girder related to these soil forces.

4. The abutment wall should be designed for shear and moments resulting from both expansion and contraction movements. The resistance to contraction should

include friction on the bottom of the footing and soil pressure from the berm soil on the front face of the abutment.

5. Sufficient drainage, distance from the face of the slope, and slope protection are essential to keep soil from washing out below the footing.

The following recommendations pertain to deeper abutments on spread footings intended to accommodate end movement by bending in the abutment wall:

1. The distribution of soil pressure on the wall shown in figure 5-14 assumes the footing does not move laterally. However, design forces for moment and shear may be primarily determined by the deformation demand. These forces are related to the bending in the wall and the rotation of the spread footing required to accommodate the maximum expansion and contraction movements determined for Case 1 from section 5.2.2.1. The relationships for foundation rotation and effective cracked stiffness (presented in section 5.4 for piers) can also be used for the abutment stem to determine the moments and shears caused by this expansion and contraction. The moments and shears related to the soil pressure in figure 5-14 should be based on the passive pressure coefficient, K_p, determined from figure 5-11 for the end movement, $\Delta\ell$, from Case 2 in section 5.2.2.1 for reexpansion after full contraction.

2. Detailing a hinge region in the bottom of the abutment wall may be considered to reduce moment and shear in the wall. This may be beneficial for footings on rock. However, the analysis of the pier response discussed in section 4.3 of this volume indicates that the rotational stiffness of spread footings on soil is probably low enough so that adding a hinge may not change the results significantly.

Recommendations for the distribution of wall reinforcement and maximum reinforcement spacing for crack control for stub abutments on piles are also applicable to abutments on spread footings.

5.3.3.3 *Full-Height Abutments*

These are usually used in locations where it is impractical or not economical to set the abutment up on the embankment slope. For a full-height integral abutment, the design recommendations are essentially the same as for the deeper abutments on spread footings discussed above. However, full-height wingwalls or full-height retaining walls adjacent to the abutment are required. U-type wingwalls cannot be cast integrally with the abutment because the wings would stiffen the abutment too much. Use of straight

wingwalls or integral construction with adjacent retaining walls may not be a problem for short bridges; for most bridges, however, vertical expansion joints, will probably be required between the abutment and the adjacent wingwalls or retaining walls whether U-type, flared, or straight,. Joints must allow the necessary movement and must contain the soil behind the wall.

An alternative approach is provided by a semi-integral abutment in which the bridge superstructure is built integrally with an end diaphragm and approach slab. However, the end diaphragm is supported on elastomeric bearings and is detailed with sliding joints on top of the abutment stem. This concept is further discussed in section 5.3.6. In addition, alternatives proposed by Nicholson, et al.,[52] for locations requiring a full-height abutment are shown in figure 5-15.

5.3.4 Wingwalls.

The design of wingwalls depends on their orientation relative to the abutment stem, their method of support, and the skew of the abutment.

Three possible wingwall arrangements are shown in figure 5-16 for right bridges. The U-shaped abutment is recommended for integral bridges because it minimizes the passive pressure developed on the wingwalls resulting from longitudinal bridge movement. The U-shaped wingwalls will also help contain the soil behind the abutment to decrease lateral movement or bulging of the embankment soil as the abutment expands into the backfill. This lateral movement is one of the mechanisms observed by Schaefer and Koch as contributing to the development of the voids under the approach slab.[25] In addition, U-shaped wingwalls help resist transverse movement of the abutments in skewed bridges, as described in section 4.4.4.

If flared or straight wingwalls are used, the longitudinal thermal movement of the abutment causes passive pressure distribution to be developed in the wingwalls. Depending on the flexibility of the wingwall, the passive pressure can be expected to decrease with the distance from the abutment stem. However, the variations in passive pressure are difficult to predict; therefore, the wingwalls should be designed for the same passive pressure as the stem. This passive pressure is balanced by the thrust and moment in the superstructure. Therefore, the wingwalls must be designed to transfer this soil load to the deck through flexure, shear, and torsionAs shown in figure 5-17, wingwalls may be supported on piles or they may be cantilevered from the abutment stem. In the cantilever arrangement for U-shaped wingwalls, the weight of the wingwall produces torsion in the abutment wall, and this torsional moment is resisted by a negative moment developed at

the end of the fascia beams. For flared or straight wingwalls, the weight of the wingwalls produces a combination of torsion and bending or simple bending in the abutments.

Piles can also be used to support the wingwalls. However, piles under the wings add to the forces developed from thermal movement. Therefore, shear and moment developed in the wingwall piles must also be transferred through the wingwall structure to the abutment and bridge superstructure. U-shaped wingwalls on piles also produce significantly more restraint to abutment rotation (about a horizontal axis parallel to the abutment face) near the ends of the abutments. This rotational restraint creates partial fixity for beam-end moments for the outside or fascia beams. Therefore, as seen in section 5.3.5, additional end moments should be considered when designing the connections of these outside beams to the integral abutment.

For bridge skews greater than 20°, transverse movement as described in section 5.2.2.2 is to be expected, and the wingwalls should be designed for soil and pile forces in the transverse direction.

An alternative to designing the wingwalls, abutments, and girder connections for the restraint forces on the wingwalls is to separate the wingwalls from the abutment wall. The wingwalls could be supported independently on piles with a joint to allow movement independent of the abutment itself. However, any such joints must be able to accommodate the entire range of bridge movements without interference.

5.3.5 Beam-to-Abutment Connection

The forces on the abutment foundation and abutment wall generated by expansion and contraction of the bridge are typically resisted by the bridge beam and deck slab. The superstructure acts as a compression strut during expansion and a tension tie during contraction, carrying the abutment load from one end abutment to the other. Therefore, the beam-to-abutment connection should be adequate for these loads.

Generally, the rotational stiffness of the abutment is relatively small and this connection can be considered a pin support for live load and secondary continuity moment effects. Therefore, connection forces are generally determined from the reactions of the pile, abutment, and soil to the longitudinal movements, as described in sections 5.3.3 and 5.3.4. These reaction forces are determined directly from the calculated abutment movements.

When a bridge expands, forces from the abutment develop a negative moment on the beam with compression on the bottom of the beam, and tensile reinforcement is required

on the backside of the abutment. These bars should be hooked into the deck. However, the more critical load to be transferred is the compression in the bottom flange of the beams. As discussed in section 5.3.3, punching shear of the backwall near the bottom region of the beams should be checked for moment and shear transfer analogous to a slab-to-column connection, according to ACI 318-02, section 11.12.6. Any of the following, whether bottom bolts and dowel bars, shear studs, stiffener plates, or angles added to the bottom flange or web, can be used to transfer the compression from the bottom of the steel beam to the abutment concrete.

For bridge contraction, forces on the abutment develop a positive moment with tension on the bottom of the beam. The transfer of the bottom flange tension into the abutment is therefore critical. For steel beams with bottom bolts, dowel bars, shear studs, shear lugs, etc., a shear cone failure of these anchorage mechanisms should be considered. Reinforcement of horizontal ties should be considered to transfer anchorage forces from bolts, studs, etc., to near the backside of the abutment. For prestressed and reinforced concrete beams, continuity connection details similar to those used at pier diaphragms can be used to make the beam-to-abutment connection.

For abutments with straight wingwalls, forces caused by pile and soil loads on the wings should be added to the connection forces for the fascia beams. For abutments with U-shaped wingwalls on piles, the rotational stiffness of the abutment becomes significant for the outside beams. Therefore, live load on the bridge and also secondary moment effects may add significant moments to the outside beam-to-abutment connections. In this case, detailed structural analyses of the fascia beam and abutment can be carried out to determine additional connection forces. However, as a conservative simplification, an abutment with U-type wingwalls on piles can be taken as providing a fixed-end condition for the outside beams. Therefore, additional negative moment for the outside beam connection can be determined conservatively by analysis of the fascia beams for live load with fixed-end conditions at the abutment.

Secondary moment effects will cause additional positive moment at the outside beam-to-abutment connection for U-shaped abutments with pile supports on the wingwalls. The analyses described in section 4.5 of this volume indicate that, for composite steel girders, additional positive-moment stresses generated by secondary effects do not exceed 25 percent of the allowable stresses. Therefore, an upperbound for additional positive moment for the outside girder connection can be determined from the moment associated with a tensile stress of 25 percent of the allowable stress. For prestressed girders, it is

proposed that the same connection details used at the diaphragms, which would yield prior to developing excessive positive moments (as will be further discussed in section 5.5), be used at the outside beam-to-abutment connection for U-shaped abutments with pile supports on the wingwalls.

5.3.6 Semi-Integral Abutments

For situations where an integral abutment on flexible piles is not feasible, a semi-integral abutment can be used to eliminate deck joints. Semi-integral abutments allow translation and/or rotation of the superstructure with respect to the pile cap. Semi-integral abutments may be required when:

1. Expected bridge end movement is too large to be accommodated by a single row of piles with a fixed-end condition for the pile-to-abutment connection.
2. Poor soil conditions require multiple rows of piles.
3. The bridge location necessitates a full-height abutment, as described in section 5.3.3.3.
4. Existing bridges are retrofitted with existing abutments supported on multiple rows of piles.

Burke has described the application of a semi-integral concept as implemented by Ohio DOT.[51] An example of this type of semi-integral abutment is shown in figure 5-18. The end diaphragm is supported on elastomeric bearings on an abutment supported on multiple rows of piles. A sheet seal is provided to keep backfill away from the elastomeric bearings. Because the bearings allow movement both longitudinally and transversely, guide bearings are necessary to keep the sliding superstructure within the fixed portion of the abutment. This is particularly true in the case of skewed bridges where the skew tends to cause rotation in plan, as described in section 4.4.4 of this volume. Therefore, the guide bearings and supporting structure need to be designed for the forces required to resist transverse movement, as discussed in section 4.4.4.2, along with other transverse loads, such as wind and earthquake loads.

As discussed by Burke, this type of semi-integral concept has been used by several State DOTs for both new construction and retrofitting existing bridges.[69] In his paper, Burke provides the results of a survey of State DOTs concerning their experiences with this type of jointless bridge.[69] He also provides representative semi-integral bridge details and a discussion of attributes and limitations for this type of bridge.

A second type of semi-integral abutment is illustrated in figure 5-19. This type of abutment is similar to a semi-integral pier connection. Essentially, a pinned connection is established so that the pile cap translates with the abutment wall; however, rotation is allowed so that the pile has a pinned-head condition. Using the same relationships as in designing flexible piles as described in section 5.3.1, a pinned-end condition will allow more displacement prior to reaching a displacement limit. However, vertical load capacity will decrease more rapidly with increasing deflection.

5.4 DESIGN OF PIERS

There are mainly two classes of connections between the piers and the superstructure: integral and pinned (or expansion). The former requires a moment connection between the pier and the bridge superstructure and develops greater shear and some moment forces in the pier. The integral pier eliminates the mass of the pier cap for seismic design and provides increased clearance. The other piers use some kind of bearing connection between the pier cap and the superstructure to transfer vertical reactions and lateral shear forces, and to allow free rotation and sometimes translation of the bridge superstructure. Lateral shear forces develop at the top of piers, with pinned connections to the superstructure inducing bending moments in the pier, with the maximum moment occurring at the base of the pier.

The total longitudinal movement expected at the top of integral piers is accommodated by two modes of deformation: longitudinal movement through rotation of the soil-foundation system and longitudinal movement through flexural deflection of the pier. The latter takes into account both elastic and inelastic responses.

5.4.1 Foundation Rotational Stiffness

Zederbaum presented an equation that approximates the soil rotation under an external moment (M).[31] The equation is based on the infinite elastic semi-continuum theory and consideration of an ideal earth prism below the footing. The top of the prism has the same dimensions as the footing base and a depth, t, which is equal to one-third of the footing width, b. The angle of rotation, θ, of the upper face of the prism (under the assumption that no tension is developed at the interface) is given by Zederbaum's equation:

$$\theta = \frac{Mb}{3E_s I_f} \tag{5-40}$$

where,

E_s = the compressibility modulus (or modulus of elasticity) of the soil

I_f = the moment of inertia of the footing base.

The rotational stiffness (K_θ) of a soil-foundation system, under spread footings, can be estimated using Zederbaum's equation as follows:

$$K_\theta = \frac{M}{\theta} \tag{5-41}$$

Combining the two equations:

$$K_\theta = \frac{3E_s I_f}{b} \tag{5-42}$$

Rotational stiffnesses determined by the above equation were compared with rotational stiffnesses obtained from the CANDE[19] computer analyses of piers supported on spread footings (as discussed in section 4.3). There was consistent agreement of the results indicated for three soil conditions (rock, stiff clay, and medium stiff clay). Therefore, it is recommended that Zederbaum's equation be used to estimate the rotational stiffness of the soil-foundation system for piers supported on spread footings.

The rotational stiffness of a pile-supported foundation system can be estimated from the elastic stiffness of the piles. The rotation of the pile cap is primarily attributed to the elastic shortening and elongation associated with axial deformations of a pile system consisting of two or three rows of piles. The same approach has been proposed by Witecki and Raina for estimating the horizontal movement of piers resulting from the rotation of pile foundations.[32]

For a single-row pile foundation system (a common condition in the design of integral and semi-integral abutments), rotational stiffness can be calculated assuming a cantilever beam of an equivalent length, following the design model of Abendroth, et al.[2]

5.4.2 Equivalent Flexural Stiffness

The inelastic behavior of concrete, primarily caused by cracking, can be a significant factor in reducing the flexural stiffness of the pier. The results of a parametric study performed on pier models, discussed in section 4.3.2 of this volume, indicate that the ratio of inelastic moment to elastic moment can vary from 0.52 to 0.96. The lower value of the moment ratio corresponds to increased cracking (i.e., reduced stiffness).

To estimate the reduced stiffness of the pier resulting from inelastic behavior, the horizontal deflection of the pier caused by the rotation of the soil-foundation system is determined and subtracted from the total deflection induced at the top of the pier. The net deflection is caused by flexure of the pier (including the inelastic response of the concrete). The flexural deflection is then used with inelastic moment data from PBEAM[33] to obtain the reduced (equivalent) stiffness of the pier, based on the beam theory equation of a cantilever.

The procedures used above could be followed to determine the equivalent stiffness of piers if inelastic moment data were available. However, it may not be practical for a designer to perform a similar analysis. Therefore, equation 9-8 of ACI 318-02 was revised to account for the inelastic effects and to provide the best correlation with the data determined from the PBEAM analyses, as described in section 4.3.2 of this volume. The revised equation was essentially the same as equation 9-8 of ACI 318-02, except that an exponent of 1.25 was found to provide the best correlation, and that the cracking moment, M_{cr}, is determined from both the axial stress, P/A, and the modulus of rupture, f_r. The following equation is, therefore, recommended to estimate the equivalent moment of inertia (I_e) for the pier:

$$I_e = \left(\frac{M_{cr}}{M_a}\right)^{1.25} I_g + \left[1 - \left(\frac{M_{cr}}{M_a}\right)^{1.25}\right] I_{cr}^{\,1.25} < I_g \qquad (5\text{-}43)$$

where,

M_a = calculated elastic moment at the base of the pier based on assumed bridge movement

I_g = moment of inertia of gross concrete section about the centroidal axis, neglecting reinforcement

I_{cr} = moment of inertia of cracked section with rebar transformed to concrete

M_{cr} = cracking moment calculated as follows:

$$M_{cr} = \left(\frac{P}{A} + f_r\right)\frac{I_g}{y} \qquad (5\text{-}44)$$

where,

P = applied vertical load

A = cross-sectional area of concrete, neglecting reinforcement

y = half-thickness of pier section

f_r = modulus of rupture of concrete

= $0.62\sqrt{f'_c}$, MPa $\left(7.5\sqrt{f'_c}\ \text{lbf/inch}^2\right)$

f'_c = compressive strength of concrete.

5.4.3 Point of Fixity

The distribution of forces transferred to the substructure from the expansion/contraction of the bridge deck depends on the location of the point of fixity (theoretical point of zero movement). To determine the point of fixity, it would be necessary to estimate the lateral stiffnesses of the piers and abutment walls, and the horizontal stiffnesses of the bearings (if used). Pier and abutment stiffnesses should include the effect of foundation rotations. The bearing stiffness depends on the type used.

Based on a review of a PCI survey of DOTs in the United States and Canada, piers with pinned connections to the superstructure are commonly used in jointless bridges.[50] Therefore, the discussion in this section will be limited to the design of those piers. However, similar concepts can be used for integrally connected piers.

As discussed previously, almost all piers transfer some shear forces at the top of the pier. As described by Zederbaum, the point of fixity can then be determined for jointless bridges with pinned bearings on the piers as follows: [31]

$$\bar{x} = \frac{\sum K_x L_x}{\sum K_x} \tag{5-45}$$

where $\bar{x}$ is the coordinate of the point of fixity and L_x is the horizontal distance along the longitudinal axis from the centerline of the piers/abutments to the zero point on the axis. K_x is the stiffness of the piers/abutments in the x direction, respectively, taking into account the effect of foundation rotation and bending in the pier. Witecki and Raina have presented procedures to incorporate the stiffness of elastomeric bearings and sliding (expansion) bearings in the calculations for the point of fixity.[32]

5.4.4 Analyses to Determine Design Moment

A simplified method that can be used for the design of piers as follows:

1. Determine the point of fixity using equation 5-45 presented in section 5.4.3 of this volume, while ignoring the rotational stiffnesses of the foundations.
2. Calculate the total end movements caused by bridge expansion and contraction ($\Delta\ell$) for Case 1 on both sides of the point of fixity, as described in section 5.2.
3. Calculate the expected longitudinal movement at each pier location, based on $\Delta\ell$ times the ratio of the distance from the point of fixity to the pier in question over the distance from the point of fixity to the end support.
4. Conservatively assume that 30 percent of the pier's expected longitudinal movement at the top of the pier is caused by the rotation of the foundation. The remaining 70 percent represents the flexural deflection of the pier shaft.
5. The pier's design-bending moment is given by the following equation:

$$M = 3EI_e \Delta b/H^2 \qquad (5\text{-}46)$$

   where E is the modulus of elasticity of concrete, Δb is the flexural deflection determined from Step 4, and H is the pier height. The term I_e represents the equivalent moment of inertia of the pier. Equation 5-46 needs to be solved simultaneously with equation 5-43 (presented in section 5.4.2 of this volume) to determine the values of the two unknowns, I_e and M.

It should be noted that the conservative assumption of 30 percent of the longitudinal movement at the top of the pier being caused by foundation rotation was based on the results of the PBEAM parametric study of the piers, as described in section 4.3 of this volume. The ratio of pier lateral movement caused by foundation rotation relative to the total expected pier lateral movement varied from approximately 30 percent to 80 percent, with an average value of approximately 45 percent. The following more comprehensive iterative method can be used to more accurately account for foundation rotation:

1. Determine the rotational stiffness of the foundation ($K\theta$), as discussed in section 5.4.1.
2. Determine the point of fixity using equation 5-45 presented in section 5.4.3, while ignoring the rotational stiffness of the foundation.

3. Calculate the movements caused by bridge expansion and contraction ($\Delta\ell$) on both sides of the point of fixity.

4. Calculate the expected longitudinal movement at each pier location, based on $\Delta\ell$ times the distance from the point of fixity to the pier in question divided by the distance from the point of fixity to the end support.

5. As a starting point, assume that 45 percent of the pier's expected longitudinal movement is caused by the rotation of the foundation, and that the remaining 55 percent is caused by the flexural deflection of the pier. The corresponding deflections will be Δr and Δb, where:

   Δr = deflection at the top of the pier caused by foundation rotation

   Δb = deflection at the top of the pier caused by bending in the pier.

6. Calculate the pier design moment (M) from the foundation rotation relationship, using $K\theta$ from equation 5-42 as follows:

$$M = K\theta \ \Delta r / H \tag{5-47}$$

7. Use the moment calculated from equation 5-47 to determine the equivalent moment of inertia of the pier (I_e) from equation 5-43 presented in section 5.4.2 of this volume.

8. Apply the moment value calculated from equation 5-47 and the effective moment of inertia calculated from equation 5-43 into equation 5-46, then and solve for Δb. Also, find the ratio of $\Delta b / \Delta\ell$.

9. Estimate the lateral stiffness for the longitudinal movement at the top of the piers (K), taking into account the effect of foundation rotation. The following equation can be used:

$$K = \frac{1}{\frac{H^3}{3EI_e} + \frac{H^2}{K_\theta}} \tag{5-48}$$

10. Determine the longitudinal stiffness of the abutment from the pile analyses in section 5.3.1 and the soil response resisting expansion as described in section 5.3.3.

11. Determine the point of fixity (zero movement) using equation 5-45 from section 5.4.3 of this volume and the lateral stiffnesses determined from the previous step.

12. Repeat Steps 3 and 4. Determine the revised values of Δr and Δb based on the ratio of $\Delta b/\Delta \ell$ determined in Step 8.

13. Repeat Steps 6 through 8 and compare the new values of Δr and Δb to the values calculated in the previous step. If the differences are within an acceptable range, then use the final data for the design of the pier. If the differences are not within an acceptable range, then reiterate until acceptable results are obtained.

5.5 CONSIDERATION OF SECONDARY CONTINUITY FORCES

The analyses presented in section 4.5 indicate that, at service conditions, secondary continuity moments in composite steel beams will generally not be significant. However, the secondary moments caused by creep, shrinkage, and thermal effects in PS/C beams made continuous for live load can be on the same order of magnitude as the primary moments caused by the applied dead and live loads. These secondary moments must therefore be considered properly to ensure satisfactory performance. Based on the results of the analyses presented in section 4.5, the following design considerations and recommendations are presented with respect to secondary continuity forces.

5.5.1 Continuity Moments

5.5.1.1 *Continuity Moments in Composite Steel Bridge Beams*

Temperature gradients and differential coefficients of thermal expansion in continuous composite steel beams produce both positive and negative secondary moments, while the shrinkage of deck concrete and the heat of hydration locked-in strains produce negative secondary moments. Deck-slab cracking partially relieves negative secondary moments.

The parametric studies reported in section 4.5 indicate that stresses in both the concrete deck slab and steel beams can be expected not to exceed the allowable stresses specified by AASHTO under the positive continuity moments. Therefore, explicit calculations considering the secondary effects of shrinkage and temperature gradient resulting in positive secondary moments are not necessary. As explained in section 4.5, however, this conclusion may not apply to bridges with skew angles greater than 30° if moment reduction factors for live load are used. Separate analyses for heavily skewed bridges may be required to evaluate the secondary moment effects.

The analyses for negative secondary moments in composite steel beams indicated that, under certain circumstances, calculated compressive stresses in the bottom flange exceeded the allowable stresses based on the working stress provisions of AASHTO, even after allowance for redistribution of the stresses because of deck cracking. The analyses included the effects of temperature gradient and the restraint of longitudinal expansion provided by passive pressure in backfill and the lateral force in the piles of the integral abutments.

In addition to designing the beams as continuous for dead load and live load, the following steps are recommended for checking the bottom flange stresses near the pier supports under the combined effects of applied load and secondary continuity moment. Calculation details are provided in chapter 8 of the analytical report.[15]

1. Compute girder stress for a continuous beam under dead and live loads, based on uncracked section properties: $f_{s_{DL}}$, $f_{s_{LL}}$.

2. Compute stress in the girder flange using 0.67 of the full longitudinal restraint force developed in the abutment: $f_{s\,longitudinal}$. (Note: the 0.67 factor is used because experimental data indicate that maximum longitudinal expansion and maximum negative thermal gradient are not coincidental. See section 4.5.2.2.)

3. Compute stress in the bottom flange, based on uncracked section properties for the thermal gradient secondary moment, sufficient to cause deck cracking, from equations 4-33 and 4-34: $f_{s\,gradient}$.

4. Combine the calculated stresses using modification factors of 0.8 for live load and 0.6 for secondary moment to allow for the redistribution of stresses caused by deck cracking, as discussed at the end of section 4.5.2.2:

$$f_{s1} = f_{s\,DL} + f_{s\,gradient} + f_{s\,longitudinal} \tag{5-49}$$

$$f_{s2} = f_{s\,DL} + 0.8\, f_{s\,LL} + 0.6\, f_{s\,gradient} + f_{s\,longitudinal} \tag{5-50}$$

5. Compare calculated stresses, f_{s1} and f_{s2} with 125 percent of the allowable stress specified in the AASHTO specifications.[59]

If the compression flange is partially supported or unsupported, the allowable bending stress is governed by the lateral torsional buckling requirements. The effect of the axial stress caused by the restraint of passive pressure can be considered as an equivalent moment $M' = Sf_{s_{longitudinal}}$, where S is the uncracked transformed section modulus of the

composite section for equation 5-49 and S is the cracked transformed section modulus of the composite section for equation 5-50. The moment M' is added to the moments from the applied load and temperature gradient (without any modification factors for redistribution) in the calculations for allowable bending stress. In most cases, this will involve a minor adjustment in the allowable stress..

Based on the parametric studies discussed in section 4.5, the combined stress check described above becomes critical only for larger beam spacings. It was found that, for stringer spacing less than 2.1 m (7 ft) for Grade A36 beams, and 2.7 m (9 ft) for Grade A572 beams, an explicit check of the combined stress effects is not necessary. This conclusion, however, may not apply to bridges with skew angles greater than 30° designed using the skew moment reduction factors for live load.

Treatment of the combined load effects in the AASHTO LRFD specifications is significantly different from the allowable stress provisions of AASHTO. A load factor of 0.5 is specified for the uniform temperature effects at the strength-limit states, while the load factor for the temperature gradient effects (γ_{TG}) may be neglected at the strength-limit states.

Presumably, the AASHTO LRFD approach neglects the temperature gradient effect at the strength state because the temperature gradient is typically self-limiting (i.e., it dissipates with cracking and large deformations associated with reaching the strength state). However, for integral abutment bridges with steel beams, the combination of the restraint of the uniform temperature expansion, TU, and the negative temperature gradient, TG, do occur in combination. TU results primarily from restraint from the abutments and is not self-limiting. The combination of TU and TG could result in lateral torsional buckling of the bottom flange near the piers prior to yielding of the beam section, if the bottom flange is not fully supported to develop yield stress.

Therefore, for jointless integral abutment bridges with composite steel beams, to allow for conditions where temperature gradient effects may be a critical load case (i.e., negative temperature gradient in the composite steel girders with a relatively large girder spacing), it is recommended that either the compression flange in the negative-moment region be supported to develop full yielding in the compression flange, or an additional load combination be adopted as follows:

$$Q = 1.25\ D + 1.35\ L + 0.5\ TU + 1.0\ TG \qquad (5\text{-}51)$$

where,

D = load effect caused by dead load

L = load effect caused by normal vehicular load

TU = load effect caused by uniform temperature

TG = load effect caused by temperature gradient.

Note that this load combination is similar to STRENGTH II, except that STRENGTH II applies to owner-specified special vehicles.

For situations where the load effect caused by uniform temperature may be critical, an additional load combination is suggested for jointless integral abutment bridges with composite steel beams as follows:

$$Q = 1.25\ D + 1.35\ L + 1.0\ TU + 0.5\ TG \qquad (5\text{-}52)$$

5.5.1.2 *Continuity Moments in Prestressed Concrete Girder Bridges*

As discussed in section 4.5.3.1, significant levels of positive moment can develop at interior supports in PS/C beams because of creep combined with a positive temperature gradient, depending on the amount of positive-moment reinforcement provided. However, because of the uncertainty associated with calculations of positive continuity moments resulting from the variability of the creep and shrinkage effects, differential coefficients of expansion effects, temperature gradient, locked-in heat of hydration effects, and cracking, the following simplified approaches are recommended:

1. Option 1: Do not provide any positive continuity moment reinforcement at the piers. This should prevent the development of positive secondary continuity moments in the pier diaphragms. Analyze the girders as simply supported for dead plus live loads at service levels, but analyze them as continuous beams for strength design for live load. At ultimate load, sufficient inelastic deformations will occur to close the positive-moment cracks at the diaphragm, resulting in a continuous structure for live loads. Detail the girder/diaphragm interface to allow relative movement and provide a crack control joint.
2. Option 2: Design the positive-moment capacity of the connection at the pier diaphragms to act as a fuse that will yield prior to development of 125 percent of the allowable tensile stress in the bottom of the beam near midspan under secondary effects plus dead and live loads. To accomplish this, calculate the

service-level moment near midspan for dead load and live load plus superimposed dead load, as if the beams were simply supported. Then determine the positive end moments that, when superimposed on this service-level positive moment, result in a total tensile stress in the bottom of the beam near midspan of 1.25 x 0.5 $\sqrt{f'_c}$ = 0.62$\sqrt{f'_c}$, MPa (1.25 x 6$\sqrt{f'_c}$ = 7.5$\sqrt{f'_c}$, lbf/inch^2). The positive-moment reinforcement for the connections at the pier should be designed to yield at these end moments to protect the midspan region from overstress. Provide a crack control joint at the beam-to-diaphragm interface.

3. Option 3: Option 2 will result in a relatively small amount of positive-moment reinforcement at the end diaphragms. If greater reinforcement is desired, calculate the resultant increase in yield moment and superimpose this moment on the dead and live load simple beam moments at midspan. Additional prestressing will be needed to limit the midspan service-level stress to 125 percent of the allowable stress to 125 percent of the allowable stress (1.25 x 0.5 $\sqrt{f'_c}$ = 0.62$\sqrt{f'_c}$, MPa [1.25 x 6 $\sqrt{f'_c}$ = 7.5 $\sqrt{f'_c}$, lbf/inch^2) for the combination of dead and live loads with secondary effects. Provide a crack control joint at the beam-to-diaphragm interface.

4. Option 4: Calculate the upperbound positive secondary moments using gross-section (uncracked) analyses considering deck placement at an early girder age, upperbound creep coefficients, positive temperature gradients, and lowerbound shrinkage strains. Superimpose these effects on the moments obtained by conventional analysis of the beams treated as simply supported for dead load and as fully continuous for live load plus superimposed dead load. Neglect the heat of hydration component, because it would reduce the positive secondary moment and, in addition, its magnitude is very uncertain. Also, neglect longitudinal restraint, because it would reduce bottom-flange tensile stresses and, in addition, the value occurring simultaneously with the maximum positive secondary moments is uncertain. The positive secondary moments can be calculated with the analytical tools discussed in section 4.5.3. The BRIDGERM computer program can be used to calculate the continuity moments caused by creep and shrinkage, and Priestley's modified equations, discussed in section 4.5, can be used to calculate the continuity moments caused by the temperature gradients. As in the previous options, midspan service-level stress will be limited to 125 percent of the allowable stress when including the secondary effects. Provide a crack control joint.

If a positive-moment connection is used over the piers, the beam section must also be checked near the ends where prestressing is decreased. The reinforcement used to develop the positive-moment connection should also be extended far enough into the prestressed girders to ensure that the positive restraint moment will not cause excessive cracking near the supports.

In cases where negative continuity moments are developed (for example, when the deck and diaphragms are cast when the concrete girders are older), negative-moment reinforcement in the deck can be designed for applied dead and live loads only where the moments are calculated based on uncracked section properties. The girder is assumed to be simply supported for dead load and fully continuous for live and superimposed dead loads (because of the parapets, barrier walls, wear surface, etc.). The analyses discussed in section 4.5 indicate that, if cracking occurs in the deck, sufficient moment redistribution occurs to prevent the deck reinforcement from becoming overstressed as a result of the secondary effects. This conclusion, however, may not apply to bridges with skew angles greater than 30° and designed using the live load moment reduction factors.

5.5.2 Increase in End Reactions and Beam Shear Caused by Secondary Continuity Moment

Secondary moments in bridge girders cause a redistribution of dead load reactions and change in beam shear, particularly in the end spans. Positive continuity moments increase the end abutment reaction and beam shear at the face of the abutments. Negative continuity moments increase the reactions at the first pier and beam shear in the end span at the face of the pier.

The following recommendations regarding increased reactions and beam shear are based on the studies of secondary continuity moments for both the steel and PS/C beams:

1. For positive continuity moments in composite steel bridge beams, analyses based on uncracked sections discussed in section 4.5 indicated that the increase in flexural steel stress is less than the 25 percent increase in the allowable stresses. Based on this observation, the increase in stresses caused by the change in the shear and reaction at the abutment will also be less than a 25 percent increase in the allowable stresses. Therefore, explicit calculations for increased end reactions and shear caused by positive continuity moments are not required. This conclusion, however, may not apply to bridges skewed greater than 30° that were designed using the live load moment reduction factors.

2. Parametric studies for negative secondary moment effects in composite steel bridge beams indicate that, when combined with probable concurrent stresses related to the restraint of longitudinal expansion by integral abutments, stresses calculated in the bottom flange may exceed the allowable stresses based on the AASHTO provisions[59] even after allowance for redistribution of stresses caused by deck cracking in the negative-moment regions. The maximum total stress indicated by the parametric study was 147 percent of the allowable stress. Negative secondary moment also produces increased shear in the girders at the face of the first pier. However, the shear span for the negative secondary moment is the entire length of the end span. Also, cracking in the deck redistributes some of the live load shear from the first pier to the abutment. The net effect is that, although the negative secondary moment can be significant, the increase in shear will be less than 25 percent of the shear from the dead and live loads. Therefore, explicit calculations for the increase in the reactions and shear resulting from the negative continuity moments in composite steel beams are not required. This conclusion, however, may not apply to bridges skewed greater than 30° that were designed using live load moment reduction factors.

3. For positive secondary continuity moments in PS/C beams:

    a. For Option 1, described in section 5.5.1.2, there would be no positive secondary continuity moment developed. Therefore, there are no changes in end-span shear or reactions.

    b. For Options 2 and 3, the maximum change in the end-span shear and abutment reactions can be calculated based on the yield moment of the positive-moment connection at the first pier.

    c. For Option 4, the maximum change in the end-span shear and abutment reactions can be determined from the calculated secondary moment.

4. Analyses for negative secondary moment effects in PS/C beams indicate that, if cracking occurs in the negative-moment region of the deck, sufficient moment redistribution occurs to prevent the deck reinforcement from becoming overstressed. Based on this observation, the increase in shear stress caused by the secondary moment effects will not be significant. Therefore, explicit calculations for consideration of increases in shear and reactions at the first pier resulting from negative secondary moments are not necessary. Once again, this conclusion may

not apply to bridges skewed greater than 30° that were designed using the live load moment reduction factors.

5.6 DESIGN OF APPROACH SLABS

Approach slabs are required behind integral abutments because of the potential settlement of backfill behind the abutment wall. As described by Schaefer and Koch, even with high compaction of the backfill, a void will occur under the approach slab, which is related to the thermally induced movements of integral abutments.[25] Based on a survey of bridge approaches and on a full-scale abutment test, Schaefer and Koch concluded that "there is virtually no way to eliminate the development of a void space under an approach slab when an integral abutment is part of the system." Therefore, the approach slab is needed as a structural slab to span this void.

As shown in figure 5-20, the approach slab is typically supported on the abutment and on a sleeper pad where the approach slab meets the roadway pavement. Sleeper pad details suggested by Wasserman and Walker[64] are shown in figure 5-21.

The length of the approach slab is dictated by the extent of the backfill behind the abutment wall, and is usually in the range of 3.0 to 7.6 m (10 to 25 ft). A California Department of Transportation (Caltrans) study of the approach slabs indicated that the rate of backfill settlement was at a maximum within 6.1 m (20 ft) of the abutment, but decreased rapidly beyond 6.1 m (20 ft).[70] Several States specify a minimum approach-slab length in the range of 6.1 m to 7.6 m (20 ft to 25 ft). Tests by Schaefer and Koch showed that failure wedge and backfill movements are confined to an area from about 1.0 horizontal to 1.0 vertical to approximately 1.5 horizontal to 1.0 vertical.[25] The extent of the wedge and void development is primarily a function of abutment movement: that is, longer bridges and/or larger temperature ranges will develop larger voids.

Based on the above observations, it is recommended that the approach-slab length be determined from a 2.0 horizontal to 1.0 vertical intercept line from the bottom of the abutment with a minimum of 6.1 m (20 ft). Also, the sleeper pad should not be placed on the wedge of soil excavated and then backfilled behind the abutment. The assumption used by State agencies regarding the span length of the approach slab for strength design varies between one-half and full span length.[52] Reinforcement for skewed approach slabs should follow the 1998 AASHTO LRFD requirements for skewed decks.[43]

The end of the approach slab should be parallel to the abutment wall for both right-angle and skewed bridges. For interfaces with concrete pavement, special considerations are

suggested, as discussed in section 5.7, item 9. The approach slab should be free to settle relative to curbs, safety shapes, and wingwalls. To minimize resistance to horizontal movement, Wasserman and Walker recommended that the slab be placed on two layers of 0.10 mm- (0.004 inches-) thick polyethylene sheet.[64] However, analyses in this study, discussed in section 4.4.3 of this volume, indicate minimal horizontal forces in the approach slab from soil friction. Therefore, the polyethylene sheets may not be needed.

5.7 DETAILS

The following recommendations are related to the details for accommodating movement. These recommendations are based on observations of distress noted in the field survey of jointless bridges (and discussed in section 3.6 of this volume).

1. Vertical cracks were often evident at the bottom of diaphragms between the precast (prestressed) concrete beams over the piers (i.e., the positive-moment connection region) for the fascia girders. For interior beams with ends encased in the diaphragm concrete, spalling of the diaphragm concrete near the bottom flange was frequently observed. This spalling results from slipping of the bottom flange outward from the diaphragm with end rotation of the girder associated with creep and thermal gradients.

   Vertical cracks in the diaphragm and end rotation of the girders serve to relieve tensile stresses developed because of creep, shrinkage, and positive temperature gradients; in general, these are not considered to be detrimental to the long-term performance of the structure. Attempts at over-reinforcement of the positive-moment connection may result in cracking in far less desirable locations (i.e., within the span where the added reinforcement terminates or at midspan). Recommendations for the design of this connection are provided in section 5.5.1.2. Section 4.5.3.1 of this volume presents further suggestions for details to allow slipping of the bottom of the girder with respect to the diaphragm and to tie the superstructure to the top of the pier caps.

2. Horizontal cracks and efflorescence were commonly seen on the forward face of integral abutments at the construction joint at the top of the pile cap. The efflorescence was typically most noticeable directly below the beam supports. However, the efflorescence was distributed across the entire abutment face on some bridges. Section 5.3.3.1 discusses reinforcement requirements for moments applied across the construction joint and for spacing and distribution of

reinforcement for crack control. However, it is also recommended that consideration be given to providing a sheet seal, similar to that shown in figure 5-18, or some other method of water stoppage on the backface across the construction joint in the abutment wall.

3. Washout and/or settlement of the soil beneath the pile cap were noted at several abutments so that several inches of the abutment piles were clearly visible. Proper drainage material and perforated soil pipes are required behind the abutment. In addition, however, the use of filter fabric to contain the backfill soil on the backface of the abutment should be considered, as should directing surface water away from the bridge approach system. NCHRP Synthesis 234, *Settlement of Bridge Approaches*, provides some further recommendations for drainage.[71]

   Proper drainage is also important to minimize the potential for frozen soil behind the abutment. Frozen soil is limited to cold weather when the bridge superstructure is in an overall contracted state. However, there will be lower-level expansion and contraction cycles occurring daily. The magnitude of the potential restraint forces from the frozen soil is unknown, but can be minimized with proper drainage.

4. Observations concerning slope pavement on the front face of abutments indicated that the slope pavement was typically cast directly against the forward face of the abutment with or without a thin layer of preformed joint material. A gap was typically observed between the slope pavement and abutment, presumably caused, in part, by the abutment pulling the slope pavement back during contraction and then leaving a gap when it reexpanded. In addition, the slope pavement was frequently cracked where it was cast around the first interior piers. These observations indicated that the slope pavement may be acting as a compression strut between the abutment and the lower region of the pier, to partially restrain the initial contraction of the abutments and place additional forces on the piers.

   Slope protection should be constructed to allow sufficient unrestrained contraction. The use of broken stone for slope protection rather than concrete pavement should be considered in locations where such use is allowed.

5. The approach slab should bear on the abutment in a notch or on a haunch and should be tied to the abutment with reinforcement to effect a pin connection, to minimize moment in the approach slab (see figure 5-18).

6. Settlement of the end of the approach slab away from the bridge abutments was commonly observed. The settlement is partially associated with washout from drainage. It is also partially attributed to settlement of the backfill behind the abutment with cyclic contraction and expansion associated with creep, shrinkage, and thermal strains, combined with the use of relatively short approach spans such that the far ends of the approach slabs are within a zone of soil influenced by abutment movement. Section 5.6 includes recommendations on the length of approach slabs, to minimize settlement from cyclic movement of the soil wedge. In addition, it is recommended that the bridge deck runoff be intercepted by the drainage system before reaching the sleeper-pad region supporting the end of the approach slab.

7. Settlement of the approach slab can cause damage to the attached barrier walls. Barrier walls attached to the approach slab should be jointed to accommodate differential settlement.

8. Transverse movement of integral abutments associated with large skews or horizontal curves should be anticipated in the details for the barrier walls, the drainage structures, and the ends of the approach slabs.

9. Two bridges included in the inspection survey had concrete pavement adjacent to the approach slab. In both cases, the approach slabs were in good condition, whereas the pavement was significantly cracked with faulting cracks. Also, NCHRP Synthesis 234 indicated that bridges with rigid approach pavement had more severe roughness than bridges with flexible approach pavement.[71] Typically, the ends of the approach slabs settle, and relatively rigid concrete pavement cannot adequately accommodate the settlement. Based on this observation, it is recommended that, when rigid concrete pavement is used, a transition zone of flexible approach pavement be used between the end of the approach slab and the rigid pavement. It is recommended that the length of the approach pavement be approximately equal to the length of the approach slab. The flexible approach pavement will help to accommodate sleeper-pad settlement, but will also act as a pressure-relief zone for pavement expansion. In addition, for skewed bridges, the edge of the flexible approach pavement can be parallel to the skewed abutment at the interface with the approach slab, and the edge of the flexible approach pavement can be perpendicular to the pavement alignment at the interface with the rigid pavement. This would eliminate the

cracking observed in the acute corners of rigid pavement adjoining a skewed approach slab.

10. The majority of the bridges inspected had asphalt pavement adjacent to the approach slabs. Asphalt patching was commonly observed for releveling the pavement-to-approach-slab interface region. This interface is essentially the expansion joint to accommodate bridge movements in jointless bridges. Experience in Tennessee indicates that movement up to 50 mm (2 inches) can be accommodated.[72] Based on analyses and testing, the lateral deformation capacity of steel piles is significantly larger than 50 mm (2 inches), if the concept of allowing inelastic (yield) strains in the pile is used. Therefore, the ability of the details to accommodate the movement at the end of the approach slabs and/or the acceptance of continued maintenance of this region are among the factors that limit the length of properly designed and detailed jointless bridges.

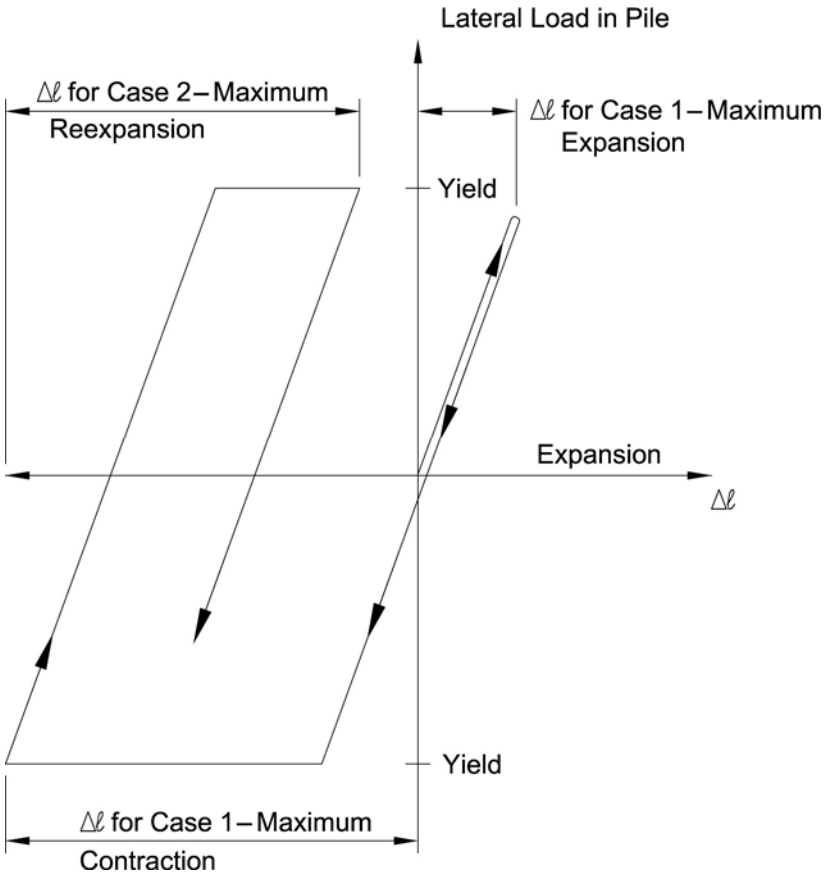

Figure 5-1. Example of pile forces with initial expansion, contraction, and reexpansion.

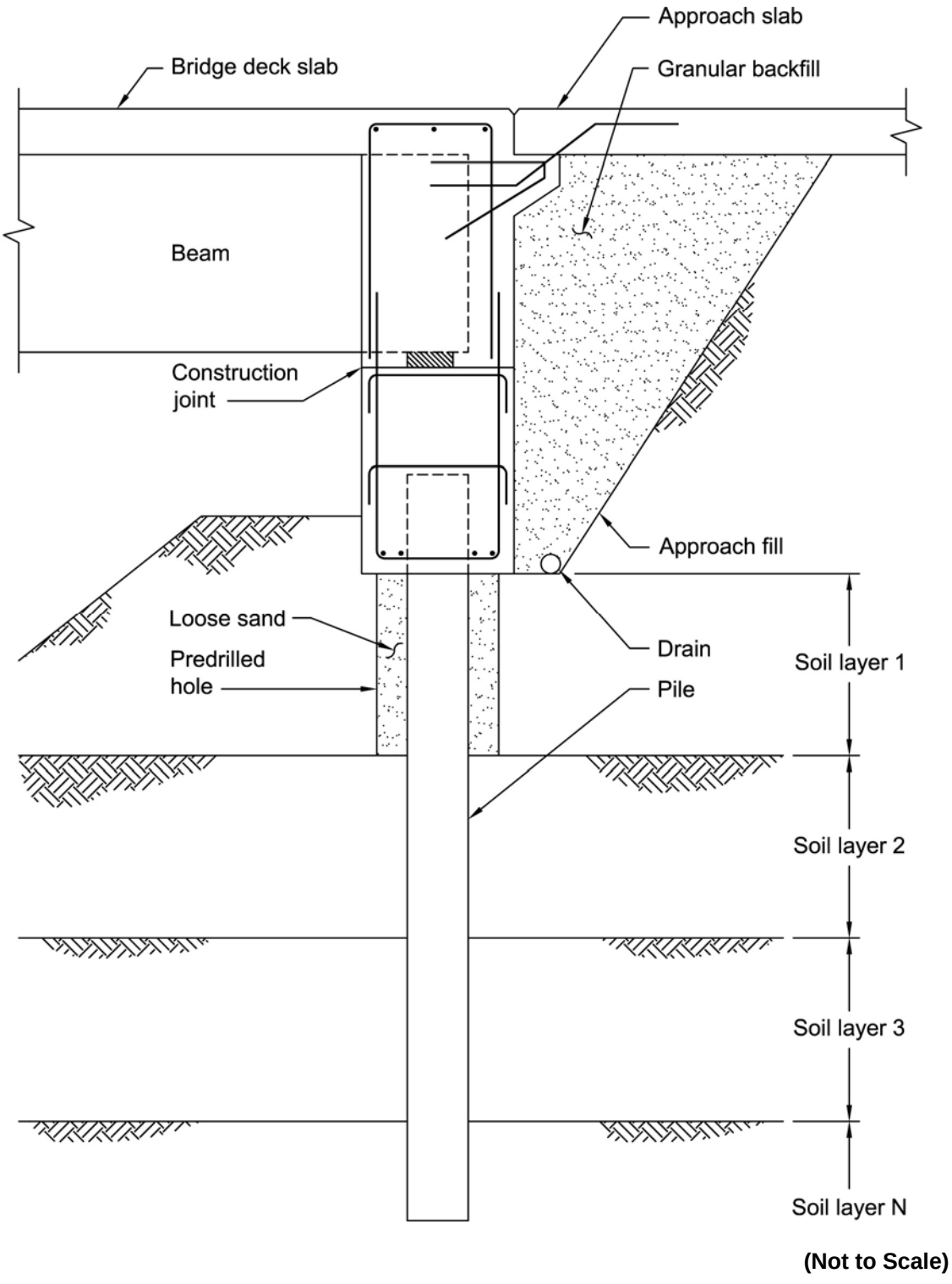

Figure 5-2. Stub abutment on pile arrangement.

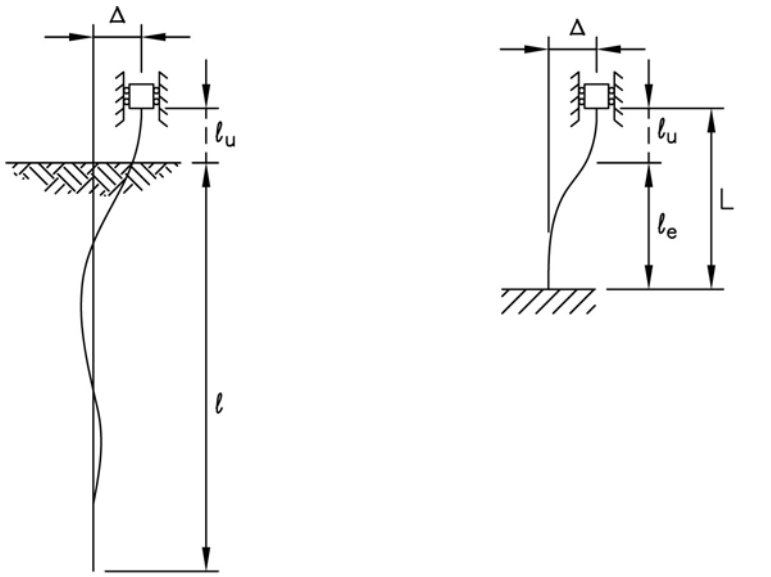

Actual System Equivalent Cantilever

(a) Fixed-Head Condition.

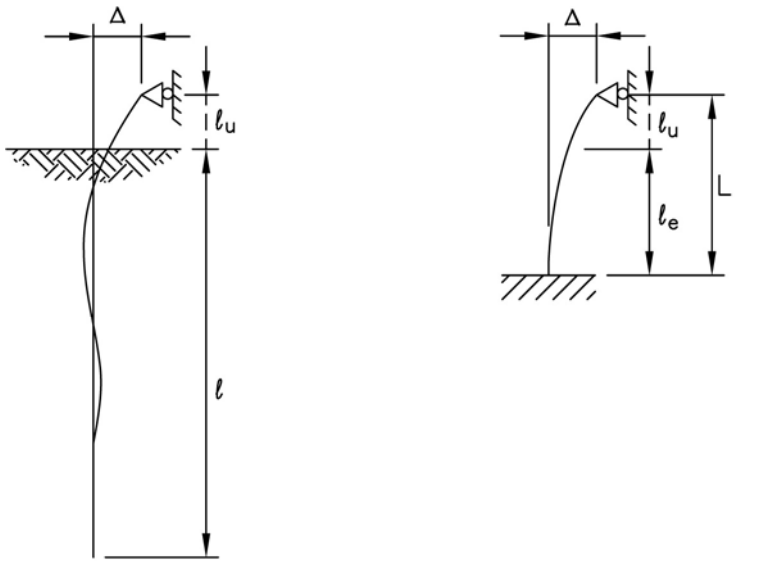

Actual System Equivalent Cantilever

(b) Pinned-Head Condition.

Figure 5-3. Cantilever idealization of the pile.[26]

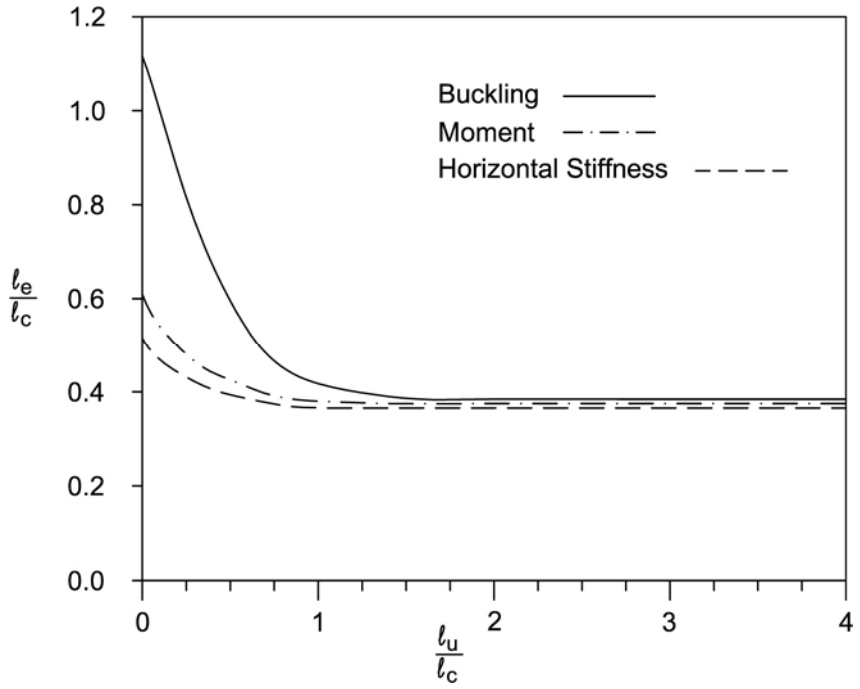

Figure 5-4(a). Equivalent cantilevers for fixed-head piles embedded in a uniform soil.[26]

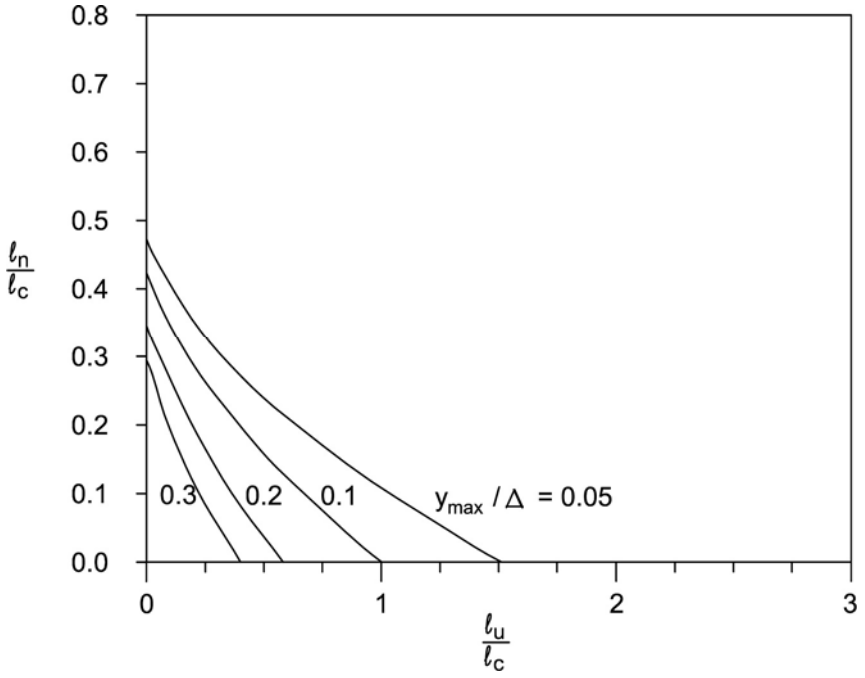

Figure 5-4(b). Equivalent cantilevers for pinned-head piles embedded in a uniform soil.[26]

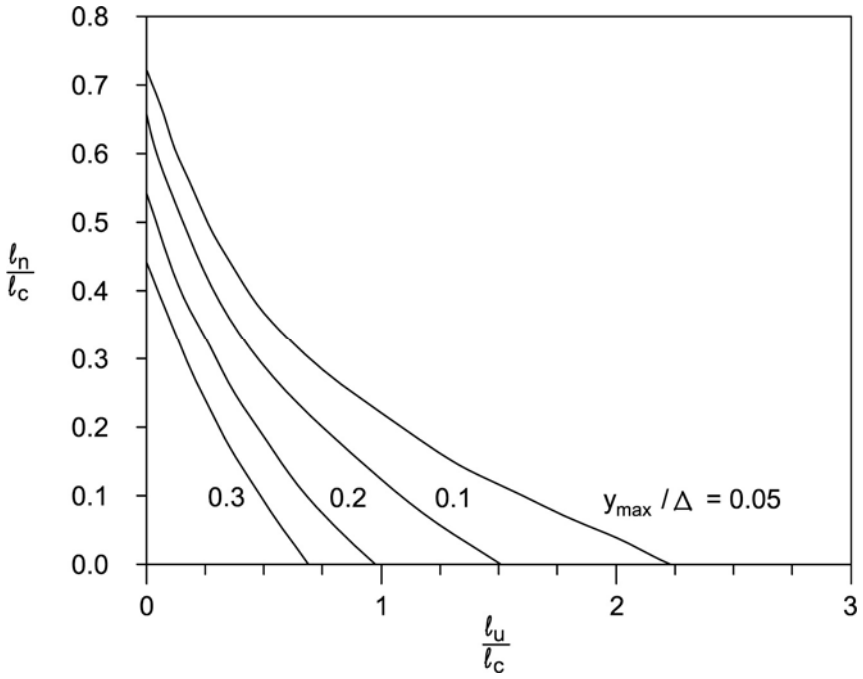

(a) Displacement for a fixed-head pile embedded in a uniform soil.

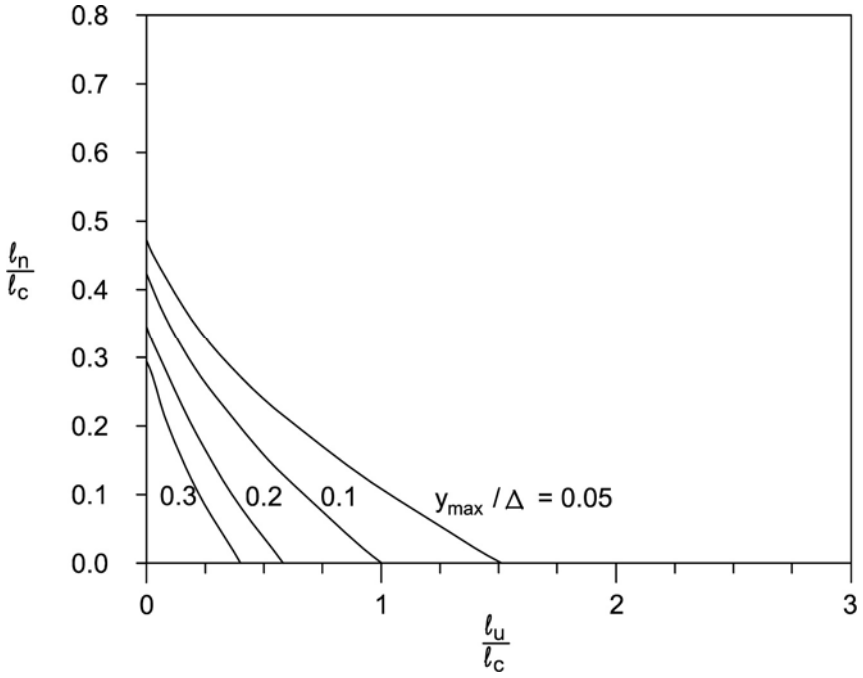

(b) Displacement for a pinned-head pile embedded in a uniform soil.

Figure 5-5. Length of pile, ℓ_n, to be neglected for frictional resistance.[26]

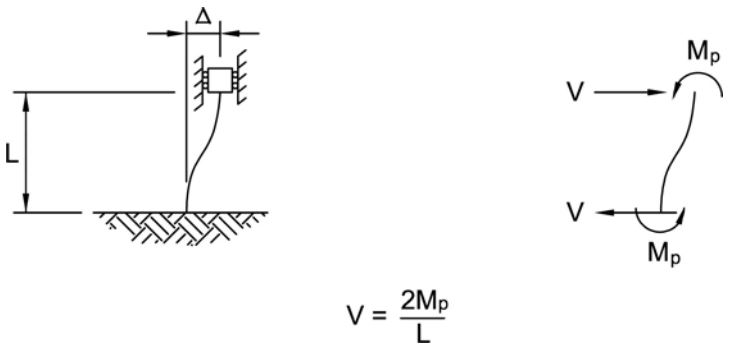

Figure 5-6. Moments and shears in displaced pile.

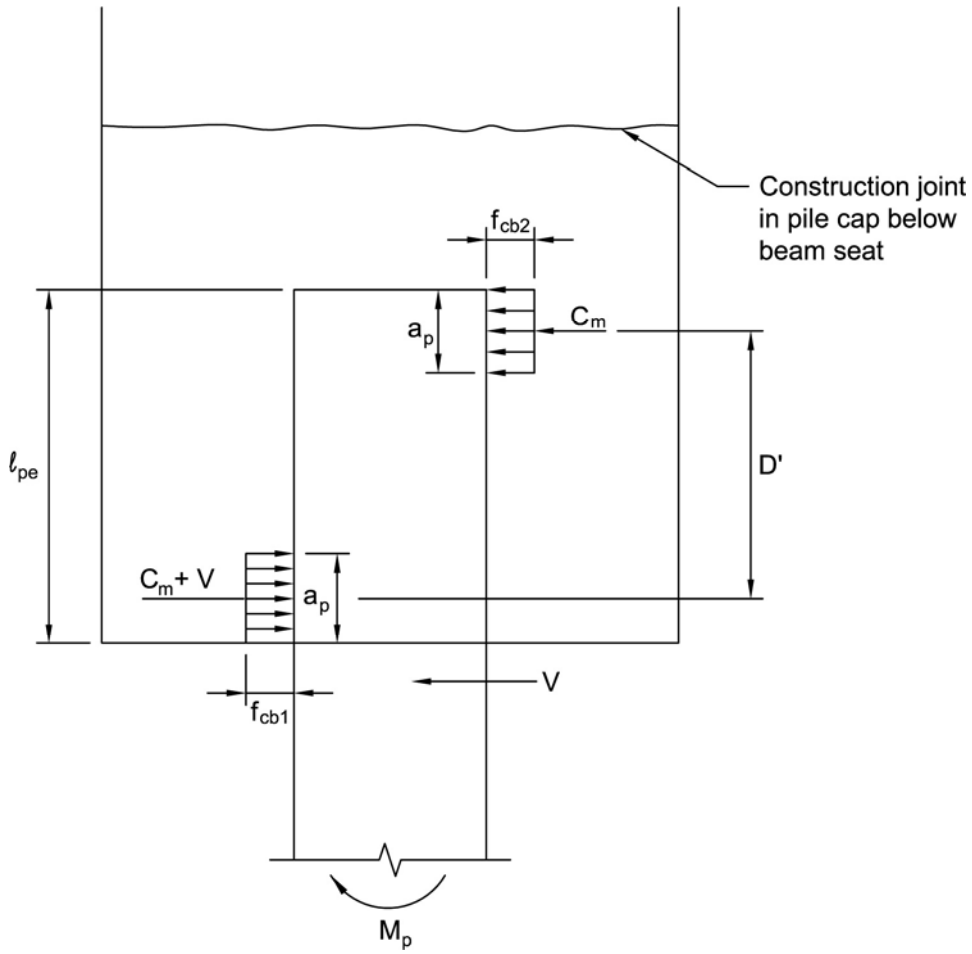

Figure 5-7. Transfer of pile moments to pile cap.

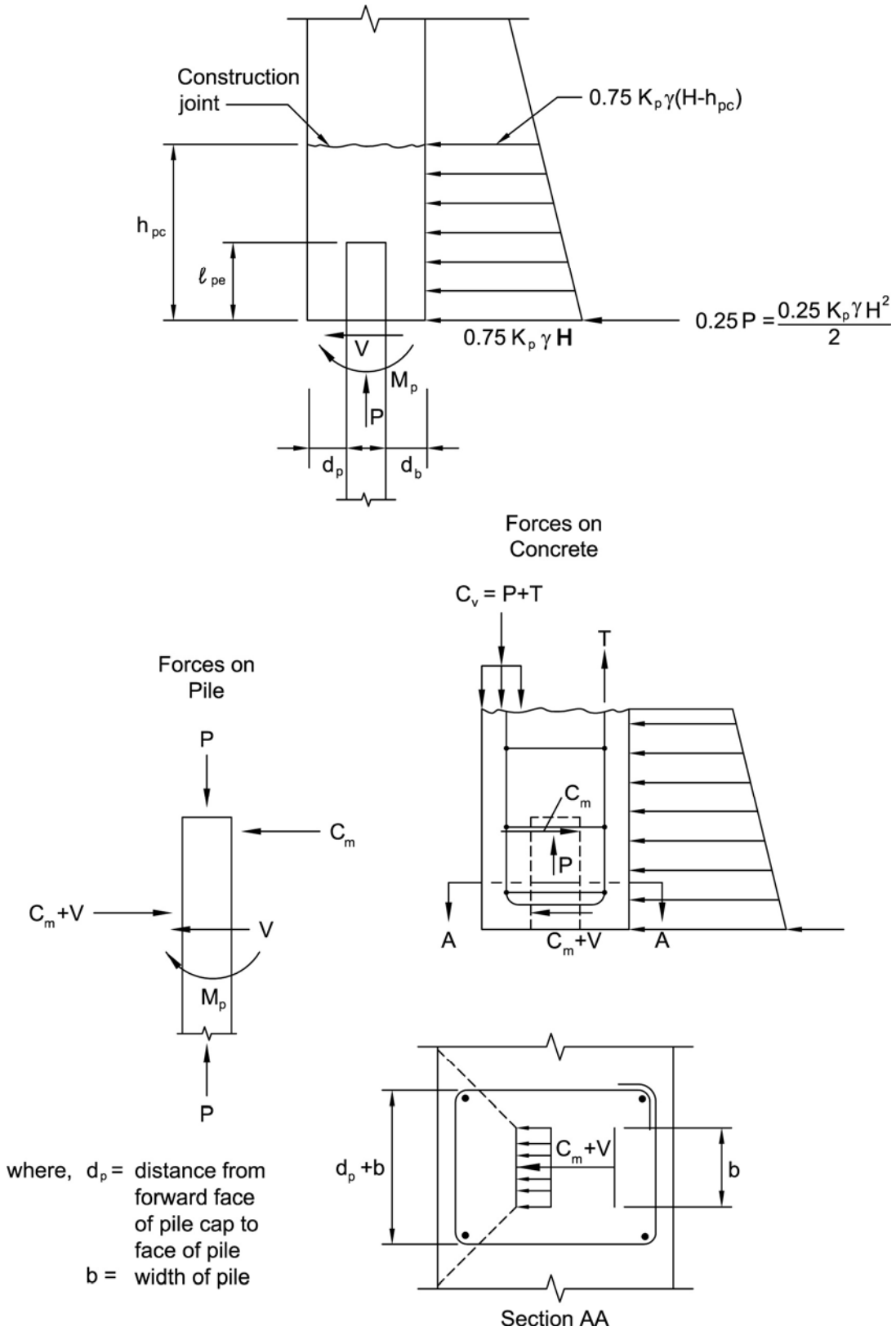

Figure 5-8. Forces on pile cap.

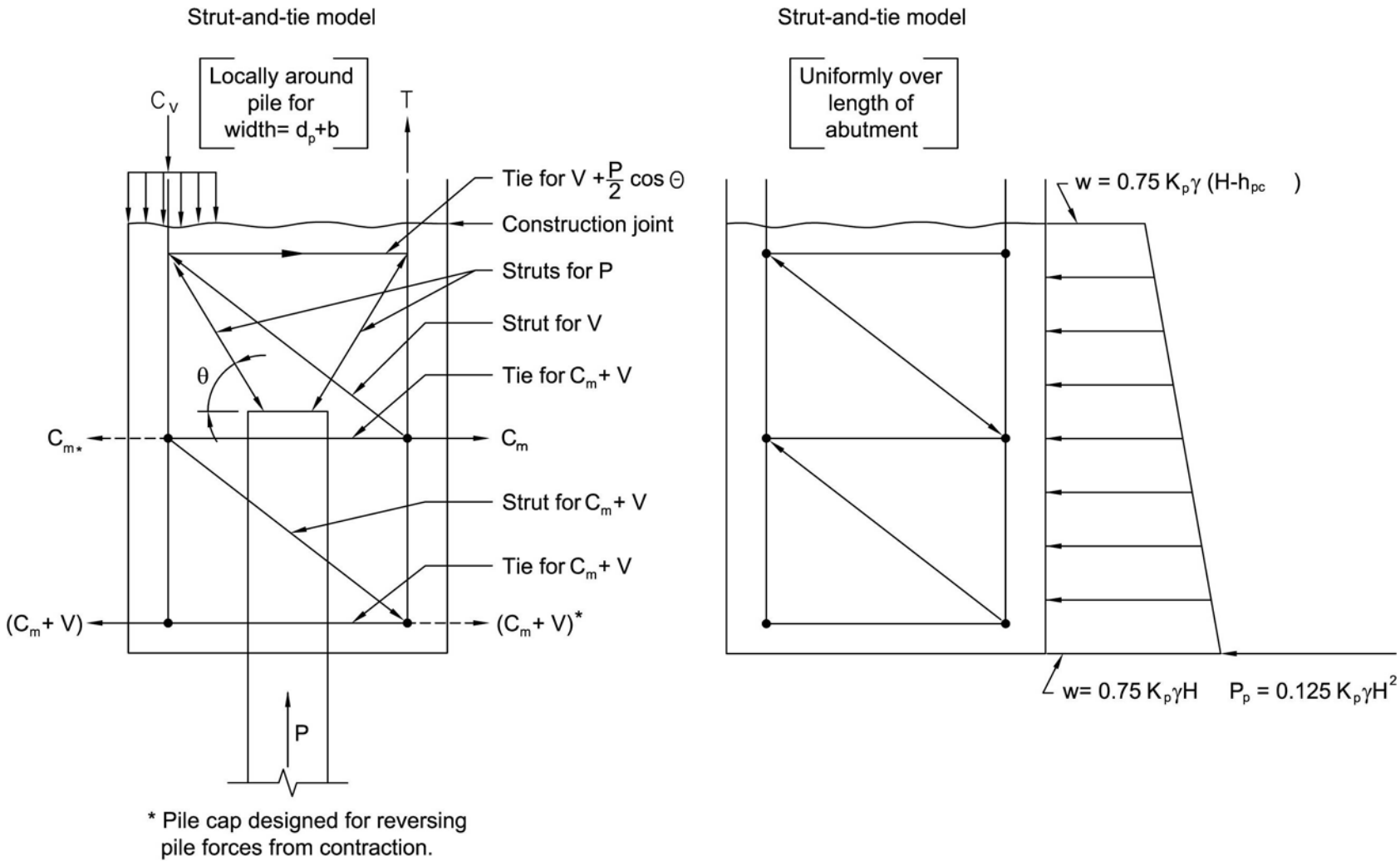

(a) Strut-and-tie model for pile forces.

(b) Strut-and-tie model for soil forces.

Figure 5-9. Strut-and-tie models for pile cap.

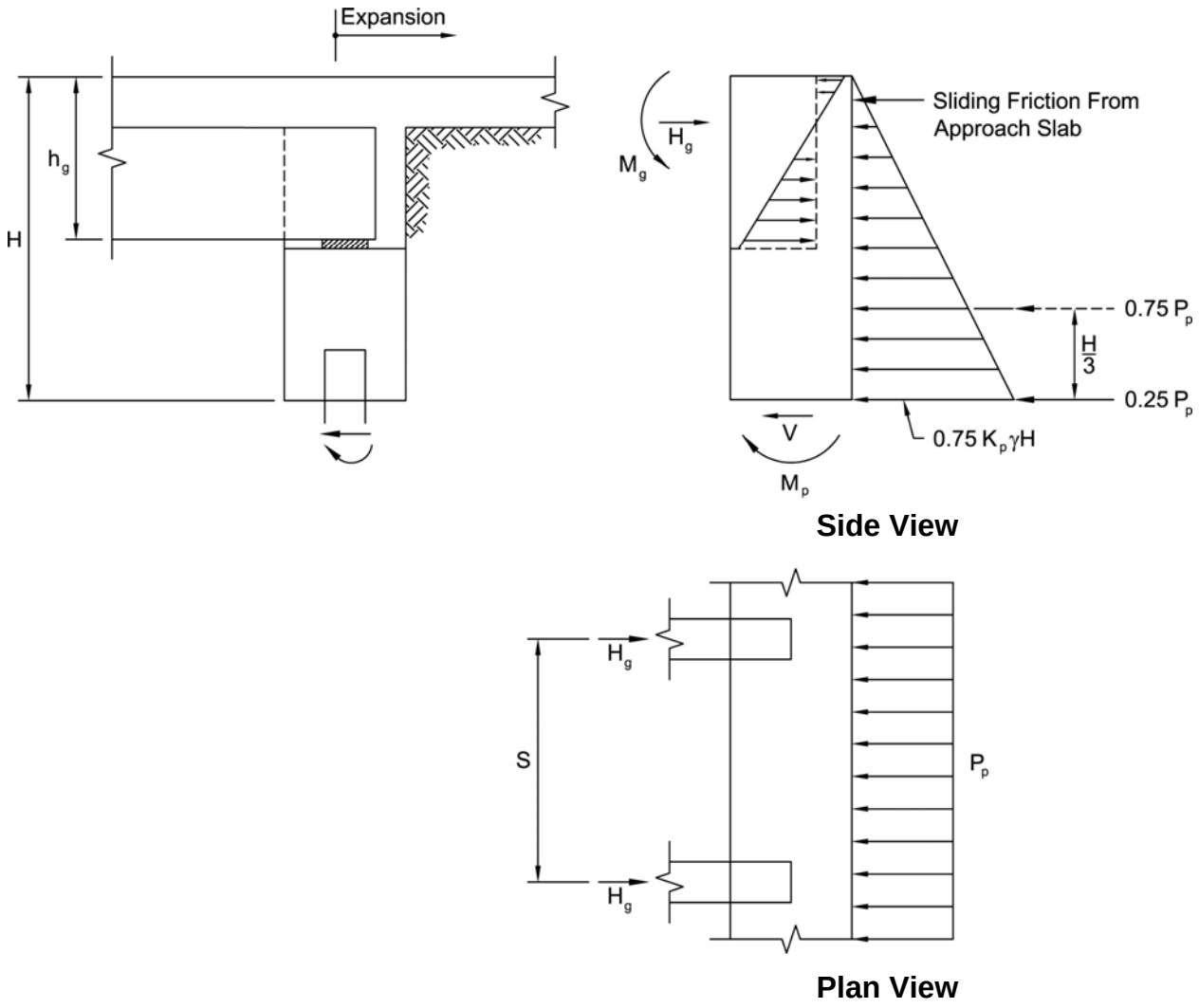

Figure 5-10. Forces acting on abutment during thermal expansion.

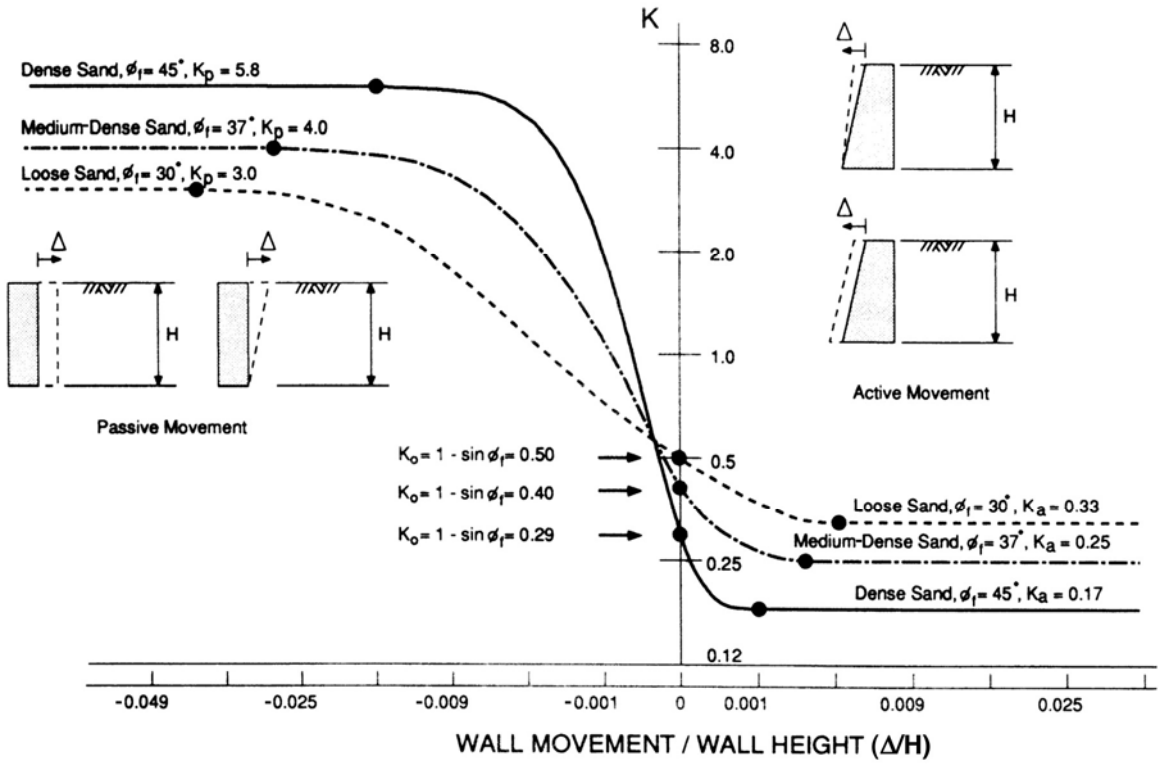

Figure 5-11. Relationship between abutment wall movement and earth pressure.[11,23]

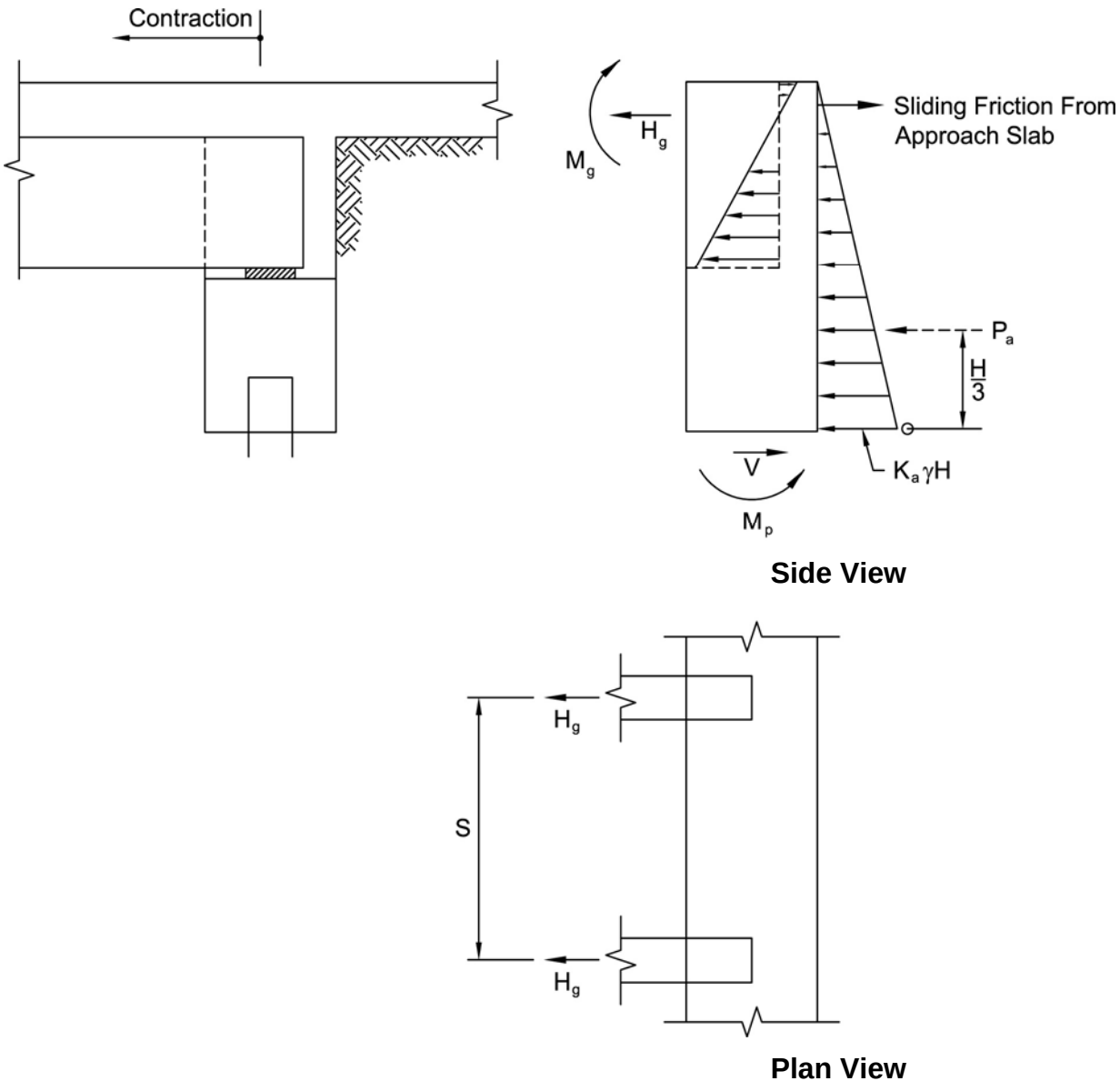

Figure 5-12. Force acting on abutment during thermal contraction.

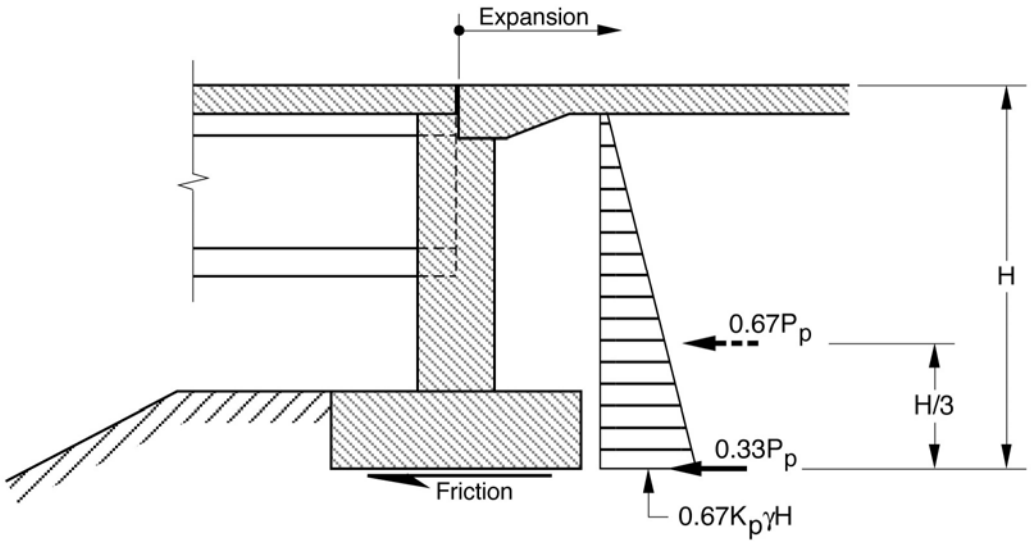

Figure 5-13. Location of passive pressure resultants and soil friction for design of short integral abutments on spread footings with sliding of the footing.

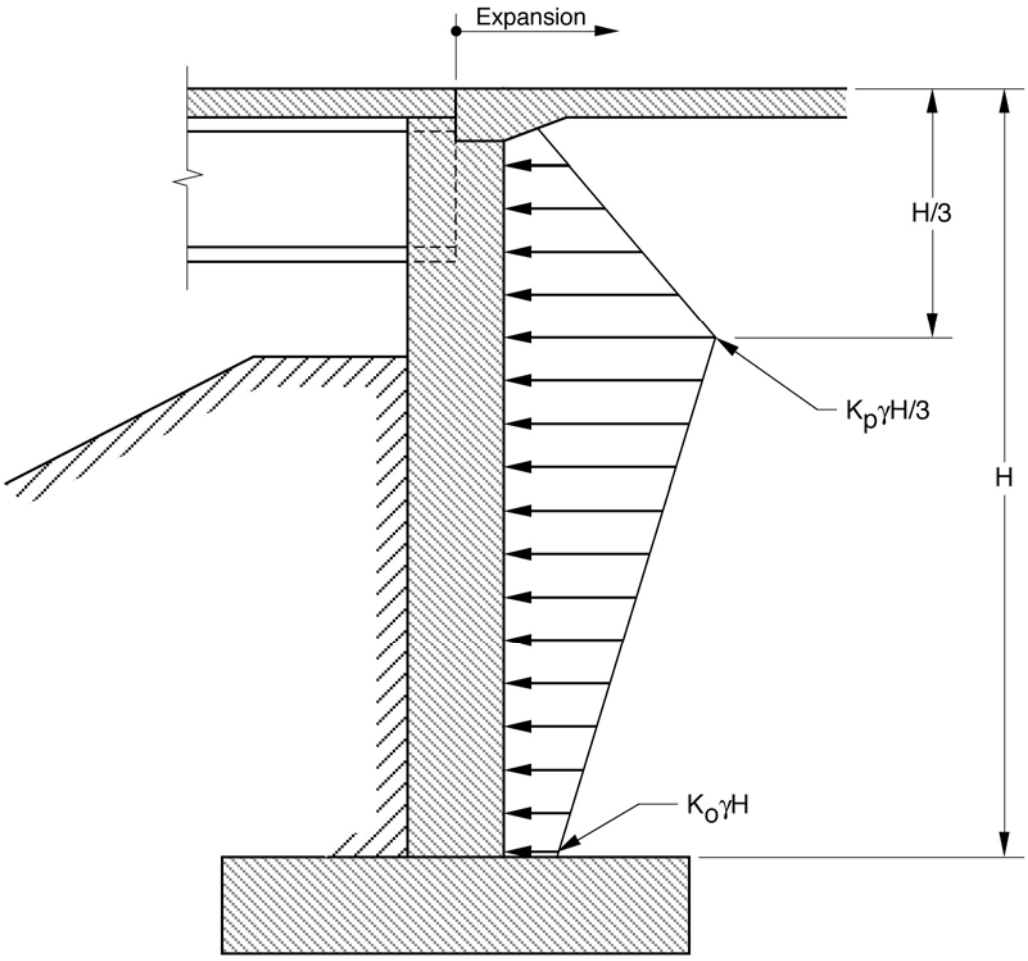

Figure 5-14. Passive pressure distribution for deeper spread-footing abutments with end movements accommodated by bending in the abutment wall.

(a) Semi-integral or stub integral abutment on spread footing. The reinforced soil must be allowed to settle before constructing the bridge and approach pavement.

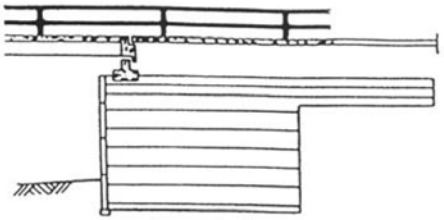

(b) Piled integral abutment. The piles are surrounded by an earth-pressure relieving sleeve.

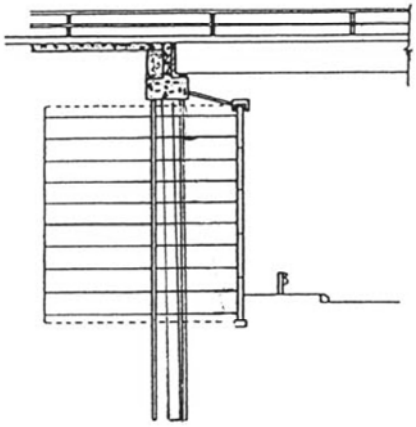

(c) Semi-integral abutment in front of reinforced soil.

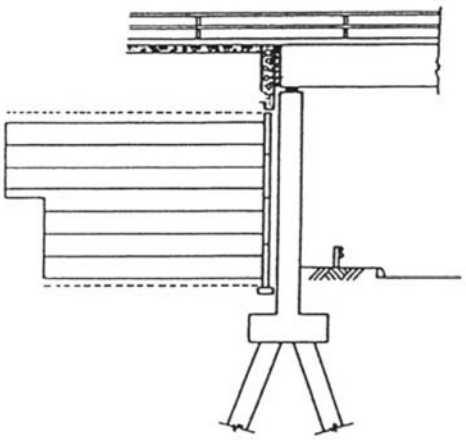

(d) Integral stub abutments on spread footing. The reinforced soil must be allowed to settle before constructing the bridge and the full-height reinforced concrete facing.

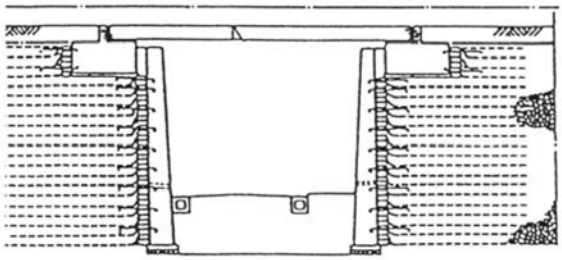

Figure 5-15. Alternatives to integral full-height wall abutments using reinforced soil retaining structure.[52]

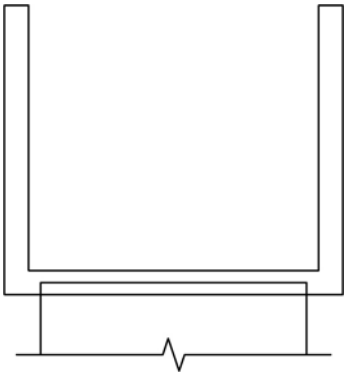

(a) U-shaped wingwalls.

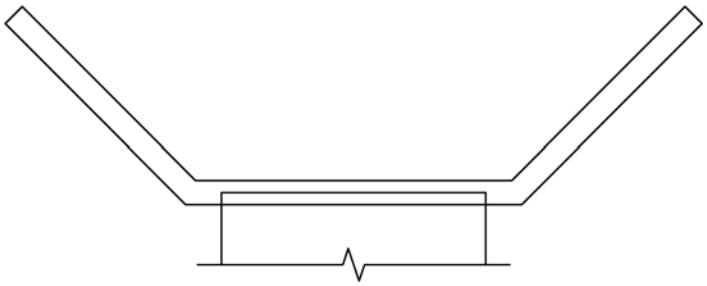

(b) Flared wingwalls.

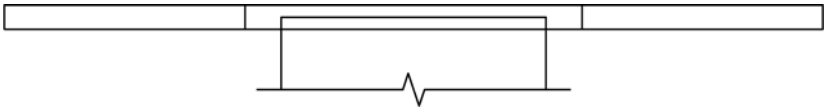

(c) Straight wingwalls (or trapezoidal) abutment.

Figure 5-16. Wingwall configurations.

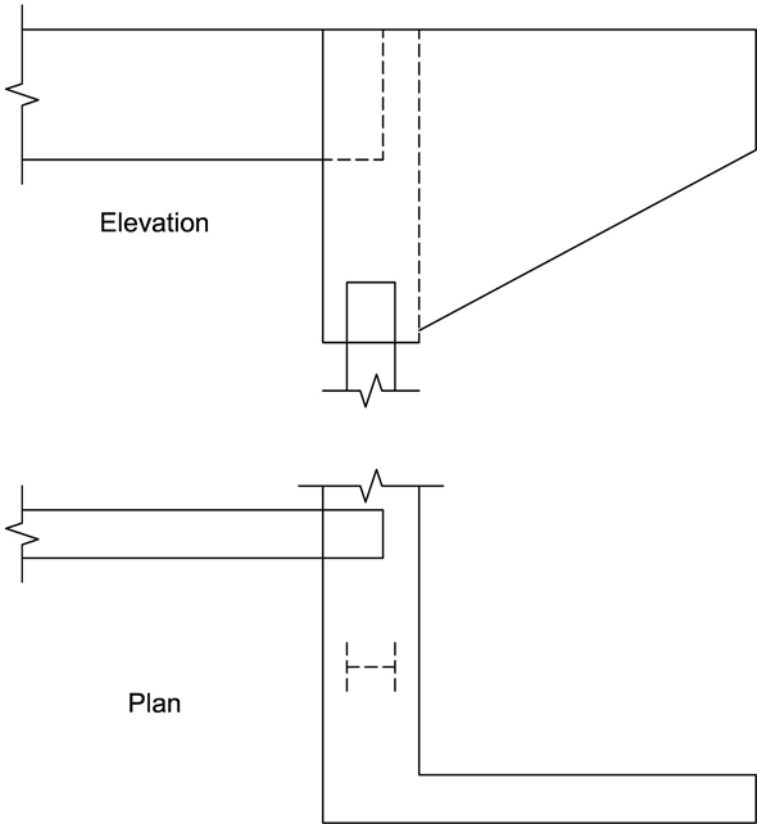

(a) Wingwall cantilevered from front wall.

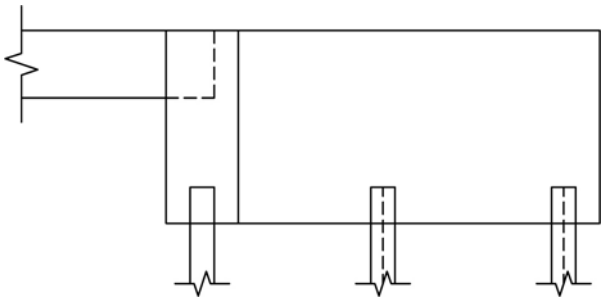

(b) Wingwall supported on piles.

Figure 5-17. Wingwall support arrangements.

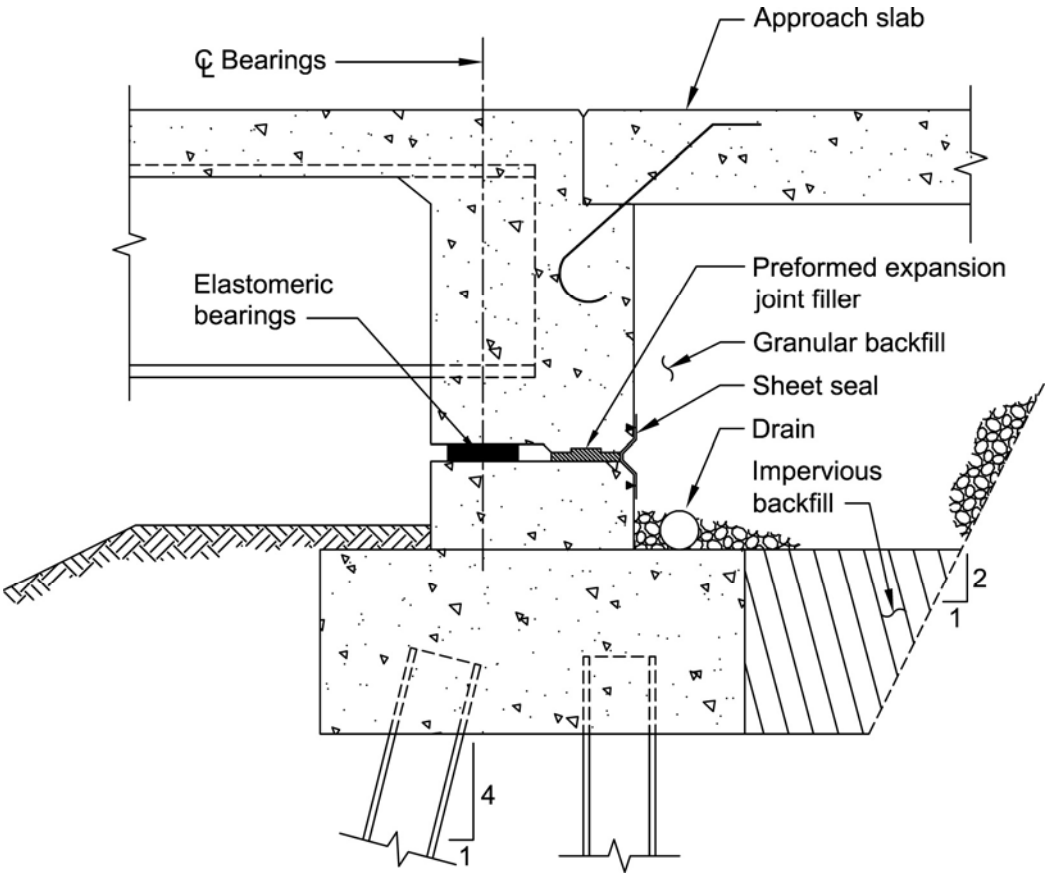

Figure 5-18. A semi-integral abutment concept for single- and multiple-span continuous bridges.[51]

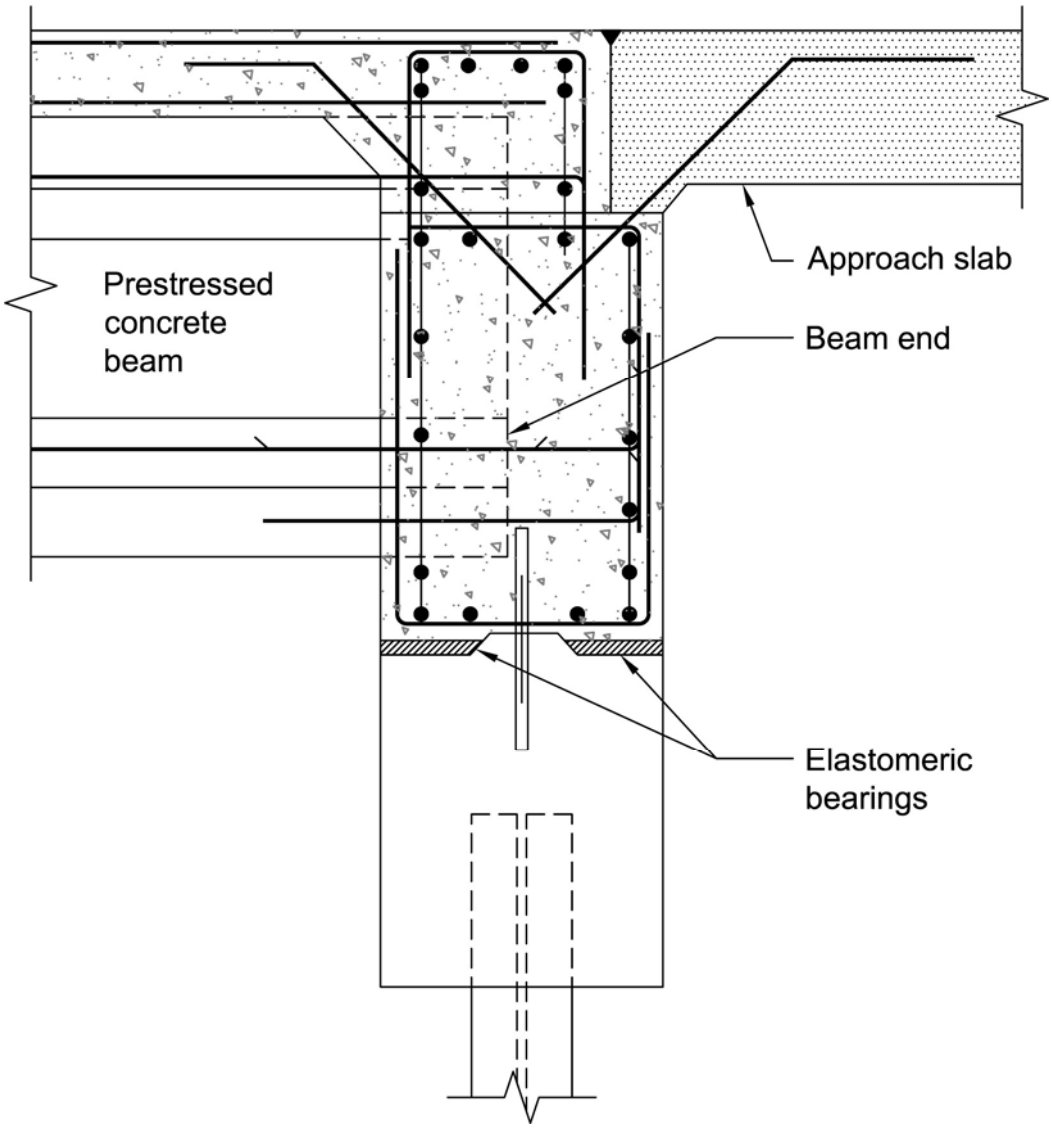

Figure 5-19. Semi-integral abutment concept with pinned connection of superstructure to pile cap.

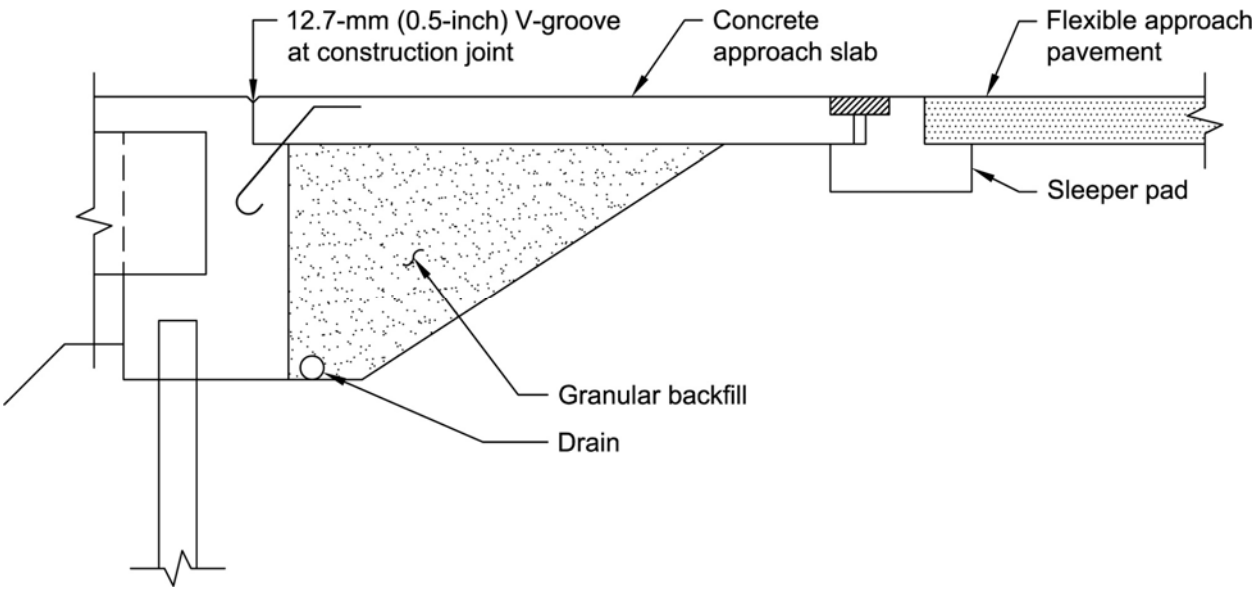

Figure 5-20. Approach slab arrangement.

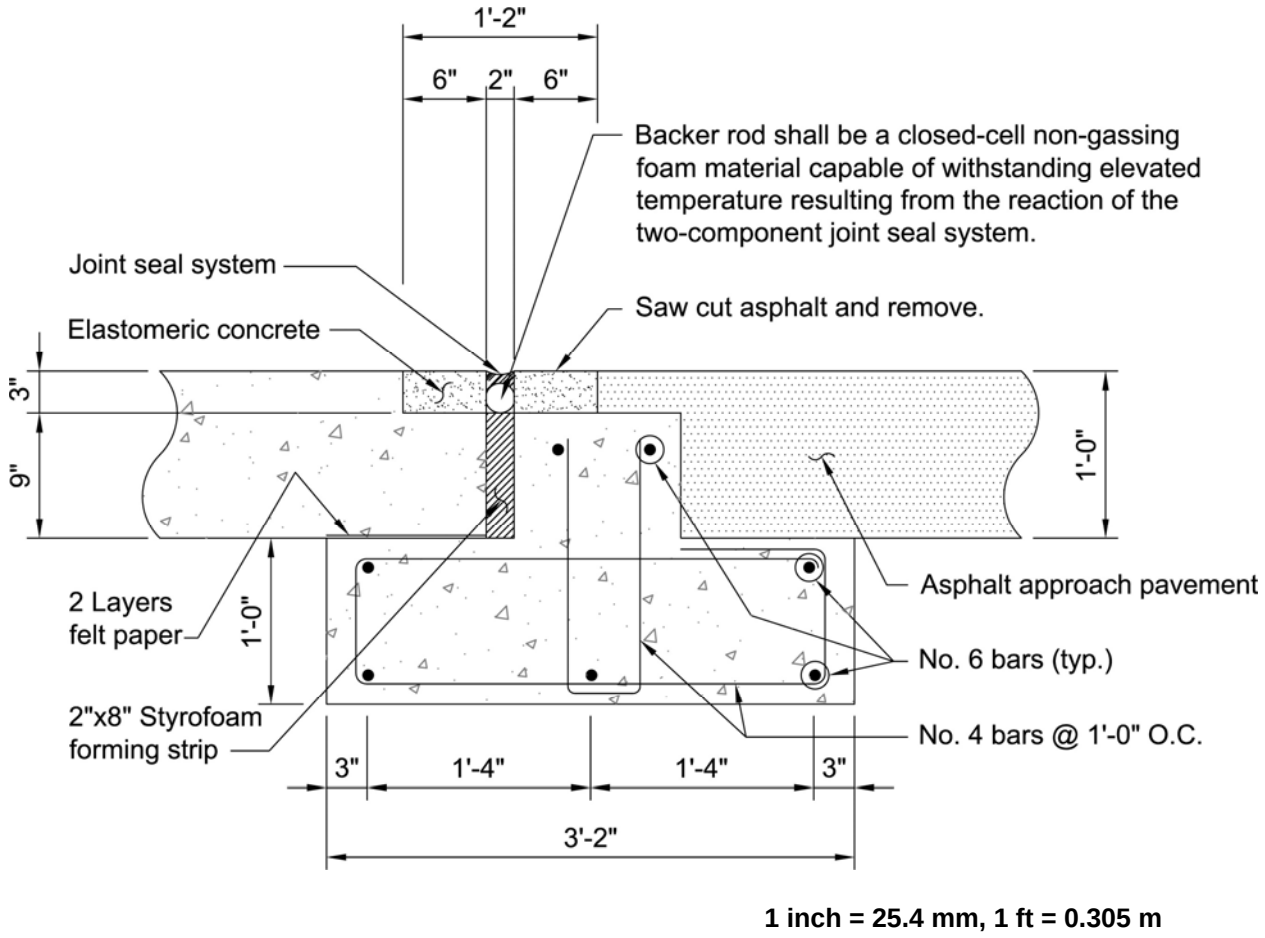

Figure 5-21. Sleeper pad detail suggested by Wasserman and Walker.[64]

6. RETROFITTING EXISTING BRIDGES

6.1 INTRODUCTION

A . very large percentage of the bridges built between 1950 and today in the United States have been constructed using simple supports. This reflects the difficulty in both designing indeterminate structures before computers and constructing these structures. The percentage of bridges classified as structurally deficient in the National Bridge Inventory is higher for simple-beam bridges compared to those that are continuous. Consequently, many simple-span bridges will need repair and upgrading. Once that is accomplished, it will be possible to consider retrofitting the simple spans into continuous ones, while eliminating all deck joints.

FHWA Technical Advisory T5140.16 recommends that during the rehabilitation of bridge decks, the joints and structural layout should be studied to determine which joints can be eliminated.[73] When the elimination of existing joints is considered, the Technical Advisory indicates that design studies should consider the following:

"1. The capability of the existing structural elements to properly function without the existing joints should be considered.

2. Provision for movement should be in accordance with AASHTO Highway Bridge Specifications.

3. Whether the existing bridge requires complete deck replacement or only minor rehabilitation, several simple spans should be grouped into a continuous unit, if appropriate. Continuity can be accomplished by making the deck slab continuous through several spans, or by making the stringers continuous, if structurally feasible.

4. All obsolete, and deteriorated bearings beyond repair,,should be replaced with elastomeric bearing devices.

5. If the abutment is unrestrained, a fixed integral condition can be developed for many of the shorter bridges. An unrestrained abutment is assumed to be one that is free to rotate, such as a stub abutment on one row of piles or an abutment hinged at the footing."[73]

When rehabilitation of existing joints is considered, a straightforward approach, such as that shown in figure 6-1, may be used.[73]

The information provided in this chapter is intended to assist bridge engineers in eliminating joints in existing bridges. This chapter achieves this by presenting a review of current practices and research by others, and a review of information provided in chapter 5 of this volume that is relevant to the retrofitting of existing bridges.

6.2 REVIEW OF CURRENT PRACTICES

Three potential options are available for rehabilitation of existing jointed bridges into jointless bridges. These include:

1. Making the beams continuous for dead and live loads.
2. Making the beams continuous for live loads only.
3. Making only the deck slab continuous.

All three of these options can be used with or without integral abutments.

The first option may not always be practical because the dead load of the structure is already in place. Continuity for dead load will require removing or temporarily negating the dead load on the structure, which is not likely to be economically or technically feasible. The second option is to provide negative-moment continuity over the piers for live loads only, with or without positive-moment continuity over the piers. The third option is to make only the deck slab continuous; with this option, the slab is jointless, but the beams are simply supported. This continuous-deck option involves removing a length of slab at the ends of the adjacent beams, splicing the existing reinforcement and adding new rebars, and recasting that part of the deck. This appears to be the simplest approach. Alternatively, a concrete overlay containing additional reinforcement can be placed to provide continuity. This has the disadvantage of increasing the deadweight of the structure and is not as good. The following discussion explains some procedures in current use to accomplish one of these three options.

Bridge Inspection and Rehabilitation, A Practical Guide provides a brief discussion of deck joint elimination.[74] It recommends a structural analysis to assess the strength and deformation capacity of the existing bridge components under thermal restraint forces. If these components are found to be adequate, the cost of deck joint elimination can be minimized and retrofitting is feasible. Bridges with short spans and tall or flexible substructures fall into this category. If the analysis indicates the need for extensive strengthening and modifications, then deck joint elimination will be more expensive than rehabilitation or replacement of the joints, at least in the short run. Bridges with long

spans and short, stiff substructures fall into this category. Many bridges fall between these two categories and will require a cost analysis to determine the feasibility of joint elimination.

The procedures for deck joint elimination listed in *Bridge Inspection and Rehabilitation, A Practical Guide* are essentially the same procedures described by Wasserman based on Tennessee DOT's experience.[72] A survey of current practices related to retrofitting for live load continuity by A. Scanlon, et al., found that 14 out of 58 agencies responding had experience with retrofitting for live load continuity.[75] The number of projects completed by these 14 agencies ranged from 1 in Alberta (Canada) to more than 100 in Tennessee.

Wasserman observed that the State of Tennessee's initial experience involved achieving full (live load) continuity in steel beams removing parts of the deck over the supports and installing splice plates on the top flanges.[72] This was time consuming and expensive. For moderate span lengths, the State progressed to replacement of the deck slab over the supports with tensile reinforcement spliced in. The top flanges were not spliced. However, compression splices were added to the bottom flanges. Wasserman indicated that:[72]

> "Current practice [1987] uses a 4-1/2-inch [114.3-mm] reinforced concrete overlay on the existing concrete deck [shown in figure 6-2 of this report]. Prior to placement, the existing deck is scarified to a depth of 1 inch [25.4 mm], the remaining delaminated concrete areas are removed, and the deck surface is sandblasted and cleaned. Negative-moment reinforcement is placed over the joints at the intermediate supports and the overlay is poured. Depending upon the type of girders and length of span, beam-end modifications vary. For short-span, cast-in-place, and PS/C girders, no additional modifications are employed. For longer concrete spans, compression blocks are poured between adjacent beam ends. Similarly, for short-span steel beams, no modification is required. For longer steel spans, compression flanges are jointed. In some cases, bearings must be modified. In most cases, the ends of slabs at abutments and backwalls are modified for moment connections to eliminate end-of-bridge joints.
>
> Where the foregoing modifications are employed, if structure widening is to be added, the new section will be of fully continuous composite construction."

As part of the experimental portion of this project, field surveys of jointless bridges were conducted.[14] The field survey included four retrofitted bridges in Tennessee. These are

Bridges 4, 5, 6, and 13 as described in chapter 10 of the experimental report[14] and in section 3.5 of this volume. The following is a summary of observations for those bridges:

1. Two bridges were retrofitted with continuous decks only. Typically, at least the beams on one side of the piers were connected to the pier cap to effect a pinned connection between the superstructure and the pier at each pier cap. The connections for the beams on the other side of each pier were detailed as expansion connections. These two bridges exhibited minor (hairline) cracks in the decks over the piers.

2. Two bridges were retrofitted to make both the decks and beams continuous. One bridge had an arch center span and three approach spans on each end. The approach-bridge spans were retrofitted with new PS/C girders with continuity connections across the diaphragms. The other bridge was a steel bridge with splice plates added to the top and bottom flanges to effect moment connections over the piers.

3. Two decks (Bridges 4 and 6) were retrofitted by removal and replacement of the entire deck slab. One deck (Bridge 5) was retrofitted by scarifying the existing slab 25.4 mm (1 inch) and adding a 114.3-mm (4.5-inch) overlay. Additional reinforcement was placed in the overlay over the piers. One deck (Bridge 13) was retrofitted by scarifying the existing slab 6.35 mm (0.25 inch) and adding a 31.75-mm (1.25-inch) polymer concrete overlay. No reinforcement was placed in the overlay. However, a 710-mm- (2.33-ft-) wide strip of the existing deck on each side of the existing expansion joints was removed to the full depth while retaining its reinforcement. The existing bars were spliced with No. 4 bars at 152.4 mm (6 inches) to form a continuous reinforced concrete slab.

4. For three retrofitted bridges, the existing abutment pile caps were used to support the beams. The ends of the girders were then encased with new concrete dowelled into the existing pile cap to make the abutments integral. Drawings indicated some existing battered piles under the abutments (probably every other pile was battered forward at a slope of 2H:12V); however, there was no attempt made to release the abutment from these battered piles.

5. All new integral abutments were built for the fourth retrofitted bridge.

6. The length of the retrofitted bridges varied from 61 m (200 ft) to 107 m (350 ft).

Further descriptions for each of these bridges are provided in the detailed experimental report.[14]

In addition to Tennessee's retrofitting experience, details were obtained for 12 bridges retrofitted by the Ohio DOT. These bridges were typically three- or four-span continuous bridges with joints at the ends. Their abutments were retrofitted to be either integral or semi-integral, depending on the condition of the existing abutments. Details are similar to those shown in figure 6-3.

When using these concepts with existing stub abutments on a single row of piles, it is recommended to:

1. Ensure that existing pile-to-abutment connections can resist the forces associated with the expected movement.
2. Remove the existing abutment to the top of the piles and replace with reinforced concrete cast around the beams and connect to the approach slab.
3. Excavate to the bottom of the pile cap and provide drainage, backfill, and approach slabs behind the newly constructed integral abutment.

For existing stub abutments with multiple rows and/or heavily battered pile, it is recommended to:

1. Remove the existing abutment to near the top of the piles.
2. Rebuild with a sliding surface between the pile cap and the abutment stem cast integrally with the beam ends and approach slab.
3. Provide details for both horizontal and vertical sliding joints with lateral guide bearings, sheet seals to keep soil and water out of the joints, and drainage and backfill typically used with newly constructed semi-integral abutments.

This semi-integral abutment retrofit concept can also be used for existing full-height wall abutments.

6.3 REVIEW OF RESEARCH BY OTHERS

6.3.1 Continuous Deck Only

F. Gastal and P. Zia studied the behavior of continuous decks on simply supported beams, which are referred to as "deck-continuous beams."[76] The studies included nonlinear finite element analyses of beams connected with link elements simulating the

continuous deck over the joint between the beams at the piers. These analyses indicated a range of behavior that is dependent on the support conditions. As shown in figure 6-4, combined bending and horizontal movement at the top of the beams at the beam joint, depends on the horizontal fixity of the supports on the bottom of the beams. For the two - hinged bearings at the center support shown in figure 6-4(a), the link would be expected to be in tension and to provide some degree of live load continuity. For the two roller bearings at the center support shown in figure 6-4(b), analyses indicated that the deck link would be in compression and the beams would behave as simply supported.

The analyses by Gastal and Zia were validated by comparisons with the results of tests of simply supported beams without the bridge deck link.[76] Further work by A. Caner and P. Zia included testing of large-scale, two-span composite steel and reinforced concrete girders with a continuous deck across the center joint.[77] These tests demonstrated that the girders essentially behave as simply supported regardless of the horizontal restraint of the support conditions. Also, the tests showed that link slabs act as relatively flexible beams that bend to conform to the end rotations of the girders.

This observation is similar to the conclusions reached from the analysis of a PS/C bridge girder without a positive-moment connection at the piers, which was carried out in this jointless bridge project; this analysis was included in the analytical task discussed in section 4.4.3 of this volume. This analysis showed that the deck section alone is very flexible and that stress in the deck reinforcement is determined by deformations, primarily the rotation at the ends of the girder caused by creep and shrinkage. Restraint of contraction from the integral abutment pile and friction from dragging the approach slab in the PS/C bridge analyzed in this project had very little effect on the stress in the reinforcement in the deck over the supports.

Based on observations from test girders, Caner and Zia proposed a design method that includes:[77]

1. Considering each span as simply supported and using standard design procedures without considering the effects of the link slabs on the girders.
2. Debonding the link slab over the joint for a length equal to 5 percent of each span to further reduce the stiffness of the link.
3. Determining the maximum end rotations of the girders as simply supported under service loads and imposing the end rotations on the link slab to determine a design moment for the link slab.

4. Designing the reinforcement using crack-control criteria to limit the crack width at the surface of the link slab. Preliminary design tables are provided by Caner and Zia to determine stress in the link-slab reinforcement.

Other design considerations may include rotations caused by the differential thermal strains and the restraint of contraction in jointless bridges, as further discussed in section 6.4 below.

6.3.2 Standard Details and Design Information

In a study undertaken to develop standard details and supporting design information for retrofitting existing simple-span bridges for continuity, Scanlon, et al., considered both continuous-deck bridges (referred to as partial continuity by Scanlon) and bridges made continuous for live load only (referred to as full continuity).[78]

The results of the study for continuous-deck retrofitting included:

1. Limiting spans to 21 m (70 ft) to limit crack widths in the link slab (until further experience is gained).
2. Providing a minimum reinforcement ratio of 1.5 percent (A_s/bd) in a layer 65 mm (2.5 inches) from the top of the slab to further improve crack control.

The report produced by Scanlon, et al., includes proposed retrofitting details, design procedures, and design examples for continuous-deck bridges and for bridges made continuous for live load.[78] Details and design procedures are included for PS/C I-beams, adjacent box beams, spread box beams, and steel beams.

6.4 REVIEW OF DESIGN RECOMMENDATIONS FOR RELEVANCE TO RETROFITTING

As noted in section 6.1 above, while planning for the rehabilitation of bridge decks, the existing bridge should be studied to determine the capability of existing structural components to function properly without expansion joints so that existing joints can be eliminated, as appropriate. The study requires structural analyses for the response to restrained movement. However, most of the uncertainties for structural analyses for new jointless bridges also pertain to retrofitted bridges. Similarly, though, most of the design recommendations in chapter 5 of this volume for new jointless bridges are also relevant for retrofitting bridges to eliminate expansion joints.

In the following section of this volume, each section of chapter 5 is reviewed for relevance to retrofitting existing bridges to be jointless.

6.4.1 Determination of Expected Movements

The procedures recommended for determining the expected movements, including the determination of effective temperatures and maximum expected movements, are all applicable to retrofitted bridges, with the exception that no significant creep is expected to occur in the older PS/C girders. Therefore, the analyses for the expected movement of retrofitted PS/C bridges that retain the existing PS/C beam would be the same as for reinforced concrete bridges.

6.4.2 Design of Abutments

Analyses for the response of a single row of vertical piles supporting an integral abutment, as presented in section 5.3.1, are also appropriate for retrofitted bridges. One particular condition to check, however, is the embedment of the piles into the pile cap and the ability of the pile cap to develop the forces at the pile-to-pile-cap connection, as described in section 5.3.2.

If the existing abutment will resist the longitudinal movement with battered piles, a semi-integral abutment may be required. However, because of simpler construction and simpler details, the use of an integral abutment is recommended over the use of a semi-integral abutment when the superstructure can handle the expected restraint forces. Therefore, a recommendation with respect to existing abutments with battered piles is to consider analyses of the stiffness of the battered piles, to assess the need for a semi-integral abutment versus an integral abutment retrofit. This is particularly pertinent for existing abutments with battered piles in the same row as vertical piles and also for relatively short bridges. Battered piles are usually designed for lateral forces without consideration of stiffness. Analyses of the lateral forces in battered piles under the maximum expected movement of integral abutments may indicate that the bridge superstructure and the connection of the girders to the abutment can conservatively resist the restraint forces in battered piles, particularly with short bridges and/or bridges in regions that have small annual temperature ranges.

H. G. Poulos and E. H. Davis describe methods for the analysis of the stiffness of battered piles.[79] Also, NCHRP Report 343[23] refers to A. Hrennikoff's linear elastic procedure to solve for pile forces and displacements in two dimensions.[80] W. E. Saul[81] expanded Hrennikoff's solution to three dimensions. O'Neill, Ghazzaly, and Ha,[82] and

O'Neill and Tsai[83] have developed a method for analyzing three-dimensional pile groups, that considers nonlinear soil response and pile-soil interaction.

6.4.3 Wingwalls and Piers

The recommendations for the forces on the abutments' wingwalls and for the design of piers presented in sections 5.3 and 5.4 are all relevant for assessing the feasibility of jointless retrofitting.

6.4.4 Secondary Effects

For consideration of the secondary continuity forces discussed in section 5.5, the response of retrofitted jointless bridges depends primarily on whether the retrofit is continuous-deck only with simply supported beams or whether it is fully continuous with moment-resistant splices over the piers.

6.4.4.1 *Continuous Deck-Only Retrofit*

For a continuous deck-only retrofit, as demonstrated by Caner and Zia, the beams will behave essentially as simply supported and the link slabs should be designed for the moment associated with the end rotations of the girders.[77]

For secondary effects that generally produce positive moments in continuous structures, such as positive temperature gradients and differential coefficients of expansion, the response of a simply supported girder in a deck-only retrofit is an upward camber. With upward camber caused by positive gradient effects, the moments on the link slabs of the deck-only retrofit are opposite to the live load moments and place the top surface of the slab in compression. Also, the maximum positive temperature gradient occurs simultaneously with overall bridge expansion, and longitudinal restraint from the abutments and pier may place the link slabs in compression. Therefore, positive secondary effects are beneficial.

Note that upward camber caused by creep in prestressed girders should not be significant in existing girders. However, for retrofit work that involves widening with new PS/C stringers placed adjacent to existing ones, there should be consideration given to allowing the new girders to age prior to tying in the new deck, to minimize the differential long-term response between the new and old members.

For secondary effects that produce negative secondary moments in continuous structures, such as negative temperature differentials and differential coefficients of thermal expansion (and deck shrinkage and heat-of-hydration contraction in retrofits with full

deck replacement), the response of a simply supported beam in deck-only retrofits is a downward deflection. The end rotations of girders caused by the negative secondary effects are additive to live load rotations. In addition, the beam tests conducted as part of the experimental project (and described in section 3.3 of this report) demonstrated that the maximum unrestrained negative curvatures, calculated from measured temperatures along the depth of the girder, occurred in cold weather simultaneously with maximum contraction of the bridge length. Therefore, maximum tension in the link slabs from the restraint of contraction from integral abutments will occur simultaneously with maximum negative secondary effects.

The analyses described in section 4.4.3 indicate that cracking and creep in the deck will not significantly relieve the tension in the link slab from longitudinal restraint forces from integral abutments. However, cracking in the debonded length of the link slab, as recommended by Caner and Zia,[77] would help reduce the bending stresses in the link slab caused by end rotations of the girders.

The parametric studies carried out in this project for secondary effects, as described in section 4.5, did not include deck-only structures. This is an area for further research. Until this further research is conducted to quantify the relative effects of beam-end rotations under live load, of negative gradients, and of overall restraint to contraction, it is recommended that these three conditions (live load, negative gradient, and contraction) be superimposed for the design of the link slabs. Because crack width is the limiting criteria, these three conditions should be superimposed at the service-load levels to assess the potential for cracking. Additionally, however, it is known that the z-factor approach for crack control used in the AASHTO bridge design procedures and also referred to by Caner and Zia[77] is unduly restrictive when concrete covers exceed 51 mm (2 inches). Therefore, it is recommended that the spacing requirement in equations 5-37 and 5-38 be used for crack control and that a minimum reinforcement ratio of 1.5 percent (A_s/bd), as recommended by Scanlon, et al.,[78] be provided in a layer 65 mm (2.5 inches) below the top of the slab in the link-slab regions.

6.4.4.2 *Retrofit With Girder Continuity*

For bridges that have been retrofitted by making the beams continuous, whether for dead plus live loads or for live load only, there will be secondary effects.

For composite steel bridges, positive secondary moment effects will only occur if bottom flanges are spliced over the piers. The simply supported beams were originally designed for total dead plus live loads with positive-moment bending. Based on the analyses

described in section 4.5, stresses from positive secondary moments should be proportionately less significant when compared to dead and live load stresses in a retrofitted bridge, and explicit calculations for positive secondary moments are unnecessary except for the bottom flange splice. If the beam retrofit includes continuity for live load only (the more likely case), then the positive secondary effects will place this splice in tension daily as the deck is heated during the day, and live load will cause fatigue stresses in the connection. The splice design should consider the tension caused by the positive temperature gradient and the stress range from live load.

For negative secondary effects in composite steel girders retrofitted with bottom flanges spliced over the piers, stress in the bottom flanges should be checked for the same load conditions, as discussed in sections 4.5.2 and 5.5.1.1. In particular, the bottom flanges should be checked for proper lateral support to resist the new compressive stresses.

For precast, PS/C girders without extended end reinforcement for positive-moment connections, it would be very difficult to provide a positive-moment connection across the joint. However, based on the testing and analyses carried out in this project, the positive-moment connection is not needed, and PS/C-beam bridges need not be retrofitted for positive moment over the piers. The bridge will behave as if only the deck is continuous and the positive secondary moments can be ignored.

When a compression block is cast between the beam ends, cracking will relieve the negative secondary moments, as described in section 4.5.3. Therefore, the reinforcement in the deck over the piers can be designed as for a bridge continuous for live load only. Also, the beams can be considered continuous for factored loads. For service-level stresses at midspan, the bridge may behave as a simple span if end rotations from a positive temperature gradient open a gap at the compression block between the ends of the beams. This should not be a problem, however, because they were originally designed as simply supported.

6.4.5 Approach Slabs and Other Details

The recommendations in section 5.6 for approach slabs and in section 5.7 for details to accommodate movement are all applicable to retrofitted jointless bridges. The only difference in the approach slab behavior noted in the field survey for retrofitted bridges is that there may be less settlement of the far ends of the approach slabs because of less settlement in the existing embankment. However, the void development and approach slab settlement associated with cyclic movement of integral abutments should still be anticipated.

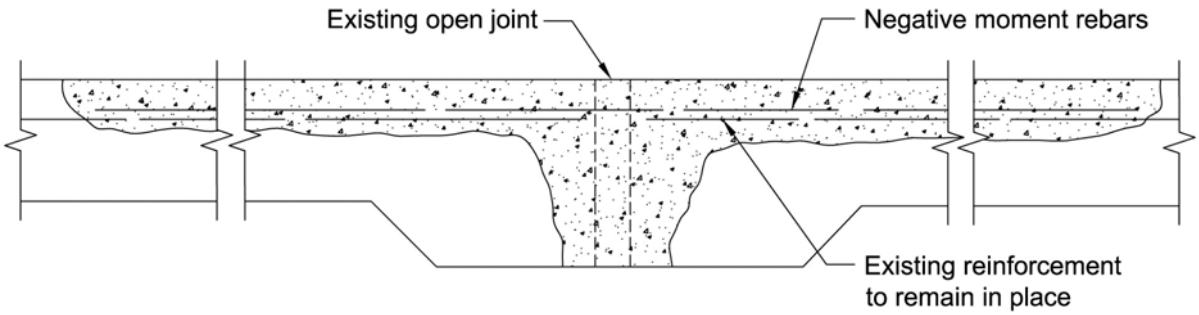

"Where feasible, develop continuity in deck slab. Remove concrete as necessary to eliminate existing armoring, and add negative moment steel at the level of existing top-deck steel sufficient to resist transverse cracking. Generally reconstruct with regular concrete to original grade."

Figure 6-1. Option for conversion of open joint according to FHWA Technical Advisory T5140.16.[73]

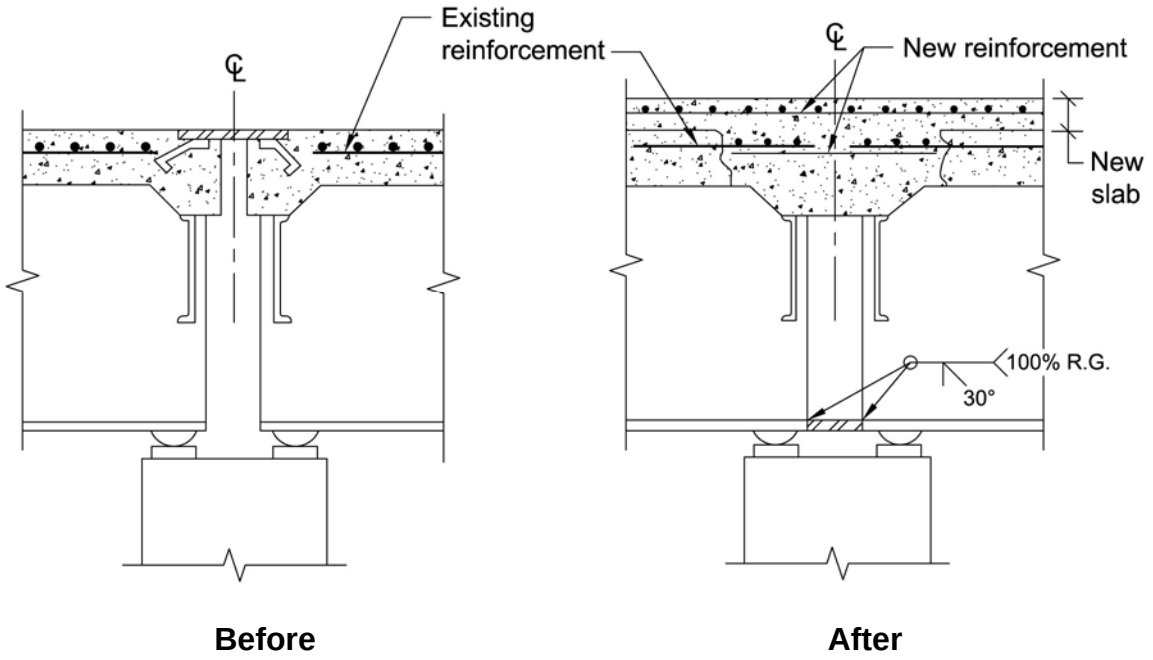

Figure 6-2. Joint-element details used in Tennessee.[72]

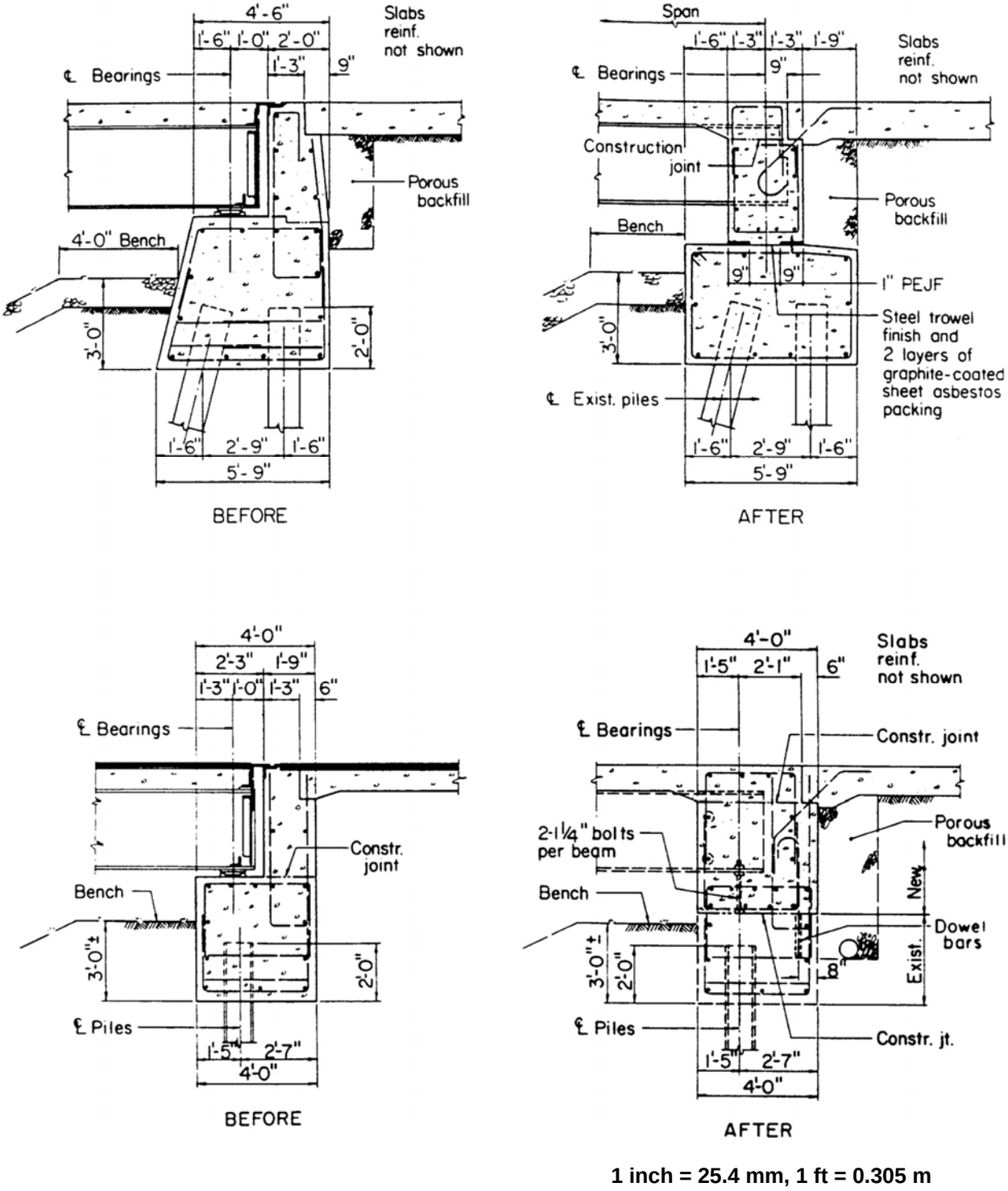

Figure 6-3. Retrofitting of stub abutments.[84]

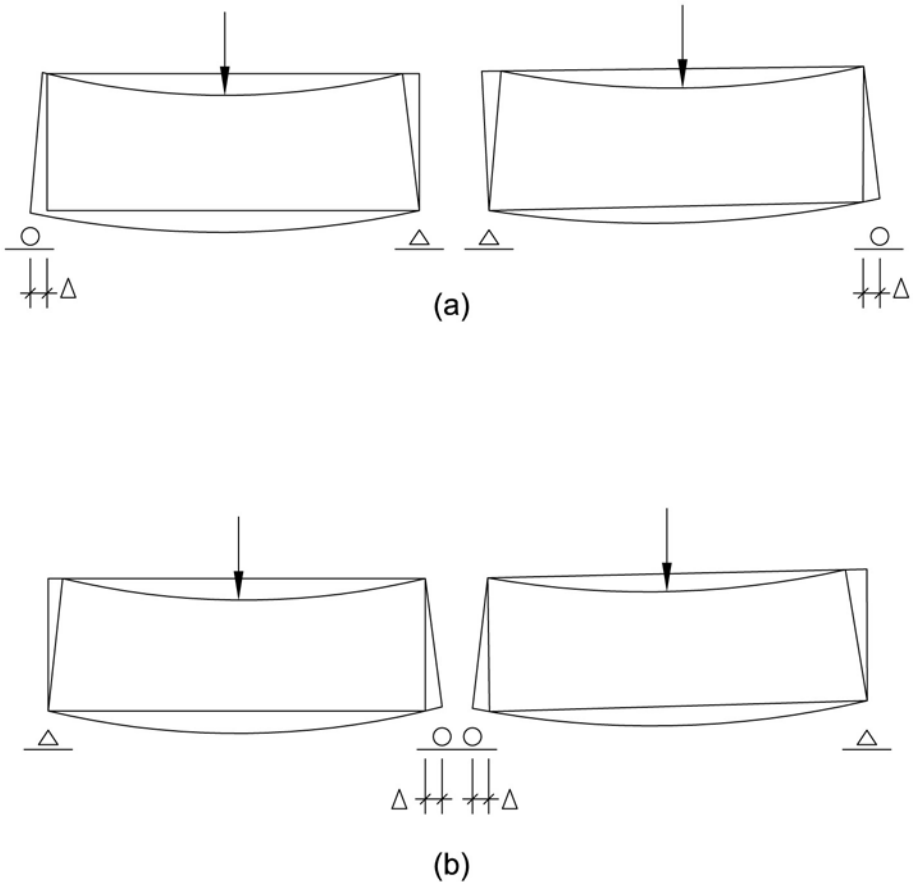

Figure 6-4. Girder movements under different supporting conditions.[76]

7. RECOMMENDATIONS FOR FURTHER RESEARCH

The following are suggested areas for further research to improve the design of jointless bridges and to develop a better understanding of their behavior.

1. Trial Use of Design Recommendations: The design recommendations for newly constructed and retrofitted jointless bridges in chapters 5 and 6 are synthesized from improved knowledge based on testing, analyses, and field observations. However, many of the design recommendations have not had any trial use. A series of design calculations using these recommendations to test the efficacy of the procedures and to provide design examples would be a valuable step in implementing the results of this project.

2. Development of Improved Details to Accommodate End Movements: The primary factors limiting the length of jointless bridges are the capacity of the abutment piles to sustain vertical load under lateral movement and details at the approach slab/pavement interface to accommodate the bridge movements. This interface essentially is the expansion joint in a jointless bridge. Based on field observations, this is the region that required continued maintenance in jointless bridges. Tennessee DOT's experience indicates that movement up to 50 mm (2 inches) can be accommodated.[72] Based on analyses and testing, the lateral deformation capacity of a steel pile is significantly larger than 50 mm (2 inches) if the concept of allowing inelastic (yield) strains in the pile is used. Therefore, the length for which the jointless bridge concept is appropriate is currently limited by the movement that can be accommodated at the ends of the approach slabs.

3. Testing to Evaluate Concrete-Filled Pipe Piles: Analyses of concrete-filled pipe piles indicated that this type of pile should have even more lateral deformation capacity than steel H-piles. Tests on concrete-filled steel tubular columns demonstrate the ductility available for this concept. However, reversing cyclic load tests of concrete-filled pipes, in the configuration used for the support of integral abutments (as were carried out for steel H-piles and PS/C piles), are recommended to evaluate the deformation capacity of concrete-filled pipe piles and to refine the design recommendations.

4. Curved Bridges: Thermal expansion of curved jointless bridges involves transverse (radial) movement at the abutments and piers in combination with expansion and contraction in the tangential direction. Integral abutments partially

restrain the movement. There is uncertainty concerning the magnitude of the movement and the internal forces in the bridge related to the restraint by the abutments and piers. In addition, the relative magnitude of the secondary moment effects, as compared to a straight right bridge, is unknown. Some States restrict the use of the jointless integral abutment concept to tangent bridges. However, as demonstrated by the field survey described in section 3.5, the jointless integral abutment concept has been used successfully for curved bridges. Further analytical studies are recommended to better understand the expected movements and the internal forces in this type of bridge.

5. Development of Improved Continuity Connections for Precast, Prestressed Girders: Testing and analyses of precast, prestressed girders made continuous for live load indicate that positive secondary effects, principally from the combined effects of girder creep and positive temperature gradient, could totally negate the beneficial effects from live load continuity. Therefore, the preferred design option recommended in chapter 5 is to eliminate the use of positive-moment connectivity at the piers and to design the girders as simply supported for dead and live loads. The jointless bridge will, therefore, essentially be a deck-only continuous bridge for service loads, but will be continuous for factored loads. Development of connection details and/or construction sequences to improve live load continuity for precast, prestressed girders would be beneficial for the efficiency of this type of bridge.

   One apparent misconception is that live load continuity for this type of bridge can be improved by increasing the stiffness of the positive-moment connection to keep the cracks in the bottom of the diaphragms tight. This approach, however, will also increase the positive secondary moments such that, based on analyses presented in NCHRP Report 322,[49] there is no net gain in reducing midspan positive-moment stresses in the prestressed girders by adding more positive-moment reinforcement over the piers.

   An approach to increasing live load continuity that may be beneficial to some extent is to age the girders to allow a large portion of the creep to occur prior to casting of the decks and diaphragms. This approach can significantly decrease one of the two major contributing factors to positive-secondary moment and thereby increase live load continuity. This approach, however, increases the

potential for negative-moment deck cracking, which may be detrimental to the durability of the bridge.

Another approach to increase live load continuity that would not increase the potential for deck cracking is to preload the negative-moment reinforcement in the deck so that some dead load continuity is achieved prior to casting of the concrete in the negative-moment region of the deck.[85] Research to develop the details and construction procedures for improving continuity in precast, prestressed bridge girders is recommended.

6. Continuous Deck-Only Bridges: A viable concept for retrofitting bridges to eliminate expansion joints is to have jointless bridges with continuous decks supported on existing simply supported girders. As described in chapter 6, the girders should be designed as simply supported, with the resulting end rotations applied to the unbonded length of deck slab connecting the tops of the girders (link slabs). The cracked-section moment in the link slab (induced by the end rotations of the girders) is used to determine reinforcement stress and to estimate crack width in the top of the link slabs. As discussed in chapter 6, negative secondary effects (deck contracting with respect to the girder) will add to the girder-end rotation from the live load. In addition, with integral abutments, the maximum restraint to the overall bridge contraction and the maximum negative secondary effects can occur simultaneously. Therefore, the recommendations in chapter 6 include superimposing these two thermal conditions on live load (at the service-load level) to estimate the expected crack width. However, no analyses were carried out in this project to assess the relative magnitude of the thermal effects and the live load. Parametric studies may indicate that the superimposed conditions are not necessary or may indicate ranges of parameters where the thermal effects become significant, so that the design recommendations can be refined.

7. Secondary Effects in Skewed Bridges: The analyses for the effects of secondary moments presented in section 4.5 indicate that positive secondary effects (e.g., positive temperature gradient) do not cause a significant stress increase in the continuous composite steel beams and that negative secondary effects do not cause a significant stress increase in the continuous PS/C beams. These conclusions were based on parametric studies indicating that the increase in stresses from the secondary effects was not more than 25 percent of the stresses

from the dead plus live loads. However, in skewed bridges with a skew angle greater than 30°, 1998 AASHTO LRFD specifications allow a reduction in live load moments because of the improved lateral distribution of live load in skewed bridges.[43] Analyses presented in section 4.5.5 demonstrate that the skew angle does not reduce secondary moments. Therefore, stresses caused by secondary effects may become proportionately larger in bridges with skew angles greater than 30° and designed using reduction factors for live load moment. Further analyses to investigate secondary effects in bridges with a skew angle greater than 30° could determine conditions under which explicit analyses for secondary moments may or may not be needed.

8. Transverse Secondary Forces: The three-dimensional analyses presented in section 4.5.3 of this volume demonstrate that there is a transverse redistribution of beam shear caused by restraint of thermal gradient effects by intermediate diaphragms. This type of redistribution occurs with differential strain between the deck and the diaphragm when intermediate diaphragms are used in simply supported or continuous superstructures, with or without integral abutments. The effect is greatest in right bridges with intermediate diaphragms forming continuous transverse beams. Further parametric studies could be carried out to evaluate the significance of this effect.

8. REFERENCES

1. AASHTO, *AASHTO LRFD Bridge Design Specifications*, First Edition, Washington, DC, 1994.

2. Abendroth, R.E.; Greimann, L.F.; and Ebner, P.E., "Abutment Pile Design for Jointless Bridges," *Journal of Structural Engineering*, ASCE Vol. 115, No. 11, 1989, pp. 2914–2929.

3. TRB, *Bridge Deck Joint-Sealing Systems, Evaluation and Performance Specification*, NCHRP Report 204, National Research Council, Washington, DC, 1979.

4. Russell, H.G.; Oesterle, R.G.; Tabatabai, H.; Refai, T.M.; and Glikin, J.P., *Jointless Bridges—Literature Review*, Interim Report to FHWA, January 1993, 57 pp.

5. Emerson, M., *Bridge Temperatures Estimated From the Shade Temperature*, TRRL Laboratory Report 696, TRRL, Crowthorne, Berkshire, Great Britain, 1976, 54 pp.

6. Price, W.J., "Bridge Temperatures, *Proceedings, Symposium Held at TRRL*, Crowthorne, Berkshire, Great Britain, Oct. 5, 1977, TRRL Supplemental Report 442, TRRL, Crowthorne, Berkshire, Great Britain, 1978, 96 pp.

7. Imbsen, R.A., et al., *Thermal Effects in Concrete Bridge Superstructures*, NCHRP Report 276, TRB, Washington, DC, September 1985, 99 pp.

8. Potgieter, I.C., and Gamble, W.L., "Response of Highway Bridges to Nonlinear Temperature Distributions," *Civil Engineering Studies*, Structural Research Series No. 505, Report No. UILU-ENG-85-2007, University of Illinois at Urbana-Champaign, Urbana, IL, April 1983, 291 pp.

9. Potgieter, I.C., and Gamble, W.L., "Nonlinear Temperature Distributions in Bridges at Different Locations in the United States," *PCI Journal*, Precast/Prestressed Concrete Institute, July–August 1989, pp. 80–103.

10. Wah, T., and Kirksey, R.E., *Thermal Characteristics of Highway Bridges*, Unpublished Report to NCHRP, Summary of Progress, Highway Research Board, Washington, DC, 1970, pp. 79–85.

11. Clough, G.W., and Duncan, J.M., "Earth Pressures," *Foundation Engineering Handbook*, Second Edition, Edited by H.Y. Fung, Van Nostrand Reinhold, New York, NY, 1991, pp. 223–235.

12. Wolde-Tinsae, A.M., and Klinger, J.E., *Integral Abutment Bridge Design and Construction*, State Highway Administration Research Report No. AW087-313-046, Maryland DOT, January 1987, 65 pp.

13. Greimann, L.F.; Wolde-Tinsae, A.M.; and Yang, P.S., "Skewed Bridges with Integral Abutments," *Bridges and Culverts*, Transportation Research Record 903, TRB, Washington, DC, 1983, pp. 64–72.

14. Tabatabai, H.; Oesterle, R.G., and Lawson, T.J., *Jointless Bridges, Experimental Research and Field Studies*, Volume I, Final Report to FHWA, August 2005, 972 pp.

15. Oesterle, R.G.; Refai, T.M.; Volz, J.S.; Scanlon, A.; and Weiss, W.J., *Jointless Bridges, Analytical Research and Proposed Design Procedures*, Volume II, Final Report to FHWA, February 2005.

16. AASHTO, *Standard Specifications for Highway Bridges*, 16th Edition, Washington, DC, 1996, 686 pp.

17. Shih-Tower, W., and Reese, L.C., *COM624P: Laterally Loaded Pile Analysis Program for Microcomputer, Version 2.0*, Report No. FHWA-5A-91-048, Office of Technology Applications, FHWA, Washington, DC, 1991.

18. Kamel, M.R.; Benak, J.F.; Tadros, M.K.; and Jamshidi, M., "Prestressed Concrete Piles in Jointless Bridges," *PCI Journal*, March–April 1996, pp. 56–65.

19. Musser, S.C., *CANDE-89 User Manual*, Report No. FHWA-RD-89-169, FHWA, McLean, VA, 1989, 236 pp.

20. Selig, E.T., "Soil Parameters for Design of Buried Pipelines," *Proceedings, Pipeline Infrastructure Conference*, ASCE, 1988, pp. 99–116.

21. Rowe, P.W., and Peaker, K., "Passive Earth Pressure Measurements," *Geotechnique*, Vol. XV, The Institution of Civil Engineers, London, England, 1965, pp. 57–77.

22. Hoppe, E.J., and Gomez, J.P., *Field Study of an Integral Backwall Bridge With Data Set for Route 257 Over I-81 Field Monitoring Results, June 8, 1993, to January 27, 1996*, Report No. VTRC97-R7, Virginia Transportation Research Council, October 1996, 47 pp.

23. Barker, R.M.; Duncan, J.M.; Rojiani, K.B.; Ooi, P.S.K.; Tan, C.K.; and Kim, S.G., *Manual for the Design of Bridge Foundations*, NCHRP Report 343, Transportation Research Board (TRB), Washington, DC, December 1991, 308 pp.

24. Lee, H.W., and Sarsam, M.B., Analysis of Integral Abutment Bridges, Department of Civil Engineering, South Dakota State University, Brookings, SD, March 1973, 231 pp.

25. Schaefer, V.R., and Koch, J.C., *Void Development Under Bridge Approaches*, Report No. SD90-03, South Dakota State University, Brookings, SD, November 1992, 147 pp.

26. Greimann, L.F.; Abendroth, R.E.; Johnson, D.E.; and Ebner, P.B., *Pile Design and Tests for Integral Abutment Bridges*, Final Report to the Highway Division, Iowa DOT Project HR-273, Iowa DOT, 1987, 302 pp.

27. Bowles, T.E., *Foundation Analysis and Design*, McGraw-Hill Book Company, 1982, 816 pp.

28. AASHTO, *Standard Specifications for Highway Bridges*, 14th Edition, Washington, DC, 1989, 420 pp.

29. Shams, M., and Saadeghvaziri, M.A., "State of the Art of Concrete-Filled Steel Tubular Columns," *ACI Structural Journal*, ACI, September–October 1997, pp. 558–571.

30. Tennessee Structures Memorandum 045, "Thermal Expansion and Contraction," July 1989, 6 pp.

31. Zederbaum, J., "Factors Influencing the Longitudinal Movement of Concrete Bridge System With Special Reference to Deck Contraction," *Concrete Bridge Design*, ACI Publication No. SP-23, ACI, Detroit, MI, 1969, pp. 75–95.

32. Witecki, A.A. and Raina, V.K., "Distribution of Longitudinal Horizontal Forces Among Bridge Supports," *Concrete Bridge Design*, ACI Publication SP-23, ACI, Detroit, MI, 1969, pp. 803–815.

33. Suttikan, C., *A Generalized Solution for Time-Dependent Response and Strength of Noncomposite and Composite Prestressed Concrete Beams*, Ph.D. Dissertation, University of Texas at Austin, 1978, 350 pp.

34. ACI Committee 318, *Building Code Requirements for Structural Concrete*, Report No. ACI 318-02, and *Commentary*, Report No. ACI 318R-02, ACI, Detroit, MI, 2002, 443 pp.

35. AASHTO, *AASHTO Guide Specifications for Thermal Effects in Concrete Bridge Superstructures*, Washington, DC, 1989.

36. Girton, D.D., et al., *Validation of Design Recommendations for Integral-Abutment Piles*, Iowa DOT Research Project HR-292, Iowa State University, College of Engineering, September 1989.

37. U.S. Department of Commerce, *Climatic Atlas of the United States*, Ashville, NC, June 1968.

38. National Climatic Data Center, "Daily Normals of Temperature, Precipitation, and Heating and Cooling Degree-Days, 1961–1990," *Climatography of the United States,* No. 84, Ashville, NC.

39. *Climatic Atlas of the United States*, Harvard University Press, Cambridge, MA, 1954.

40. ASHRAE, *Fundamentals Handbook*, American Society of Heating, Refrigerating, and Air-Conditioning Engineers (ASHRAE), New York, NY, 1993.

41. Tennessee DOT Research Project No. 77-27-2, *Thermal Movements of Continuous Concrete and Steel Structures, Final Report*, University of Tennessee, Civil Engineering Department, January 1982.

42. Jorgenson, J.L., *Behavior of Abutment Piles in an Integral Abutment Bridge*, Report No. FHWA-ND-1-75-B, Engineering Experiment Station, North Dakota State University, Fargo, ND, November 1981.

43. AASHTO, *AASHTO LRFD Bridge Design Specifications*, Second Edition, Washington, DC, 1998.

44. ACI Committee 209, *Prediction of Creep, Shrinkage, and Temperature Effects in Concrete Structures*, Report No. ACI 209R-92, ACI, Detroit, MI, 1992, 47 pp.

45. Kosmatka, S.H., and Panarese, W.C., "Chapter 13, Volume Changes in Concrete," *Design and Control of Control Mixtures*, 13th Edition, Portland Cement Association (PCA), Skokie, IL, 1988, pp. 151–162.

46. Bazant, Z.P., and Panula, L., "Creep and Shrinkage Characterization for Analyzing Prestressed Concrete Structures," *PCI Journal*, May/June 1980, pp. 86–121.

47. Emanuel, J.H., and Hulsey, J.L., "Prediction of the Thermal Coefficient of Expansion of Concrete," *Journal of American Concrete Institute*, Vol. 74, No. 4, April 1977, pp. 149–155.

48. FHWA, *Standard Plans for Highway Bridges, Vols. IV, 1975 Edition, and IV(A), 1984 Edition,* Washington, DC.

49. Oesterle, R.G., et al., *Design of Precast Prestressed Bridge Girders Made Continuous*, NCHRP Report 322, Transportation Research Board, Washington, DC, November 1989, 97 pp.

50. Chandra, V., et al., *Draft Report on Precast Prestressed Concrete Integral Bridges, State-of-the-Art*, Precast/Prestressed Concrete Institute, 1995, 113 pp.

51. Burke Jr., M.P., "Semi-Integral Bridges: A Concept Whose Time Has Come?," *Continuous and Integral Bridges*, EAFN Spon, 1994, pp. 213–224.

52. Nicholson, B.A.; Barr, J.M.; Cooke, R.S.; Hickman, R.P.; Jones, C.J.F.P.; and Taylor, H.P.J., *Integral Bridges: Report of a Study Tour to North America*, Concrete Bridge Development Group, U.K., 1997, 93 pp.

53. Emerson, M. *Temperature Differences in Bridges: Basis of Design Requirements*, TRRL Laboratory Report 765, TRRL, Crowthorne, Berkshire, Great Britain, 1977, 39 pp.

54. Hoffman, P.C., et al., "Temperature Study of an Experimental Segmental Concrete Bridge," *PCI Journal*, Precast/Prestressed Concrete Institute, March-April 1983, pp. 79–97.

55. Priestley, M.J.N., "Design of Concrete Bridges for Temperature Gradients," *ACI Journal*, ACI, No. 5, May 1978, pp. 209–217.

56. Thurston, S.J., *Thermal Stresses in Concrete Structures*, Ph.D. Dissertation, Research Report No. 78-21, University of Canterbury, Department of Civil Engineering, New Zealand, November 1978, 351 pp.

57. Krauss, P.D., and Rogalla, E.A., *Transverse Cracking in Newly Constructed Bridge Decks*, NCHRP Report 380, Transportation Research Board, Washington, DC, 1996, 126 pp.

58. Branson, D.E., "Time-Dependent Effects in Composite Concrete Beams, " *ACI Journal*, Vol. 61, No. 2, February 1964, pp. 213–230.

59. AASHTO, *Standard Specifications for Highway Bridges*, 15th Edition, Washington, DC, 1992, 686 pp.

60. Mattock, A.H., "Precast–Prestressed Concrete Bridges 5, Creep and Shrinkage Studies," *Journal of the PCA Research and Development Laboratories*, Vol. 3, No. 2, May 1961, pp. 32–66. Reprinted as PCA Bulletin D46.

61. Bakht, B. "Analysis of Some Skew Bridges as Right Bridges," *Journal of Structural Engineering*, ASCE Vol. 114, No. 10, 1988, pp. 2307–2322.

62. Fouad, F.H., *Inspection of Precast Prestressed Girder Bridges on I-565 in Madison County, Alabama*, Report to Sherman Prestressed Concrete, Pelham, AL, May 1994, 9 pp.

63. Yang, P.S.; Wolde-Tinsae, A.M.; and Greimann, L.F., "Effects of Predrilling and Layered Soils on Piles," *Journal of Geotechnical Engineering*, ASCE, Vol. 111, No. 1, January 1985, pp. 18–31.

64. Wasserman, E.P., and Walker J.H., "Integral Abutments for Steel Bridges," *Highway Structures Design Handbook*, VII, Chapter 5, American Iron and Steel Institute, 1996, 40 pp.

65. Burdette, E.G.; Jones, W.D.; and Fricke, K.E., "Concrete Bearing Capacity Around Large Inserts," *Journal of Structural Engineering*, ASCE Vol. 109, No. 6, 1983, pp 1375–1386.

66. Oesterle, R.G., "The Role of Concrete Cover in Crack Control Criteria and Corrosion Protection," PCA R&D Serial No. 2054, PCA, Skokie, IL, 1997, 34 pp.

67. Moulton, L.K.; Gangarao, H.V.S.; and Halvorsen, G.T., *Tolerable Movement Criteria for Highway Bridges*, Report No. FHWA/RD-85/107, Washington, DC, 1985, 109 pp.

68. Hearn, G., *Faulted Pavements at Bridge Abutments*, Colorado Transportation Institute Synthesis, University of Colorado at Boulder, October 1995, 181 pp.

69. Burke Jr., M. P., and Gloyd, S., "Semi-Integral Bridges: A Revelation," Submitted for Presentation at 75th TRB Annual Meeting, Washington, DC, 1996.

70. Gangarao, H.V.S., and Thippeswamy, H.K., *Study of Jointless Bridge Behavior and Development of Design Procedures*, RP-89 submitted to West Virginia DOT, Charleston, WV, 1994.

71. Briaud, J.L.; James, R.W.; and Hoffman, S.B., *Settlement of Bridge Approaches*, NCHRP Synthesis of Highway Practice 234, TRB, Washington, DC, 1997, 75 pp.

72. Wasserman, E., "Jointless Bridge Decks," *Engineering Journal*, American Institute of Steel Construction, Vol. 24, No. 3, 1987, pp. 93–100.

73. Technical Advisory T5140.16, "Bridge Deck Joint Rehabilitation (Retrofit)," Dissertation, FHWA, 1980, 6 pp.

74. *Bridge Inspection and Rehabilitation, A Practical Guide*, Edited by L.G. Silano, Parsons Brinckerhoff, John Wiley and Sons, Inc., New York, NY, 1993, pp. 230–234.

75. Scanlon, A., and Prestash, T.A., *Bridge Superstructure Research, Task 1: Data Gathering for Continuous Structure Designs, Summary Report*, Research Project 90-11, PennDOT, 1991, 9 pp.

76. Gastal, F., and Zia, P., "Analysis of Bridge Beams With Jointless Decks," *Proceedings of IASBE Symposium*, Lisbon, Portugal, September 1989, pp. 555–560.

77. Caner, A., and Zia, P., "Behavior and Design of Link Slabs for Jointless Bridge Decks," *PCI Journal*, May–June 1998, pp. 68–80.

78. Scanlon, A.; Patel, I.C.; and Angelo, S., *Bridge Superstructure Research, Task 3: Final Designs and Details for Simple-Span Bridges Made Continuous, Final Report*, Research Project 90-11, PennDOT, 1994, 230 pp.

79. Poulos, H.G., and Davis, E.H., *Pile Foundation Design and Analysis*, John Wiley and Sons, 1980, 397 pp.

80. Hrennikoff, A., "Analysis of Pile Foundations with Batter Piles," ASCE, CXV, 1950.

81. Saul, W.E., "Static and Dynamic Analysis of Pile Foundations," *ASCE Journal*, Structural Division, ASCE Vol. 94, No. ST5, May 1968, pp. 1077–1100.

82. O'Neill, M.W.; Ghazzaly, O.I.; and Ha, H.B., *Analysis of Three-Dimensional Pile Groups With Non-Linear Soil Response and Pile-Soil-Pile Interaction*, Ninth Annual Offshore Technology Conference, Houston, TX, May 1977, pp. 245–256.

83. O'Neill, M.W., and Tsai, C.N., *An Investigation of Soil Nonlinearity and Pile-Soil-Pile Interaction in Pile Group Analysis*, Research Report No. UHUC 84-9, Department of Civil Engineering, University of Houston, Houston, TX, November 1984, prepared for U.S. Army Corp of Engineers Waterways Experiment Station, Vicksburg, MS.

84. Burke Jr., M.P., "Integral Bridges," Transportation Research Record No. 1275, *Bridges and Structures*, TRB, Washington, DC, 1990, pp. 53–61.

85. Saleh, M.A.; Einea, A.; and Tadros, M.K., "Creating Continuity in Precast Girder Bridges," *Concrete International*, ACI, Detroit, MI, August 1995, pp. 27–32.

8.1 OTHER REFERENCES OF INTEREST

Burke Jr., M.P., "The Design of Integral Bridges," *Concrete International*, Vol. 15, No. 6, June 1993, pp. 37–42.

Burke Jr., M.P., "Integral Bridges: Attributes and Limitations," Paper No. 930104, Presented at the 72nd TRB Annual Meeting, Washington, DC, January 1993.

Burke Jr., M.P., "The Longitudinal, Lateral and Rotational Movement of Semi-Integral Bridges," Submitted for Presentation at TRB 73rd Annual Meeting, Washington, DC, 1994.

Dunker, K.F., and Rabbat, B.G., "Highway Bridge Type and Patterns," *Journal of Performance of Constructed Facilities*, ASCE, Vol. 4, No. 3, August 1990, pp. 161–173.

Dunker, K.F., and Rabbat, B.G., "Performance of Highway Bridges," *Concrete International,* Vol. 12, No. 8, August 1990, pp. 40–43.

Emerson, M., *Extreme Values of Bridge Temperatures for Design Purposes*, TRRL Laboratory Report 744, TRRL, Crowthorne, Berkshire, Great Britain, 1976, 51 pp.

Greimann, L.F., et al., "Nonlinear Analysis of Integral Abutment Bridges," *Journal of Structural Engineering*, ASCE, Vol. 112, No. 10, October 1986, pp. 2263–2280.

Greimann, L.F., and Wolde-Tinsae, A.M., "Design Model for Piles in Jointless Bridges," *Journal of Structural Engineering*, ASCE, Vol. 114, No. 6, June 1988, pp. 1354–1371.

Technical Report No. 65, *Expansion Joints in Buildings*, Standing Committee on Structural Engineering of the Federal Construction Council Building Research Advisory Board, Division of Engineering, National Research Council, National Academy of Sciences, Washington, DC, 1974.

APPENDIX A. TABLE OF CLIMATIC CONDITIONS FOR THE UNITED STATES

Temperature ranges presented in table A-1 are based on data from the ASHRAE *Fundamentals Handbook*, "Chapter 24: Weather Data," American Society of Heating, Refrigerating, and Air-Conditioning Engineers, 1993. For each station, the latitude, longitude, elevation, and minimum and maximum shade air temperatures are provided. The mean construction-season shade air temperature is also provided. The mean construction- temperature data are based on Technical Report No. 65, *Expansion Joints in Buildings*, National Academy of Sciences, 1979. The mean construction-season shade air temperature is defined as the mean shade air temperature during the normal construction season for the locality listed. The normal construction season is defined as the continuous period in a year during which the minimum daily temperature equals or exceeds 0 °C (32 °F). These contiguous periods for each locality were obtained from the *Decennial Census of United States Climate: Daily Normals of Temperature and Heating Degree Days*, and the mean construction-season shade air temperatures were calculated from the mean monthly temperatures extracted from local *Climatological Data Summaries* from the National Weather Service (NWS).

When airport temperature observations were used to develop design data, the designation "AP" follows the station name ("AFB" is used to denote that the observation was taken at an Air Force base). Data for stations followed by "CO" come from office locations within an urban area and generally reflect the influence of the surrounding area. Stations without designations can be considered semirural. For interpolating between stations, the shade air temperatures should be adjusted at a rate of 1 °C/100 m (1 °F/200 ft) of elevation change. For a lower elevation, increase the temperature values given in table A-1; for a higher elevation, decrease the temperature values given in table A-1. It is important to note that local meteorological data may be more applicable in sheltered, low-lying areas where frost pockets may develop.

Table A-1. Climatic conditions for the United States.

State and Station	Location Latitude °	′N	Longitude °	′W	Elev. m	Shade Temperature Min. °C	Max. °C	Mean* Constr. °C
Alabama								
Alexander City	32	57	85	57	201	-8	36	–
Anniston AP	33	35	85	51	183	-8	36	–
Auburn	32	36	85	30	199	-8	36	–
Birmingham AP	33	34	86	45	189	-8	36	17
Decatur	34	37	86	59	177	-12	35	–
Dothan AP	31	19	85	27	114	-5	34	–
Florence AP	34	48	87	40	177	-8	36	–
Gadsden	34	1	86	0	169	-9	36	–
Huntsville AP	34	42	86	35	185	-12	35	16
Mobile AP	30	41	88	15	64	-4	35	–
Mobile CO	30	40	88	15	64	-4	35	20
Montgomery AP	32	23	86	22	52	-6	36	19
Selma, Craig AFB	32	20	87	59	51	-6	36	–
Talladega	33	27	86	6	172	-8	36	–
Tuscaloosa AP	33	13	87	37	52	-7	37	–
Alaska								
Anchorage AP	61	10	150	1	35	-31	22	11
Barrow	71	18	156	47	9	-43	14	3
Fairbanks AP	64	49	147	52	133	-46	28	10
Juneau AP	58	22	134	35	4	-20	23	9
Kodiak	57	45	152	29	22	-12	21	–
Nome AP	64	30	165	26	4	-35	19	7
Arizona								
Douglas AP	31	27	109	36	1249	-3	37	–
Flagstaff	35	8	111	40	2135	-19	29	14
Fort Huachuca AP	31	35	110	20	1422	-4	35	–
Kingman AP	35	12	114	1	1079	-8	39	–
Nogales	31	21	110	55	1158	-2	37	–
Phoenix AP	33	26	112	1	339	-1	43	21
Prescott AP	34	39	112	26	1527	-16	36	18
Tucson AP	32	7	110	56	780	-2	40	19
Winslow AP	35	1	110	44	1492	-15	36	19
Yuma AP	32	39	114	37	65	2	44	22
Arkansas								
Blytheville AFB	35	57	89	57	80	-12	36	–
Camden	33	36	92	49	35	-8	37	–
El Dorado AP	33	13	92	49	84	-8	37	–
Fayetteville AP	36	0	94	10	381	-14	36	–
Fort Smith AP	35	20	94	22	141	-11	38	18

*Mean construction season shade air temperature.

Table A-1. Climatic conditions for the United States (continued).

State and Station	Location Latitude °	′N	Longitude °	′W	Elev. m	Shade Temperature Min. °C	Max. °C	Mean* Constr. °C
Hot Springs	34	29	93	6	163	-8	38	–
Jonesboro	35	50	90	42	105	-12	36	–
Little Rock AP	34	44	92	14	78	-9	37	18
Pine Bluff AP	34	18	92	5	73	-9	38	–
Texarkana AP	33	27	93	59	119	-8	37	18
California								
Bakersfield AP	35	25	119	3	145	-1	40	18
Barstow AP	34	51	116	47	587	-3	41	–
Blythe AP	33	37	114	43	120	-1	44	–
Burbank AP	34	12	118	21	236	3	35	18
Chico	39	48	121	51	73	-2	39	–
Concord	37	58	121	59	61	-4	38	–
Covina	34	5	117	52	175	0	37	–
Crescent City AP	41	46	124	12	12	-1	20	–
Downey	33	56	118	8	35	3	34	–
El Cajon	32	49	116	58	112	6	28	–
El Centro AP	32	49	115	40	-13	2	44	–
Escondido	33	7	117	5	201	4	32	–
Eureka, Arcata AP	40	59	124	6	66	-1	20	11
Fairfield, Travis AFB	38	16	121	56	19	-2	37	–
Fresno AP	36	46	119	43	100	-2	39	17
Hamilton AFB	38	4	122	30	1	-1	32	–
Laguna Beach	33	33	117	47	11	5	28	–
Livermore	37	42	121	57	166	-4	38	–
Lompoc, Vandenberg AFB	34	43	120	34	112	2	24	–
Long Beach AP	33	49	118	9	9	5	28	17
Los Angeles AP	33	56	118	24	30	5	28	17
Los Angeles CO	34	3	118	14	82	3	34	17
Merced, Castle AFB	37	23	120	34	57	-2	39	–
Modesto	37	39	121	0	28	-2	38	–
Monterey	36	36	121	54	12	2	24	–
Napa	38	13	122	17	17	-1	38	–
Needles AP	34	46	114	37	278	-1	44	–
Oakland AP	37	49	122	19	2	1	29	14
Oceanside	33	14	117	25	8	5	28	–
Ontario	34	3	117	36	290	-1	39	–
Oxnard	34	12	119	11	15	1	28	–
Palm Springs	33	49	116	32	125	1	44	–
Palmdale AP	34	38	118	6	775	-8	39	–
Pasadena	34	9	118	9	263	0	37	–
Petaluma	38	14	122	38	5	-3	34	–
Pomona CO	34	3	117	45	285	-2	39	–
Redding AP	40	31	122	18	151	-2	41	–

Table A-1. Climatic conditions for the United States (continued).

State and Station	Location Latitude °	′N	Longitude °	′W	Elev. m	Shade Temperature Min. °C	Max. °C	Mean* Constr. °C
Redlands	34	3	117	11	402	-1	39	–
Richmond	37	56	122	21	17	1	29	–
Riverside, March AFB	33	54	117	15	467	-2	38	–
Sacremento AP	38	31	121	30	5	-1	38	–
Salinas AP	36	40	121	36	23	-1	23	–
San Bernardino, Norton	34	8	117	16	343	-1	39	–
San Diego AP	32	44	117	10	4	6	28	17
San Fernando	34	17	118	28	294	3	35	–
San Francisco AP	37	37	122	23	2	2	28	13
San Francisco CO	37	46	122	26	22	3	23	13
San Jose AP	37	22	121	56	17	1	29	–
San Luis Obispo	35	20	120	43	76	1	33	–
Santa Ana AP	33	45	117	52	35	3	32	–
Santa Barbara AP	34	26	119	50	3	1	27	–
Santa Cruz	36	59	122	1	38	2	24	–
Santa Maria AP	34	54	120	27	72	-1	27	14
Santa Monica CO	34	1	118	29	20	5	28	–
Santa Paula	34	21	119	5	80	1	32	–
Santa Rosa	38	31	122	49	38	-3	37	–
Stockton AP	37	54	121	15	7	-2	38	–
Ukiah	39	9	123	12	190	-3	37	–
Visalia	36	20	119	18	99	-2	39	–
Yreka	41	43	122	38	800	-11	35	–
Yuba City	39	8	121	36	24	-2	40	–
Colorado								
Alamosa AP	37	27	105	52	2297	-29	29	16
Boulder	40	0	105	16	1660	-17	34	–
Colorado Springs AP	38	49	104	43	1873	-19	33	16
Denver AP	39	45	104	52	1610	-21	34	17
Durango	37	17	107	53	1996	-18	32	–
Fort Collins	40	35	105	5	1524	-23	34	–
Grand Junction AP	39	7	108	32	1476	-17	36	18
Greeley	40	26	104	38	1417	-24	36	–
Lajunta AP	38	3	103	30	1268	-19	38	–
Leadville	39	15	106	18	3095	-22	29	–
Pueblo AP	38	18	104	29	1415	-22	36	18
Sterling	40	37	103	12	1201	-22	35	–
Trinidad AP	37	15	104	20	1749	-19	34	–
Connecticut								
Bridgeport AP	41	11	73	11	8	-14	30	16
Hartford, Brainard Field	41	44	72	39	6	-16	33	16
New Haven AP	41	19	73	55	2	-16	31	15

Table A-1. Climatic conditions for the United States (continued).

State and Station	Location Latitude °	′N	Longitude °	′W	Elev. m	Shade Temperature Min. °C	Max. °C	Mean* Constr. °C
New London	41	21	72	6	18	-15	31	–
Norwalk	41	7	73	25	11	-14	30	–
Norwich	41	32	72	4	6	-16	32	–
Waterbury	41	35	73	4	257	-20	31	–
Windsor Locks, Bradley	41	56	72	41	52	-18	33	–
Delaware								
Dover AFB	39	8	75	28	9	-12	33	–
Wilmington AP	39	40	75	36	23	-12	33	17
District of Columbia								
Andrews AFB	38	5	76	5	85	-12	33	–
Washington, National AP	38	51	77	2	4	-10	34	17
Florida								
Belle Glade	26	39	80	39	5	5	33	–
Cape Kennedy AP	28	29	80	34	5	2	32	–
Daytona Beach AP	29	11	81	3	9	0	33	21
E. Fort Lauderdale	26	4	80	9	3	6	33	–
Fort Myers AP	26	35	81	52	5	5	34	23
Fort Pierce	27	28	80	21	8	3	33	–
Gainesville AP	29	41	82	16	46	-2	35	–
Jacksonville AP	30	30	81	42	8	-2	36	20
Key West AP	24	33	81	45	1	13	32	25
Lakeland CO	28	2	81	57	65	4	34	22
Miami AP	25	48	80	16	2	7	33	24
Miami Beach CO	25	47	80	17	3	7	32	24
Ocala	29	11	82	8	27	-1	35	–
Orlando AP	28	33	81	23	30	2	34	22
Panama City, Tyndall AFB	30	4	85	35	5	-2	33	–
Pensacola CO	30	25	87	13	17	-4	34	20
St. Augustine	29	58	81	20	3	-1	33	–
St. Petersburg	27	46	82	80	11	2	33	–
Sanford	28	46	81	17	27	2	34	–
Sarasota	27	23	82	33	8	4	34	–
Tallahassee AP	30	23	84	22	17	-3	34	20
Tampa AP	27	58	82	32	6	2	33	22
West Palm Beach AP	26	41	80	6	5	5	33	24
Georgia								
Albany Turner AFB	31	36	84	5	68	-4	36	–
Americus	32	3	84	14	139	-6	36	–
Athens	33	57	83	19	244	-8	34	16
Atlanta AP	33	39	84	26	308	-8	34	17

Table A-1. Climatic conditions for the United States (continued).

State and Station	Location Latitude °	′N	Longitude °	′W	Elev. m	Shade Temperature Min. °C	Max. °C	Mean* Constr. °C
Augusta AP	33	22	81	58	44	-7	36	18
Brunswick	31	15	81	29	8	-2	33	–
Columbus, Lawson AFB	32	31	84	56	74	-6	35	18
Dalton	34	34	84	57	219	-8	34	–
Dublin	32	20	82	54	66	-6	36	–
Gainesville	34	11	83	41	15	-4	36	–
Griffin	33	13	84	16	299	-8	34	–
LaGrange	33	1	85	4	216	-7	34	–
Macon AP	32	42	83	39	108	-6	36	18
Marietta, Dobins AFB	33	55	84	31	326	-8	34	–
Savannah	32	8	81	12	15	-4	36	19
Valdosta-Moody AFB	30	58	83	12	71	-2	36	–
Waycross	31	15	82	24	45	-3	36	–
Hawaii								
Hilo AP	19	43	155	5	11	16	29	23
Honolulu AP	21	20	157	55	4	17	31	24
Kaneohe Bay MCAS	21	27	157	46	5	18	29	–
Wahiawa	21	3	158	2	274	14	30	–
Idaho								
Boise AP	43	34	116	13	865	-16	36	16
Burley	42	32	113	46	1267	-19	37	–
Coeur d'Alene AP	47	46	116	49	906	-22	32	–
Idaho Falls AP	43	31	112	4	1445	-24	32	16
Lewiston AP	46	23	117	1	431	-18	36	16
Moscow	46	44	116	58	811	-22	32	–
Mountain Home AFB	43	2	115	54	913	-14	37	–
Pocatello AP	42	55	112	36	1358	-22	34	16
Twin Falls AP	42	29	114	29	1265	-19	37	–
Illinois								
Aurora	41	45	88	20	227	-21	34	–
Belleville, Scott AFB	38	33	89	51	138	-17	34	–
Bloomington	40	29	88	57	267	-21	33	–
Carbondale	37	47	89	15	127	-17	35	–
Champaign/Urbana	40	2	88	17	237	-19	35	–
Chicago, Midway AP	41	47	87	45	185	-21	34	16
Chicago, O'Hare AP	41	59	87	54	201	-22	33	16
Chicago CO	41	53	87	38	180	-19	34	16
Danville	40	12	87	36	212	-20	34	–
Decatur	39	50	88	52	207	-19	34	–
Dixon	41	50	89	29	212	-22	34	–
Elgin	42	2	88	16	231	-22	33	–

Table A-1. Climatic conditions for the United States (continued).

State and Station	Location Latitude °	′N	Longitude °	′W	Elev. m	Shade Temperature Min. °C	Max. °C	Mean* Constr. °C
Freeport	42	18	89	37	238	-23	33	–
Galesburg	40	56	90	26	233	-22	34	–
Greenville	38	53	89	24	172	-18	34	–
Joliet	41	31	88	10	177	-21	34	–
Kankakee	41	5	87	55	190	-20	34	–
La Salle/Peru	41	19	89	6	158	-22	34	–
Macomb	40	28	90	40	214	-21	35	–
Moline AP	41	27	90	31	177	-23	34	17
Mt. Vernon	38	19	88	52	146	-18	35	–
Peoria AP	40	40	89	41	199	-22	33	16
Quincy AP	39	57	91	12	234	-19	36	–
Rantoul, Chanute AFB	40	18	88	8	230	-20	34	–
Rockford	42	21	89	3	226	-23	33	17
Springfield AP	39	50	89	40	179	-19	34	17
Waukegan	42	21	87	53	213	-21	33	–
Indiana								
Anderson	40	6	85	37	280	-18	35	–
Bedford	38	51	86	30	204	-18	35	–
Bloomington	39	8	86	37	258	-18	35	–
Columbus, Bakalar AFB	39	16	85	54	198	-16	35	–
Crawfordsville	40	3	86	54	207	-19	34	–
Evansville AP	38	3	87	32	116	-16	35	18
Fort Wayne AP	41	0	85	12	241	-20	33	17
Goshen AP	41	32	85	48	252	-19	33	–
Hobart	41	32	87	15	183	-20	33	–
Huntington	40	53	85	30	244	-20	33	–
Indianapolis AP	39	44	86	17	241	-19	33	17
Jeffersonville	38	17	85	45	139	-15	35	–
Kokomo	40	25	86	3	261	-20	33	–
La Porte	41	36	86	43	247	-19	34	–
Lafayette	40	2	86	5	183	-19	34	–
Marion	40	29	85	41	262	-20	33	–
Muncie	40	11	85	21	292	-19	33	–
Peru, Grissom AFB	40	39	86	9	248	-21	32	–
Richmond AP	39	46	84	50	348	-19	33	–
Shelbyville	39	31	85	47	229	-18	34	–
South Bend AP	41	42	86	19	236	-19	33	16
Terre Haute AP	39	27	87	18	178	-19	35	–
Valparaiso	41	31	87	2	244	-19	34	–
Vincennes	38	41	87	32	128	-17	35	–
Iowa								

Table A-1. Climatic conditions for the United States (continued).

State and Station	Location Latitude °	′N	Longitude °	′W	Elev. m	Shade Temperature Min. °C	Max. °C	Mean* Constr. °C
Ames	42	2	93	48	335	-24	34	–
Burlington AP	40	47	91	7	211	-22	34	18
Cedar Rapids AP	41	53	91	42	263	-23	33	–
Clinton	41	50	90	13	181	-22	33	–
Council Bluffs	41	20	95	49	369	-22	34	–
Des Moines AP	41	32	93	39	286	-23	34	18
Dubuque	42	24	90	42	322	-24	32	17
Fort Dodge	42	33	94	11	354	-24	33	–
Iowa City	41	38	91	33	201	-24	33	–
Keokuk	40	24	91	24	175	-21	35	–
Marshalltown	42	4	92	56	274	-24	33	–
Mason City AP	43	9	93	20	370	-26	32	–
Newton	41	41	93	2	285	-23	34	–
Ottumwa AP	41	6	92	27	256	-22	34	–
Sioux City AP	42	24	96	23	334	-24	35	18
Waterloo	42	33	92	24	265	-26	33	17
Kansas								
Atchison	39	34	95	7	288	-19	36	–
Chanute AP	37	40	95	29	299	-16	38	–
Dodge City AP	37	46	99	58	787	-18	38	18
El Dorado	37	49	96	50	391	-16	38	–
Emporia	38	20	96	12	369	-17	38	–
Garden City AP	37	56	100	44	878	-18	37	–
Goodland AP	39	22	101	42	1114	-21	37	18
Great Bend	38	21	98	52	576	-18	38	–
Hutchinson AP	38	4	97	52	470	-16	39	–
Liberal	37	3	100	58	875	-17	37	–
Manhattan, Ft. Riley	39	3	96	46	325	-18	37	–
Parsons	37	20	95	31	274	-15	38	–
Russell AP	38	52	98	49	569	-18	38	–
Salina	38	48	97	39	388	-18	39	–
Topeka AP	39	4	95	38	267	-18	37	21
Wichita AP	37	39	97	25	403	-16	38	20
Kentucky								
Ashland	38	33	82	44	166	-15	34	–
Bowling Green AP	35	58	86	28	163	-16	34	–
Corbin AP	36	57	84	6	358	-16	34	–
Covington AP	39	3	84	40	265	-17	33	17
Hopkinsville, Ft. Campbell	36	40	87	29	174	-16	34	–
Lexington AP	38	2	84	36	294	-16	34	17
Louisville AP	38	11	85	44	145	-15	35	18

Table A-1. Climatic conditions for the United States (continued).

State and Station	Location Latitude °	′N	Longitude °	′W	Elev. m	Shade Temperature Min. °C	Max. °C	Mean* Constr. °C
Madisonville	37	19	87	29	134	-15	36	–
Owensboro	37	45	87	10	124	-15	36	–
Paducah AP	37	4	88	46	126	-14	37	–
Louisiana								
Alexandria AP	31	24	92	18	28	-5	35	–
Baton Rouge AP	30	32	91	9	20	-4	35	20
Bogalusa	30	47	89	52	31	-4	35	–
Houma	29	31	90	40	4	-1	35	–
Lafayette AP	30	12	92	0	13	-3	35	–
Lake Charles AP	30	7	93	13	3	-3	35	20
Minden	32	36	93	18	76	-7	37	–
Monroe AP	32	31	92	2	24	-7	37	–
Natchitoches	31	46	93	5	40	-6	36	–
New Orleans AP	29	59	90	15	1	-2	34	21
Shreveport AP	32	28	93	49	77	-7	37	19
Maine								
Augusta AP	44	19	69	48	108	-22	31	–
Bangor, Dow AFB	44	48	68	50	59	-24	30	–
Caribou AP	46	52	68	1	190	-28	29	13
Lewiston	44	2	70	15	61	-22	31	–
Millinocket AP	45	39	68	42	126	-25	31	–
Portland	43	39	70	19	13	-21	31	14
Waterville	44	32	69	40	92	-22	31	–
Maryland								
Baltimore AP	39	11	76	40	45	-12	34	17
Baltimore CO	39	20	76	25	6	-10	33	17
Cumberland	39	37	78	46	241	-14	33	–
Frederick AP	39	27	77	25	95	-13	34	17
Hagerstown	39	42	77	44	215	-13	34	–
Salisbury	38	20	75	30	18	-11	34	–
Massachusetts								
Boston AP	42	22	71	2	5	-14	33	14
Clinton	42	24	71	41	121	-19	32	–
Fall River	41	43	71	8	58	-15	31	–
Framingham	42	17	71	25	52	-16	32	–
Gloucester	42	35	70	41	3	-17	32	–
Greenfield	42	3	72	4	62	-22	31	–
Lawrence	42	42	71	10	17	-21	32	–
Lowell	42	39	71	19	27	-20	33	–

Table A-1. Climatic conditions for the United States (continued).

State and Station	Location Latitude °	′N	Longitude °	′W	Elev. m	Shade Temperature Min. °C	Max. °C	Mean* Constr. °C
New Bedford	41	41	70	58	24	-15	29	–
Pittsfield AP	42	26	73	18	364	-22	31	14
Springfield, Westover AFB	42	12	72	32	75	-21	32	–
Taunton	41	54	71	4	6	-15	32	–
Worcester AP	42	16	71	52	301	-18	31	14
Michigan								
Adrian	41	55	84	1	230	-18	33	–
Alpena AP	45	4	83	26	186	-24	32	14
Battle Creek AP	42	19	85	15	287	-17	33	–
Benton Harbor AP	42	8	86	26	196	-17	33	–
Detroit	42	25	83	1	189	-16	33	14
Escanaba	45	44	87	5	185	-24	31	13
Flint AP	42	58	83	44	235	-20	32	16
Grand Rapids AP	42	53	85	31	239	-17	33	17
Holland	42	42	86	6	207	-17	31	–
Jackson AP	42	16	84	28	311	-17	33	–
Kalamazoo	42	17	85	36	291	-17	33	–
Lansing AP	42	47	84	36	266	-19	32	15
Marquette CO	46	34	87	24	224	-24	29	13
Mt. Pleasant	43	35	84	46	243	-18	33	–
Muskegon AP	43	10	86	14	190	-17	30	15
Pontiac	42	40	83	25	299	-18	32	–
Port Huron	42	59	82	25	179	-18	32	–
Saginaw AP	43	32	84	5	203	-18	33	–
Sault Ste. Marie AP	46	28	84	22	220	-24	29	13
Traverse City AP	44	45	85	35	190	-19	32	–
Ypsilanti	42	14	83	32	218	-17	33	–
Minnesota								
Albert Lea	43	39	93	21	372	-27	32	–
Alexandria AP	45	52	95	23	436	-30	33	–
Bemidji AP	47	31	94	56	423	-35	31	–
Brainerd	46	24	94	8	374	-29	32	–
Duluth AP	46	50	92	11	435	-29	29	13
Fairbault	44	18	93	16	286	-8	33	–
Fergus Falls	46	16	96	4	369	-29	33	–
International Falls AP	48	34	93	23	359	-34	29	14
Mankato	44	9	93	59	306	-27	33	–
Minneapolis/St. Paul AP	44	53	93	13	254	-27	33	17
Rochester AP	43	55	92	30	395	-27	32	16
St. Cloud AP	45	35	94	11	318	-26	33	16
Virginia	47	30	92	33	437	-32	29	–
Willmar	45	7	95	5	344	-26	33	–

Table A-1. Climatic conditions for the United States (continued).

State and Station	Location Latitude °	′N	Longitude °	′W	Elev. m	Shade Temperature Min. °C	Max. °C	Mean* Constr. °C
Winona	44	3	91	38	199	-26	33	–
Mississippi								
Biloxi, Keesler AFB	30	25	88	55	8	-2	34	–
Clarksdale	34	12	90	34	54	-10	36	–
Columbus AFB	33	39	88	27	67	-9	35	–
Greenville AFB	33	29	90	59	42	-9	35	–
Greenwood	33	30	90	5	45	-9	35	–
Hattiesburg	31	16	89	15	45	-4	36	–
Jackson AP	32	19	90	5	94	-6	36	19
Laurel	31	40	89	10	72	-4	36	–
McComb AP	31	15	90	28	143	-6	36	–
Meridian AP	32	20	88	45	88	-7	36	18
Natchez	31	33	91	23	59	-5	36	–
Tupelo	34	16	88	46	110	-10	36	–
Vicksburg CO	32	24	90	47	80	-6	36	19
Missouri								
Cape Girardeau	37	14	89	35	107	-13	37	–
Columbia AP	38	58	92	22	237	-18	36	18
Farmington AP	37	46	90	24	283	-16	36	–
Hannibal	39	42	91	21	149	-19	36	–
Jefferson City	38	34	92	11	195	-17	37	–
Joplin AP	37	9	94	30	299	-14	38	–
Kansas City AP	39	7	94	35	241	-17	37	18
Kirksville AP	40	6	92	33	294	-21	36	–
Mexico	39	11	91	54	236	-18	36	–
Moberly	39	24	92	26	259	-19	36	–
Poplar Bluff	36	46	90	25	116	-12	37	–
Rolla	37	59	91	43	367	-16	34	–
St. Joseph AP	39	46	94	55	251	-19	36	19
St. Louis AP	38	45	90	23	163	-17	36	18
St. Louis CO	38	39	90	38	141	-16	37	18
Sedalia, Whiteman AFB	38	43	93	33	265	-18	35	–
Sikeston	36	53	89	36	99	-13	37	–
Springfield AP	37	14	93	23	386	-16	36	18
Montana								
Billings AP	45	48	108	32	1087	-26	34	16
Bozeman	45	47	111	9	1356	-29	32	–
Butte AP	45	57	112	30	1692	-31	30	–
Cut Bank AP	48	37	112	22	1170	-32	31	–
Glasgow AP	48	25	106	32	841	-30	33	16
Glendive	47	8	104	48	755	-28	35	–

Table A-1. Climatic conditions for the United States (continued).

State and Station	Location Latitude °	′N	Longitude °	′W	Elev. m	Shade Temperature Min. °C	Max. °C	Mean* Constr. °C
Great Falls AP	47	29	111	22	1116	-29	33	14
Havre	48	34	109	40	760	-28	34	14
Helena AP	46	36	112	0	1167	-29	33	14
Kalispell AP	48	18	114	16	906	-26	33	13
Lewistown AP	47	4	109	27	1256	-30	32	–
Livingstown AP	45	42	110	26	1407	-29	32	–
Miles City AP	46	26	105	52	803	-29	37	17
Missoula AP	46	55	114	5	972	-25	33	14
Nebraska								
Beatrice	40	16	96	45	376	-21	37	–
Chadron AP	42	50	103	5	1010	-22	36	–
Columbus	41	28	97	20	442	-21	37	–
Fremont	41	26	96	29	366	-21	37	–
Grand Island AP	40	59	98	19	567	-22	36	18
Hastings	40	36	98	26	596	-22	36	–
Kearney	40	44	99	1	650	-23	36	–
Lincoln CO	40	51	96	45	360	-21	37	18
McCook	40	12	100	38	844	-21	37	–
Norfolk	41	59	97	26	473	-22	36	18
North Platte AP	41	8	100	41	847	-22	36	18
Omaha AP	41	18	95	54	298	-22	34	18
Scottsbluff AP	41	52	103	36	1206	-22	35	17
Sidney AP	41	13	103	6	1341	-22	35	–
Nevada								
Carson City	39	10	119	46	1425	-16	34	–
Elko AP	40	50	115	47	1539	-22	34	16
Ely AP	39	17	114	51	1906	-23	32	15
Las Vegas AP	36	5	115	10	664	-4	42	19
Lovelock AP	40	4	118	33	1190	-13	37	–
Reno AP	39	30	119	47	1342	-15	35	17
Reno CO	39	30	119	47	1343	-14	36	–
Tonopah AP	38	4	117	5	1654	-15	34	–
Winnemucca AP	40	54	117	48	1311	-18	36	17
New Hampshire								
Berlin	44	3	71	1	338	-26	31	–
Claremont	43	2	72	2	128	-23	32	–
Concord AP	43	12	71	30	104	-22	32	16
Keene	42	55	72	17	149	-24	32	–
Laconia	43	3	71	3	154	-23	32	–
Manchester, Grenier AFB	42	56	71	26	71	-22	33	–
Portsmouth, Pease AFB	43	4	70	49	31	-19	32	–

Table A-1. Climatic conditions for the United States (continued).

State and Station	Location Latitude °	′N	Longitude °	′W	Elev. m	Shade Temperature Min. °C	Max. °C	Mean* Constr. °C
New Jersey								
Atlantic City CO	39	23	74	26	3	-12	33	16
Long Branch	40	19	74	1	5	-12	34	–
New Brunswick	40	29	74	26	38	-14	33	–
Newark AP	40	42	74	10	2	-12	34	17
Paterson	40	54	74	9	30	-14	34	–
Phillipsburg	40	41	75	11	55	-17	33	–
Trenton CO	40	13	74	46	17	-12	33	16
Vineland	39	29	75	0	34	-13	33	–
New Mexico								
Alamogordo, Holloman AFB	32	51	106	6	1247	-10	37	–
Albuquerque AP	35	3	106	37	1619	-11	36	18
Artesia	32	46	104	23	1012	-11	39	–
Carlsbad AP	32	20	104	16	1004	-11	39	–
Clovis AP	34	23	103	19	1309	-13	35	–
Farmington AP	36	44	108	14	1677	-17	35	–
Gallup	35	31	108	47	1970	-18	32	–
Grants	35	10	107	54	1988	-18	32	–
Hobbs AP	32	45	103	13	1125	-11	38	–
Las Cruces	32	18	106	55	1385	-9	37	–
Los Alamos	35	52	106	19	2258	-15	32	–
Raton AP	36	45	104	30	1942	-20	33	18
Roswell, Walker AFB	33	18	104	32	1120	-11	38	21
Santa Fe CO	35	37	106	5	1922	-14	32	–
Silver City AP	32	38	108	10	1659	-15	35	–
Socorro AP	34	3	106	53	1409	-11	36	–
Tucumcari AP	35	11	103	36	1231	-13	37	–
New York								
Albany AP	42	45	73	48	84	-21	33	16
Albany CO	42	39	73	45	6	-20	33	16
Auburn	42	54	76	32	22	-19	32	–
Batavia	43	0	78	11	281	-17	32	–
Binghamton AP	42	13	75	59	485	-19	30	19
Buffalo AP	42	56	78	44	215	-17	31	15
Cortland	42	36	76	11	344	-21	31	–
Dunkirk	42	29	79	16	211	-16	31	–
Elmira AP	42	10	76	54	291	-20	32	–
Geneva	42	45	76	54	187	-19	32	–
Glens Falls	43	20	73	37	100	-24	31	–
Gloversville	43	2	74	21	232	-22	32	–

Table A-1. Climatic conditions for the United States (continued).

State and Station	Location Latitude °	′N	Longitude °	′W	Elev. m	Shade Temperature Min. °C	Max. °C	Mean* Constr. °C
Hornell	42	21	77	42	404	-20	31	–
Ithaca	42	27	76	29	283	-21	31	–
Jamestown	42	7	79	14	424	-18	31	–
Kingston	41	56	74	0	85	-19	33	–
Lockport	43	9	79	15	194	-16	32	–
Massena AP	44	56	74	51	63	-25	30	–
Newburgh, Stewart AFB	41	30	74	6	144	-18	32	–
NYC-Central Park	40	47	73	58	48	-12	33	15
NYC-Kennedy AP	40	39	73	47	4	-11	32	15
NYC-La Guardia AP	40	46	73	54	3	-12	33	15
Niagara Falls AP	43	6	79	57	180	-16	32	–
Olean	42	14	78	22	646	-19	31	–
Oneonta	42	31	75	4	541	-22	30	–
Oswego CO	43	28	76	33	91	-17	30	–
Plattsburg AFB	44	39	73	28	72	-25	30	–
Poughkeepsie	41	38	73	55	50	-18	33	–
Rochester AP	43	7	77	40	167	-17	33	15
Rome, Griffiss AFB	43	14	75	25	157	-24	31	–
Schenectady	42	51	73	57	115	-20	32	–
Suffolk County AFB	40	51	72	38	20	-14	30	–
Syracuse AP	43	7	76	7	125	-19	32	15
Utica	43	9	75	23	218	-24	31	–
Watertown	43	59	76	1	99	-24	30	–
North Carolina								
Asheville AP	35	26	82	32	652	-12	32	16
Charlotte AP	35	13	80	56	224	-8	35	16
Durham	35	52	78	47	132	-9	34	–
Elizabeth City AP	36	16	76	11	4	-11	34	–
Fayetteville, Pope AFB	35	10	79	1	66	-8	35	–
Goldsboro	35	20	77	58	33	-8	34	–
Greensboro AP	36	5	79	57	273	-10	34	18
Greenville	35	37	77	25	23	-8	34	–
Henderson	36	22	78	25	146	-11	35	–
Hickory	35	45	81	23	362	-10	33	–
Jacksonville	34	50	77	37	29	-7	33	–
Lumberton	34	37	79	4	39	-8	35	–
New Bern AP	35	5	77	3	6	-7	33	–
Raleigh/Durham AP	35	52	78	47	132	-9	34	17
Rocky Mount	35	58	77	48	37	-8	34	–
Wilmington AP	34	16	77	55	9	-5	34	17
Winston-Salem AP	36	8	80	13	295	-9	34	17

Table A-1. Climatic conditions for the United States (continued).

State and Station	Location Latitude °	′N	Longitude °	′W	Elev. m	Shade Temperature Min. °C	Max. °C	Mean* Constr. °C
North Dakota								
Bismarck AP	46	46	100	45	502	-31	35	16
Devil's Lake	48	7	98	54	442	-32	33	14
Dickinson AP	46	48	102	48	788	-29	34	–
Fargo AP	46	54	96	48	273	-30	33	15
Grand Forks AP	47	57	97	24	278	-32	33	–
Jamestown AP	46	55	98	41	455	-30	34	–
Minto AP	48	25	101	21	508	-31	33	15
Williston	48	9	103	35	572	-32	33	15
Ohio								
Akron, Canton AP	40	55	81	26	368	-17	32	16
Ashtabula	41	51	80	48	210	-16	31	–
Athens	39	20	82	6	213	-18	35	–
Bowling Green	41	23	83	38	206	-19	33	–
Cambridge	40	4	81	35	246	-17	34	–
Chillicothe	39	21	83	0	195	-18	35	–
Cincinnati CO	39	9	84	31	231	-17	33	17
Cleveland AP	41	24	81	51	237	-17	33	16
Columbus AP	40	0	82	53	247	-18	33	16
Dayton AP	39	54	84	13	305	-18	33	16
Defiance	41	17	84	23	213	-18	34	–
Findlay AP	41	1	83	40	245	-17	33	–
Fremont	41	20	83	7	183	-19	32	–
Hamilton	39	24	84	35	198	-18	33	–
Lancaster	39	44	82	38	262	-18	34	–
Lima	40	42	84	2	297	-18	34	–
Mansfield AP	40	49	82	31	395	-18	32	16
Marion	40	36	83	10	280	-18	34	–
Middletown	39	31	84	25	194	-18	33	–
Newark	40	1	82	28	268	-18	34	–
Norwalk	41	16	82	37	204	-19	32	–
Portsmouth	38	45	82	55	165	-15	35	–
Sandusky CO	41	27	82	43	185	-17	34	16
Springfield	39	50	83	50	321	-18	33	–
Steubenville	40	23	80	38	302	-17	32	–
Toledo AP	41	36	83	48	204	-19	32	16
Warren	41	20	80	51	283	-18	32	–
Wooster	40	47	81	55	311	-17	32	–
Youngstown AP	41	16	80	40	359	-18	31	15
Zanesville AP	39	57	81	54	274	-17	34	–
Oklahoma								
Ada	34	47	96	41	309	-12	38	–

Table A-1. Climatic conditions for the United States (continued).

State and Station	Location Latitude °	′N	Longitude °	′W	Elev. m	Shade Temperature Min. °C	Max. °C	Mean* Constr. °C
Altus AFB	34	39	99	16	420	-12	39	–
Ardmore	34	18	97	1	235	-11	38	–
Bartlesville	36	45	96	0	218	-14	38	–
Chickasha	35	3	97	55	331	-12	38	–
Enid, Vance AFB	36	21	97	55	398	-13	39	–
Lawton AP	34	34	98	25	334	-11	38	–
McAlester	34	50	95	55	237	-10	37	–
Muskogee AP	35	40	95	22	186	-12	38	–
Norman	35	15	97	29	360	-13	37	–
Oklahoma City AP	35	24	97	36	392	-13	38	18
Ponca City	36	44	97	6	304	-15	38	–
Seminole	35	14	96	40	264	-12	37	–
Stillwater	36	10	97	5	300	-13	38	–
Tulsa AP	36	12	95	54	198	-13	38	18
Woodward	36	36	99	31	660	-14	38	–
Oregon								
Albany	44	38	123	7	70	-8	33	–
Astoria AP	46	9	123	53	2	-4	24	10
Baker AP	44	50	117	49	1028	-18	33	–
Bend	44	4	121	19	1096	-19	32	–
Corvallis	44	30	123	17	75	-8	33	–
Eugene AP	44	7	123	13	109	-8	33	11
Grants Pass	42	26	123	19	282	-7	37	–
Klamath Falls AP	42	9	121	44	1247	-16	32	–
Medford AP	42	22	122	52	396	-7	37	13
Pendleton AP	45	41	118	51	452	-19	36	14
Portland AP	45	36	122	36	6	-8	32	11
Portland CO	45	32	122	40	23	-8	32	11
Roseburg AP	43	14	123	22	160	-8	34	12
Salem AP	44	55	123	1	60	-8	33	11
The Dalles	45	36	121	12	30	-11	34	–
Pennsylvania								
Allentown AP	40	39	75	26	118	-16	33	16
Altoona CO	40	18	78	19	458	-18	32	–
Butler	40	52	79	54	335	-17	32	–
Chambersburg	39	56	77	38	195	-16	34	–
Erie AP	42	5	80	11	223	-16	31	15
Harrisburg AP	40	12	76	46	94	-14	34	16
Johnstown	40	19	78	50	696	-19	30	–
Lancaster	40	7	76	18	123	-16	34	–
Meadville	41	38	80	10	325	-18	31	–
New Castle	41	1	80	22	251	-17	33	–

Table A-1. Climatic conditions for the United States (continued).

State and Station	Location Latitude °	′N	Longitude °	′W	Elev. m	Shade Temperature Min. °C	Max. °C	Mean* Constr. °C
Philadelphia AP	39	53	75	15	2	-12	34	17
Pittsburgh AP	40	30	80	13	347	-17	32	17
Pittsburgh CO	40	27	80	0	310	-16	33	17
Reading CO	40	20	75	38	81	-13	33	16
Scranton/Wilkes-Barre	41	20	75	44	283	-17	32	16
State College	40	48	77	52	358	-16	32	–
Sunbury	40	53	76	46	136	-17	33	–
Uniontown	39	55	79	43	291	-15	33	–
Warren	41	51	79	8	390	-19	32	–
West Chester	39	58	75	38	137	-13	33	–
Williamsport AP	41	15	76	55	160	-17	33	16
York	39	55	76	45	119	-13	34	–
Rhode Island								
Newport	41	30	71	20	3	-15	31	–
Providence AP	41	44	71	26	16	-15	32	16
South Carolina								
Anderson	34	30	82	43	236	-7	34	–
Charleston AFB	32	54	80	2	14	-4	34	19
Charleston CO	32	54	79	58	1	-4	34	19
Columbia AP	33	57	81	7	65	-7	36	18
Florence AP	34	11	79	43	45	-6	34	18
Georgetown	33	23	79	17	4	-5	33	–
Greenville AP	34	54	82	13	292	-8	34	16
Greenwood	34	10	82	7	189	-8	35	–
Orangeburg	33	30	80	52	79	-7	36	–
Rock Hill	34	59	80	58	143	-7	36	–
Spartanburg AP	34	58	82	0	251	-8	34	16
Sumter, Shaw AFB	33	54	80	22	52	-6	35	–
South Dakota								
Aberdeen AP	45	27	98	26	395	-28	34	–
Brookings	44	18	96	48	499	-27	35	–
Huron AP	44	23	98	13	390	-28	36	17
Mitchell	43	41	98	1	410	-26	36	–
Pierre AP	44	23	100	17	531	-26	37	–
Rapid City AP	44	3	103	4	964	-24	35	16
Sioux Falls AP	43	34	96	44	432	-26	34	17
Watertown AP	44	55	97	9	530	-28	34	–
Yankton	42	55	97	23	397	-25	34	–
Tennessee								
Athens	35	26	84	35	286	-11	35	–

Table A-1. Climatic conditions for the United States (continued).

State and Station	Location Latitude °	′N	Longitude °	′W	Elev. m	Shade Temperature Min. °C	Max. °C	Mean* Constr. °C
Bristol-Tri City AP	36	29	82	24	459	-13	33	17
Chattanooga AP	35	2	85	12	203	-11	36	16
Clarksville	36	33	87	22	116	-14	35	–
Columbia	35	38	87	2	210	-12	36	–
Dyersburg	36	1	89	24	105	-12	36	–
Greeneville	36	4	82	50	402	-12	33	–
Jackson AP	35	36	88	55	129	-12	37	–
Knoxville AP	35	49	83	59	299	-11	34	16
Memphis AP	35	3	90	0	79	-11	37	17
Murfreesboro	34	55	86	28	183	-13	36	–
Nashville AP	36	7	86	41	180	-13	36	17
Tullahoma	35	23	86	5	325	-13	36	–
Texas								
Abilene AP	32	25	99	41	544	-9	38	18
Alice AP	27	44	98	2	55	-1	38	–
Amarillo AP	35	14	101	42	1098	-14	37	19
Austin AP	30	18	97	42	182	-4	38	20
Bay City	29	0	95	58	15	-2	36	–
Beaumont	29	57	94	1	5	-3	35	–
Beeville	28	22	97	40	58	-1	37	–
Big Spring AP	32	18	101	27	792	-9	38	–
Brownsville AP	25	54	97	26	6	2	34	23
Brownwood	31	48	98	57	422	-8	38	–
Bryan AP	30	40	96	33	84	-4	37	–
Corpus Christi AP	27	46	97	30	12	-1	35	22
Corsicana	32	5	96	28	130	-7	38	–
Dallas AP	32	51	96	51	147	-8	39	19
Del Rio, Laughlin AFB	29	22	100	47	329	-3	38	–
Denton	33	12	97	6	192	-8	38	–
Eagle Pass	28	52	100	32	269	-3	38	–
El Paso AP	31	48	106	24	1194	-7	38	18
Fort Worth AP	32	50	97	3	164	-8	38	19
Galveston AP	29	18	94	48	2	-1	32	21
Greenville	33	4	96	3	163	-8	38	–
Harlingen	26	14	97	39	11	2	36	–
Houston AP	29	58	95	21	29	-3	36	20
Houston CO	29	59	95	22	33	-2	36	20
Huntsville	30	43	95	33	151	-6	38	–
Killeen, Robert Gray AFB	31	5	97	41	259	-7	37	–
LaMesa	32	42	101	56	904	-11	37	–
Laredo AFB	27	32	99	27	156	0	39	23
Longview	32	28	94	44	101	-7	37	–
Lubbock AP	33	39	101	49	992	-12	37	19

Table A-1. Climatic conditions for the United States (continued).

State and Station	Location Latitude °	′N	Longitude °	′W	Elev. m	Shade Temperature Min. °C	Max. °C	Mean* Constr. °C
Lufkin AP	31	25	94	48	84	-4	37	–
McAllen	26	12	98	13	37	2	36	–
Midland AP	31	57	102	11	869	-9	38	19
Mineral Wells AP	32	47	98	4	283	-8	38	–
Palestine CO	31	47	95	38	183	-5	38	–
Pampa	35	32	100	59	991	-14	37	–
Pecos	31	25	103	30	795	-9	38	–
Plainview	34	11	101	42	1027	-13	37	–
Port Arthur AP	29	57	94	1	5	-3	35	21
San Angelo, Goodfellow	31	26	100	24	572	-8	38	18
San Antonio AP	29	32	98	28	240	-4	37	21
Sherman, Perrin AFB	33	43	96	40	233	-9	38	–
Snyder	32	43	100	55	709	-11	38	–
Temple	31	6	97	21	213	-6	38	–
Tyler AP	32	21	95	16	162	-7	37	–
Vernon	34	10	99	18	369	-11	39	–
Victoria AP	28	51	96	55	32	-2	37	22
Waco AP	31	37	97	13	152	-6	38	19
Wichita Falls AP	33	58	98	29	303	-10	39	19
Utah								
Cedar City AP	37	42	113	6	1712	-19	34	–
Logan	41	45	111	49	1458	-19	34	–
Moab	38	36	109	36	1208	-14	38	–
Ogden AP	41	12	112	1	1358	-17	34	–
Price	39	37	110	50	1701	-19	34	–
Provo	40	13	111	43	1356	-17	37	–
Richfield	38	46	112	5	1606	-19	34	–
St. George CO	37	2	113	31	884	-10	39	–
Salt Lake City AP	40	46	111	58	1286	-16	36	17
Vernal AP	40	27	109	31	1609	-21	33	–
Vermont								
Barre	44	12	72	31	183	-27	29	–
Burlington AP	44	28	73	9	101	-24	31	14
Rutland	43	36	72	58	189	-25	31	–
Virginia								
Charlottesville	38	2	78	31	265	-10	34	–
Danville AP	36	34	79	20	180	-10	34	–
Fredericksburg	38	18	77	28	30	-12	36	–
Harrisonburg	38	27	78	54	418	-11	34	–
Lynchburg AP	37	20	79	12	279	-11	34	17

Table A-1. Climatic conditions for the United States (continued).

State and Station	Location Latitude °	′N	Longitude °	′W	Elev. m	Shade Temperature Min. °C	Max. °C	Mean* Constr. °C
Norfolk AP	36	54	76	12	7	-7	34	16
Petersburg	37	11	77	31	59	-10	35	–
Richmond AP	37	30	77	20	50	-10	35	18
Roanoke AP	37	19	79	58	364	-11	34	17
Staunton	38	16	78	54	366	-11	34	–
Winchester	39	12	78	10	232	-14	34	–
Washington								
Aberdeen	46	59	123	49	4	-4	27	–
Bellingham AP	48	48	122	32	48	-12	27	–
Bremerton	47	34	122	40	49	-6	28	–
Ellensburg AP	47	2	120	31	529	-17	34	–
Everett, Paine AFB	47	55	122	17	182	-6	27	–
Kennewick	46	13	119	8	119	-15	37	–
Longview	46	10	122	56	4	-7	31	–
Moses Lake, Larson AFB	47	12	119	19	361	-17	36	–
Olympia AP	46	58	122	54	66	-9	31	11
Port Angeles	48	7	123	26	30	-4	22	–
Seattle-Boeing Field	47	32	122	18	7	-6	29	11
Seattle CO	47	39	122	18	6	-6	29	11
Seattle-Tacoma AP	47	27	122	18	122	-6	29	11
Spokane AP	47	38	117	31	718	-21	34	14
Tacoma, McChord AFB	47	15	122	30	30	-7	30	–
Walla Walla AP	46	6	118	17	368	-18	36	14
Wenatchee	47	25	120	19	193	-14	37	–
Yakima AP	46	34	120	32	321	-19	36	17
West Virginia								
Beckley	37	47	81	7	763	-19	28	–
Bluefield AP	37	18	81	13	874	-19	28	–
Charleston AP	38	22	81	36	286	-14	33	17
Clarksburg	39	16	80	21	298	-14	33	–
Elkins AP	38	53	79	51	594	-17	30	–
Huntington CO	38	25	82	30	172	-15	34	17
Martinsburg AP	39	24	77	59	169	-14	34	–
Morgantown AP	39	39	79	55	378	-16	32	–
Parkersburg CO	39	16	81	34	187	-14	34	17
Wheeling	40	7	80	42	203	-17	32	–
Wisconsin								
Appleton	44	15	88	23	222	-26	32	–
Ashland	46	34	90	58	198	-29	29	–

Table A-1. Climatic conditions for the United States (continued).

State and Station	Location Latitude °	′N	Longitude °	′W	Elev. m	Shade Temperature Min. °C	Max. °C	Mean* Constr. °C
Beloit	42	30	89	2	238	-22	33	–
Eau Claire AP	44	52	91	29	271	-26	33	–
Fond du Lac	43	48	88	27	232	-24	32	–
Green Bay AP	44	29	88	8	208	-25	31	15
LaCrosse AP	43	52	91	15	198	-25	33	17
Madison AP	43	8	89	20	262	-24	33	16
Manitowoc	44	6	87	41	201	-24	32	–
Marinette	45	6	87	38	184	-26	31	–
Milwaukee AP	42	57	87	54	205	-22	32	16
Racine	42	43	87	51	222	-21	33	–
Sheboygan	43	45	87	43	198	-23	32	–
Stevens Point	44	30	89	34	329	-26	33	–
Waukesha	43	1	88	14	262	-23	32	–
Wausau AP	44	55	89	37	365	-27	33	–
Wyoming								
Casper AP	42	55	106	28	1627	-24	33	15
Cheyenne	41	9	104	49	1867	-23	32	14
Cody AP	44	33	109	4	1521	-28	32	–
Evanston	41	16	110	57	2066	-23	30	–
Lander AP	42	49	108	44	1696	-27	33	14
Laramie AP	41	19	105	41	2215	-26	29	–
Newcastle	43	51	104	13	1300	-27	33	–
Rawlins	41	48	107	12	2054	-24	30	–
Rock Springs AP	41	36	109	4	2056	-23	30	–
Sheridan AP	44	46	106	58	1208	-26	34	15
Torrington	42	5	104	13	1249	-26	34	–

APPENDIX B. EXPECTED TRANSVERSE MOVEMENT FOR SKEWED BRIDGES WITH TYPICAL INTEGRAL ABUTMENTS

To investigate the relationship between skew angle and expected transverse movement for a typical integral stub abutment, a set of relationships were derived based on the equilibrium and compatibility of end abutment forces in the plane of the bridge superstructure. For this analysis, the superstructure is assumed to act as a rigid body with rotation, β, about the center of the deck (for a longitudinally symmetrical bridge), as illustrated in figure B-1. The rotation occurs to accommodate the thermal end movement, $\Delta\ell$. Forces considered in response to this movement include soil pressure on the abutment and wingwalls, wall/soil interface friction on the abutment, and pile forces normal to and in line with the abutment and wingwalls. These forces are illustrated in figure B-2. The components of abutment movement are shown in figure B-3.

The soil pressure on the backside of the abutment wall is divided into two components, one related to passive pressure, P_p, and one related to pressure-at-rest, P_o. If the final location with the thermal expansion of abutment corners 1 and/or 2 is to the right and above the line of the initial position shown in figure B-3, passive pressure is calculated for that corner, depending on the Δ/H for the corner movements normal to the abutment wall, Δ_{n1} and Δ_{n2}.

If the final corner location is to the left and below the line of the initial position, the pressure-at-rest is calculated for that corner. Pressure-at-rest is used rather than active pressure, assuming that traffic vibrations will maintain an at-rest soil pressure as a minimum. If Corner 1 is to the left and below and Corner 2 is to the right and above the line of initial position, the passive pressure is assumed to decrease linearly to P_o at the location along the abutment where the final position of the abutment crosses the line of the initial position. Friction force on the abutment is determined from the sum of the normal soil forces multiplied by tan δ.

Soil forces on the wingwall are determined from the transverse movement at each corner. For the Corner 1 wingwall, which would be loaded by the soil sloping down from the far end to the abutment wall, the soil pressure is assumed to be triangular, with the peak passive pressure determined from Δ/H for the Corner 1 transverse movement, Δ_{t1}. For the Corner 2 wingwall, the soil within the acute angle made by the wingwall is considered to be confined, as illustrated in figure B-2. The soil pressure on this confined Corner 2 is assumed to be parallel to the abutment, with the peak passive pressure determined from Δ/H for the Corner 2 movement parallel to the abutment, Δ_{p2}.

Pile forces are determined for a component related to strong-axis bending and a component related to weak-axis bending. Lateral-force versus lateral-deflection relationships for strong-axis and weak-axis bending can be determined by using the equivalent cantilever method or the computer program COM624P.[(1)] These relationships are used with movements normal and

parallel to the abutments and wingwalls to estimate pile response. The pile orientations used in the analysis are based on the orientation typically used in Tennessee. These include strong-axis bending for movement normal to the abutment and wingwalls, and weak-axis bending for movement parallel to the abutment or wingwalls. Pile forces were limited in each direction to the lateral force associated with reaching the yield moment in each direction.

Figure B-3 illustrates the various components of movement for the abutment as related to the end thermal length change, $\Delta\ell$, and the rigid body rotation of the deck, β. The following relationships define the components of the movement.

For Corner 1:

$$\alpha_1 = \tan^{-1}\left(\frac{\frac{W}{2}}{\ell + \frac{W}{2}\tan\theta}\right) \tag{B-1[a]}$$

$$\Delta_{R1} = \beta\left[\left(\frac{W}{2}\right)^2 + \left(\ell + \frac{W}{2}\tan\theta\right)^2\right]^{0.5} \tag{B-1[b]}$$

$$\Delta_{t1} = \Delta_{R1}\cos\alpha_1 \tag{B-1[c]}$$

$$\Delta_{\ell 1} = \Delta\ell - \Delta_{R1}\sin\alpha_1 \tag{B-1[d]}$$

$$\Delta_{n1} = \Delta_{R1}\sin(\theta + \alpha_1) - \Delta\ell\cos\theta \tag{B-1[e]}$$

$$\Delta_{p1} = \Delta_{R1}\cos(\theta + \alpha_1) + \Delta\ell\sin\theta \tag{B-1[f]}$$

For Corner 2:

$$\alpha_1 = \tan^{-1}\left(\frac{\frac{W}{2}}{\ell + \frac{W}{2}\tan\theta}\right) \tag{B-2[a]}$$

$$\Delta_{R2} = \beta\left[\left(\frac{W}{2}\right)^2 + \left(\ell - \frac{W}{2}\tan\theta\right)^2\right]^{0.5} \tag{B-2[b]}$$

$$\Delta_{t2} = \Delta_{R2}\cos\alpha_2 \tag{B-2[c]}$$

$$\Delta_{\ell 2} = \Delta\ell + \Delta_{R2} \sin \alpha_2 \tag{B-2[d]}$$

$$\Delta_{n2} = \Delta\ell \cos\theta - \Delta_{R2} \sin (\theta - \alpha_2) \tag{B-2[e]}$$

$$\Delta_{p2} = \Delta\ell \sin\theta + \Delta_{R2} \cos (\theta - \alpha_2) \tag{B-2[f]}$$

where,

ℓ = length of bridge along the longitudinal axis from the point of fixity to the end of the bridge at the abutment

W = width of bridge perpendicular to the longitudinal axis

θ = skew angle.

For the length of the abutment to the right of the line of initial position:

$$x = \frac{\Delta_{\ell 2} - \Delta_{t2} \tan (\theta - \beta)}{\tan \theta - \tan (\theta - \beta)} \tag{B-2[g]}$$

$$\ell_{pp-po} = \frac{x - \Delta_{t2}}{\cos (\theta - \beta)} \tag{B-2[h]}$$

The forces related to these components of movement and their moment arms for rotational equilibrium within the plane of the superstructure are shown in table B-1, where, as shown in figure B-2:

F_{po} = total force normal to the back of the abutment resulting from the soil pressure-at-rest over $\ell_{abut} = W/\cos \theta$

$F_{pp\text{-}po}$ = additional force normal to the back of the abutment resulting from the passive soil pressure over distance $\ell_{pp\text{-}po} \leq \ell_{abut}$ with K_{pabut} determined from the passive pressure coefficient versus lateral deformation relationship for Δ_{n2}/h_{abut} if $\ell_{pp\text{-}po} < \ell_{abut}$ and for $(\Delta_{n1} + \Delta_{n2})/2\ h_{abut}$ if $\ell_{pp\text{-}po} = \ell_{abut}$

F_{af} = total force parallel to the abutment resulting from the soil interface friction

F_{s1} = total force normal to Wingwall 1 resulting from the passive soil pressure, with K_{p1} determined from the passive pressure coefficient versus lateral deformation relationship for Δ_{t1}/h_1

F_{s2} = total force on Wingwall 2 resulting from the passive soil pressure in a direction parallel to the abutment, with K_{p2} determined from the passive pressure coefficient versus lateral deformation relationship for Δ_{p2}/h_2

$F_{pas\Delta n}$ = total lateral-pile force on the abutment from N_{pa} piles for strong-axis bending determined from the pile lateral load versus deformation relationship for strong-axis bending, $f_{ps}(\Delta)$, for the movement, Δ_{n2}

F_{pasrot} = total change in lateral-pile force on the abutment from N_{pa} piles for strong-axis bending determined from the pile lateral load versus deformation relationship for strong-axis bending, $f_{ps}(\Delta)$, for the average normal movement between Corners 1 and 2 related to the superstructure rotation, β

F_{paw} = total lateral-pile force on the abutment from N_{pa} piles for weak-axis bending determined from the pile lateral load versus deformation relationship for weak-axis bending, $f_{pw}(\Delta)$, for the average movement of Corners 1 and 2 parallel to the abutment

F_{p1s} = total lateral-pile force normal to Wingwall 1 from N_{p1} piles for strong-axis bending determined from pile lateral load versus deformation relationship for strong-axis bending $f_{ps}(\Delta)$, for the transverse movement, Δ_{t1}

F_{p1w} = total lateral-pile force parallel to Wingwall 1 from N_{p1} piles for weak-axis bending determined from pile lateral load versus deformation relationship for weak-axis bending, $f_{pw}(\Delta)$, for the longitudinal movement, $\Delta_{\ell 1}$

F_{p2s} = total lateral-pile force normal to Wingwall 2 from N_{p2} piles for strong-axis bending determined from pile lateral load versus deformation relationship for weak-axis bending, $f_{ps}(\Delta)$, for the transverse movement, Δ_{t2}

F_{p2w} = total lateral-pile force parallel to Wingwall 2 from N_{p2} piles for weak-axis bending determined from pile lateral load versus deformation

relationship for weak-axis bending, $f_{pw}(\Delta)$, for the longitudinal movement, $\Delta_{\ell 2}$

γ = density of abutment backfill soil

H_{abut} = height of the abutment from the bottom of the pile cap to the top of the approach slab

h_1 = height of Wingwall 1 from the bottom of the pile cap to the upper elevation of the sloped embankment

h_2 = height of Wingwall 2 from the bottom of the pile cap to the top of the approach slab

ℓ_{1w} = horizontal length of Wingwall 1

ℓ_{2w} = horizontal length of Wingwall 2

ℓ_{abut} = horizontal length of the abutment in the direction of the skew angle

F_{psy} = lateral load in the pile at yielding for strong-axis bending

F_{pwy} = lateral load in the pile at yielding for weak-axis bending.

It should be noted that frictional forces resulting from the weight of the approach slab are approximated by defining the height of the abutment, h_{abut}, and the height of Wingwall 2, h_2, to include the height from the bottom of the abutment to the top of the approach slab.

For a given end thermal movement, $\Delta\ell$, the equilibrium position can be found using an iterative analysis by progressively increasing the rotation angle, β, until the sum of the in-plane moments is zero.

B1 REFERENCES

1. Shih-Tower, W., and Reese, L. C., *Com624P: Laterally Loaded Pile Analysis Program for Microcomputer, Version 2.0,* Report No. FHWA-5A-91-048, Office of Technology Applications, FHWA, Washington, DC, 1991.

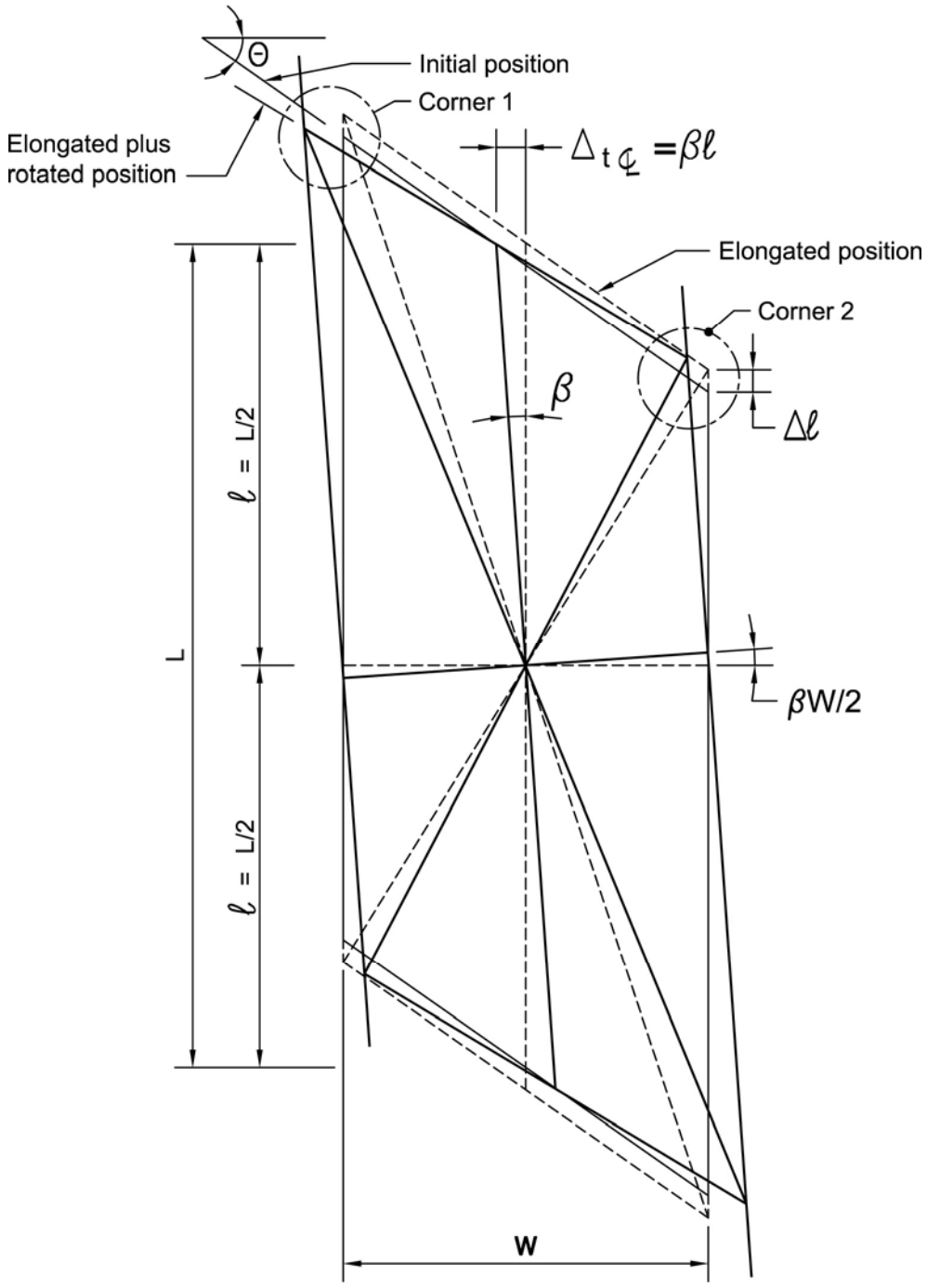

Figure B-1. Elongation, $\Delta\ell$, and rigid body rotation, β.

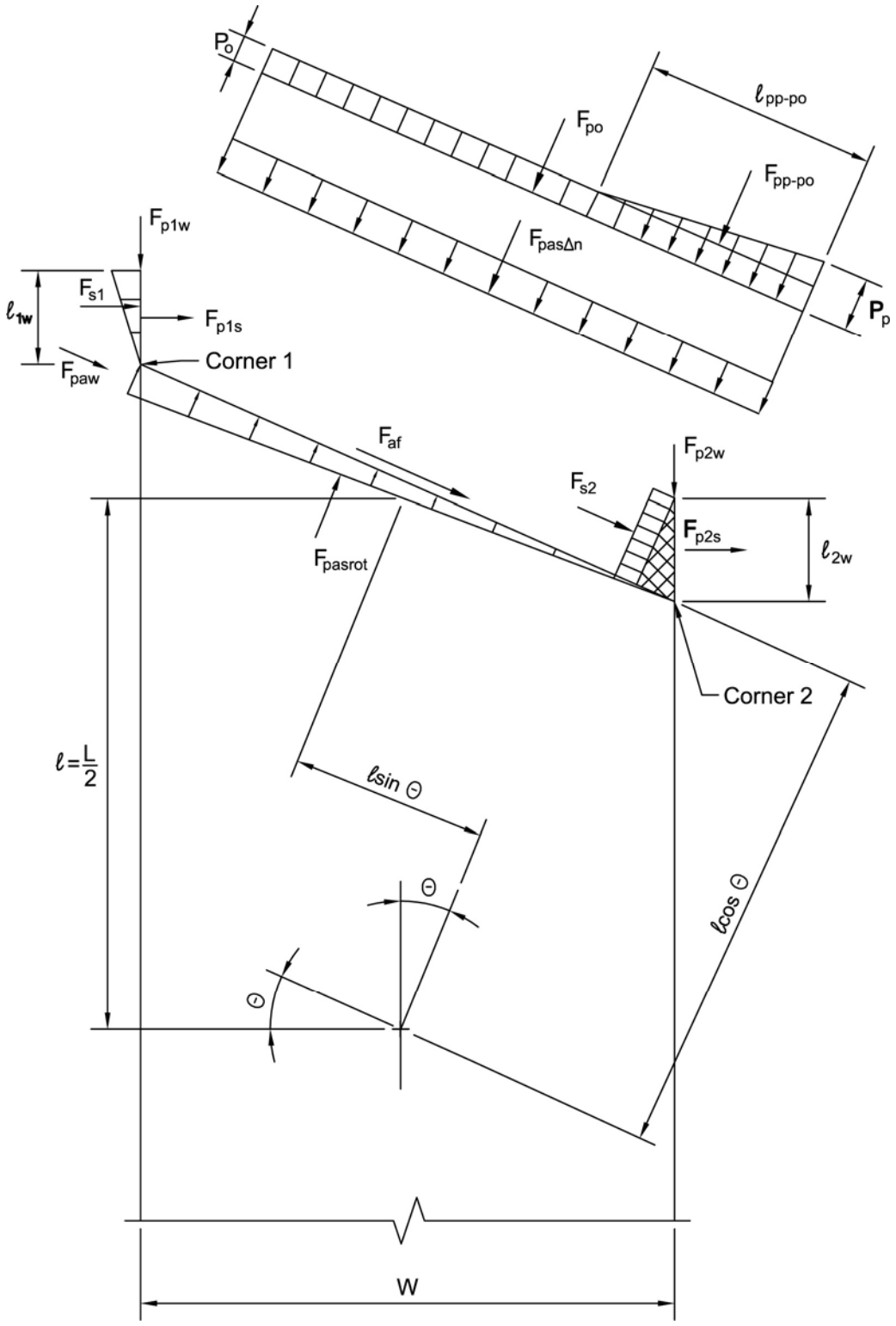

Figure B-2. Forces on end abutment of skewed bridge caused by thermal elongation, $\Delta\ell$, and rigid body rotation, β.

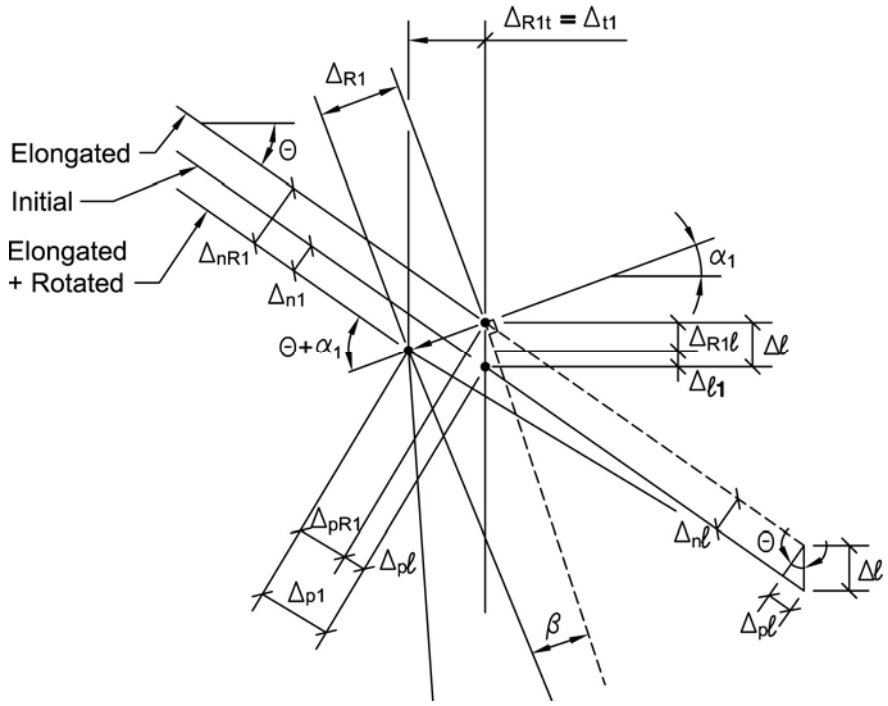

(a) Corner 1

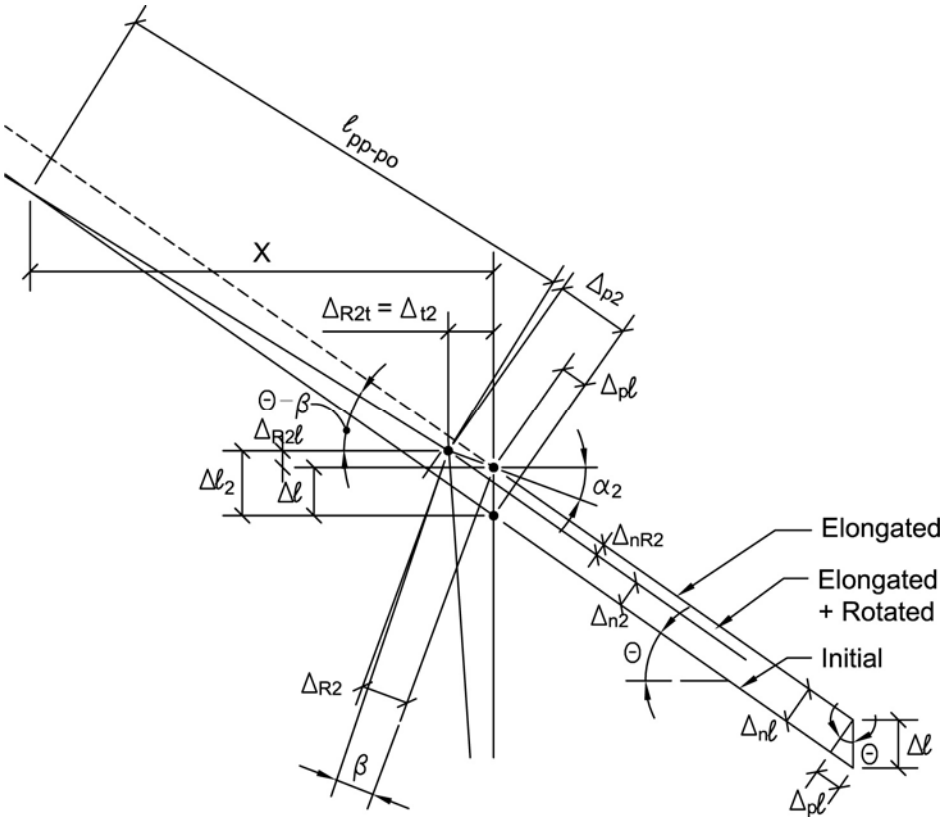

(b) Corner 2

Figure B-3. Components of abutment movement.

Table B-1. Abutment forces for rotational equilibrium.

Equations for Force	Moment Arm	Positive Direction for Force	Moment Direction
Soil Forces			
$F_{po} = (1/2)\,\gamma\,K_o\,h_{abut}^2\,(W/\cos\theta)$	$\ell \sin\theta$		
$F_{pp\text{-}po} = (1/4)\,\gamma\,(K_{pabut} - K_o)\,h_{abut}^2\,(\ell_{pp\text{-}po})$	$\ell \sin\theta - \frac{\ell_{abut}}{2} + \frac{\ell_{pp-po}}{3}$		
$F_{af} = (F_{po} + F_{pp\text{-}po})\tan\delta$	$\ell \cos\theta$	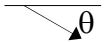	
$F_{s1} = (1/4)\,\gamma\,K_{p1}\,h_1^2\,\ell_{1w}$	$\ell + \frac{W}{2}\tan\theta + \frac{2\ell_{1w}}{3}$		
$F_{s2} = (1/2)\,\gamma\,K_{p2}\,h_2^2\,\ell_{2w}\cos\theta$	$\ell\cos\theta + \frac{\ell_{2w}\cos\theta}{2}$	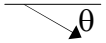	
Pile Forces			
$F_{pas\,\Delta n} = N_{pa}\,[f_{ps}(\Delta_{n2})] < N_{pa}\,f_{psy}$	$\ell \sin\theta$		
$F_{pasrot} = N_{pa}\,[f_{ps}((1/2)(\Delta_{n1} + \Delta_{n2}))]$	$\ell \sin\theta + \frac{W}{6\cos\theta}$		
$F_{paw} = N_{pa}\,[f_{pw}((1/2)(\Delta_{p1} + \Delta_{p2}))] < N_{pa}\,f_{pwy}$	$\ell \cos\theta$	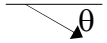	
$F_{p1s} = N_{p1}\,[f_{ps}(\Delta_{t1})] < N_{p1}\,f_{psy}$	$\ell + \frac{W}{2}\tan\theta + \frac{\ell_{1w}}{2}$		
$F_{p1w} = N_{p1}\,[f_{pw}(\Delta_{\ell 1})] < N_{p1}\,f_{pwy}$	$\frac{W}{2}$		
$F_{p2s} = N_{p2}\,[f_{ps}(\Delta_{t2})] < N_{p2}\,f_{psy}$	$\ell - \frac{W}{2}\tan\theta + \frac{\ell_{2w}}{2}$		
$F_{p2w} = N_{p2}\,[f_{pW}(\Delta_{\ell 2})] < N_{p2}\,f_{pwy}$	$\frac{W}{2}$		

APPENDIX C. ANALYSES FOR LONGITUDINAL MOVEMENT

C1 OVERVIEW

The analyses of jointless bridges subjected to longitudinal movement consisted of two-dimensional models of prestressed concrete, reinforced concrete, and composite steel bridges, including:

1. Creep and shrinkage for concrete bridges and the concrete deck of composite steel bridges.
2. Cracking in the concrete.
3. Nonlinear end-restraint stiffnesses for abutment piles, approach-slab restraint, and passive soil pressure. The passive soil pressure distribution was developed to simulate the pressure distribution calculated from the CANDE finite element model[(1)] with the highest level of compaction as described in chapter 5 of the analytical report.[(2)]
4. Stiffnesses of longitudinal restraint at the intermediate piers.
5. Time-history analyses over several years, superimposing sinusoidal annual uniform temperature change effects on creep and shrinkage effects.

Bridges used for the analyses were based on *Standard Plans for Highway Bridges, Volumes IV and IV(A)* from the U.S. Department of Transportation, Federal Highway Administration (FHWA).[(3)] The plans were modified where required to conform to typical jointless bridge details and layouts. Analyses included both a short-span and a long-span structure for each bridge type. To cover a broad range of bridge behavior and response, various combinations of starting temperature, cycling, creep, shrinkage, and bridge details were investigated. The basic bridge characteristics consisted of the following:

1. Prestressed concrete, short span: AASHTO Type III girder, 203-mm- (8-inch-) thick deck, 2.7-m (8.75-ft) girder spacing, 19.8-m (65-ft) span lengths.
2. Prestressed concrete, long span: PCI BT-72 girder, 210-mm- (8.25-inch-) thick deck, 2.8-m (9.25-ft) girder spacing, 41.5-m (136-ft) span lengths.

3. Reinforced concrete, short span: Variable-depth T-beam ranging from 0.9 m to 1.6 m (3 ft to 5.3 ft), 191-mm- (7.5-inch-) thick deck, 2.4-m (8-ft) girder spacing, 21.4-m (70-ft) span lengths.

4. Reinforced concrete, long span: 1.7-m- (5.5-ft-) deep box girder, 203-mm- (8-inch-) thick top deck, 152.4-mm- (6-inch-) thick bottom deck, 2.4-m (8-ft) web spacing, 30.5-m (100-ft) span lengths.

5. Composite steel, short span: Rolled beam with a W36x160 spliced with a W36x194 in the negative-moment region of the center pier (similar to Sheet Nos. 301 to 304, Vol. IV(A) of the standard plans[3]), 203-mm- (8-inch-) thick deck, 2.7-m (8.75-ft) beam spacing, 25.9-m (85-ft) span lengths.

6. Composite steel, long span: Nominal 1.7-m- (68-inch-) deep welded plate girder with a varying web thickness and top and bottom flange dimensions that are dependent on the location within the positive-moment and negative-moment regions (similar to Sheet Nos. 401 to 404, Vol. IV(A) of the standard plans)[3], 203-mm- (8-inch-) thick deck, 2.7-m (8.75-ft) girder spacing, 43-m (140-ft) span lengths.

The computer program PBEAM, developed by C. Suttikan,[4] was used to model the various bridges and includes all of the desired analysis features previously mentioned. Discussed in more detail in the following section, PBEAM is capable of analyzing structures of any cross-sectional shape that has one axis of symmetry. The program accounts for the effects of nonlinearity in the stress-strain responses of the materials and variations over time in strength, stiffness, creep, and shrinkage. Modifications were subsequently made to the program to incorporate cyclical temperature variations.

C2 ANALYSIS PROGRAM PBEAM

The computer program PBEAM is based on the discrete-element method as developed by C. A. Hays and H. Matlock.[5] The discrete-element method is applicable to structures with widely varying and discontinuous stiffnesses, support conditions, and loadings. The method is also readily adaptable to time-dependent response analysis by including a version of the direct-stiffness approach. In this instance, a step-by-step method was used in the time-dependent analysis with a tangent-stiffness method implemented for solving the nonlinear response. The program will thus account for the effects of nonlinearity in the stress-strain responses of the materials and variations over time in strength, stiffness, creep, and shrinkage. In addition, modifications have been subsequently made to the program to incorporate cyclical temperature variations.

PBEAM is capable of analyzing structures of any cross-sectional shape having one axis of symmetry. The shape is discretized into a series of rectangular fibers distributed over the depth of the cross section. Element deformations and forces are estimated by analyzing the stress-strain relationships of a series of fibers over the cross-sectional depth. It is assumed that the strain in each fiber is constant at the centroidal axis of the fiber and the strain distribution varies linearly through the depth of the section. For each time step, equilibrium at each element is maintained by determining the time-dependent stress corresponding to the level of strain in each fiber. Stress multiplied by area is summed over all of the fibers and the force equilibrium is checked. If necessary, the strain distribution is adjusted and the process is repeated until the forces balance.

PBEAM also allows unlimited flexibility in analyzing various construction sequences and live load applications. The analysis of the construction sequence is such that casting of the various parts of the bridge can be done at any time and in any sequence. Therefore, the simple-span behavior of a PS/C girder before deck and diaphragm casting, and the continuous behavior thereafter, can be correctly modeled. Live load can also be applied at any stage of the service life and in any configuration. The program can therefore be used to investigate behavior under a wide variety of conditions likely to be encountered in actual practice.

The program's capabilities also allow for a realistic analysis of the influence of concrete cracking on the behavior of PS/C, reinforced concrete, and composite steel bridges. Depending on the stress level and the time-dependent material properties, the program accounts for cracking of the deck and girder (if applicable) concrete under positive or negative moments. For each time step of the analysis, the program stores the stress-strain relationship in every fiber of each element. These stored conditions serve as the starting point for the behavior calculation for the succeeding time step. In this way, the program can follow both crack development and crack closing.

The applicability of PBEAM has been verified by comparison with a variety of test data. Suttikan compared analysis results with instantaneous and time-dependent test results from five different types and studies of prestressed beams.[4] In general, PBEAM was able to accurately predict instantaneous load-deflection response, time-dependent response, and failure load response for both composite and noncomposite prestressed beams, and in both simply supported and continuously supported conditions. Oesterle, et al., further verified PBEAM for predicting time-dependent deformations and restraint moments induced in multispan bridges built of simply supported PS/C beams that were

made continuous.[6] Analysis results were compared with PCA test observations conducted by A. H. Mattock.[7] Accurate correlation was again obtained between test observations and analytical results.

Modifications were subsequently made in the program to incorporate cyclical temperature variations. Following these modifications, a comparison was made with experimental longitudinal bridge displacement data versus time for the Boone River and Maple River bridges located in Iowa.[8] PBEAM was able to accurately predict the 2-year cyclical variation in overall bridge length, based on the input of daily effective bridge temperature values.

C3 REPRESENTATIVE ANALYSIS RESULTS

The following section contains representative results of the PBEAM analyses that depict the behavior and response of the three different bridge types under the influence of longitudinal movement.

C3.1 Prestressed Concrete Bridges

The first series of analyses involved cyclic, uniform temperature variations over a 2-year period. The effective bridge temperatures varied from a maximum of 35 °C (95 °F) in July to a minimum of -29 °C (-21 °F) in January, and followed an annual sinusoidal variation between these months. Three different casting temperatures (setting temperatures) were used for the starting points of the analyses. These temperatures, 21 °C, 32 °C, and 13 °C (70 °F, 90 °F, and 55 °F), represented average, hot, and cold weather casting conditions, respectively. This first series was also based on a purely elastic analysis and neglected the effects of creep, shrinkage, and cracking. In this way, this series studied the behavior and response of the bridges under uniform temperature variations alone.

Figures C-1, C-2, and C-3 are plots of bridge axial displacement as a function of time for each of the three starting temperatures, 21 °C, 32 °C, and 13 °C (70 °F, 90 °F, and 55 °F), respectively. The plots contain the results from the PBEAM analyses superimposed on the free bridge displacements, the product of the coefficient of thermal expansion, the length, and the change in the effective bridge temperature. The comparisons indicate that the longitudinal movement of the bridge is essentially unchanged by the abutment and pier restraint as compared to its free displacement. In other words, the axial stiffness of

the bridge cross section significantly exceeds the longitudinal resistance provided by the abutment (and the soil for expansion) and the intermediate piers.

Figures C-4, C-5, and C-6 are plots of girder moment at the abutment, first interior support, and second interior support as a function of time for each of the three starting temperatures. For all three conditions, the girders reach a maximum positive restraint moment of approximately 610 kN-m (450 kip-ft) at the abutment, which corresponds to yielding of the abutment support piles and dragging of the approach slab. This plateau, reached for all three starting temperatures including the lowerbound value of 13 °C (55 °F), represents an upperbound on the abutment restraint force. Furthermore, this moment is statically determinant and simply equal to the moment and horizontal shear from the abutment piles plus the horizontal shear caused by the frictional resistance of the approach slab, with values calculated at the girder centroid. It should be noted that except for relatively short bridges (total length, not individual span length), thermal movement alone results in yielding of the abutment support piles, even with a lowerbound starting temperature of 13 °C (55 °F).

Figures C-4, C-5, and C-6 also reveal another important aspect about bridge contraction and the positive end-restraint moment provided by the abutment: namely, that the positive end-restraint moment, primarily caused by the eccentricity of the pile from the girder centroid, diminishes rapidly along the bridge length, resulting in a relatively small negative moment at the first interior support.

The next series of analyses included concrete creep, shrinkage, and cracking, but did not include any thermal effects. The concrete creep and shrinkage values were based on ACI 209R-92 equations and relationships applied to the specific bridge cross sections analyzed.[9] Figure C-7 contains a plot of the girder moments from the analysis for the condition of an early-age girder at the time of continuity. In this instance, creep of the girders under prestressing predominates the response and results in positive continuity moments at the intermediate piers. It is important to note three aspects revealed by this plot: (1) The positive restraint moment at the abutment, again, reaches a maximum value of approximately 610 kN-m (450 kip-ft), which corresponds to yielding of the abutment support piles and dragging of the approach slab; (2) The secondary continuity moments resulting from creep and shrinkage at the intermediate piers significantly exceed the moments caused by the abutment end restraint, as shown by comparing figures C-4 and C-7; and (3) The concrete creep and cracking did not relieve enough of the axial displacement to prevent the abutment piles from yielding.

The next series of analyses included concrete creep, shrinkage, and cracking with thermal effects. The thermal effect included in this study is uniform temperature variation. Thermal gradients were not included. Figure C-8 contains a plot of the girder moments from the analysis for the condition of an early-age girder at the time of continuity and a starting temperature of 21 °C (70 °F). As indicated by the figure, even with the addition of cyclic, uniform temperature variations, creep of the girders under prestressing predominates the response and results in positive continuity moments at the intermediate piers. Furthermore, creep of the girders is so dominant that the resulting moments are essentially identical to those determined previously for the same conditions, except without the annual longitudinal thermal effects. In other words, the same three conclusions apply: (1) The positive restraint moment at the abutment reaches a maximum value of approximately 610 kN-m (450 kip-ft); (2) The secondary continuity moments resulting from creep and shrinkage at the intermediate piers significantly exceed the moments caused by the abutment end restraint; and (3) The concrete creep and cracking did not relieve enough of the axial displacement to prevent the abutment piles from yielding. These conclusions were identical for all three starting temperatures.

Figure C-9 is a plot of bridge axial displacement as a function of time for the analysis with creep, shrinkage, cracking, and uniform thermal change. The plot contains the results from the PBEAM analysis superimposed on the free thermal displacements, (the product of the coefficient of thermal expansion, the bridge length, and the change in the effective bridge temperature). The comparison indicates that longitudinal contraction is significantly affected by creep in the girders from prestressing, with the maximum contraction more than doubled as compared to the free thermal displacements. Furthermore, the creep results in the bridge never returned to their original starting position.

The next series of analyses included concrete creep, shrinkage, and cracking with uniform thermal change, but without a connection for positive moment at the piers. Figure C-10 contains a plot of the girder moments from the analysis for the condition of an early-age girder at the time of continuity and a starting temperature of 21 °C (70 °F). The results indicate that once positive-moment cracking occurs at the diaphragm, the moment drop offs to a value of essentially zero without the presence of any positive continuity moment reinforcement at the piers. A plot of deck reinforcement stress (the reinforcement is continuous through the diaphragm joint) in figure C-11 reveals that once positive-moment cracking occurs at the piers, the deck reinforcement attempts to carry the positive secondary continuity moments. However, the deck section alone is very flexible and cannot resist the positive secondary continuity moments that developed. In other words, the stress

in the deck reinforcement is primarily related to a volume-change phenomenon (bowing caused by creep and shrinkage in the girders) and extra reinforcement would not reduce the deck stress. The deck reinforcement strain is a function of the bowing of the beams and is essentially independent of the amount of deck reinforcement. These conclusions were identical for all three starting temperatures.

Analyses were also completed for the condition of late-age girders at the time of continuity. In this instance, relative shrinkage of the deck predominates the response and results in negative continuity moments at the intermediate piers. However, the same conclusions can be drawn for this condition as for the early-age girder analyses: the positive restraint moment at the abutment reaches a maximum value of approximately 610 kN-m (450 kip-ft), the secondary continuity moments resulting from creep and shrinkage at the intermediate piers significantly exceed the moments caused by the abutment end restraint, and concrete creep and cracking did not relieve enough of the axial displacement to prevent the abutment piles from yielding.

C3.2 Composite Steel Bridges

As with the PS/C bridges, the first series of analyses involved cyclic, uniform temperature variations over a 2-year period. The effective bridge temperatures were varied from a maximum of 35 °C (95 °F) in July to a minimum of -29 °C (-21 °F) in January and followed an annual sinusoidal variation between these months. Three different deck casting temperatures (setting temperatures) were used for the starting points of the analyses. These temperatures, 21 °C, 32 °C, and 13 °C (70 °F, 90 °F, and 55 °F), represented average, hot, and cold weather casting conditions, respectively. This first series was also based on a purely elastic analysis and neglected the effects of creep, shrinkage, and cracking. In this way, this series studied the behavior and response of the bridges under uniform temperature variation alone.

Figure C-12 is a plot of bridge axial displacement as a function of time for a starting temperature of 32 °C (90 °F). The plot contains the results from the PBEAM analyses superimposed on the free bridge displacements. The comparison indicates that longitudinal movement of the bridge is essentially unchanged by the abutment and pier restraint as compared to its free displacement. In other words, *the axial stiffness of the bridge cross section significantly exceeds the longitudinal resistance provided by the abutment (and the soil for expansion) and the intermediate piers*. These results were identical for all three starting temperatures.

Figure C-13 is a plot of beam moment at the abutment, first interior support, and second interior support as a function of time for the starting temperature of 32 °C (90 °F). The girder reaches a maximum positive restraint moment of approximately 560 kN-m (410 kip-ft) at the abutment, which corresponds to yielding of the abutment support piles and dragging of the approach slab. This plateau represents an upperbound on the abutment restraint force. Furthermore, this moment is statically determinant and simply equal to the moment and horizontal shear from the abutment piles plus the horizontal shear caused by the frictional resistance of the approach slab, with values calculated at the girder centroid. It should be noted that except for relatively short bridges (total length, not individual span length), thermal movement alone results in yielding of the abutment support piles, even with a lowerbound starting temperature of 13 °C (55 °F).

Figure C-13 also reveals another important aspect about bridge contraction and the positive end-restraint moment provided by the abutment: namely, that the positive end-restraint moment, primarily caused by the eccentricity of the pile from the girder centroid, diminishes rapidly along the bridge length, resulting in a relatively small negative moment at the first interior support.

The next series of analyses included concrete creep, shrinkage, and cracking, but did not include any thermal effects. The concrete creep and shrinkage values were based on ACI 209R-92 equations and relationships applied to the specific bridge cross sections analyzed.[9] Figure C-14 contains a plot of the girder moments from the analysis. In this instance, shrinkage of the deck predominates the response and results in negative continuity moments at the piers. It is important to note three aspects revealed by this plot: (1) The positive restraint moment at the abutment, again, reaches a maximum value of approximately 560 kN-m (410 kip-ft) at the abutment, which corresponds to yielding of the abutment support piles and dragging of the approach slab; (2) The secondary continuity moments resulting from shrinkage at the piers significantly exceed the moments caused by the abutment end restraint, as shown by comparing figures C-13 and C-14; and (3) The concrete creep and cracking did not relieve enough of the axial displacement to prevent the abutment piles from yielding.

C3.3 Reinforced Concrete Bridges

As with the PS/C bridges and the composite steel bridges, the first series of analyses involved cyclic, uniform temperature variations over a 2-year period. The effective bridge temperatures were varied from a maximum of 35 °C (95 °F) in July to a minimum of -29 °C (-21 °F) in January and followed a sinusoidal variation between these months.

Three different casting temperatures (setting temperatures) were used for the starting points of the analyses. These temperatures, 21 °C, 32 °C, and 13 °C (70 °F, 90 °F, and 55 °F), represented average, hot, and cold weather casting conditions, respectively. This first series was also based on a purely elastic analysis and neglected the effects of creep, shrinkage, and cracking. In this way, this series studied the behavior and response of the bridges under uniform temperature variation alone.

Figure C-15 is a plot of bridge axial displacement as a function of time for a starting temperature of 21 °C (70 °F). The plot contains the results from the PBEAM analyses superimposed on the unrestrained bridge displacements. The comparison indicates that longitudinal movement of the bridge is essentially unchanged by the abutment and pier restraint as compared to its free displacement. In other words, the axial stiffness of the bridge cross section significantly exceeds the longitudinal resistance provided by the abutment (and the soil for expansion) and the piers. These results were identical for all three starting temperatures.

Figure C-16 is a plot of girder moment at the abutment, first interior support, and second interior support as a function of time for the starting temperature of 21 °C (70 °F). The girder reaches a maximum positive restraint moment of approximately 405 kN-m (300 kip-ft) at the abutment, which corresponds to yielding of the abutment support piles and dragging of the approach slab. This plateau represents an upperbound on the abutment restraint force. Furthermore, this moment is statically determinant and simply equal to the moment and horizontal shear from the abutment piles plus the horizontal shear resulting from the frictional resistance of the approach slab, with values calculated at the girder centroid. It should be noted that except for relatively short bridges (total length, not individual span length), thermal movement alone results in yielding of the abutment support piles, even with a lowerbound starting temperature of 13 °C (55 °F).

Figure C-16 also reveals another important aspect of bridge contraction and the positive end-restraint moment provided by the abutment: namely, that the positive end-restraint moment, primarily caused by the eccentricity of the pile from the girder centroid, diminishes rapidly along the bridge length, resulting in a relatively small negative moment at the first interior support.

The next series of analyses included concrete creep, shrinkage, and cracking, but did not include any thermal effects. The concrete creep and shrinkage values were based on ACI 209R-92 equations and relationships applied to the specific bridge cross sections analyzed.[8] Figure C-17 contains a plot of the girder moments from the analysis.

The reinforced concrete bridge modeled for these analyses was a concrete box girder bridge similar to the bridge shown on Sheet Nos. 301 through 305 of Vol. IV of the standard plans.[2] Because the box section has a 203-mm- (8-inch) thick top flange and a 152-mm- (6-inch) thick bottom flange, the volume-to-surface ratio is higher in the top flange. Therefore, using the coefficients from ACI 209R-92,[8] the top flange has less shrinkage than the bottom flange. This differential relative shrinkage within the cross section causes positive moments at the interior supports. The restraint from the abutment pile to the overall shortening of the bridge resulting from the shrinkage causes positive moment at the abutment, a smaller negative moment at the first interior support, and a smaller yet positive moment at the second interior support. The data plotted in figure C-17 superimposed the moments caused by the relative shrinkage in the cross section onto the moments caused by abutment restraint. Because the bridge is not PS/C, the only creep strains involved are the creep strains in response to stresses caused by the shrinkage strains.

Based on the plot, it is evident that for this bridge type, secondary continuity moments at piers, caused by relative shrinkage within the cross section, are relatively minor and are on the same order of magnitude as moments caused by abutment end restraint. Furthermore, the positive restraint moment at the abutment again reaches a maximum value of approximately 405 kN-m (300 kip-ft) at the abutment, which corresponds to yielding of the abutment support piles and dragging of the approach slab. Concrete creep and cracking did not relieve enough of the axial displacement to prevent the abutment piles from yielding.

C4 REFERENCES

1. Musser, S.C., CANDE-89 User Manual, Report No. FHWA-RD-89-169, FHWA, McLean, VA, 1989, 236 pp.

2. Oesterle, R.G.; Refai, T.M.; Volz, J.S.; Scanlon, A.; and Weiss, W.J., *Jointless Bridges, Analytical Research and Proposed Design Procedures*, Volume II, Final Report to FHWA, February 2005.

3. FHWA, *Standard Plans for Highway Bridges, Vols. IV, 1975 Edition, and IV(A), 1984 Edition*, Washington, DC.

4. Suttikan, C., *A Generalized Solution for Time-Dependent Response and Strength of Noncomposite and Composite Prestressed Concrete Beams*, Ph.D. Dissertation, University of Texas at Austin, 1978, 350 pp.

5. Hays, C.A., and Matlock, H., "A Nonlinear Analysis of Statically Loaded Plane Frames Using a Discrete Element Model," *Research Report No. 56-23*, Center of Highway Research, The University of Texas, Austin, TX, May 1972.

6. Oesterle, R.G., et al., *Design of Precast Prestressed Bridge Girders Made Continuous*, NCHRP Report 322, Transportation Research Board, Washington, DC, November 1989, 97 pp.

7. Mattock, A.H., "Precast-Prestressed Concrete Bridge 5, Creep and Shrinkage Studies," *Journal of the PCA Research and Development Laboratories*, Vol. 3, No. 2, May 1961, pp. 32–66. Reprinted as PCA Bulletin D46.

8. Girton, D.D., et al., *Validation of Design Recommendations for Integral-Abutment Piles*, Iowa DOT Research Project HR-292, Iowa State University, College of Engineering, September 1989.

9. American Concrete Institute, Committee 209, *Prediction of Creep, Shrinkage, and Temperature Effects in Concrete Structures*, ACI 209R-92, Detroit, MI, 1992, 47 pp.

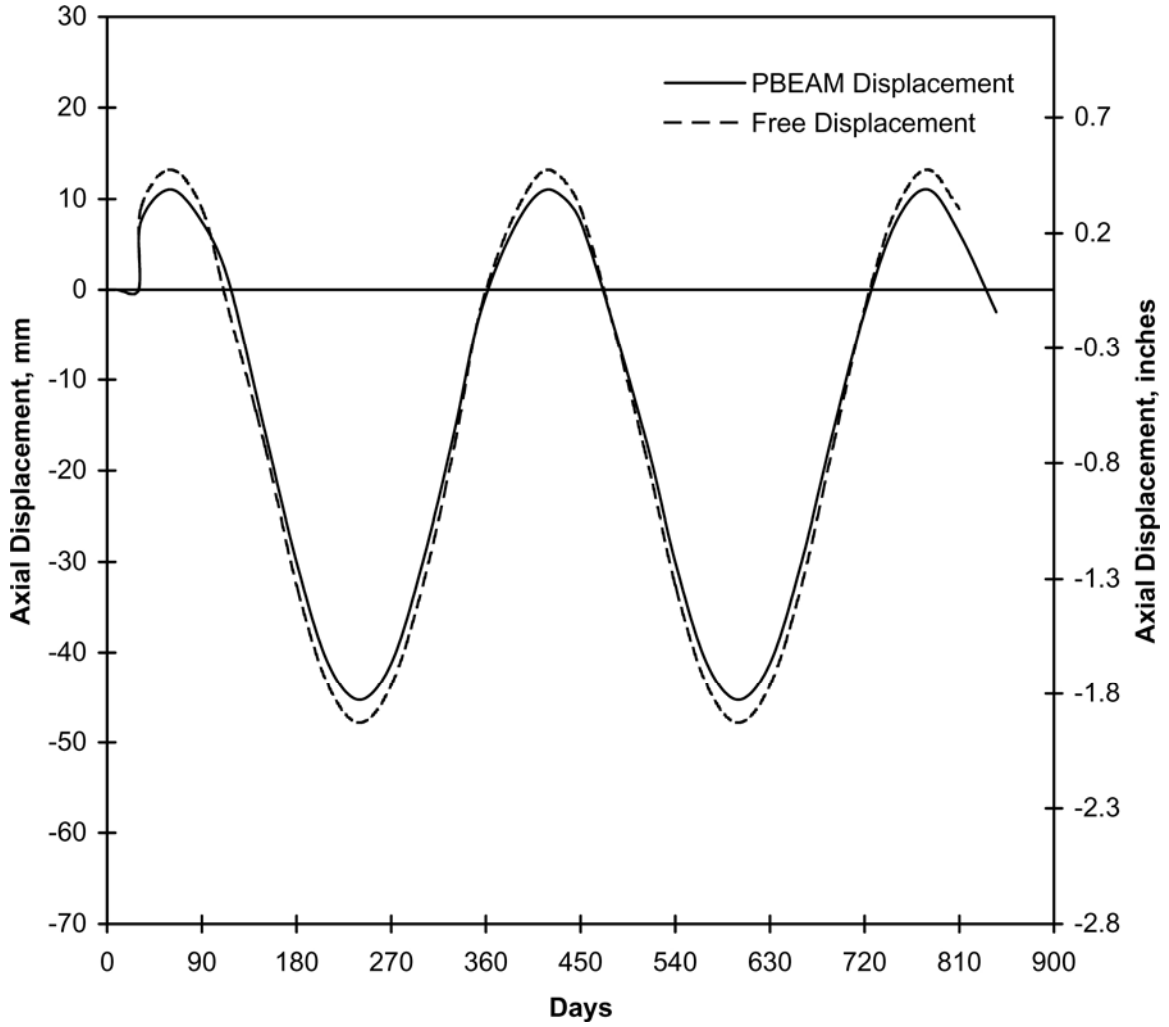

Figure C-1. Prestressed concrete bridge, axial displacement, bridge cast at 21 °C (70 °F).

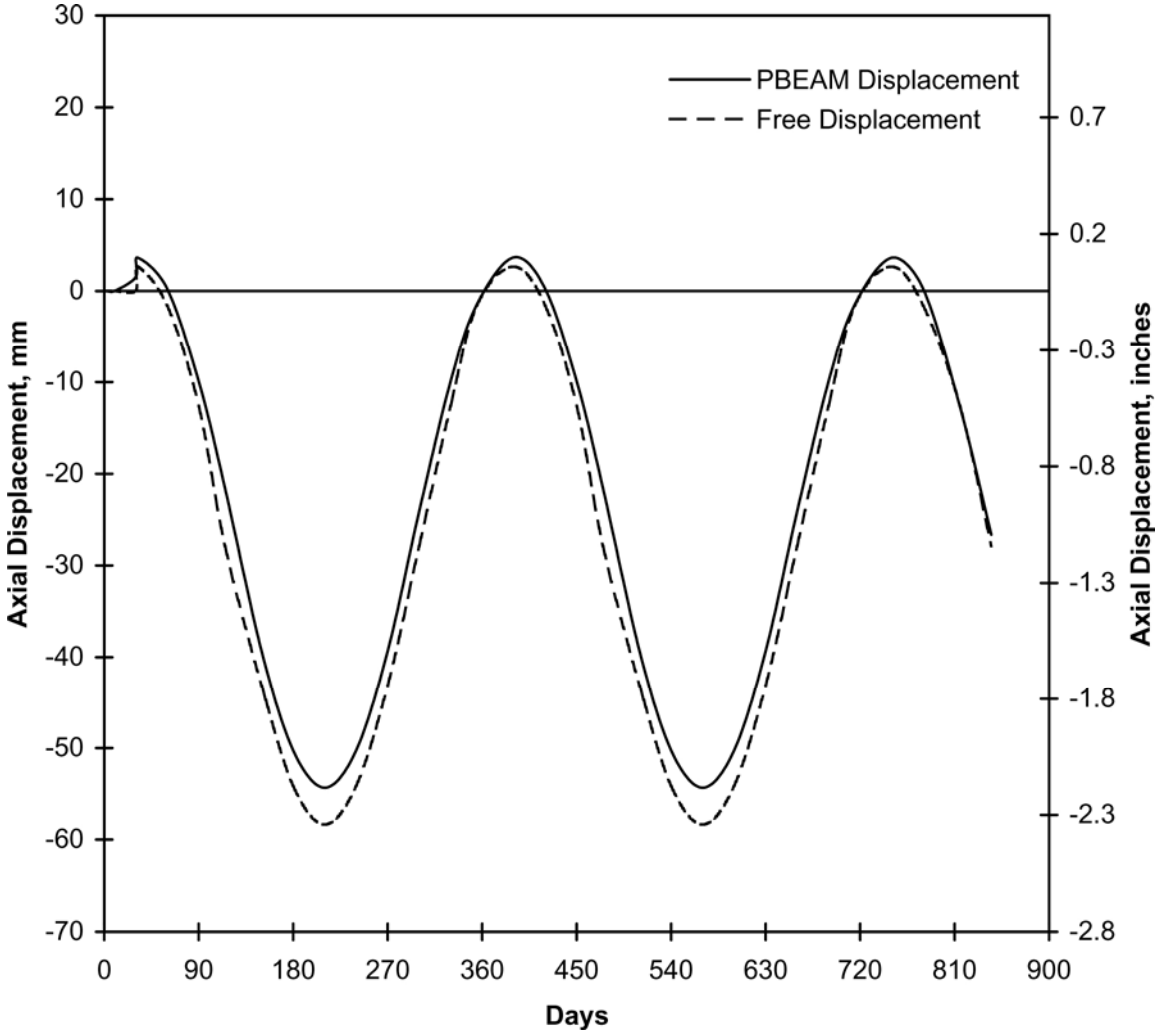

Figure C-2. Prestressed concrete bridge, axial displacement, bridge cast at 32 °C (90 °F).

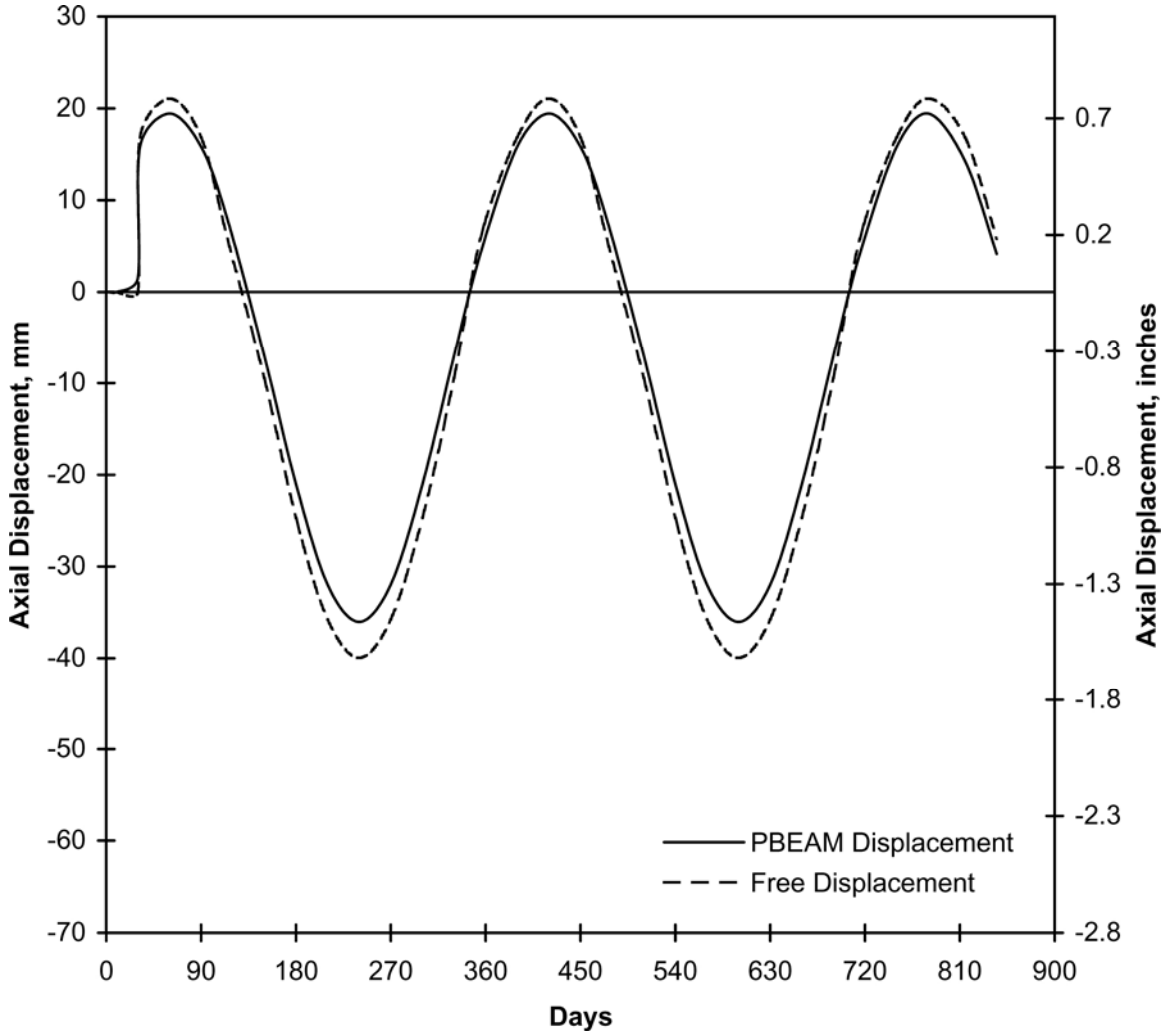

Figure C-3. Prestressed concrete bridge, axial displacement, bridge cast at 13 °C (55 °F).

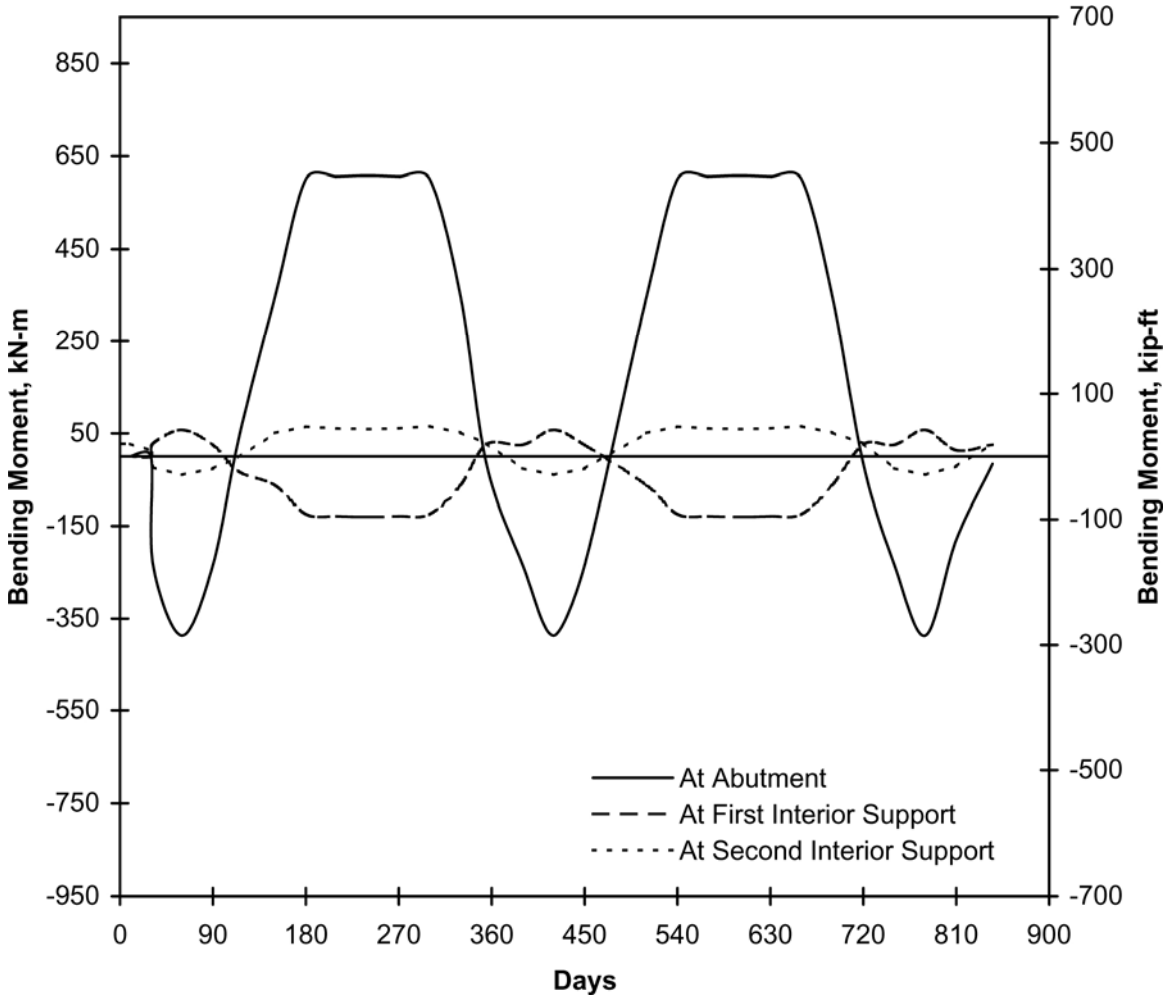

Figure C-4. Prestressed concrete bridge, girder moment, bridge cast at 21 °C (70 °F), thermal elastic analysis.

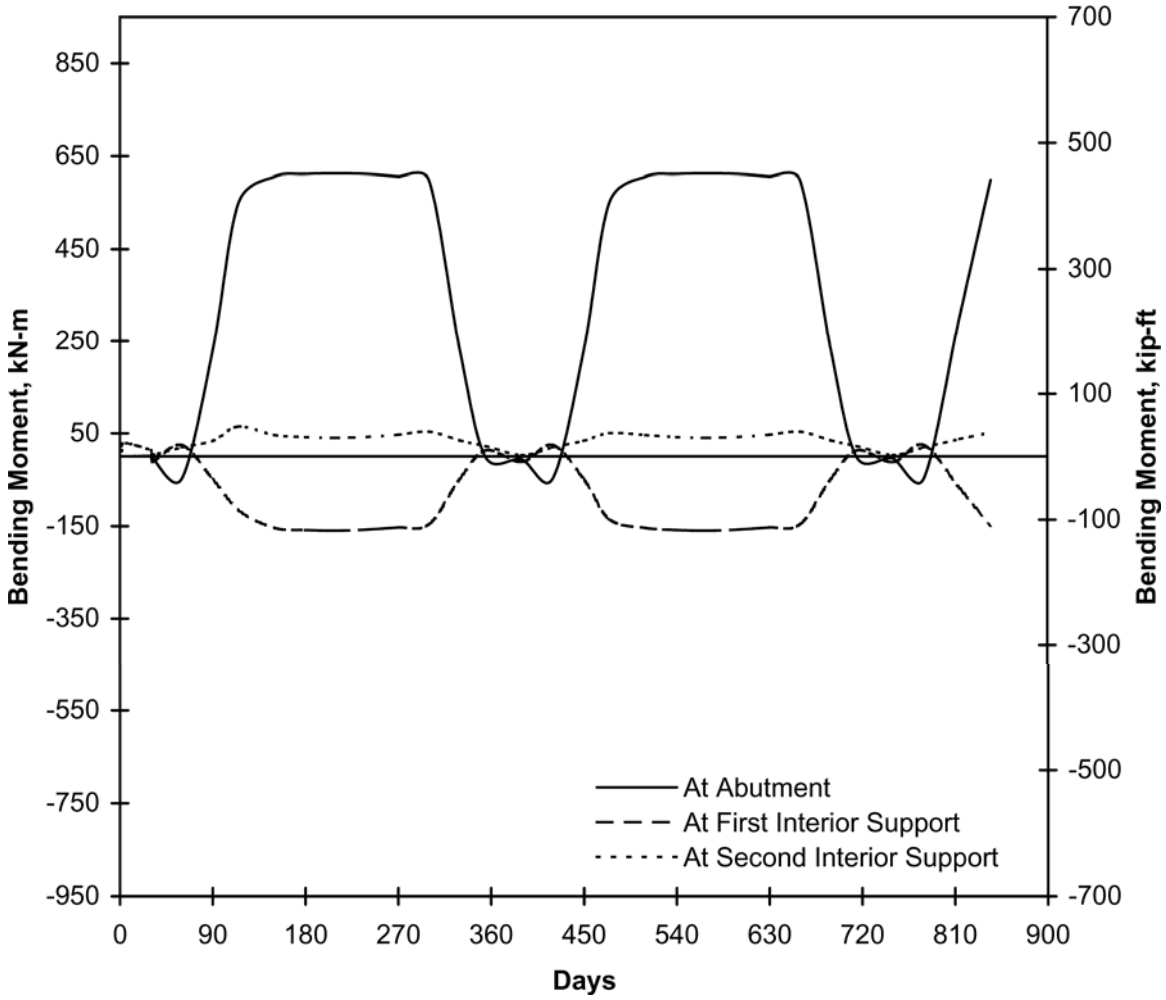

Figure C-5. Prestressed concrete bridge, girder moment, bridge cast at 32 °C (90 °F), thermal elastic analysis.

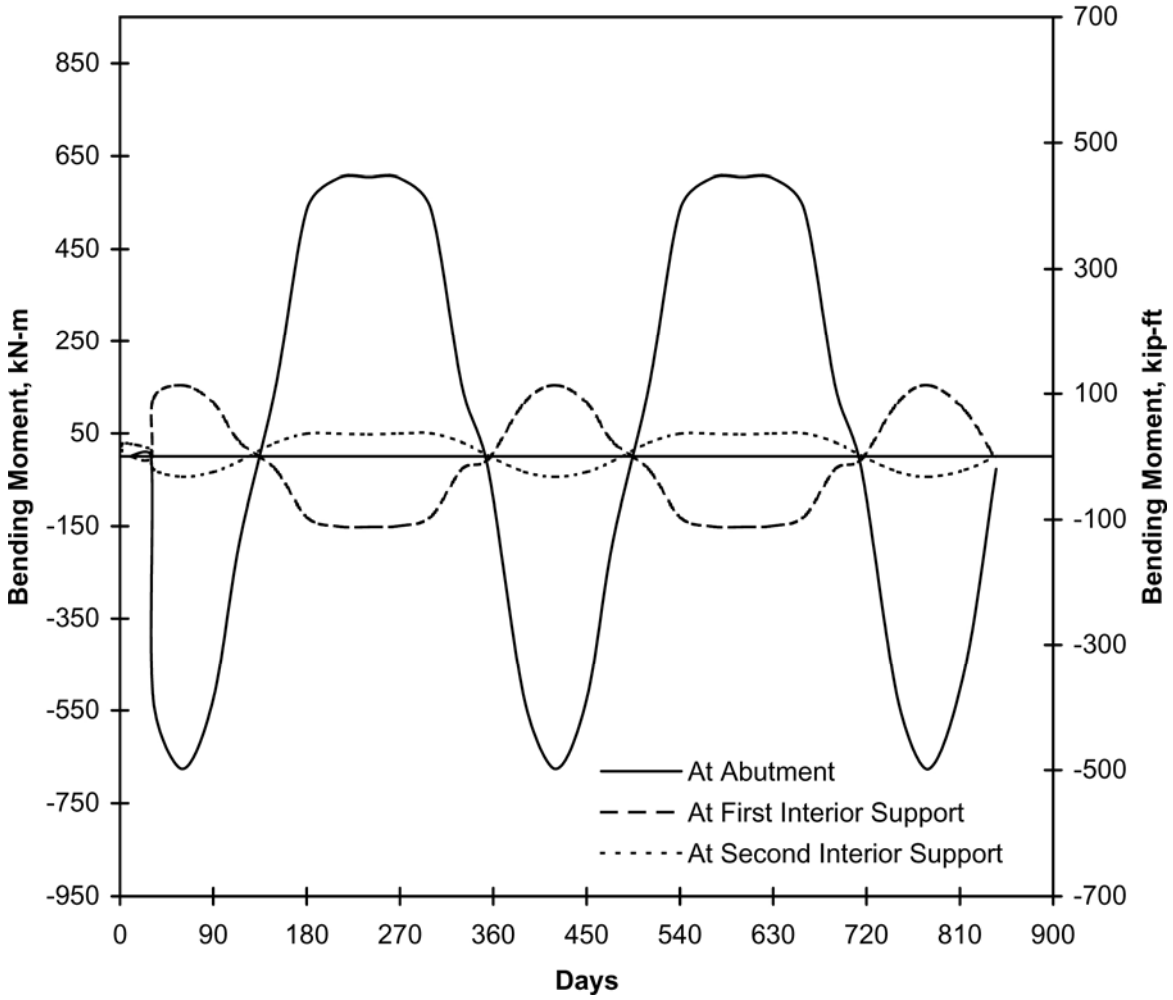

Figure C-6. Prestressed concrete bridge, girder moment, bridge cast at 13 °C (55 °F), thermal elastic analysis.

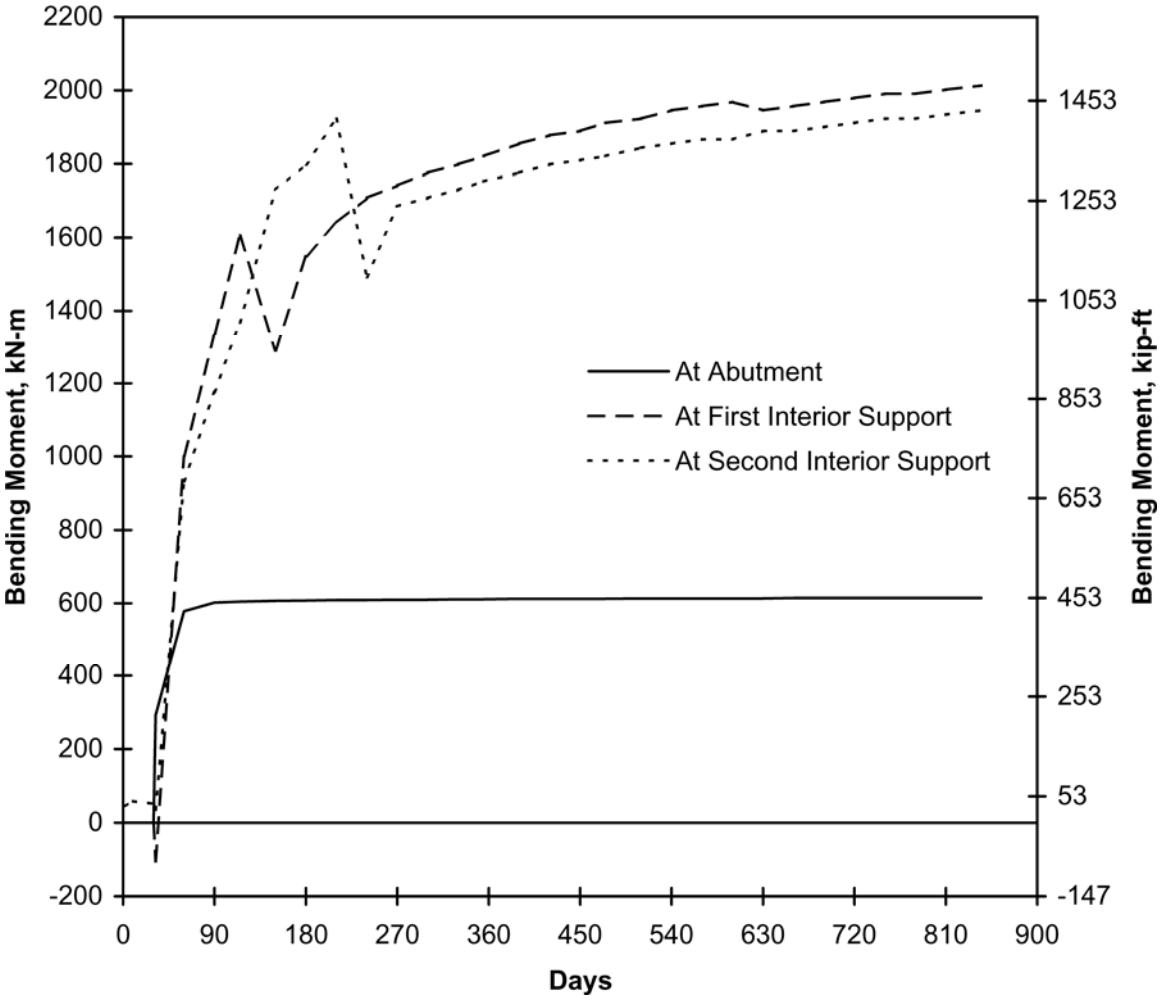

Figure C-7. Prestressed concrete bridge, girder moment, analysis for creep, shrinkage, and cracking.

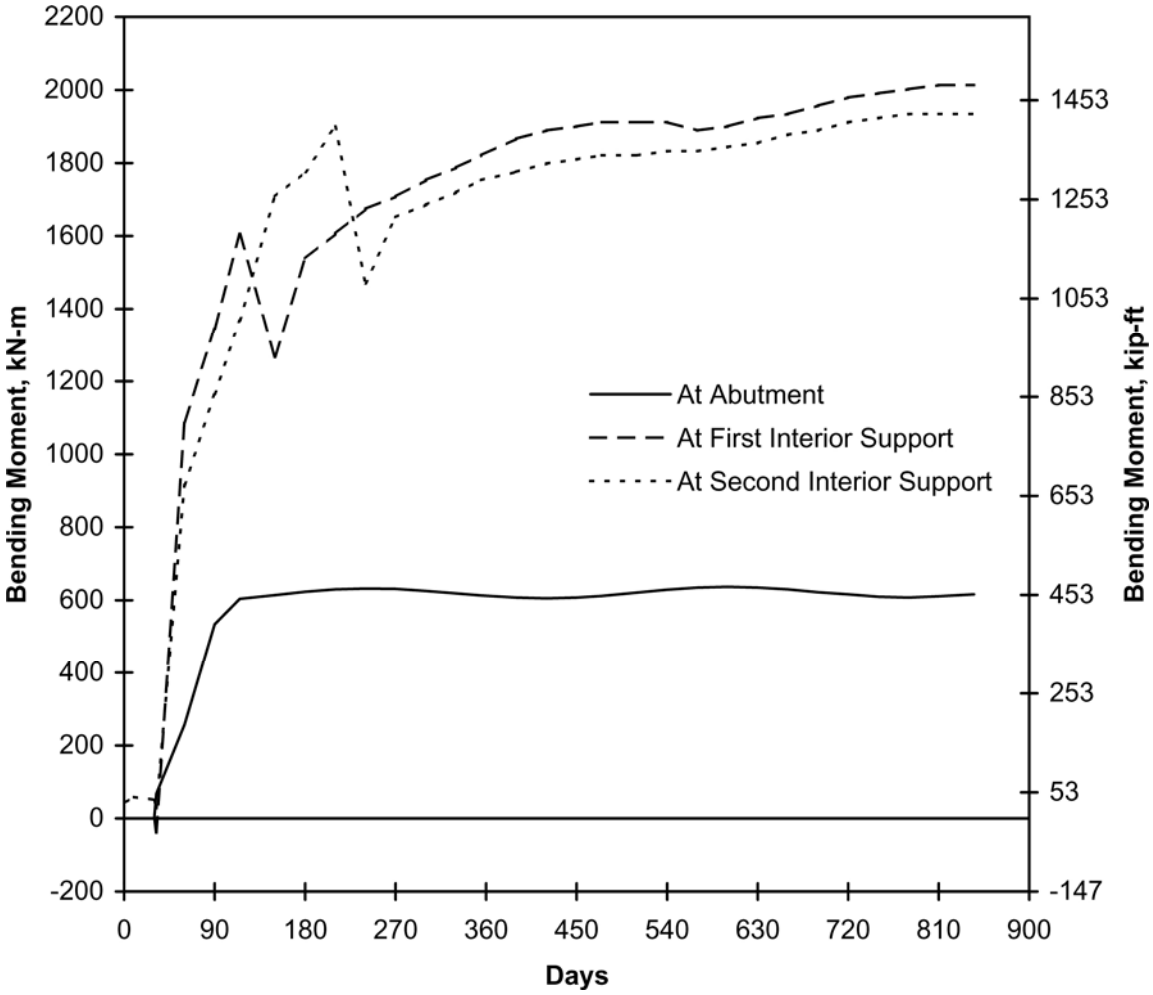

Figure C-8. Prestressed concrete bridge, girder moment, analysis for creep, shrinkage, cracking, and thermal effects, bridge cast at 21 °C (70 °F).

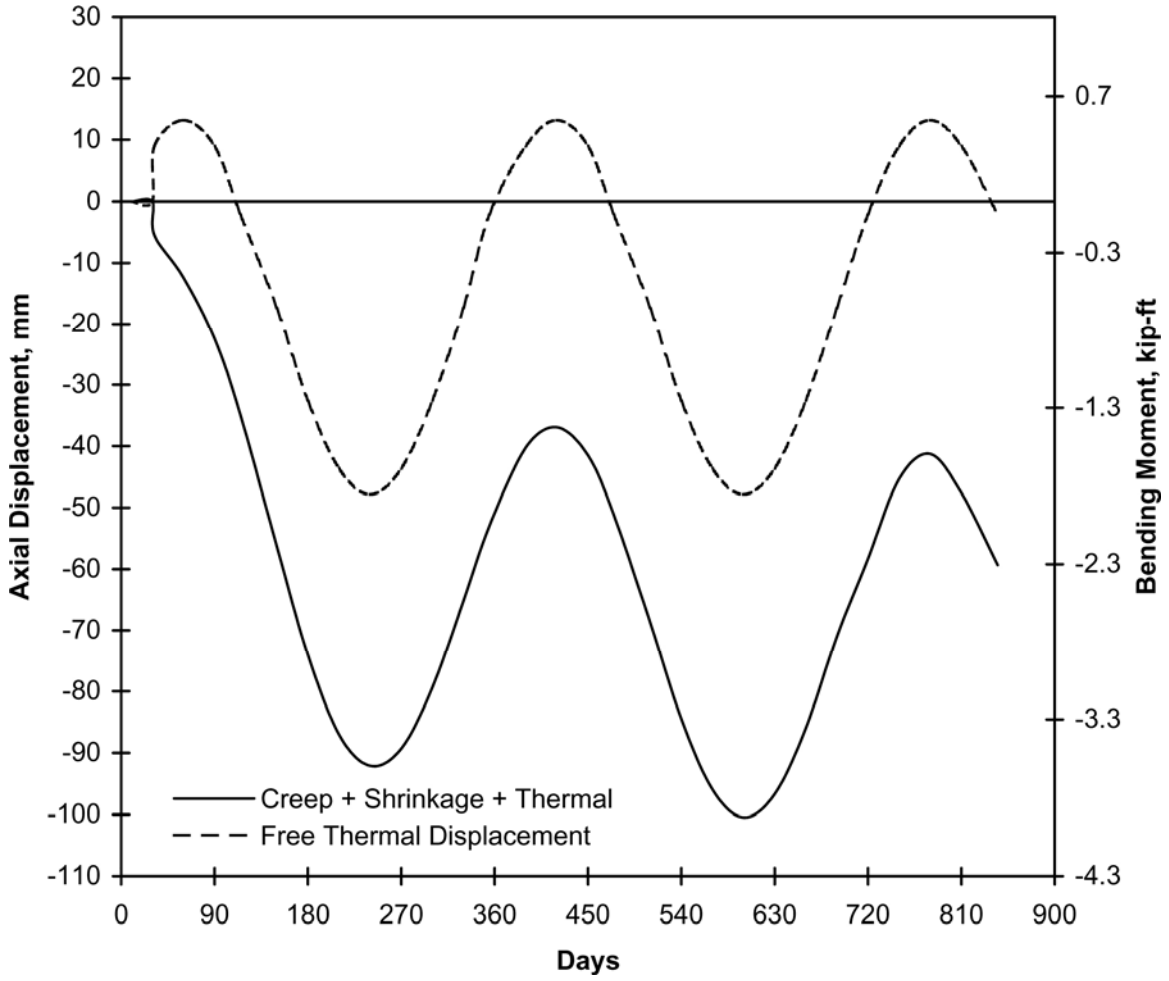

Figure C-9. Prestressed concrete bridge, axial displacement, analysis for creep, shrinkage, cracking, and thermal effects, bridge cast at 21 °C (70 °F).

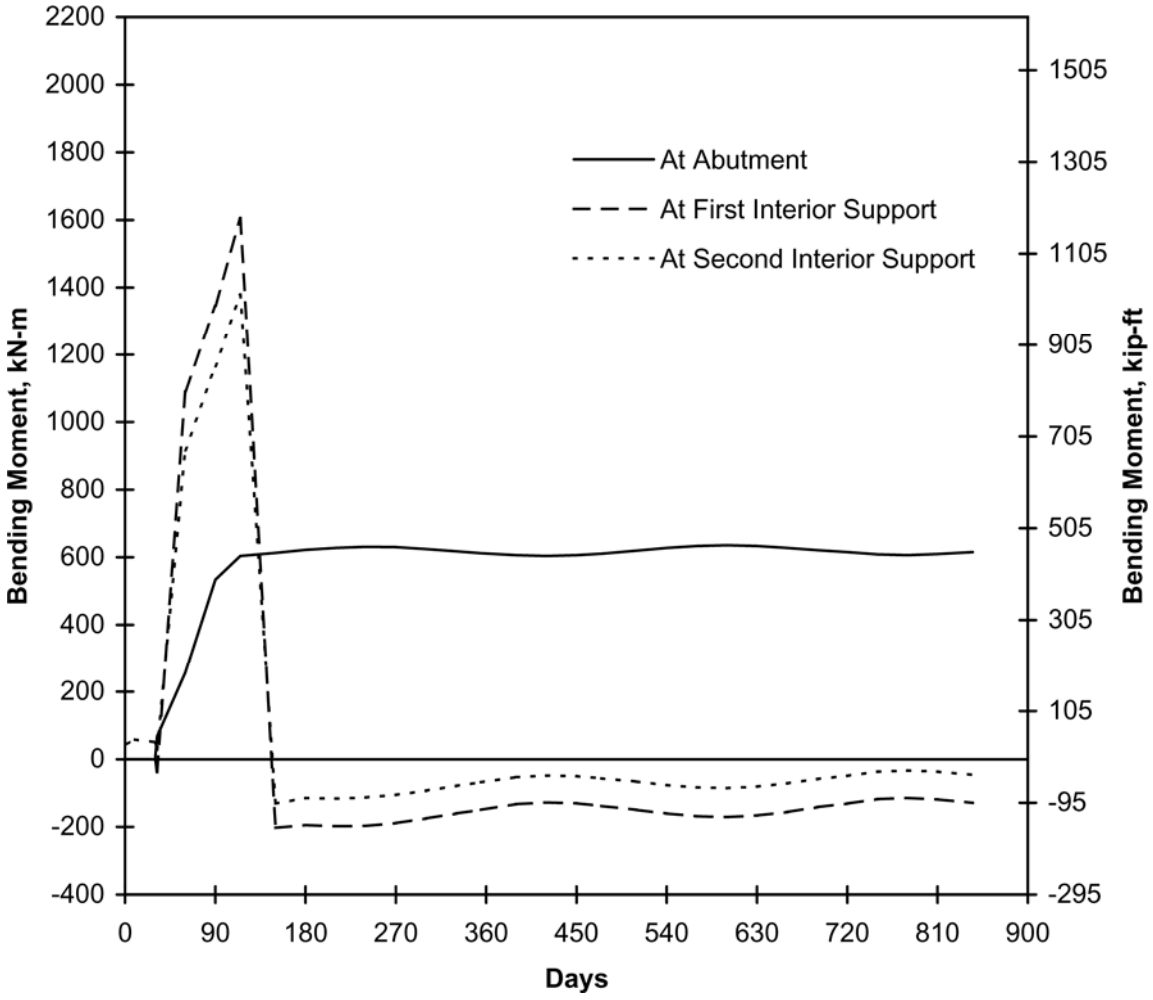

Figure C-10. Prestressed concrete bridge, girder moment, analysis for creep, shrinkage, cracking, and thermal effects without positive-moment connection at piers, bridge cast at 21 °C (70 °F).

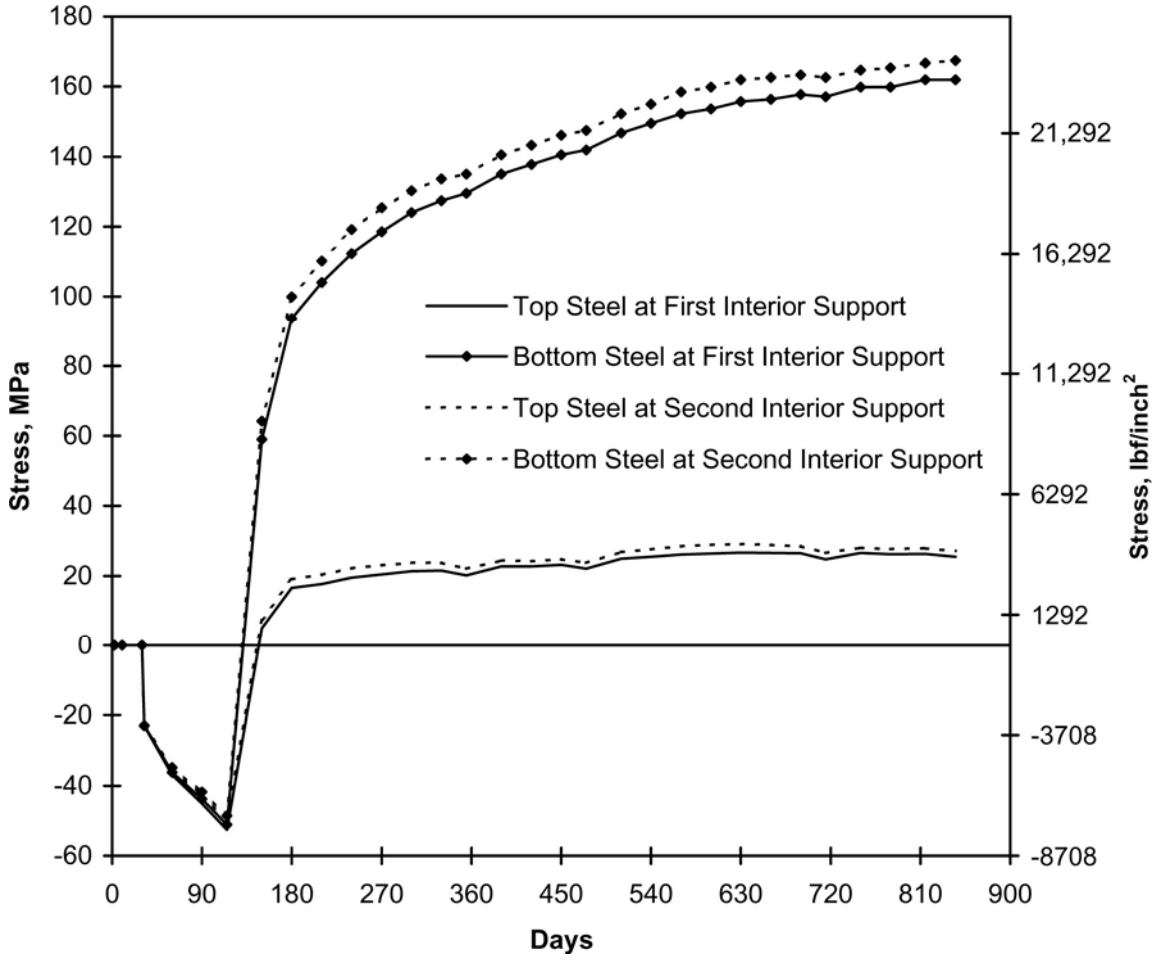

Figure C-11. Prestressed concrete bridge, deck reinforcement stress, analysis without positive-moment connection at piers.

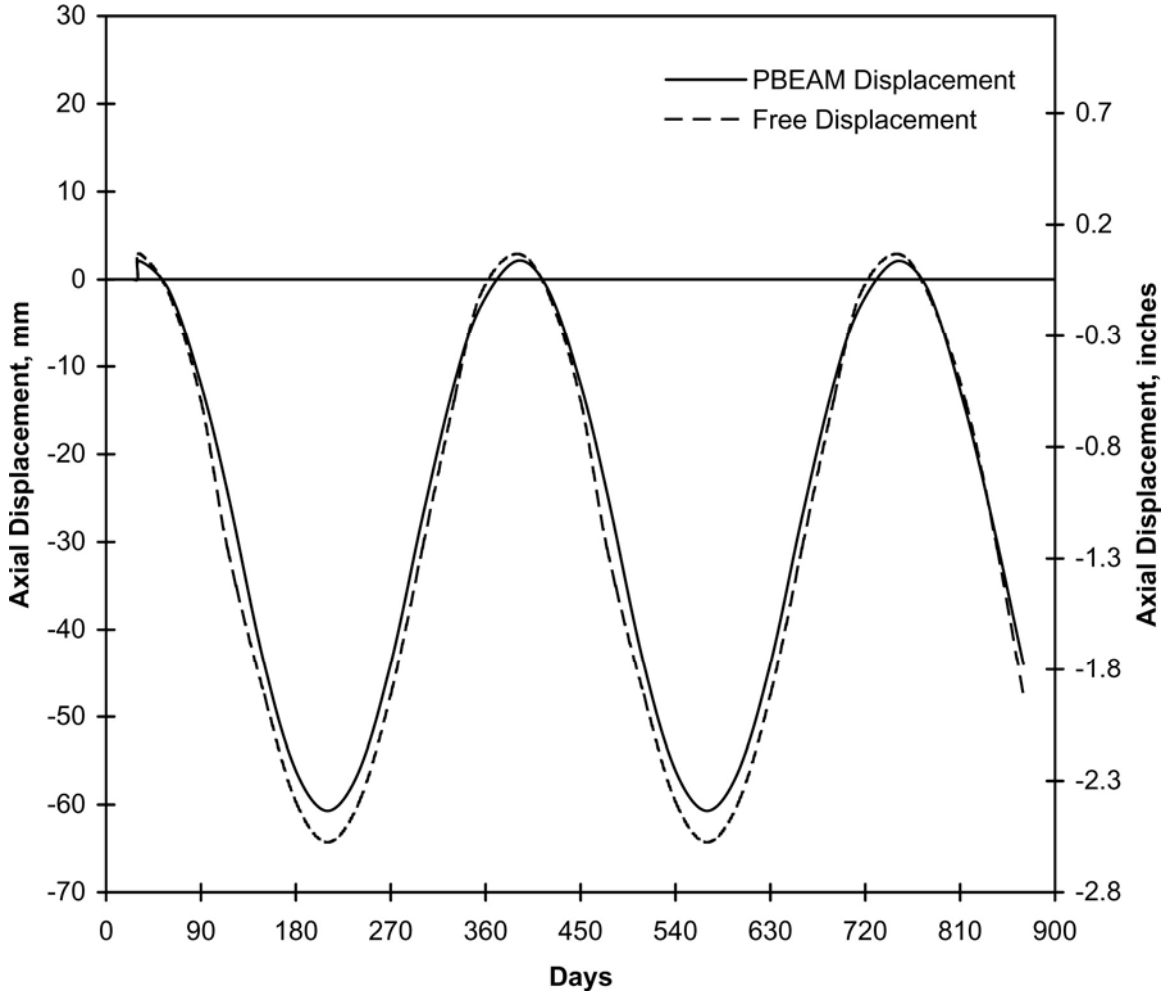

Figure C-12. Composite steel bridge, axial displacement, bridge cast at 32 °C (90 °F).

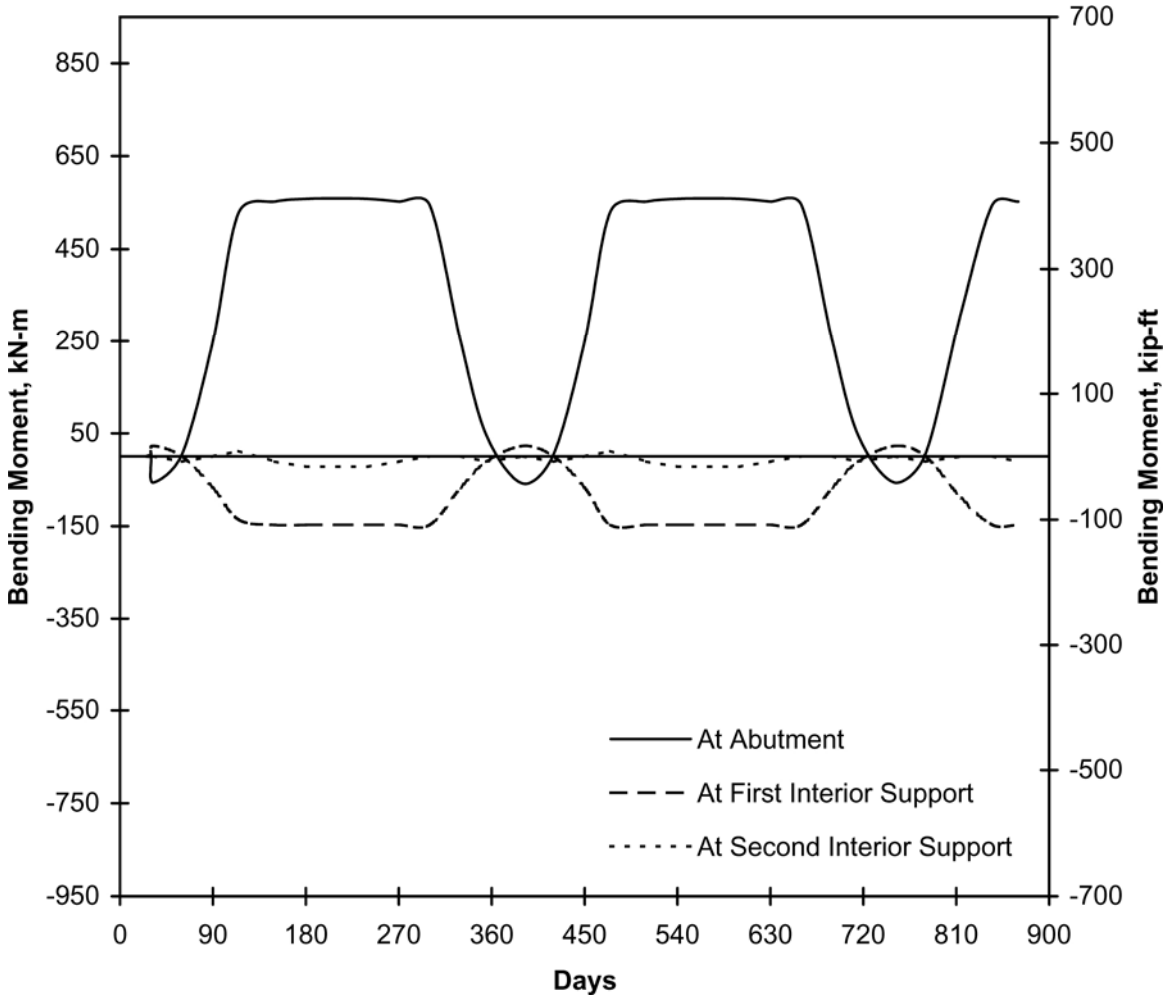

Figure C-13. Composite steel bridge, girder moment, bridge cast at 32 °C (90 °F), thermal elastic analysis.

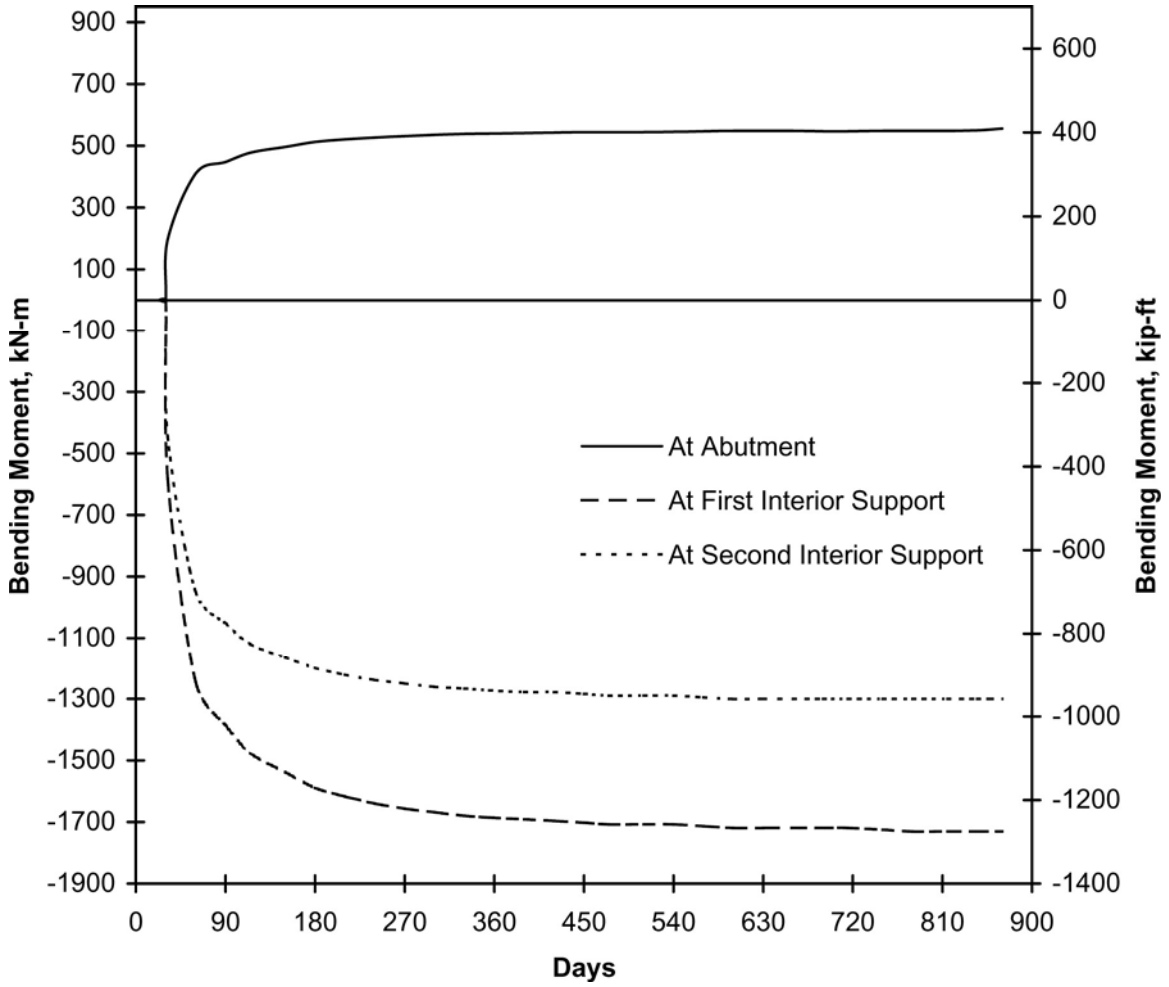

Figure C-14. Composite steel bridge, girder moment, analysis for creep, shrinkage, and cracking.

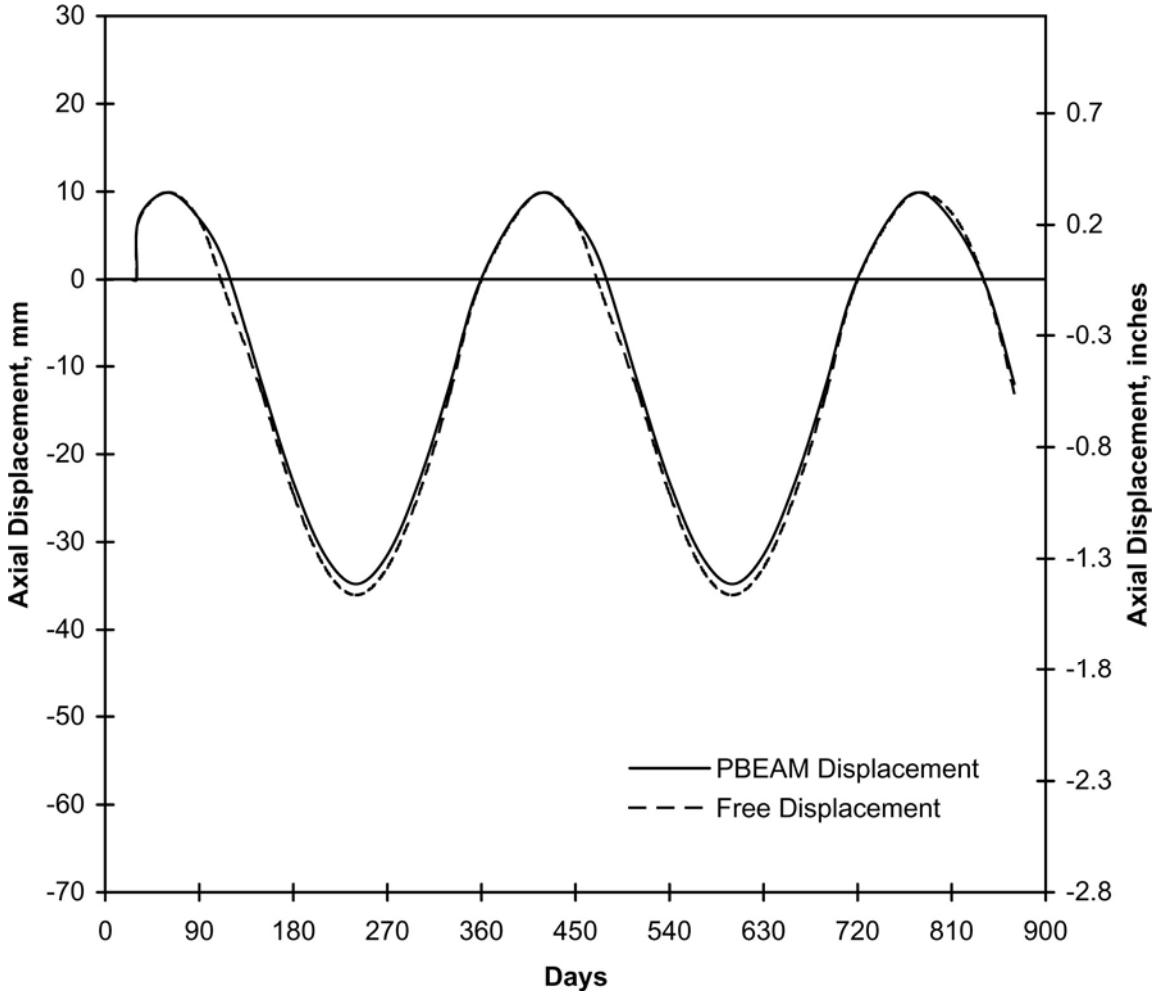

Figure C-15. Reinforced concrete bridge, axial displacement, bridge cast at 21 °C (70 °F).

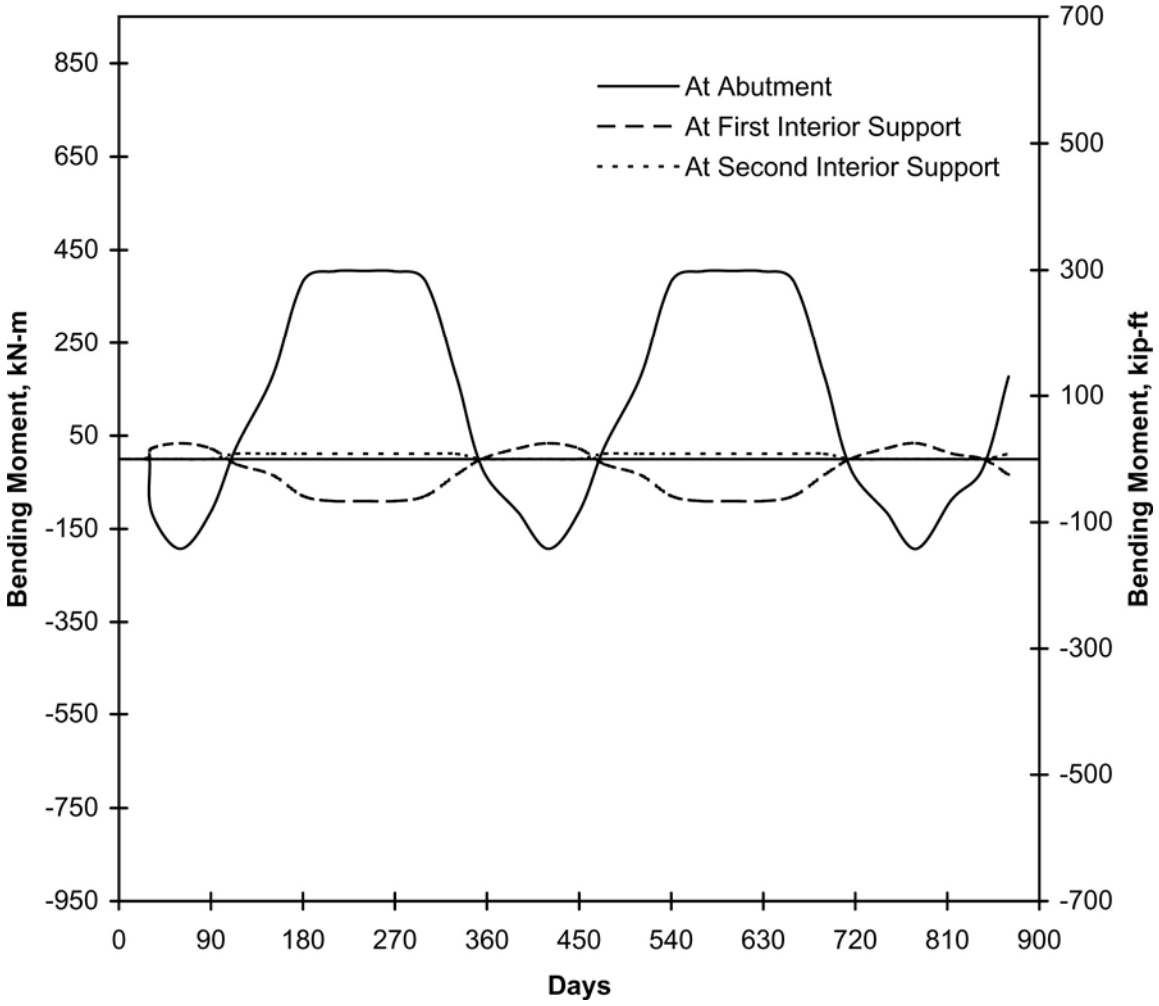

Figure C-16. Reinforced concrete bridge, girder moment, bridge cast at 21 °C (70 °F), thermal elastic analysis.

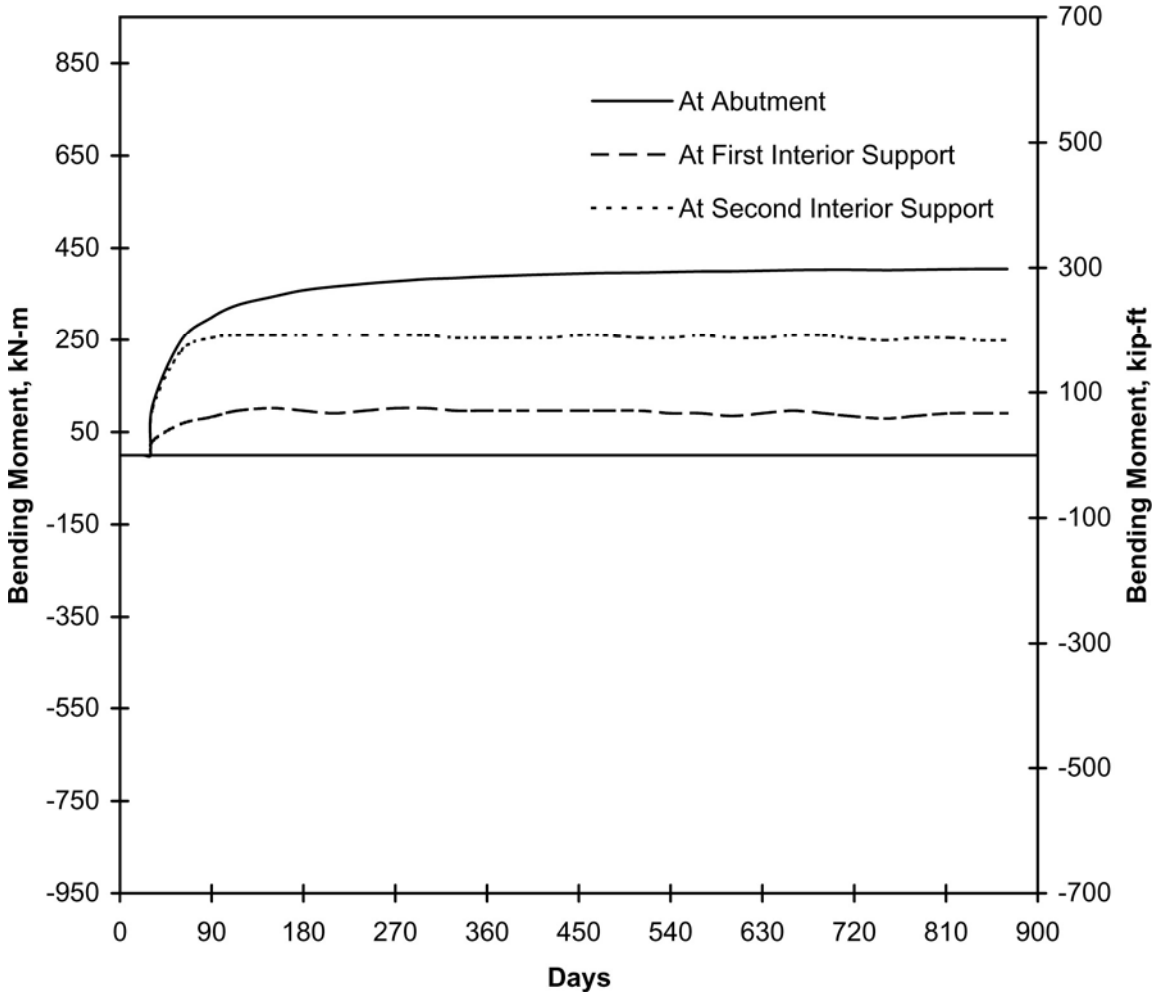

Figure C-17. Reinforced concrete bridge, girder moment, analysis for creep, shrinkage, and cracking.

APPENDIX D. DERIVATION OF SECONDARY CONTINUITY EQUATIONS

This appendix contains derivations of the equations used for studying the effects of secondary continuity forces on continuous jointless bridges.

D1 BRANSON EQUATIONS

Deck and beam stresses can be calculated for the condition of a uniform inelastic strain in the deck from equations developed by Branson.[1] The equations are applicable to a simply supported beam and include the eigenstress component. Referred to as the composite section method, the equations consist of the following:

$$f_c = -\left[\frac{Q}{A'} + \frac{Qe}{S'_c}\right]\frac{1}{n} + E_c\varepsilon_f \tag{D-1}$$

$$f_s = -\frac{Q}{A'} + \frac{Qe}{S'_s} \tag{D-2}$$

where,

f_c = stress in the top of the deck

f_s = stress in the bottom of the beam

Q = $E_c A_{deck} \varepsilon_f$

E_c = deck modulus of elasticity

A_{deck} = cross-sectional area of the deck

ε_f = free strain in the deck caused by the negative thermal gradient, shrinkage, heat of hydration, etc.

n = E_s/E_c, modular ratio

E_s = girder modulus of elasticity

A' = composite cross-sectional area with deck transformed to equivalent girder material

S'_c = composite section modulus to the top of the deck with deck transformed to equivalent girder material

S'_s = composite section modulus to the bottom of the girder with deck transformed to equivalent girder material

e = distance from deck centroid to composite centroid.

Equations D-1 and D-2 can be modified to calculate the girder stress when the deck just reaches the cracking stress by dividing equation D-1 by E_c to obtain the final deck strain, setting this value equal to the cracking strain, and solving for ε_f as:

$$\varepsilon_f = \frac{\varepsilon_{cr}}{\left[1 - \frac{A_{deck}}{nA'} - \frac{A_{deck}e}{nS'_c}\right]} \quad \text{(D-3)}$$

where,

ε_{cr} = cracking strain in the deck, equal to 0.62 $\sqrt{f'_c}$ / E_c, MPa (7.5 $\sqrt{f'_c}$ / E_c, lbf/inch^2).

The girder stress at cracking of the deck is then calculated from equation D-2.

However, equations D-2 and D-3 need to be modified to include the continuity effects for multispan conditions. The calculation of the continuity effects as a function of bridge cross section and the number and relative length of each span comprising the bridge is discussed in detail in section 8.4.1. Applying those relationships to equations D-2 and D-3 by modifying the restraint term to include a continuity moment term results in the following equations:

$$\varepsilon_f = \frac{\varepsilon_{cr}}{\left[1 - \frac{A_{deck}}{nA'} + m\left(\frac{A_{deck}e}{nS'_c}\right)\right]} \quad \text{(D-4)}$$

$$f_s = -\frac{E_c A_{deck}\varepsilon_f}{A'} - m\left(\frac{E_c A_{deck}\varepsilon_f e}{S'_s}\right) \quad \text{(D-5)}$$

where,

m = support condition multiplier, equal to 0.5 for two spans, 0.2 for three spans, 0.27 at the first interior support of a multispan beam, and 0.0 at all other interior supports.

All other variables are as previously defined.

D2 COMPOSITE STEEL BEAM EQUATIONS

Equations D-4 and D-5 assume the deck just reaches the cracking strain, but has not yet cracked. Therefore, relationships similar to equations D-4 and D-5 were derived to calculate the steel-beam stress resulting from the secondary effects after cracking has occurred in a portion of the deck. The following assumptions were included in the derivation:

1. Cracking in the deck extends one-quarter of the span length from each pier.
2. Deck reinforcement at the pier is equal to the AASHTO minimum requirement of 1 percent.
3. Fifty percent of the inelastic strain in the deck is caused by the thermal effects, with shrinkage accounting for the remaining inelastic strain.

The revised relationship is derived for the two-span beam shown in figure D-1(a). First, the center support is removed (figure D-1[b]), and the internal restraint forces are calculated in a procedure similar to Branson's. The deck is released from the girder and allowed to contract. The force required to pull the deck back and restore compatibility is then applied to the composite section. For Section 1 (the cracked deck portion), any tension stiffening will be minimal and the stiffness of the deck can be represented by the reinforcement alone ($A_s = 0.01\ A_{deck}$ for 1 percent reinforcement). Also, in the cracked deck section, the ε_f resulting from shrinkage does not have to be restored because it is relieved by the cracking; only that portion of ε_f caused by the thermal gradients needs to be restored. Therefore, the force required to restore compatibility in Section 1 becomes:

$$\begin{aligned} Q_1 &= A_s E_s (0.5\ \varepsilon_f) \\ &= (0.01 A_{DECK})\ E_s\ (0.5 \varepsilon_f) \\ &= 0.005\ A_{DECK}\ E_s \varepsilon_f \end{aligned} \qquad \text{(D-6)}$$

This force is then applied to the composite section for Section 1 to calculate the stress in the girder bottom flange as:

$$f_{s_1} = -\frac{Q_1}{A'_1} + \frac{Q_1 e_1}{S'_{s_1}} \tag{D-7}$$

The restraint moment equals $Q_1 e_1$. For section 2, the equations are identical to equations D-2 and D-3, and the restraint moment equals $Q_2 e_2$.

The next step is to restore the center redundant support. The deflection resulting from bowing of the girder caused by the deck inelastic strains can be calculated from the conjugate beam method. This deflection is equal to the moment from the M/EI diagram shown in figure D-1(c). Let $\phi_1 = Q_1 e_1 / E_s I'_1$ and $\phi_2 = Q_2 e_2 / E_s I'_2$, and this deflection becomes:

$$\Delta_1 = \frac{7\phi_1 L^2}{128} + \frac{9\phi_2 L^2}{128} \tag{D-8}$$

which is reduced to the typical value of $\phi L^2/8$ in the case of no cracking. To restore the redundant support, the deflection resulting from a concentrated load at midspan can also be calculated from the conjugate beam method and the M/EI diagram shown in figure D-1(d) as:

$$\Delta_2 = \frac{37PL^3}{3072 E_s I'_1} + \frac{27PL^3}{3072 E_s I'_2} \tag{D-9}$$

which is reduced to the typical value of $PL^3/48EI$ in the case of no cracking.

Set the two deflections equal to solve for the center reaction, P, as:

$$P = \frac{24(7\phi_1 + 9\phi_2)}{L\left(\frac{37}{E_s I'_1} + \frac{27}{E_s I'_2}\right)} \tag{D-10}$$

Then, the moment at the pier is equal to PL/4 or:

$$M_{pier} = 6(7\phi_1 + 9\phi_2) / \left(\frac{37}{E_s I_1'} + \frac{27}{E_s I_2'} \right) \tag{D-11}$$

The total stress in the beam is then equal to the internal restraint stress plus the continuity moment stress, or:

$$f_{s_1} = -\frac{Q_1}{A_1'} + \frac{Q_1 e_1}{S_{s_1}'} - \frac{M_{pier}}{S_{s_1}'} \tag{D-12}$$

where,

ε_f = free strain in the deck required to initiate cracking, caused by negative thermal gradient, shrinkage, heat of hydration, etc.

f_{s_1} = stress in the beam at the pier (a negative value indicates compression)

ε_{cr} = cracking strain in the deck, equal to 0.62 $\sqrt{f'_c}/E_c$, MPa (7.5 $\sqrt{f'_c}/E_c$, lbf/inch^2)

n = E_s/E_c, modular ratio

E_s = girder modulus of elasticity

E_c = deck modulus of elasticity

A_{deck} = cross-sectional area of the deck

A_1' = cross-sectional area of the beam and deck composite steel section

I_1' = moment of inertia for beam and deck composite steel section

S_{s_1}' = section modulus to bottom of the beam for beam and deck composite steel section

e_1 = distance from deck steel centroid to centroid of beam and deck composite steel section

A_2' = cross-sectional area of composite section with deck transformed to equivalent beam material

I_2' = moment of inertia for composite section with deck transformed to equivalent beam material

S'_{c_2} = section modulus to top of deck for composite section with deck transformed to equivalent beam material

S'_{s_2} = section modulus to bottom of beam for composite section with deck transformed to equivalent beam material

e_2 = distance from deck centroid to centroid of composite section with deck transformed to equivalent beam material.

$$M_{pier} = 6\,(7\phi_1+9\phi_2) \Big/ \left(\frac{37}{E_s I'_1}+\frac{27}{E_s I'_2}\right)$$

$\phi_1 = Q_1 e_1 / E_s I'_1$

$Q_1 = 0.005\, n A_{deck}\, E_c \varepsilon_f$

$\phi_2 = Q_2 e_2 / E_s I'_2$

$Q_2 = A_{deck}\, E_c\, \varepsilon_f$

D3 PRESTRESSED CONCRETE BEAM EQUATIONS

The only variation for the prestressed concrete beams is that the deck reinforcement stress is calculated instead of the bottom flange stress. Therefore, the equations are identical except for the addition of another term to account for the tension force applied to the deck reinforcement to restore compatibility, Q_1/A_s. As a result, the equations become:

$$\varepsilon_f = \frac{\varepsilon_{cr}}{\left[1-\frac{A_{deck}}{n A'_2}+0.5\left(\frac{A_{deck} e_2}{n S'_{c_2}}\right)\right]} \tag{D-13}$$

$$f_{s_1} = \frac{Q_1}{A_s}-\frac{Q_1}{A'_1}-\frac{Q_1 e_1}{S'_{s_1}}+\frac{M_{pier}}{S'_{s_1}} \tag{D-14}$$

where,

ε_f = free strain in the deck required to initiate cracking, caused by negative thermal gradient, shrinkage, heat of hydration, etc.

f_{s_1} = stress in the deck reinforcement at the pier (a positive value indicates tension)

ε_{cr} = cracking strain in the deck, equal to $0.62\sqrt{f'_c}/E_c$, MPa ($7.5\sqrt{f'_c}/E_c$, lbf/inch^2)

n = E_s/E_c, modular ratio

E_s = deck reinforcement modulus of elasticity

E_c = deck concrete modulus of elasticity

A_{deck} = cross-sectional area of the deck concrete

A_s = cross-sectional area of the deck reinforcement

A'_1 = cross-sectional area of the girder and deck reinforcement composite section with girder transformed to equivalent deck steel material

I'_1 = moment of inertia for girder and deck reinforcement composite section with girder transformed to equivalent deck steel material

S'_{s_1} = section modulus to deck reinforcement for girder and deck reinforcement composite section with girder transformed to equivalent deck steel material

e_1 = distance from deck reinforcement centroid to centroid of girder and deck reinforcement composite section with girder transformed to equivalent deck steel material

A'_2 = cross-sectional area of the girder and concrete deck composite section with both materials transformed to equivalent deck steel material

I'_2 = moment of inertia for girder and concrete deck composite section with both materials transformed to equivalent deck steel material

S'_{c_2} = section modulus to the top of the concrete deck for girder and concrete deck composite section with both materials transformed to equivalent deck steel material

e_2 = distance from concrete deck centroid to centroid of girder and concrete deck composite section with both materials transformed to equivalent deck steel material

M_{pier} = $6\,(7\phi_1+9\phi_2) \Big/ \left(\dfrac{37}{E_s I'_1}+\dfrac{27}{E_s I'_2}\right)$

$\phi_1 = Q_1 e_1 / E_s I'_1$

$Q_1 = 0.5\ A_s E_s \varepsilon_f$

$\phi_2 = Q_2 e_2 / E_s I'_2$

$Q_2 = A_{deck}\ E_c\ \varepsilon_{f.}$

D4 REFERENCES

1. Branson, D.E., "Time-Dependent Effects in Composite Concrete Beams," ACI Journal", Vol. 61, No. 2, February 1964, pp. 213–230.

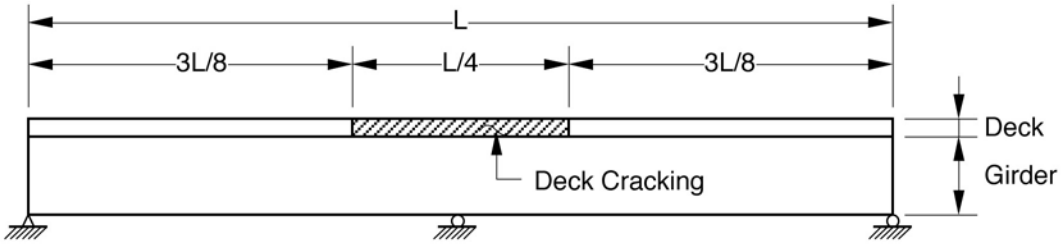

(a) Two-span girder.

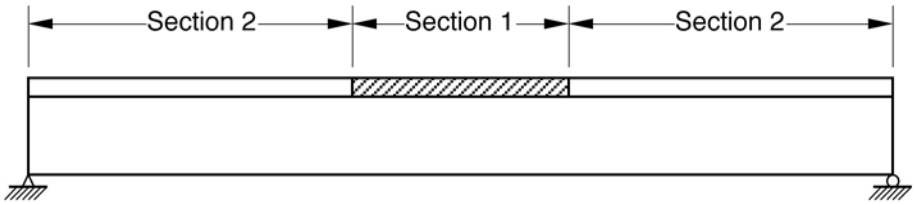

(b) Redundant support removed.

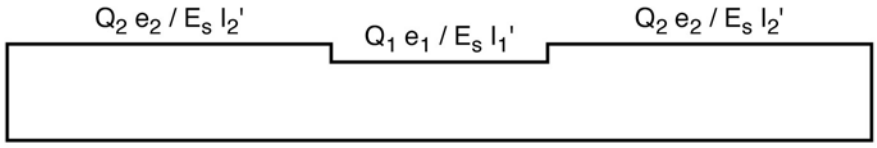

(c) M/EI diagram for restraint moments.

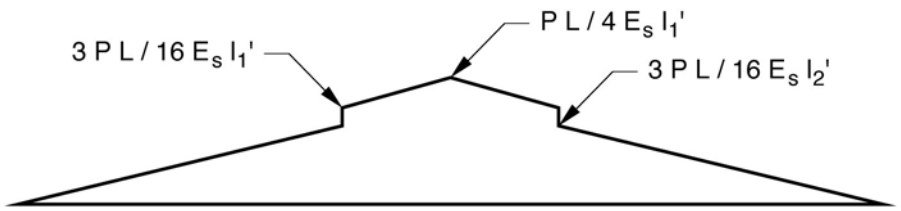

(d) M/EI diagram for a concentrated load at midspan.

Figure D-1. Two-span girder with secondary continuity effects.

HRDI-07/05-07(WEB)E